Methods in Molecular Biology 1444

Springer Protocols

Mingfeng Bai *Editor*

In Vivo Fluorescence Imaging

Methods and Protocols

Humana Press

METHODS IN MOLECULAR BIOLOGY

Series Editor
John M. Walker
School of Life and Medical Sciences
University of Hertfordshire
Hatfield, Hertfordshire, AL10 9AB, UK

For further volumes:
http://www.springer.com/series/7651

In Vivo Fluorescence Imaging

Methods and Protocols

Edited by

Mingfeng Bai

University of Pittsburgh, Pittsburgh, PA, USA

Humana Press

Editor
Mingfeng Bai
University of Pittsburgh
Pittsburgh, PA, USA

ISSN 1064-3745 ISSN 1940-6029 (electronic)
Methods in Molecular Biology
ISBN 978-1-4939-3719-6 ISBN 978-1-4939-3721-9 (eBook)
DOI 10.1007/978-1-4939-3721-9

Library of Congress Control Number: 2016939974

Printed on acid-free paper

This Humana Press imprint is published by Springer Nature
The registered company is Springer Science+Business Media LLC New York

Preface

Fluorescence imaging is widely used for biomedical research due to its high sensitivity and resolution, as well as low instrument cost. Although conventionally used to study biology at cellular and tissue levels, fluorescence imaging is emerging as a valuable tool for investigating physiological and pathophysiological processes in living systems. In the clinical setting, fluorescence imaging techniques, particularly those utilizing light in the near infrared (NIR) spectroscopic region where deep tissue penetration and low interference by tissue autofluorescence are offered, have been successfully used to provide real-time guidance in oncologic surgery. Undoubtedly, in vivo fluorescence imaging will continue to significantly impact biological research, drug discovery, and clinical practice.

The fast-growing field of in vivo fluorescence imaging has attracted new researchers, who often express the desire and need for detailed procedures, methods, and troubleshooting guides. This book was prepared to meet this need, which includes a rich variety of applications using various instrumentations (fluorescence reflectance imaging, fluorescence lifetime imaging, fluorescence molecular tomography, diffuse optical tomography, two-photon microscopy, and goggle system for intraoperative imaging), probes (fluorescent dyes, proteins, targeted and activatable probes, and nanoparticles), disease models (cancer, inflammation, and aplastic anemia), and targets (cancer cells, tumor microenvironment, and intracellular metals) to account for the multidisciplinary nature of the field. We have also included chapters on the emerging fields of cell tracking, image-guided treatment, and fluorescence imaging in the second NIR window. In addition, protocols for evaluation methods before and after in vivo imaging are also presented. Furthermore, this book includes reviews on bioconjugation and biostatistical analysis methods to provide guidance on fluorescent probe development and imaging data analysis. All procedures are described in a practical manner, and we very much hope that researchers from different fields will find this book valuable for them to become familiar with in vivo fluorescence imaging.

Pittsburgh, PA, USA *Mingfeng Bai*

Contents

Preface . . . . . *v*
Contributors . . . . . *ix*

1 Before In Vivo Imaging: Evaluation of Fluorescent Probes Using Fluorescence Microscopy, Multiplate Reader, and Cytotoxicity Assays 1
Shaojuan Zhang

2 Bioconjugation Methods for Coupling Targeting Ligands with Fluorescent Dyes 15
Xiaoxi Ling

3 In Vivo Fluorescence Reflectance Imaging with Subcutaneous Mouse Tumor Models 27
Jie Cao and Mingzhou Zhou

4 FRET Imaging of Enzymatic Activities Using Smart Probes 37
Jinbo Li, Yan Zhang, and Zhen Cheng

5 Fluorescence Imaging of Inflammation in Live Animals 45
Mingzhou Zhou, Jie Cao, and Walter J. Akers

6 Fluorescence Lifetime Imaging of Cancer In Vivo 55
Owen Peng and Walter J. Akers

7 Noninvasive Imaging of Fluorescent Reporters in Small Rodent Models Using Fluorescence Molecular Tomography 67
Weizhou Hou and Steve H. Thorne

8 In Vivo Tumor Angiogenesis Imaging Using Peptide-Based Near-Infrared Fluorescent Probes 73
Rui Huang, Peter S. Conti, and Kai Chen

9 Intraoperative Fluorescence Imaging and Multimodal Surgical Navigation Using Goggle System 85
Christopher A. Mela, Francis A. Papay, and Yang Liu

10 Utilization of Near-Infrared Fluorescent Imaging for Pharmaceutically Relevant Applications 97
Jelena M. Janjic, Sravan Kumar Patel, and Christina Bagia

11 In Vivo Cell Tracking Using Two-Photon Microscopy 109
Daniela Malide

12 Small-Animal Imaging Using Diffuse Fluorescence Tomography 123
Scott C. Davis and Kenneth M. Tichauer

13 In Vivo Metal Ion Imaging Using Fluorescent Sensors 139
Genevieve C. Van de Bittner and Tasuku Hirayama

14 Using Fluorescence Imaging to Track Drug Delivery and Guide Treatment Planning In Vivo 153
Qiaoya Lin, Huang Huang, Juan Chen, and Gang Zheng

15 In Vivo Fluorescence Imaging in the Second Near-Infrared Window Using Carbon Nanotubes 167
Guosong Hong and Hongjie Dai

16 Ex Vivo Imaging, Biodistribution, and Histological Study in Addition to In Vivo Imaging. 183
Shaojuan Zhang

17 Experimental Design and Data Analysis of In Vivo Fluorescence Imaging Studies 193
Ying Ding and Hui-Min Lin

Index. *211*

Contributors

Walter J. Akers • *Department of Radiology, Washington University School of Medicine, St. Louis, MO, USA*

Christina Bagia • *Graduate School of Pharmaceutical Sciences, Mylan School of Pharmacy, Duquesne University, Pittsburgh, PA, USA*

Genevieve C. Van de Bittner • *Department of Radiology, Athinoula A. Martinos Center for Biomedical Imaging, Massachusetts General Hospital, Harvard Medical School, Charlestown, MA, USA*

Jie Cao • *Optical Radiology Lab, Department of Radiology, Washington University in St. Louis, St. Louis, MO, USA*

Juan Chen • *Princess Margaret Cancer Center, University Health Network, Toronto, ON, Canada*

Kai Chen • *Molecular Imaging Center, Department of Radiology, Keck School of Medicine, University of Southern California, Los Angeles, CA, USA*

Zhen Cheng • *Molecular Imaging Program at Stanford (MIPS), Department of Radiology and Bio-X Program, Stanford University, Stanford, CA, USA*

Peter S. Conti • *Molecular Imaging Center, Department of Radiology, Keck School of Medicine, University of Southern California, Los Angeles, CA, USA*

Hongjie Dai • *Department of Chemistry, Stanford University, Stanford, CA, USA*

Scott C. Davis • *Thayer School of Engineering, Dartmouth College, Hanover, NH, USA*

Ying Ding • *Department of Biostatistics, University of Pittsburgh, Pittsburgh, PA, USA*

Tasuku Hirayama • *Laboratory of Medicinal and Pharmaceutical Chemistry, Gifu Pharmaceutical University, Gifu, Japan*

Guosong Hong • *Department of Chemistry and Chemical Biology, Harvard University, Cambridge, MA, USA; Department of Chemistry, Stanford University, Stanford, CA, USA*

Weizhou Hou • *Department of Radiology, Hillman Cancer Center, University of Pittsburgh, Pittsburgh, PA, USA*

Huang Huang • *Princess Margaret Cancer Center, University Health Network, Toronto, ON, Canada; DLVR Therapeutics Inc., Toronto, ON, Canada*

Rui Huang • *Molecular Imaging Center, Department of Radiology, Keck School of Medicine, University of Southern California, Los Angeles, CA, USA*

Jelena M. Janjic • *Graduate School of Pharmaceutical Sciences, Mylan School of Pharmacy, Duquesne University, Pittsburgh, PA, USA*

Jinbo Li • *School of Chemistry and Chemical Engineering, Nanjing University, Nanjing, China*

Hui-Min Lin • *Department of Biostatistics, University of Pittsburgh, Pittsburgh, PA, USA*

Qiaoya Lin • *Princess Margaret Cancer Center, University Health Network, Toronto, ON, Canada; Department of Medical Biophysics, University of Toronto, Toronto, ON, Canada; Britton Chance Center for Biomedical Photonics, Wuhan National Laboratory for Optoelectronics, Huazhong University of Science & Technology, Wuhan, China*

Xiaoxi Ling • *Department of Radiology, University of Pittsburgh, Pittsburgh, PA, USA*

Yang Liu • *Department of Biomedical Engineering, The University of Akron, Akron, OH, USA*
Daniela Malide • *Light Microscopy Core Facility, National Heart, Lung, and Blood Institute, National Institute of Health, Bethesda, MD, USA*
Christopher A. Mela • *Department of Biomedical Engineering, The University of Akron, Akron, OH, USA*
Francis A. Papay • *Department of Dermatology and Plastic Surgery Institute, Cleveland Clinic, Cleveland, OH, USA*
Sravan Kumar Patel • *Graduate School of Pharmaceutical Sciences, Mylan School of Pharmacy, Duquesne University, Pittsburgh, PA, USA*
Owen Peng • *Department of Radiology, Washington University School of Medicine, St. Louis, MO, USA*
Steve H. Thorne • *Department of Radiology, Hillman Cancer Center, University of Pittsburgh, Pittsburgh, PA, USA*
Kenneth M. Tichauer • *Armour College of Engineering, Illinois Institute of Technology, Chicago, IL, USA*
Shaojuan Zhang • *Molecular Imaging Lab, Department of Radiology, University of Pittsburgh, Pittsburgh, PA, USA*
Yan Zhang • *School of Chemistry and Chemical Engineering, Nanjing University, Nanjing, China*
Gang Zheng • *Princess Margaret Cancer Center, University Health Network, Toronto, ON, Canada; Department of Medical Biophysics, University of Toronto, Toronto, ON, Canada*
Mingzhou Zhou • *Department of Radiology, Washington University School of Medicine, St. Louis, MO, USA*

Chapter 1

Before In Vivo Imaging: Evaluation of Fluorescent Probes Using Fluorescence Microscopy, Multiplate Reader, and Cytotoxicity Assays

Shaojuan Zhang

Abstract

Fluorescent probes are widely utilized for noninvasive fluorescence imaging. Continuing efforts have been made in developing novel fluorescent probes with improved fluorescence quantum yield, enhanced target-specificity, and lower cytotoxicity. Before such probes are administrated into a living system, it is essential to evaluate the subcellular uptake, targeting specificity, and cytotoxicity in vitro. In this chapter, we briefly outline common methods used to evaluate fluorescent probes using fluorescence microscopy, multiplate reader, and cytotoxicity assay.

Key words Fluorescence microscopy, Multiplate reader, Cytotoxicity, Targeting specificity

1 Introduction

Before a fluorescent probe is administered into living animals for in vivo imaging, it is critical to investigate the biological characteristics of the probe in cells to answer the following questions. How much cellular uptake of the probe may be achieved in target cells? What is the binding affinity between the probe and the target receptor or cellular function (pH, oxygen level, ions etc.)? Is the probe safe for cellular and animal studies? An ideal fluorescent probe should have good cellular uptake, strong and specific binding affinity towards the target, and low toxicity. This collection of protocols provides a basic guide for the evaluation of fluorescent probes by addressing each of these essential questions, and includes the following sections: (1) evaluation of cellular uptake and localization using fluorescence microscopy, (2) evaluation of binding specificity using multiplate reader, and (3) evaluation of safety profile using cytotoxicity assay.

The uptake and localization of fluorescent probes in cells is typically visualized using a fluorescence microscope. To confirm

Mingfeng Bai (ed.), *In Vivo Fluorescence Imaging: Methods and Protocols*, Methods in Molecular Biology, vol. 1444,
DOI 10.1007/978-1-4939-3721-9_1,

the subcellular localization or targeted cellular function, the signal from an in vivo fluorescent probe and the signal from fluorescent staining that specifically label particular cell organelle or cellular function are often compared to provide an observation if the two are closely related. This is called colocalization study and often done by overlapping the same cellular images taken through filter sets with different wavelength windows. These staining agents are widely available from commercial sources. Caution should be exercised when selecting the appropriate fluorescent staining agents. It is critical to choose a staining agent with distinct spectroscopic region from that of the in vivo fluorescent probe to avoid signal mixing. Some of staining agents prefer living cells; some others can only be used in fixed cells; whereas the rest may work in both conditions. Many agents have been developed to indicate specific cellular structures, such as plasma membrane, cytoskeleton, cytosol, endoplasmic reticulum, endosomes, Golgi complex, mitochondria, nucleus, lysosomes, and peroxisome. Advanced fluorescent staining agents can also act as sensors to provide physiological information such as pH value [1], intracellular oxygen level [2], or reactive oxygen species (ROS) production level [3]. Some can even be activated and switched on/off upon binding with specific target [4] or cleaved by certain enzymes [5]. As such, fluorescent microscopy has become a powerful tool to evaluate fluorescent probes in vitro.

While fluorescence microscopy offers qualitative visualization of fluorescent probes in cells, multiplate reader allows for rapid quantification of the overall fluorescence signal from cells in batch. Multiplate reader also provides an alternative method to determine receptor binding affinities of fluorescent probes [6], which have been historically determined using radioligands, a costly and less desirable technology that involves working with radioactive hazardous materials. Multiplate reader can quickly quantify fluorescent probe binding to targeted receptor in living cells using multi-well plates, analogous to whole-cell radioligand binding assays, but with inherent safety and cost advantages.

Cytotoxicity of fluorescent probes must be evaluated before they are shown the green light to in vivo study. Cell cytotoxicity assays are commonly used to such purpose by discriminating dead cells population from living cells. Various cell functions can be utilized by these assays to differentiate dead or living cells, including enzyme activity, cell membrane permeability, cell adherence, ATP production, coenzyme production, and nucleotide uptake activity. Traditionally, cell viability is tested with dye exclusion assays, which involves counting dead cells after staining with a vital dye, or clonogenic assays, which measures the percentage of cells capable of giving rise to clones. For example, dye exclusion test using Trypan blue is a simple way to evaluate cell membrane integrity (and thus assume cell proliferation or death). However, these conventional assays are labor-intensive and subjective to observer error. These limitations have been overcome with newer assays such as MTT (3-(4,5-dimethylthiazol-2-yl)-2,5-dip

henyltetrazolium bromide), which provides a simple, automated and highly efficient method for evaluating an agent's toxicity in vitro [7]. MTT, a yellow tetrazole salt, is reduced to purple formazan in the mitochondria of living cells, and the absorbance of the resulting purple solution can be quantified by a spectrophotometer. This reduction takes place only when mitochondrial reductase is active, hence in living cells. Therefore, the absorption intensity can be directly related to the number of viable (living) cells. In this chapter, MTT assay is used as an example for the evaluation of cytotoxicity.

2 Materials

2.1 Cell Culture Related Equipment and Reagents

1. Sterile biosafety cabinet.
2. Humidified CO_2 incubator.
3. Pipette-aid.
4. Corning Cell Culture Treated T-75 Flasks (COSH HEALTHCARE: #1012637).
5. 24-well cell culture plates.
6. 5 mL and 10 mL sterile serological pipettes (VWR INTERNATIONAL: #89130-896 and #89130-898).
7. 2 mL VWR disposable polystyrene aspirating pipettes (VWR INTERNATIONAL: #414004-265).
8. Deionized water.
9. Dulbecco's Modified Eagle's Medium (DMEM, Sigma Aldrich: #D6546).
10. HyClone Fetal Bovine Serum (FBS), USDA Tested (FISHER SCIENTIFIC: #SH3091003).
11. Penicillin–Streptomycin–Glutamine (100×) (Life Technologies: #10378-016).

2.2 Fluorescence Microscopy Equipment and Reagents

1. Materials listed in Subheading 2.1.
2. Fluorescence microscope.
3. Gelatin-coating solution: 0.1% gelatin (ATCC: #PCS-999-027).
4. Sterilized coverslips (Corning: #2975-225).
5. MatTek 35 mm glass bottom culture dish (MatTek: #P35G-1.5-14-C).
6. Nunc Lab-Tek II Chamber Slide (Thermo Scientific: #154534).
7. 1× PBS (phosphate buffered saline).
8. Fixative solution: 4% paraformaldehyde in PBS.
9. Triton X-100 in 1× PBS. Diluted to 0.1–0.5% (v/v) in PBS before use.
10. DAPI (4′,6-diamidino-2-phenylindole) solution (Thermo Scientific: #62248).

11. Hoechst 33342 solution (Thermo Scientific: #H3570).
12. ProLong® Gold antifade mounting medium (Life Technologies: #P36930).
13. Nail polish.
14. Image-processing and analysis software.

2.3 Plate Reader Equipment and Reagents

1. Materials listed in Subheading 2.1.
2. BioTek Synergy H4 Multi-Mode Reader.
3. 96-well Optical Bottom Plate, Black Polystyrene, Cell Culture Treated, with lid, Sterile (FISHER SCIENTIFIC: #1256670).
4. 50 mL disposable VWR Reagent Reservoirs (VWR INTERNATIONAL: #89094-676).
5. DRAQ-5 (Cell signaling: #4084S).
6. Hank's Balanced Salt Solution (HBSS, Life Technologies: #14170-112).
7. Magnesium chloride hexahydrate (Sigma Aldrich: #M9272).
8. Albumin from bovine serum (BSA, Sigma Aldrich: #A7906).
9. Sodium azide (NaN_3).
10. Binding buffer: serum-free media, or HBSS with 1 mM Mg^{2+}, 0.1% BSA, and 0.1% NaN_3.
11. Washing buffer: serum-free media, PBS, or HBSS.

2.4 Cytotoxicity Assay Equipment and Reagents

1. Materials listed in Subheading 2.1.
2. 96-well Optical Bottom Plate, Black Polystyrene, Cell Culture Treated, with lid, Sterile (FISHER SCIENTIFIC: #1256670).
3. 50 mL disposable VWR Reagent Reservoirs (VWR INTERNATIONAL: #89094-676).
4. Multichannel pipettes (Eppendorf Research).
5. CellTiter 96® Non-Radioactive Cell Proliferation Assay (MTT) (Promega: #G4000).
6. CellTiter-Glo® Luminescent Cell Viability Assay (Promega: #G7570).

3 Methods

3.1 Evaluation of Fluorescent Probes Using Fluorescence Microscopy

3.1.1 Preparation for Live-Cell imaging

1. For cell microscopy, cells must be grown in cellware (*see* **Note 1**) that are amenable to optical imaging. Cells are seeded (*see* **Note 2**) at an appropriate density and allowed to attach to the cellware (*see* **Note 3**). Cells are usually seeded 24 h prior to imaging experiments to achieve 60–80% confluence.
2. Cells are treated with a solution of the fluorescent probe in culture medium and incubated until the fluorescent probe has

bound to the target. To ensure optimal probe binding, probe concentration and incubation time should be optimized.

3. (Optional) To identify the subcellular localization of fluorescent probe, cells are often labeled with organelle-selective stains to highlight the targets of interest. Popular choices include Hoechst for nucleus staining, MitoTracker® for mitochondria, etc. (*see* **Note 4**).
4. Remove unbound probes by rinsing the cells with PBS for three times.
5. Prepare the cellware for microscopy. For chamber slide, keep the sample submerged in liquid by adding PBS and mount the slide using coverslip (*see* **Note 5**). For glass bottom dish, preserve the sample by adding PBS.

3.1.2 Preparation for Fixed-Cell Imaging

1. Prepare cells using the methods described above (**steps 1–3** under Subheading 3.1.1).
2. To fix cells, cells are treated with 4% (v/v) paraformaldehyde in PBS (*see* **Note 6**) for 20 min at room temperature followed by three sequential rinses with PBS.
3. To permeabilize the cells, cells are treated with 0.1% Triton X-100 in PBS (*see* **Note 7**) for 15 min at room temperature followed by three sequential rinses with PBS.
4. (Optional) Cells are treated with additional stains that require post-fixation condition. For example, DAPI is often applied after all other stains and fixation.
5. Remove unbound probes by rinsing the cells with PBS for three times.
6. Prepare the cellware for microscopy. Cover the cells on chamber slide using ProLong® mounting medium. Mount the slide using coverslip (*see* **Note 5**). Allow the ProLong® mounting medium to dry overnight at room temperature (*see* **Note 8**).

3.1.3 Fluorescence Imaging

1. Visualize the cells using a fluorescence microscope equipped with the appropriate filters (*see* **Note 9**).
2. Once the cells are in focus, turn off the visible light source. You will not be able to see the fluorescent signal if the visible light is on.
3. Capture fluorescence images (*see* **Note 10**).
4. Optional: phase contrast/differential interference contrast (DIC) images can be used to provide morphological information of cells.
5. Analyze the fluorescent images using image-processing and analysis software such as Image J.

See Fig. 1 as an example [8]. The images of CB_2-mid DBT cells, which express CB_2 receptor, were acquired using three filters

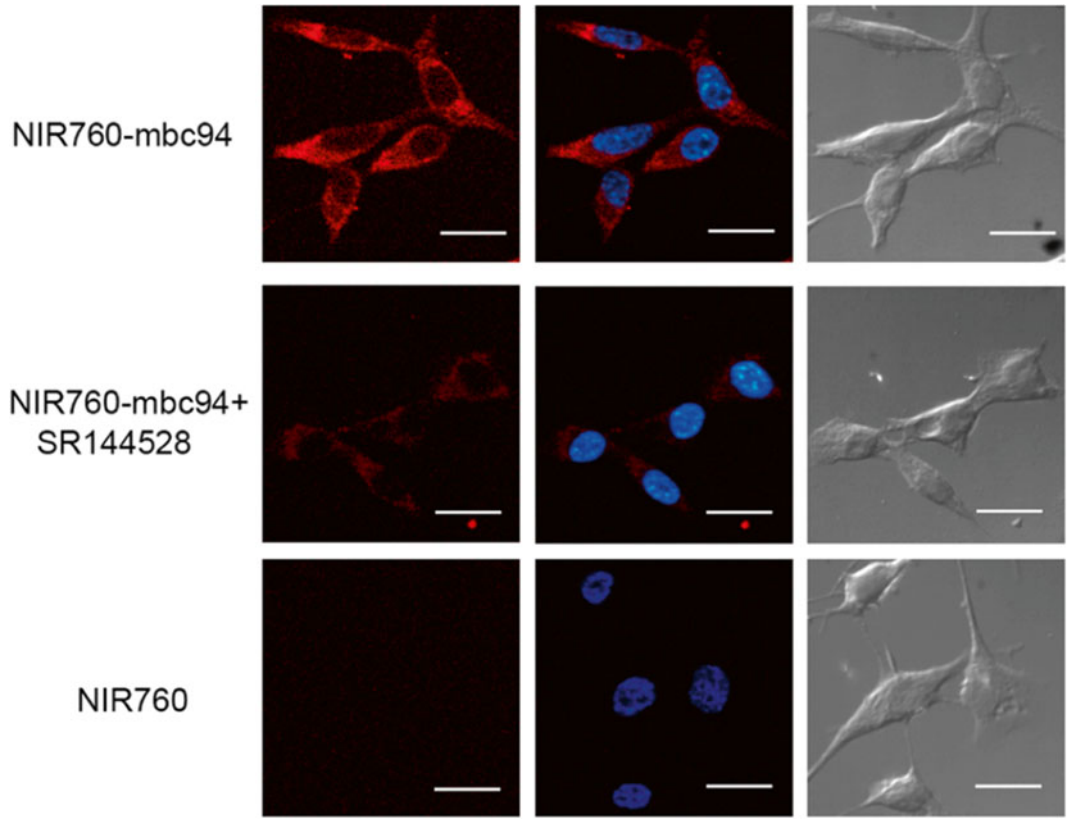

Fig. 1 Fluorescent imaging using fluorescent probe NIR760-mbc94 in CB_2-mid DBT cells. Cells were preincubated with or without blocking agent SR144528 and were then incubated with NIR760-mbc94 or free NIR760. The cell nucleus was stained with DAPI. Fluorescent cell imaging was obtained using Zeiss Axio Observer fluorescent microscopy with ApoTome 2 imaging system. From *left* to *right*: indocyanine green (*ICG*) filter (*red*), ICG filter (*red*) + DAPI filter (*blue*) merged, DIC. All fluorescence images are on the same scale. Scale bars = 20 μm. Reprinted with permission from [8]. Copyright 2013 American Chemical Society

(ICG, DAPI, and DIC). The subcellular location information of a CB_2 receptor-targeted probe (NIR760-mbc94) was demonstrated using merged images from ICG (fluorescence from NIR760-mbc94) and DAPI (nuclear staining) filter. DIC images were used to provide morphological information of cells.

3.2 Evaluation of Fluorescent Probes Using Multiplate Reader

3.2.1 Quantification of Cell Uptake and Binding Specificity Using Multiplate Reader

1. Cells of interest are grown to confluence in T75 flasks, harvested, and seeded (approximately $1–5 \times 10^4$ cells per well) into a 96-well plate (*see* **Note 11**).
2. Incubate the plate at 37 °C, 5 % CO_2 for 24 h.
3. Aspirate and replace culture medium with 100 μL binding buffer (*see* **Note 12**) containing the fluorescent probes with or without the blocking agent (competitor) (*see* **Notes 13** and **14**).

- For co-treatment, incubate cells with test fluorescent probe and the blocking agent for 30 min at 37 °C. The incubation time is subjected to optimization.
- For pretreatment, cells are treated with 100 μL culture medium with the blocking agent for 30 min at 37 °C, and then treated with the fluorescent probe for an additional 30 min at 37 °C. The incubation time is subjected to optimization.

4. Read fluorescence intensity prior to washing as the initial reading.
5. Wash the cells with 100 μL washing buffer to remove unbound fluorescent probe, and repeat 2–5 times if necessary (*see* **Note 15**).
6. Read fluorescence intensity.
7. Optional: Normalize the fluorescence intensity recorded with the initial reading (*see* **Note 16**).
8. Fix the cells with 4% paraformaldehyde in PBS for 10 min at room temperature and rinse twice with PBS.
9. Permeabilize the cells with 0.1% Triton X-100 in PBS (*see* **Note 7**) for 5 min at room temperature and rinse twice with PBS.
10. Incubate cells with DRAQ-5 (1:2500) for 5 min at room temperature and rinse twice with PBS.
11. Record fluorescence at 650/690 nm (excitation/emission) for cell number quantification.
12. Normalize the final results with cell number.

See Fig. 2 as an example [8]. Cellular uptake of NIR760-mbc94 was determined using a multiplate reader.

3.2.2 Saturation Binding Assay Using Multiplate Reader

1. Cells of interest are grown to confluence in T75 flasks, harvested, and seeded (approximately $1–5 \times 10^4$ cells per well) into a 96-well plate (*see* **Note 11**).
2. Incubate the plate at 37 °C, 5% CO_2 for 24 h.
3. Divide the cells into two groups: blocking (nonspecific binding) and non-blocking (total binding).
4. Optional: For pretreatment (to achieve better blocking results), incubate the blocking group with the final concentration of the blocking agent (e.g., 10 μM) in binding buffer at 37 °C for 30 min. Simultaneously, incubate the non-blocking group with vehicle of the same volume at 37 °C.
5. For the blocking group, prepare multiple solutions in small tubes with increasing concentration of the fluorescent probe (e.g., 5.0, 10, 20, 40, 80, 120, 160, 200, 400, 600, 800 nM, 1 μM) and the blocking agent with the predetermined final concentration (e.g., 10 μM).

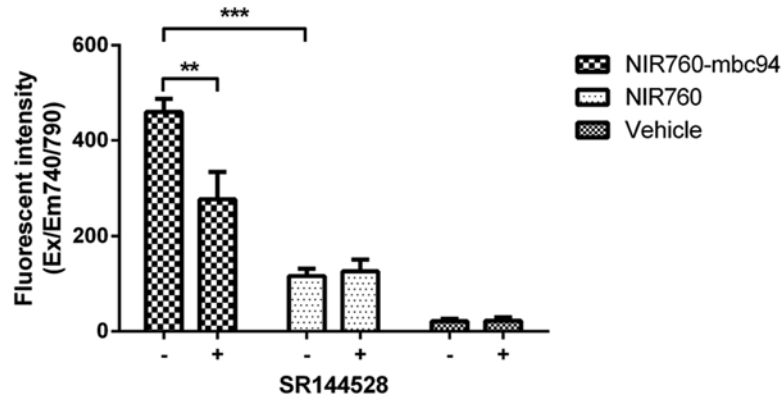

Fig. 2 Quantitative cell uptake of fluorescent probe NIR760-mbc94. CB_2-mid DBT cells were preincubated with or without blocking agent SR144528 and were then incubated with NIR760-mbc94 or free NIR760. Cells were washed to remove the unbound fluorescent probes. Fluorescent intensity was measured with a Synergy H4 Hybrid Multi-Mode Microplate Reader. Each data point represents the mean ± SD based on triplicate samples (**$p < 0.01$ and ***$p < 0.001$). Reprinted with permission from Ref. 8. Copyright 2013 American Chemical Society

6. For the non-blocking group, prepare the same multiple solutions as above with increasing concentration of the fluorescent probe (e.g., 5.0, 10, 20, 40, 80, 120, 160, 200, 400, 600, 800 nM, 1 μM), but no blocking agent.
7. Aspirate and replace culture medium with 100 μL of each solution prepared above.
8. Incubate the cells for 30 min at 37 °C (*see* **Note 14**).
9. Wash the cells with 100 μL washing buffer to remove unbound fluorescent probe, repeat 2–5 times if necessary (*see* **Note 15**).
10. Read fluorescence intensity.
11. Fix the cells with 4% paraformaldehyde in PBS for 10 min at room temperature and rinse twice with PBS.
12. Permeabilize the cells with 0.1% Triton X-100 in PBS (*see* **Note 7**) for 5 min at room temperature and rinse twice with PBS.
13. Incubate cells with DRAQ-5 (1: 2500) for 5 min at room temperature and rinse twice with PBS.
14. Record fluorescence at 650/690 nm (excitation/emission) for cell number quantification.
15. Normalize the final results with cell number.
16. Analyze saturation binding assay using GraphPad Prism v5.0 built-in functions for corresponding assay types. The specific binding is obtained by subtraction of the nonspecific binding from the total binding. The dissociation constant (K_d) and receptor density (B_{max}) are estimated from the nonlinear fitting of the specific binding versus the concentration of test fluorescent probe.

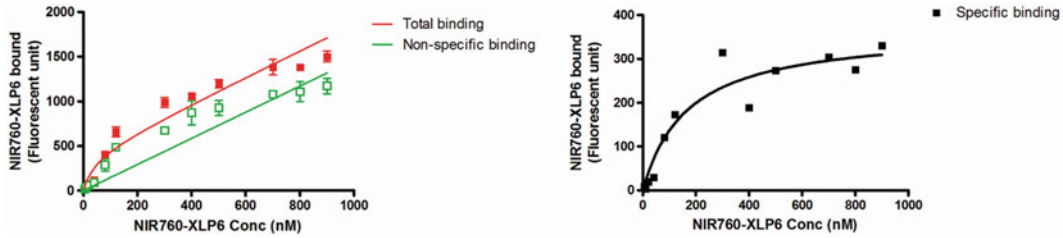

Fig. 3 Saturation binding assay of NIR760-XLP6 in DBT-CB_2 cells. *Left*: Fluorescence intensity as a function of concentration of NIR760-XLP6 in DBT-CB_2 cells with or without pretreatment of XLP4 as the total and nonspecific binding of NIR760-XLP6 in DBT-CB_2 cells, respectively. *Right*: Specific binding obtained by the subtraction of the fluorescence intensity of nonspecific binding from that of the total binding as a function of concentration of NIR760-XLP6 in DBT-CB_2 cells. Each data point represents the mean ± SEM based on triplicate samples. Reprinted with permission from Ref. 9. Copyright 2015 Elsevier Ltd

See Fig. 3 as an example [9]. The binding affinity of a CB_2 receptor-targeted fluorescent probe, NIR760-XLP6, was determined by plotting the fluorescence signal from cells treated with NIR760-XLP6 as a function of the probe concentration.

3.3 Evaluation of Fluorescent Probes Using Cytotoxicity Assays

1. Cells of interest are grown to confluence in T75 flasks, harvested, and seeded (approximately 1–5 × 10^4 cells per well) into a 96-well plate.
2. Incubate the plate at 37 °C, 5% CO_2 for 24 h prior to assay.
3. Treat cells with 100 μL of test fluorescent probes at various concentrations (e.g., 80, 40, 20, 10, 5, 2.5, 1.25, 0.625, 0 μM).
4. For control experiments, treat cells with the corresponding controls (*see* **Note 17**) at various concentrations (e.g., 80, 40, 20, 10, 5, 2.5, 1.25, 0.625, 0 μM).
5. Incubate the cells at 37 °C for 24–72 h. The time for treatment can be extended depending on the desired experimental design.
6. After the incubation, add 10 μL MTT solution (stock: 5 mg/mL in PBS) to each well (final concentration of 0.45 mg/mL).
7. Incubate for 4 h at 37 °C in a humidified, 5% CO_2 atmosphere.
8. Remove media. Do not disturb cells and do not rinse with PBS.
9. Add 100 μL MTT Solubilization Solution/Stop Mix to each well to dissolve formazan crystals.
10. Allow the plate to stand for at least 1 h (*see* **Note 18**) in a sealed container with a humidified atmosphere at room temperature.
11. Agitate cells on an orbital shaker for 15 min.
12. Read absorbance at 570 nm with a reference filter of 630–750 nm (*see* **Note 19**).

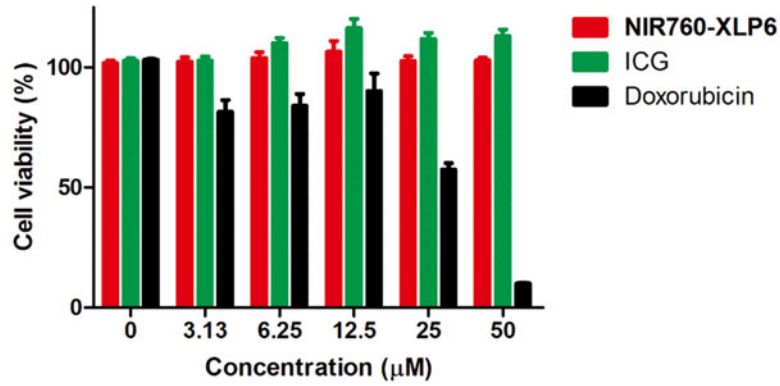

Fig. 4 Cytotoxicity of NIR760-XLP6. DBT-CB_2 cells were treated with NIR760-XLP6 (*red*), ICG (*green*), or Doxorubicin (*black*) respectively. Cell viability was assessed by the CellTiter-Glo® Luminescent Cell Viability Assay kit. Each data point represents the mean ± SEM based on triplicate samples. Reprinted with permission from Ref. 9. Copyright 2015 Elsevier Ltd

See Fig. 4 as an example [9]. Cell viability of NIR760-XLP6 at various concentrations was accessed using a multiplate reader and compared with that of indocyanine green (ICG, an FDA-approved dye) and doxorubicin (a chemotherapy drug).

4 Notes

1. Chamber slide system with multiple chambers offers a convenient tool to grow cells directly on microscopy-ready slide for different treatments. For inverted microscopes, the objective lens is below the sample. Use of glass bottom culture dish with #1.5 glass cover (160–190 μm thick) is recommended.
2. For suspension cell culture, specific coating (e.g., poly-d-lysine, collagen, fibronectin) may be required for better cell-adhering results. Refer to the literature for the appropriate coating.
3. For example, 3×10^4 cells per chamber are seeded in an 8-well chamber slide (0.7 cm^2/well). This number is subject to the growth rate of the cells and culture area.
4. When multiple stains are utilized, the emission profile of each stain should be carefully selected in advance to prevent signal overlapping. Commercialized stains with various emission wavelengths are often available.
5. The thickness of the coverslip is critical for optimal image quality. The ideal thickness of coverslip is 170 μm. For most studies, #1.5 glass coverslip is recommended. Extra caution should be paid when mounting the coverslip to avoid trapping air

bubbles. Generally, this may be achieved by gradually lowering down the coverslip on wet sample with an angle and permit the air to escape from one side.

6. Paraformaldehyde fixation can result in hydrophobic cross-linking of tissue proteins. Typical cell-fixation protocols use 4% paraformaldehyde in PBS for 10–20 min. Avoiding prolonged fixation time is advised when using paraformaldehyde as a fixing agent. Other commonly used fixing agents include organic solvents, such as methanol and acetone, which don't alter target proteins covalently. Acetone and methanol are generally used ice-cold (4 °C). Fix cells in −20 °C methanol or acetone for 5–10 min. Permeabilization step is not needed following methanol or acetone fixation.
7. This is generally achieved with a mild surfactant, which dissolves cell membranes in order to allow larger dye molecules to get inside the cells.
8. Alternatively, the coverslips may be sealed to the slide by applying nail polish or glue along the edges.
9. Select appropriate filter cube for the fluorochrome you want to image. Common filters include DAPI dye filter, fluorescein isothiocyanate dye (FITC) filter, Texas Red dye filter, and ICG filter.
10. Fluorescence microscope parameters (i.e., filter set, exposure time, gain, and other parameters) should first be optimized. When comparing fluorescent molecules (e.g., comparing a targeted fluorescent probe with the corresponding non-targeted free dye to demonstrate binding specificity). The same condition should be used throughout the subsequent experiments. It is critical that fluorescence images captured are not saturated.
11. The type of multi-well plate is critical for the success of fluorescence binding assay. A preferred microplate should have minimum back-scattered light and background fluorescence, as well as reduced autofluorescence and crosstalk between wells.
12. The presence of serum in the binding buffer has a critical role in the uptake and internalization of fluorescent probes [10]. Optimizing binding assay may involve adjusting the serum concentration in the binding buffer. For example, serum-free condition is recommended when studying G protein-coupled receptor (GPCR)-targeted fluorescent probes because there are many ligands for GPCR in serum that may lead to inaccurate results.
13. Generally, hydrophobic ligands show higher nonspecific binding. It is possible to reduce nonspecific binding with some of the following method: (a) use microplates built from different materials; (b) use 1% BSA to treat microplates prior to the addition of fluorescent probes or blocking agents; (c) add BSA, salts or detergents to the binding or washing buffer.

14. For better blocking results, the final concentration of blocking agents or fluorescent probe needs to be optimized. The ratio of the two may range from one to several thousands. Depending on the kinetics of the cellular uptake of the blocking agents and probes, the incubation time needs to be optimized. In addition to comparison between blocked and non-blocked samples, a sample with the corresponding non-targeted free dye is often used to further demonstrate the binding specificity.
15. Some fluorescent probes do not bind to the target receptor tightly, and the probe can be easily washed out from the binding site. In this case, the fluorescent signal may be decreased to a background level after a number of washing, resulting in unreliable binding affinity measurement. This problem can be solved by (a) increasing the gain of plate reader; (b) optimizing binding buffer and washing buffer with different combinations; (c) fixing and permeabilizing cells before the addition of the fluorescent probe; (d) cross check the result with radiolabeled saturation binding assay.
16. Normalization with the initial reading (fluorescence intensity before washing) is especially necessary when comparing different fluorescent probes, or when the initial fluorescence signal varies due to different treatments. This correction can minimize well-to-well fluorescence signal differences resulting from initial variations. The resulting fluorescent data are typically normalized to 1000 and expressed in terms of relative fluorescence units, RFU.
17. Typically, control experiments consist of a positive control that uses a toxic drug (e.g., Doxorubicin), a negative control that uses a known nontoxic fluorescence dye (e.g., ICG), and the vehicle in which the test probe is dissolved. The concentrations of controls should be kept the same as these of the test probe.
18. Due to the long experiment time, the result of MTT assay is often obtained on the second day. However, uneven evaporation of culture fluid in wells of multi-well plates may cause erroneous results.
19. MTT assays measure absorbance at 570 nm with a reference filter of 630–750 nm. If the absorption window of the test fluorescent probe overlaps with this range, the MTT assay result may be false. To solve this issue, ATP based CellTiter-Glo Luminescent Cell Viability Assay kit (Promega Corporation: # G7570) can be used. This assay measures the luminescence that represents the quantitation of the ATP present in living cells.

References

1. Han J, Burgess K (2010) Fluorescent indicators for intracellular pH. Chem Rev 110(5): 2709–2728
2. Quaranta M, Borisov SM, Klimant I (2012) Indicators for optical oxygen sensors. Bioanal Rev 4(2-4):115–157
3. Wang X, Fang H, Huang Z, Shang W, Hou T, Cheng A, Cheng H (2013) Imaging ROS signaling in cells and animals. J Mol Med (Berl) 91(8):917–927
4. Rao J, Dragulescu-Andrasi A, Yao H (2007) Fluorescence imaging in vivo: recent advances. Curr Opin Biotechnol 18(1):17–25
5. Weissleder R, Tung CH, Mahmood U, Bogdanov A Jr (1999) In vivo imaging of tumors with protease-activated near-infrared fluorescent probes. Nat Biotechnol 17(4): 375–378
6. Sexton M, Woodruff G, Cudaback E, Kreitzer FR, Xu C, Lin YH, Möller T, Bai M, Manning HC, Bornhop D, Stella N (2009) Binding of NIR-conPK and NIR-6T to astrocytomas and microglial cells: evidence for a protein related to TSPO. PLoS One 4(12):e8271
7. van Meerloo J, Kaspers GL, Cloos J (2011) Cell sensitivity assays: the MTT assay. In: Cree IA (ed) Cancer cell culture, vol 731, Methods in molecular biology. Humana, New York, pp 237–245
8. Zhang S, Shao P, Bai M (2013) In vivo type 2 cannabinoid receptor-targeted tumor optical imaging using a near infrared fluorescent probe. Bioconjug Chem 24(11):1907–1916
9. Ling X, Zhang S, Shao P, Li W, Yang L, Ding Y, Xu C, Stella N, Bai M (2015) A novel near-infrared fluorescence imaging probe that preferentially binds to cannabinoid receptors CB2R over CB1R. Biomaterials 57:169–178
10. Kosuge M, Takeuchi T, Nakase I, Jones AT, Futaki S (2008) Cellular internalization and distribution of arginine-rich peptides as a function of extracellular peptide concentration, serum, and plasma membrane associated proteoglycans. Bioconjug Chem 19(3):656–664

Chapter 2

Bioconjugation Methods for Coupling Targeting Ligands with Fluorescent Dyes

Xiaoxi Ling

Abstract

Targeted molecular imaging probes are essential tools for visualization of specific molecular processes in cells and living systems. Among these, targeted fluorescent probes are widely used due to the high sensitivity and resolution of fluorescence imaging. The conventional strategy for developing targeted fluorescent probes is to couple targeting ligands with fluorescent dyes by covalent bond via bioconjugation. Here, we describe several commonly used bioconjugation methods, from traditional amide and thiol coupling, to metal-catalyzed coupling reaction and catalyst free cycloaddition.

Key words Bioconjugation, Coupling reaction, Amide coupling, Thiol coupling, Targeted, Huisgen cycloaddition, Click chemistry, Michael addition, Suzuki coupling, Fluorescent probe, Molecular imaging, Inverse electron demand Diels–Alder cycloaddition

1 Introduction

This chapter details the commonly used bioconjugation methods for developing targeted fluorescent probes. Primary amino group is the most common functionality found in targeting molecules. A general bioconjugation strategy for amino group is amide coupling with a carboxylic acid group. Such a reaction typically involves coupling agents and base, and takes hours to complete. To speed up the reaction and simplify the purification process, activated carboxylic acid groups, such as *N*-hydroxysuccinimide (NHS) ester and isothiocyanate, are often used to react with primary amino group. In fact, many commercialized fluorescent dyes are designed with carboxylic acid or its activated forms as the conjugation site.

Thiol group is another popular functional group for bioconjugation, especially for peptides containing cysteine. The conventional method to conjugate thiol group is using iodoacetamide, however, Michael addition using maleimide has become more commonly used, which is faster, easier, and more selective. Some manufactures have already discontinued the supply of fluorescent

Mingfeng Bai (ed.), *In Vivo Fluorescence Imaging: Methods and Protocols*, Methods in Molecular Biology, vol. 1444,
DOI 10.1007/978-1-4939-3721-9_2,

dyes with iodoacetamide because of the more favorable maleimide functional group.

Certain metal catalysts are known for their ability to promote reactions that are otherwise difficult to take place. The Cu-catalyzed azide–alkyne cycloaddition (well known as click chemistry) and the Nobel Prize winning palladium (Pd)-catalyzed coupling reactions are both efficient and have been utilized to conjugate targeting ligands and fluorescent dyes. To meet the increasing interest of bioorthogonal chemistry that allows coupling in living systems, catalyst free inverse electron demand Diels–Alder reaction has been recently reported [1, 2], which can efficiently conjugate two molecules under mild conditions.

2 Materials

All solvents and reagents (*see* **Note 1**) can be purchased from commercial vendors and used as received.

Many fluorescent dyes are light sensitive. Their coupling reactions should be performed in the absence of light. If a dark room is not an option, covering the reaction with aluminum foil is an efficient solution to protect the fluorescent dye from photodegradation.

2.1 Direct Amide Coupling with Phosphonium/Uronium/Guanidinium Salt

1. *O*-(Benzotriazol-1-yl)-*N*,*N*,*N*′,*N*′-tetramethyluronium hexafluorophosphate (HBTU).
2. 1-Hydroxybenzotriazole (HOBt).
3. *N*, *N*-Diisopropylethylamine (DIPEA).
4. Anhydrous *N*,*N*-dimethylformamide (DMF).

2.2 Direct Amide Coupling with Carbodiimide

1. 1-Ethyl-3-(3-dimethylaminopropyl)carbodiimide (EDC).
2. 4-Dimethylaminopyridine (DMAP).
3. Anhydrous DMF.

2.3 Indirect Amide Coupling Through NHS Ester

1. DIPEA.
2. Dimethyl sulfoxide (DMSO).

2.4 Indirect Amide Coupling Through Acyl Chloride

1. Anhydrous tetrahydrofuran (THF).
2. DMF.
3. Thionyl chloride or oxalyl chloride.
4. Triethylamine (NEt_3).

2.5 Thiourea Coupling with Isothiocyanate

1. NEt_3.
2. Dichloromethane (DCM).

2.6 Michael Addition with Maleimide and Thiol

1. DMF.

2.7 Huisgen Cycloaddition (Click Chemistry) with Azide and Alkyne

1. Copper (II) sulfate ($CuSO_4$).
2. Sodium ascorbate.
3. DMF.
4. DIPEA.

2.8 Palladium-Catalyzed Coupling

1. Palladium(II) acetate ($Pd(OAc)_2$).
2. Tri(*o*-tolyl)phosphine.
3. Anhydrous DMF.
4. DIPEA.

2.9 Catalyst Free Inverse Electron Demand Diels–Alder [4+2] Cycloaddition

1. Water.

3 Methods

3.1 Direct Amide Coupling with Phosphonium/Uronium/Guanidinium Salt

1. Dissolve carboxylic acid functionalized fluorescent dye (0.10 mmol, 1.0 equiv., *see* **Note 2**), HBTU (0.12 mmol, 1.2 equiv., *see* **Note 3**), HOBt (0.12 mmol, 1.2 equiv.), and DIPEA (0.15 mmol, 1.5 equiv.) in anhydrous DMF (1.0 mL) under inert atmosphere at 0 °C.
2. After stirring the solution for 10 min, add the targeting ligand with primary amine (0.10 mmol, 1.0 equiv.) to the reaction. Gradually increase the reaction temperature to 25 °C.
3. After stirring the mixture for 18 h, remove the solvent by rotary evaporation and purify the product using the appropriate method.
   See Fig. 1 for sample reaction.

3.2 Direct Amide Coupling with Carbodiimide

1. Dissolve carboxylic acid functionalized fluorescent dye (0.10 mmol, 1.0 equiv.), EDC (0.10 mmol, 1.0 equiv., *see* **Note 4**), and DMAP (0.10 mmol, 1.0 equiv.) in anhydrous DMF (1.0 mL) under inert atmosphere at 25 °C.
2. After stirring for 30 min, add a solution of targeting ligand with primary amine (0.10 mmol, 1.0 equiv.) in anhydrous DMF (1.0 mL) to the reaction mixture.
3. After stirring the mixture for 18 h, remove the solvent by rotary evaporation and purify the product using the appropriate method.

   See Fig. 2 for sample reaction.

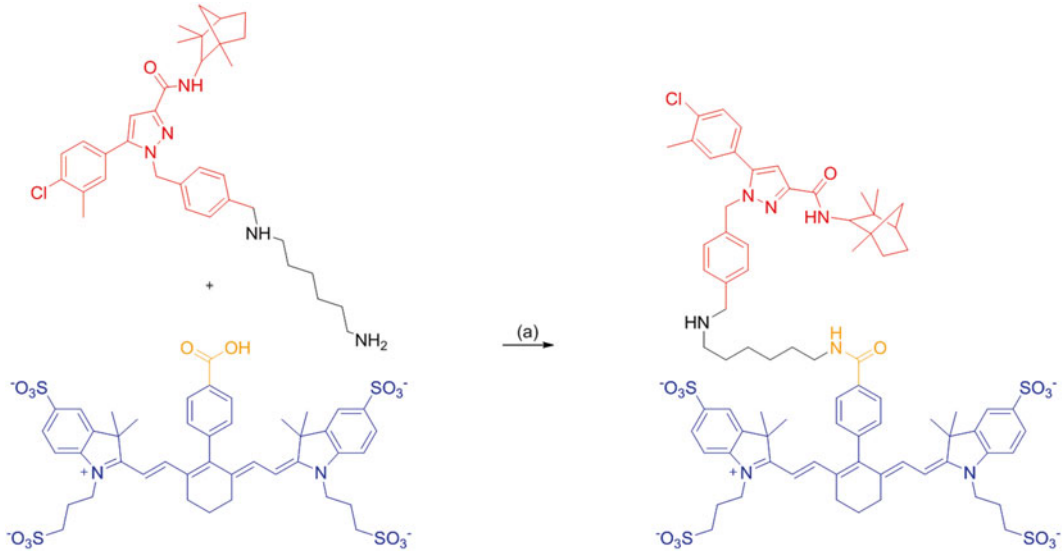

Fig. 1 Synthesis of type 2 cannabinoid receptor targeting near infrared fluorescent probe [1]: (a) HBTU, HOBt, DIPEA, DMF. Reproduced with permission from Ref. 1. Copyright (2013) American Chemical Society

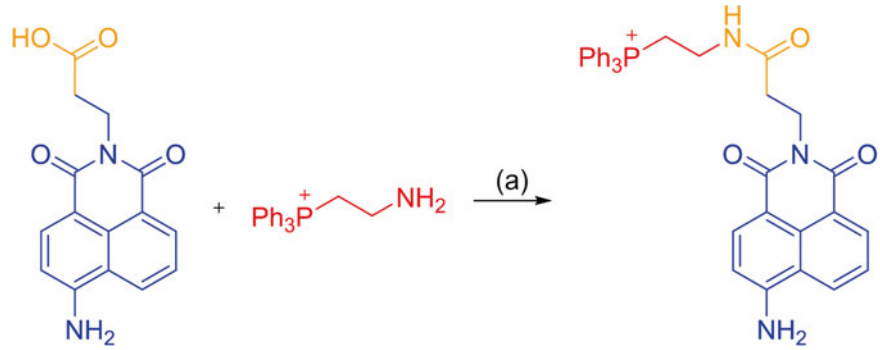

Fig. 2 Synthesis of mitochondrial-targeting naphthalimide probe [2]: (a) EDC, DMAP DMF. Reproduced with permission from Ref. 2. Copyright (2012) American Chemical Society

3.3 Indirect Amide Coupling Through NHS Ester

1. Dissolve the targeting ligand with primary amine (0.10 mmol, 1.0 equiv.), DIPEA (0.15 mmol, 1.5 equiv.), and the fluorescent dye with an NHS ester (0.10 mmol, 1.0 equiv., *see* **Note 5**) in anhydrous DMSO (1.0 mL) under inert atmosphere.
2. After stirring the mixture for 6 h, remove the solvent (*see* **Note 6**) and purify the final product using the appropriate method.

See Fig. 3 for sample reaction.

3.4 Indirect Amide Coupling through Acyl Chloride

1. Dissolve carboxylic acid functionalized fluorescent dye (1.0 mmol, 1.0 equiv.) in anhydrous THF (10 mL) (*see* **Note 7**).

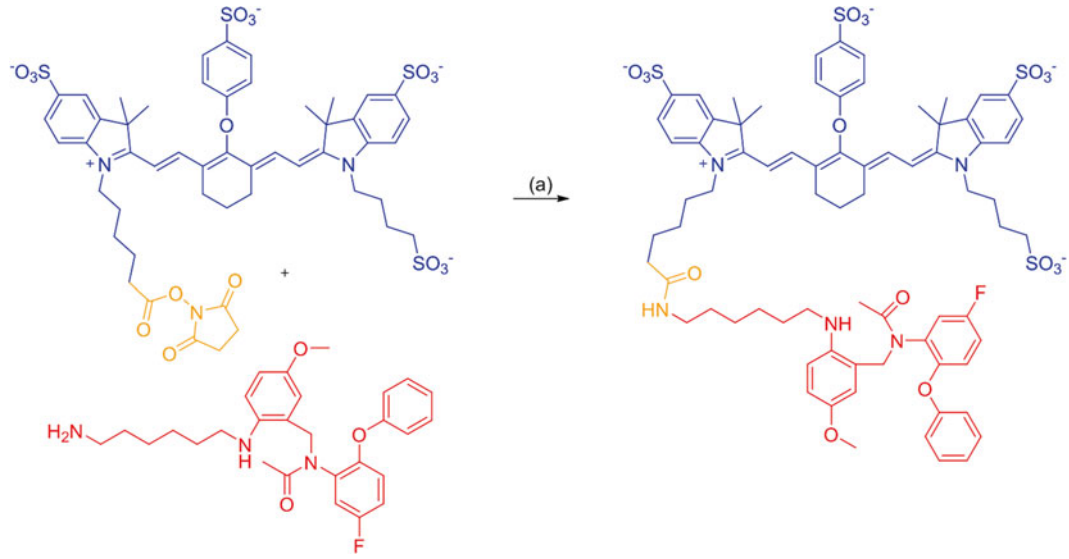

Fig. 3 Synthesis of translocator protein (TSPO) targeting imaging probe [3]: (a) DMSO. Reproduced with permission from Ref. 3. Copyright (2012) American Chemical Society

2. Carefully add thionyl chloride or oxalyl chloride (2.0 mmol, 2.0 equiv.) to the stirring solution dropwise. Add catalytic amount of DMF (one drop).
3. Monitor the reaction progress carefully until the starting material was consumed (*see* **Note 8**). The solution can be used in the next step directly (*see* **Note 9**).
4. Dissolve the targeting ligand with primary amine (1.0 mmol, 1.0 equiv.) in anhydrous THF (10 mL) and add NEt_3 (2.0 mmol, 2.0 equiv.) at 0 °C. Slowly add the acyl chloride solution to the stirring mixture dropwise. After the addition, gradually increase the reaction temperature to 25 °C.
5. Monitor the reaction progress using TLC analysis until the starting material was consumed. Purify the product using the appropriate technique.

See Fig. 4 for sample reaction.

3.5 Thiourea Coupling with Isothiocyanate

1. Dissolve the targeting ligand with primary amine (0.10 mmol, 1.0 equiv.) in DCM (10 mL) and add NEt_3 (10 mmol, 100 equiv.).
2. After stirring the mixture for 5 min, add the isothiocyanate functionalized dye molecule (0.10 mmol, 1.0 equiv.).
3. After stirring the mixture for 18 h, remove the solvent and purify the product using the appropriate method.

See Fig. 5 for sample reaction.

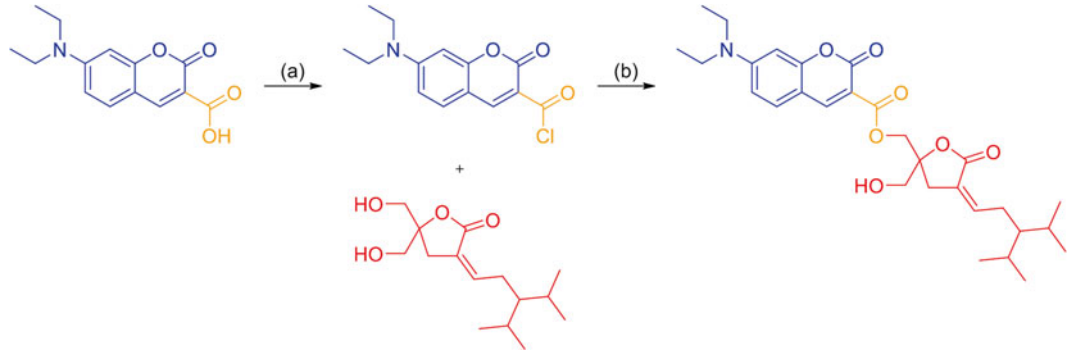

Fig. 4 Synthesis of protein kinase Cδ targeting coumarin based fluorophore [4]: (**a**) Thionyl chloride, THF, *cat.* DMF; (**b**) NEt_3, THF. Reproduced with permission from Ref. 4. Copyright (2011) American Chemical Society

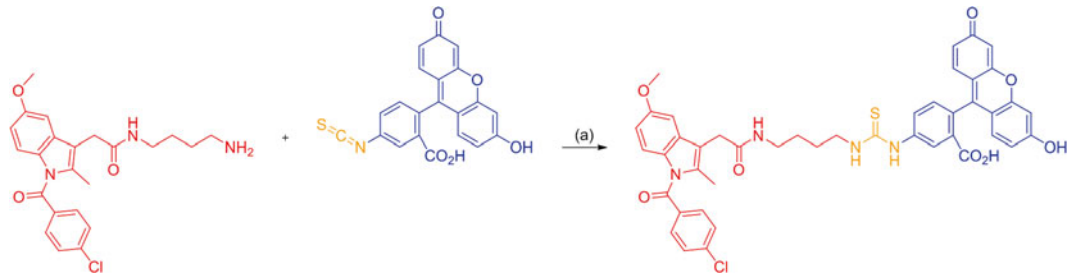

Fig. 5 Synthesis of fluorescent inhibitor of cycloxygenase-2 [5]: (a) NEt_3, DCM. Reproduced from Ref. 5 under ACS AuthorChoice

3.6 Michael Addition with Maleimide and Thiol

1. Dissolve the thiol compound (1.0 μmol, 1.0 equiv.) and maleimide functionalized dye (1.0 μmol, 1.0 equiv., *see* **Note 10**) in DMF (1.0 mL) under inert atmosphere.
2. After completion of the reaction, remove the solvent and purify the product using the appropriate method.

   See Fig. 6 for sample reaction.

3.7 Huisgen Cycloaddition (Click Chemistry) with Azide and Alkyne

1. Dissolve alkyne (0.10 mmol, 1.0 equiv., *see* **Note 11**), azide (0.12 mmol, 1.2 equiv. *see* **Note 12**), $CuSO_4$ (12 μmol, 0.12 equiv., *see* **Note 13**), and sodium ascorbate (0.05 mmol, 0.50 equiv.) in DMF (5.0 mL) under inert atmosphere.
2. Add DIPEA (0.10 mmol, 1.0 equiv.) to the stirring mixture at 25 °C. Monitor the reaction until the starting materials are consumed. Purify the product using the appropriate method.

   See Fig. 7 for sample reaction.

3.8 Palladium-Catalyzed Coupling

1. The iodinated dye (5.0 μmol, 1.0 equiv.), acetylenic targeting ligand (7.5 μmol, 1.5 equiv.), $Pd(OAc)_2$ (2.5 μmol, 0.5 equiv.), and tri(*o*-tolyl)phosphine (7.5 μmol, 1.5 equiv.) are suspended in anhydrous DMF (0.50 mL) under inert atmosphere.

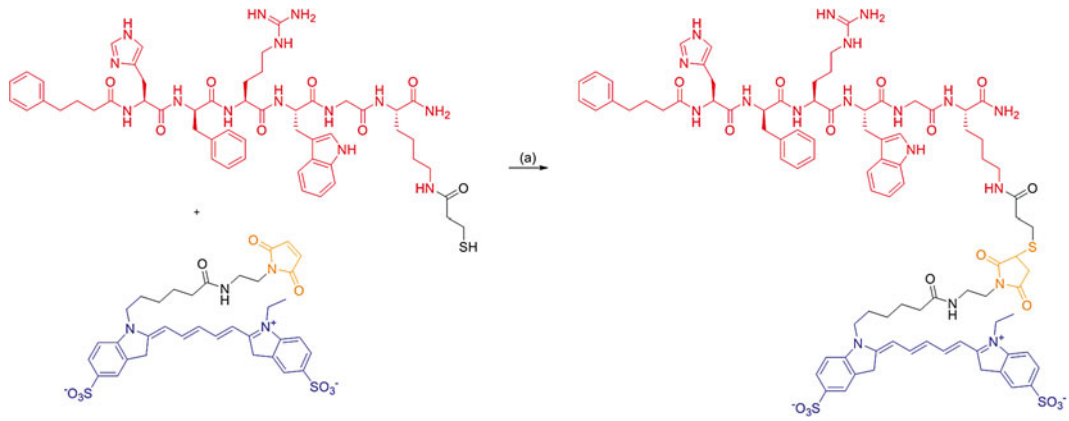

Fig. 6 Synthesis of melanoma-targeted fluorescence probe [6]: (a) DMF. Reproduced with permission from Ref. 6. Copyright (2012) American Chemical Society

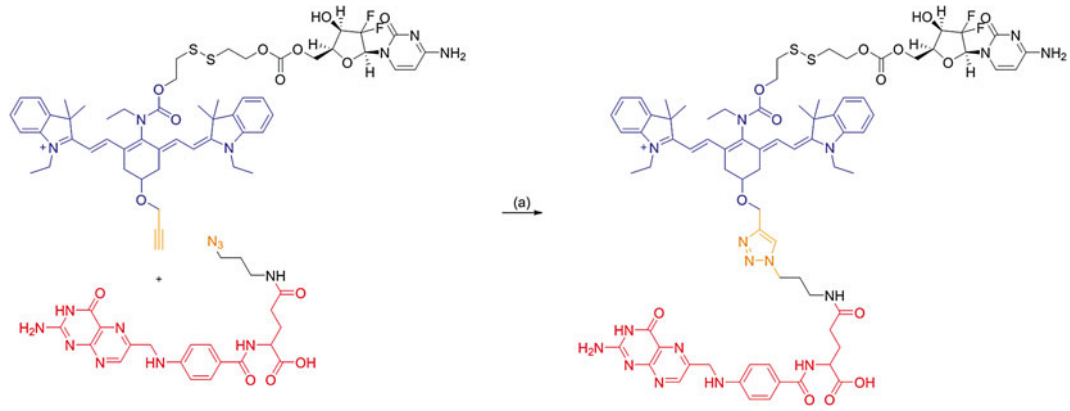

Fig. 7 Synthesis of folate-positive KB cells targeting imaging and drug delivery system [7]: (a) $Cu(ClO_4)_2$, sodium ascorbate, DIPEA, DMF. Reproduced with permission from Ref. 7. Copyright (2013) American Chemical Society

2. Add DIPEA (75 μmol, 15 equiv.) to the stirring mixture and heat the reaction to 70 °C and monitor the reaction (*see* **Note 14**). Remove the solvent by rotary evaporation and purify the product using the appropriate method (*see* **Note 15**).

   See Fig. 8 for sample reaction.

3.9 Catalyst Free Inverse Electron Demand Diels–Alder [4+2] Cycloaddition

1. Prepare a 0.25 mM aqueous solution of the targeting molecule with *trans*-cyclooctene and a 0.25 mM aqueous solution of the dye molecule with tetrazine (*see* **Note 16**).
2. Mix the two solutions in 1:1 (v/v) ratio together and stir for 5 min (*see* **Note 17**). Monitor and purify the reaction using the appropriate method.

   See Fig. 9 for sample reaction.

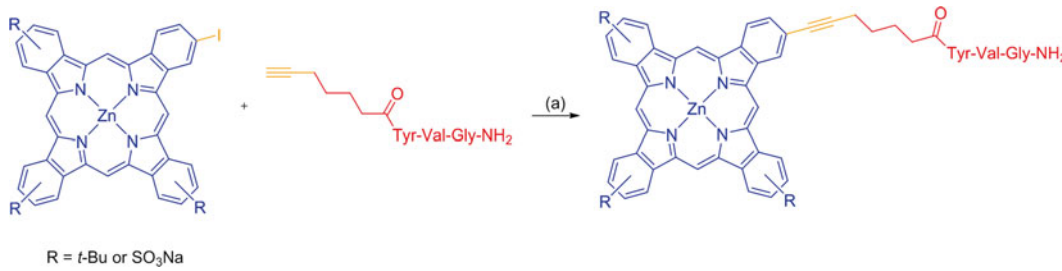

Fig. 8 In situ synthesis of integrin targeting phthalocyanine conjugate [8]: (a) $Pd(OAc)_2$, tri(*o*-tolyl)phosphine, DIPEA, DMF. Reproduced with permission from Ref. 8. Copyright (2013) American Chemical Society

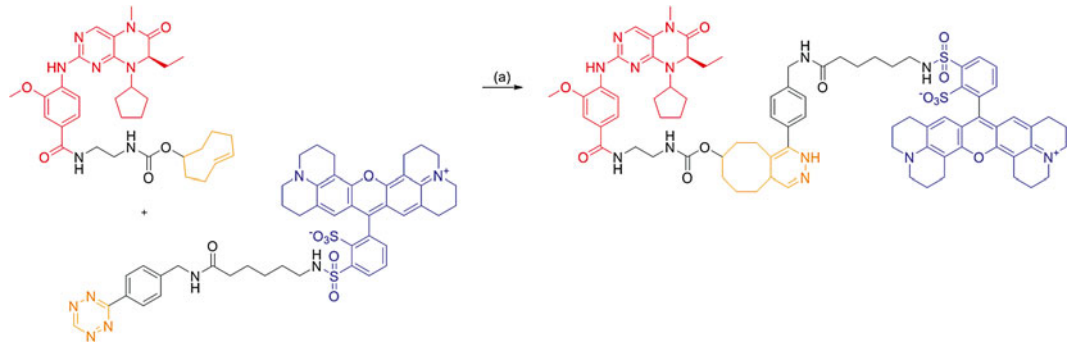

Fig. 9 In vitro synthesis of imaging probe that specifically binds to polo-like kinase 1 [9]: (a) water. Reproduced with permission from Ref. 9. Copyright (2011) John Wiley & Sons Limited

4 Notes

1. Solvents and catalysts used in this article are for general guidance. The optimum solvent and catalyst for specific reaction depends on various factors, such as the solubility and structure of the reactants and products, reaction temperature, etc.
2. Metal carboxylate salts can also be coupled with targeting amines using a modified method as recently described in Ref. 10.
3. HBTU is the most widely used coupling agent. *O*-(7-Azabenzotriazol-1-yl)-*N*,*N*,*N*′,*N*′-tetramethyluronium hexafluorophosphate (HATU) is proven to be more efficient than HBTU [11] but also more expensive. Benzotriazol-1-yl-oxy-tris-(dimethylamino)-phosphonium hexafluorophosphate (BOP) is a very effective coupling reagent. However, it generates carcinogenic side product hexamethylphosphoric triamide (HMPA). Therefore, use of benzotriazol-1-yl-oxy-tris--pyrrolidino-phosphonium hexafluorophosphate (PyBOP®) is preferred. PyBroP® was developed for coupling with steric challenging secondary amine. For other coupling reagents and recent reviews *see* Refs. 12–14.
4. Dicyclohexyl carbodiimide (DCC) and its urea byproduct are not water soluble and often used in organic synthesis. If the

reaction can be performed in organic solvent and the product is water soluble, the DCC and its urea byproduct can be easily removed by quenching the reaction with water and filtering off the precipitate.

5. The NHS ester can be prepared easily by dissolving carboxylic acid functionalized fluorescent dye (0.10 mmol, 1.0 equiv.), NHS (0.15 mmol, 1.5 equiv.), and EDC hydrochloride salt (0.15 mmol, 1.5 equiv.) in anhydrous DMF (1.0 mL) under inert atmosphere. After stirring the mixture for 18 h, remove the DMF from the reaction mixture using rotary evaporator to obtain the NHS ester. *N*-Hydroxysulfosuccinimide (NHSS) can be used to prepare water soluble reactive NHSS esters. This allows performing the conjugation step in aqueous solution.
6. DMSO is usually difficult to remove using normal rotary evaporation. A rule of thumb to remove DMSO is to dilute it with water that is ten times of the volume, freeze with dry ice, and remove all the solvent using lyophilization. Ionic dyes can also be isolated by pouring the reaction mixture into diethyl ether (50 mL). Collect the precipitation with filtration, wash with diethyl ether and dry to yield the product. For non-ionic product, dilute the reaction mixture with EtOAc or DCM, wash the organic phase with equal volume of water for five times, before removing the solvent to yield the crude product.
7. Acyl halides are very reactive species that are useful for difficult coupling reactions. However, the reactions require other reagents to endure harsh reaction condition. Such condition is not compatible with many protecting groups or unstable fluorescent dyes. Additionally, this method also applies to preparation of sulfonyl halide for sulfonamide conjugation. *See* Ref. 3 for an example.
8. This reaction is exothermic and generates excess amount of corrosive gas, which can be visually noticed as "bubbling" when working at hundreds of milligram scale. Cool the reaction flask with ice bath if necessary. The reaction flask should be well vented to prevent pressure from building up inside. If it is necessary to seal the reaction flask with a septum, punch a needle through the septum to help release the gas generated. Accordingly, the "bubbling" is also a good indication of the reaction progress. After the bubbling stops, the reactants are considered consumed.
9. Most acyl chlorides are not stable and should be prepared and used right away in situ. Some stable acyl chloride can be isolated by removing the solvent using rotary evaporation and stored for longer period of time in the refrigerator.
10. This method is preferred for commercially available dyes with maleimide group. Direct synthesis of maleimide functionalized fluorescent dyes using maleic anhydride can be challenging because it involves dehydration condition that is incompatible

with certain dye molecules. A common strategy is to couple the dye with commercially available maleimide derivatives using amide coupling [15]. For alternative maleimide synthesis strategies, *see* Refs. 16, 17. For other thiol coupling options, *see* Ref. 18.

11. Terminal alkynes are often prepared from iodo, bromo or triflate compounds with trimethylsilyl acetylene using Sonogashira reaction followed by an easy desilylation reaction with fluoride salt or potassium carbonate. For a recent review of Sonogashira reaction *see* Ref. 19.
12. Warning: Extra caution should be paid when handling azide compounds as they can be explosive and shock sensitive. Metal spatula should be replaced by plastic spoons when handling azide. Organic azides can be prepared by substitution reaction of halides or other leaving groups with sodium azide. For small molecule azide compounds, calculate the carbon to nitrogen ratio using the following equation to determine if it is stable enough to work with [20]

$$(N_C + N_O) / N_N \geq 3$$

N_C, number of carbon atoms; N_O, number of oxygen atoms; N_N, number of nitrogen atoms.

13. Cu(I) is the active catalyst in this reaction. However, it is often generated in situ using Cu(II) salt and sodium ascorbate instead of using Cu(I) salt directly.
14. When using nonpolar solvent such as THF or dioxane for Sonogashira reaction, the salt of the amine used will form a precipitate as the reaction progress.
15. Reference 21 suggests that other palladium-catalyzed coupling reactions, such as Suzuki coupling and Buchwald–Hartwig, can also be utilized for bioconjugation.
16. A common strategy to prepare *trans*-cyclooctene or tetrazine functionalized targeting ligand or dye molecule is coupling them with commercially available *trans*-cyclooctene or tetrazine NHS ester or amine using amide coupling.
17. This method is ideal when metal catalyst should be avoided. The reaction completes within minutes with high yield. For more details about this method, *see* Refs. [22, 23].

References

1. Zhang S, Shao P, Bai M (2013) In vivo type 2 cannabinoid receptor-targeted tumor optical imaging using a near infrared fluorescent probe. Bioconjug Chem 24(11):1907–1916. doi:10.1021/bc400328m
2. Lee MH, Han JH, Lee J-H, Choi HG, Kang C, Kim JS (2012) Mitochondrial thioredoxin-responding off–on fluorescent probe. J Am Chem Soc 134(41):17314–17319. doi:10.1021/ja308446y
3. Bai M, Rone MB, Papadopoulos V, Bornhop DJ (2007) A novel functional translocator protein ligand for cancer imaging. Bioconjug Chem 18(6):2018–2023. doi:10.1021/bc700251e

4. Nomura W, Ohashi N, Okuda Y, Narumi T, Ikura T, Ito N, Tamamura H (2011) Fluorescence-quenching screening of protein kinase c ligands with an environmentally sensitive fluorophore. Bioconjug Chem 22(5):923–930. doi:10.1021/bc100567k
5. Uddin MJ, Crews BC, Ghebreselasie K, Marnett LJ (2013) Design, synthesis, and structure–activity relationship studies of fluorescent inhibitors of cycloxygenase-2 as targeted optical imaging agents. Bioconjug Chem 24(4):712–723. doi:10.1021/bc300693w
6. Tafreshi NK, Huang X, Moberg VE, Barkey NM, Sondak VK, Tian H, Morse DL, Vagner J (2012) Synthesis and characterization of a melanoma-targeted fluorescence imaging probe by conjugation of a melanocortin 1 receptor (MC1R) specific ligand. Bioconjug Chem 23(12):2451–2459. doi:10.1021/bc300549s
7. Yang Z, Lee JH, Jeon HM, Han JH, Park N, He Y, Lee H, Hong KS, Kang C, Kim JS (2013) Folate-based near-infrared fluorescent theranostic gemcitabine delivery. J Am Chem Soc 135(31):11657–11662. doi:10.1021/ja405372k
8. Ranyuk E, Cauchon N, Klarskov K, Guérin B, van Lier JE (2013) Phthalocyanine–peptide conjugates: receptor-targeting bifunctional agents for imaging and photodynamic therapy. J Med Chem 56(4):1520–1534. doi:10.1021/jm301311c
9. Budin G, Yang KS, Reiner T, Weissleder R (2011) Bioorthogonal probes for polo-like kinase 1 imaging and quantification. Angew Chem Int Ed 50(40):9378–9381. doi:10.1002/anie.201103273
10. Goodreid JD, Duspara PA, Bosch C, Batey RA (2013) Amidation reactions from the direct coupling of metal carboxylate salts with amines. J Org Chem 79(3):943–954. doi:10.1021/jo402374c
11. Carpino LA (1993) 1-Hydroxy-7-azabenzotriazole. An efficient peptide coupling additive. J Am Chem Soc 115(10):4397–4398. doi:10.1021/ja00063a082
12. Montalbetti CAGN, Falque V (2005) Amide bond formation and peptide coupling. Tetrahedron 61(46):10827–10852. doi:10.1016/j.tet.2005.08.031
13. Valeur E, Bradley M (2009) Amide bond formation: beyond the myth of coupling reagents. Chem Soc Rev 38(2):606–631. doi:10.1039/b701677h
14. El-Faham A, Albericio F (2011) Peptide coupling reagents, more than a letter soup. Chem Rev 111(11):6557–6602. doi:10.1021/cr100048w
15. Gruber HJ, Kada G, Pragl B, Riener C, Hahn CD, Harms GS, Ahrer W, Dax TG, Hohenthanner K, Knaus H-G (2000) Preparation of thiol-reactive Cy5 derivatives from commercial Cy5 succinimidyl ester. Bioconjug Chem 11(2):161–166. doi:10.1021/bc990107f
16. Song HY, Ngai MH, Song ZY, MacAry PA, Hobley J, Lear MJ (2009) Practical synthesis of maleimides and coumarin-linked probes for protein and antibody labelling via reduction of native disulfides. Org Biomol Chem 7(17):3400–3406. doi:10.1039/b904060a
17. Walker MA (1995) A high yielding synthesis of N-alkyl maleimides using a novel modification of the Mitsunobu reaction. J Org Chem 60(16):5352–5355. doi:10.1021/jo00121a070
18. Hoyle CE, Lowe AB, Bowman CN (2010) Thiol-click chemistry: a multifaceted toolbox for small molecule and polymer synthesis. Chem Soc Rev 39(4):1355–1387. doi:10.1039/b901979k
19. Chinchilla R, Najera C (2011) Recent advances in Sonogashira reactions. Chem Soc Rev 40(10):5084–5121. doi:10.1039/c1cs15071e
20. Bräse S, Gil C, Knepper K, Zimmermann V (2005) Organic azides: an exploding diversity of a unique class of compounds. Angew Chem Int Ed 44(33):5188–5240. doi:10.1002/anie.200400657
21. Ali H, Ait-Mohand S, Gosselin S, van Lier JE, Guérin B (2011) Phthalocyanine- peptide conjugates via palladium-catalyzed cross- coupling reactions. J Org Chem 76(6):1887–1890. doi:10.1021/jo102083g
22. Blackman ML, Royzen M, Fox JM (2008) Tetrazine ligation: fast bioconjugation based on inverse-electron-demand Diels–Alder reactivity. J Am Chem Soc 130(41):13518–13519. doi:10.1021/ja8053805
23. Taylor MT, Blackman ML, Dmitrenko O, Fox JM (2011) Design and synthesis of highly reactive dienophiles for the tetrazine–trans-cyclooctene ligation. J Am Chem Soc 133(25):9646–9649. doi:10.1021/ja201844c

Chapter 3

In Vivo Fluorescence Reflectance Imaging with Subcutaneous Mouse Tumor Models

Jie Cao and Mingzhou Zhou

Abstract

Optical imaging is undoubtedly one of the most versatile and widely used imaging techniques in both research and clinical practice. Among optical imaging technologies, fluorescence imaging is the most popularly used and has become an essential tool in biomedical science. A key component of fluorescence imaging is fluorescence-producing reporters, including fluorescent dyes and conjugates, as well as fluorescent proteins. For in vivo imaging applications, fluorophores with long emission at the near-infrared (NIR) region are generally preferred to overcome the photon attenuation in living tissue. Here, we describe the in vivo fluorescence imaging of an integrin $\alpha_v\beta_3$ targeted NIR fluorescent probe (cRGD-ICG-Der-02) using subcutaneous mouse tumor models.

Key words In vivo, Near infrared fluorescence imaging, Noninvasive, Tumor targeting probe, ICG

1 Introduction

As one of the most deadly diseases, cancer causes death of millions of people around the world every year. The earlier it is detected, the better are the chances of treating it effectively. Up to now, optical molecular imaging has been increasing in popularity in tumor early detection, due to their easy operation, better temporal resolution, and relative low cost [1–3]. In particular, near infrared (NIR) fluorescence imaging possesses many advantages as a noninvasive technique for in vivo real time monitoring the stage and precise locations of tumor to aid in directing surgery and other cancer treatments, or to check if a cancer has returned [4, 5]. Therefore, NIR imaging techniques have been designed for in vivo studies such as monitoring response to therapeutic treatment, investigating the biodistribution of drugs, and visualizing the targeted delivery of drug carriers in living animal subjects [6, 7].

To enhance the specificity of tumor imaging, there exist several approaches to increase the accumulation of various contrast agents in the required pathological areas. Certain sizes of molecules

Mingfeng Bai (ed.), *In Vivo Fluorescence Imaging: Methods and Protocols*, Methods in Molecular Biology, vol. 1444,
DOI 10.1007/978-1-4939-3721-9_3,

(typically liposomes, nanoparticles, and macromolecular drugs) tend to accumulate in tumor via enhanced permeability and retention (EPR) effect, which is usually called passive targeting. To achieve active targeting, targeting molecules (such as target-specific antibodies, ligands, peptides, and lipids) can be coupled to fluorescent dyes to allow for specific imaging of tumor cells [8].

Because there is little NIR fluorescence contrast generated by most tissues, most in vivo studies rely on administration of exogenous contrast agents. Until now, organic fluorophores including FDA approved indocyanine green (ICG) and inorganic fluorescent semiconductor nanocrystals (also called quantum dots; QDs) have been used as exogenous contrast agents [9–11]. In vivo imaging requires that the contrast agent is delivered to the target, has adequate contact time with the target for binding to occur, and is retained by the target while non-bound material is cleared from the circulation [12, 13]. Therefore, both organic fluorophores and QDs could be conjugated to targeting molecules for target-specific in vivo imaging.

Research has shown that integrins, consisting of two noncovalently bound transmembrane subunits (α and β), are a family of cell surface glycoproteins that mediate diverse biological events involving cell–cell and cell–matrix interactions [14, 15]. Integrins expressed on endothelial cells modulate cell migration and survival during angiogenesis, while integrins expressed on carcinoma cells potentiate metastasis by facilitating invasion and movement across blood vessels [16]. Integrin $\alpha_v\beta_3$ seems to play a critical role in regulating tumor growth and metastasis as well as tumor angiogenesis. Hence, integrin $\alpha_v\beta_3$ receptors have attracted intensive attention to serve as tumor targets for intervention and diagnostic imaging. Here, we recently conjugated a well-known targeting molecule, cyclic arginine–glycine–aspartic acid (RGD)-containing components (c(RGDyK)), which specifically binds to $\alpha_v\beta_3$ integrin receptor upregulated on endothelium during angiogenesis, with an NIR ICG dye (ICG-Der-02) to develop an NIR probe for in vivo tumor-targeted imaging [17]. This chapter uses this probe as an example to describe the methods used for in vivo fluorescence reflectance imaging with subcutaneous mouse tumor models.

2 Materials

2.1 Bioconjugation of NIR Probe c(RGDyK)-ICG- Der-02

The schematic structure of cyclic RGD-based NIR probe is shown in Fig. 1, and the detailed procedure is shown below:

1. ICG-Der-02 (9.97 mg, 0.01 mmol) was reacted with EDC · HCl (2.88 mg, 0.015 mmol) and NHS (1.73 mg, 0.0384 mmol) in H_2O (0.5 mL) for 3 h at room temperature.
2. The intermediate product ICG-Der-02-NHS was first confirmed by thin layer chromatography (TCL).

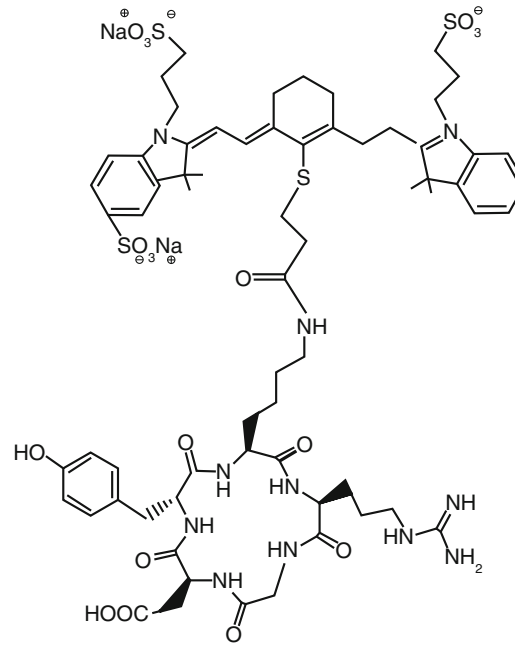

c(RGDyK)-ICG-Der-02

Fig. 1 Schematic structure of cyclic RGD-based near infrared probe: c(RGDyK)-ICG-Der-02 (Reproduced from Ref. 17 with permission from Wiley)

3. 0.01 mmol cyclic RGD was dissolved in sodium borate ($Na_2B_4O_7$, 0.1 M, pH 8.3, 1 mL) buffer.
4. ICG-Der-02-NHS was mixed with cyclic RGD solution and reacted at room temperature overnight in the dark.
5. The crude product c(RGDyK)-ICG-Der-02 was purified by filtration over Sephadex G-15.

2.2 Instruments for In Vivo Imaging

A self-built NIR imaging system is used for in vivo real-time fluorescence imaging of the probe's distribution in tumor-bearing mice. This imaging system is shown in Fig. 2. In brief, the NIR imaging system composed of an excitation laser ($\lambda = 765.9$ nm, NL-FC-2.0-763 laser light), a high sensitivity NIR CCD camera (PIXIS 512B, Princeton Instrument) and an 800-nm-long pass filter for capturing the emitting fluorescence from the tissue. Besides, another HLU32F400 808 nm laser (LIMO, Dortmund, Germany) is supplied as the background light to obtain the profile of the subjected animal. Otherwise, the imaging was completely dark except for the fluorescence spot [18]. The camera integration time for NIR optical imaging acquisition was 300 ms. For image analysis, we used Winview software, which complied with the NIR imaging system, and pseudo color mode was chosen (*see* **Note 1**).

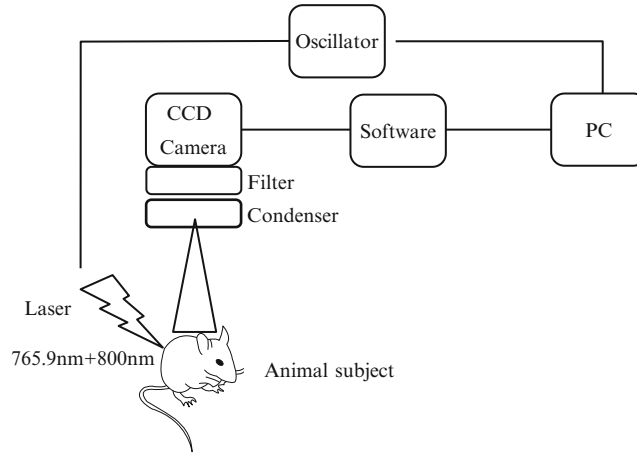

Fig. 2 Schematic diagram of NIR imaging system

2.3 Tumor Mouse Models

1. Athymic nude mice (nu/nu, aged 4–6 weeks and weight at 18–22 g) are used (*see* **Note 2**).
2. Harvest cancer cells during the exponential growth phase using 0.25% trypsin. Then suspend cells in phosphate buffered saline (PBS, 0.01 M; pH 7.2) [19] (*see* **Note 3**).
3. Quantitate the number of cells using a Coulter counter.
4. Centrifuge cells for 5 min at 1000 rpm to remove the medium. Then resuspend the cells in PBS without serum (*see* **Note 4**).
5. Lift the axillary fossa skin of the mouse to separate it from the underlying muscle and inject 100 μL of the cell suspension subcutaneously (*see* **Note 5**).
6. When the tumors reached 500 mm^3, the tumor bearing mice are used for fluorescence imaging (*see* **Note 6**).

3 Methods

Carry out all procedures at room temperature unless otherwise specified.

1. Check and make sure the tumor size is about 500 mm^3.
2. Set up the in vivo imaging system.
3. Anesthetize the mouse using rodent anesthesia system with isoflurane (2% (vol/vol) isoflurane in 0.2 L min^{-1} of O_2 flow).
4. Inject cRGD-ICG-Der-02 PBS solution in mouse via tail vein (total volume, 200 μL) (*see* **Note 7**).
5. The mouse was fixed and laid under the NIR imaging system in a dark room (*see* **Note 8**).

6. A series of images were collected from mice at assigned time intervals during 48 h post-injection (Fig. 3). We typically choose 30 min, 1, 4, 6, 12, 24, and 48 h (*see* **Note 9**).
7. As a control, a series of images are collected from non-tumor mice at assigned time intervals after intravenous injection of c(RGDyK)-ICG-Der-02. (Fig. 4).
8. To evaluate the tumor targeting capability of the RGD-based probe, free dye ICG-Der-02 is also injected into tumor-bearing mice as a control. A series of images are collected at assigned time point (Fig. 5).

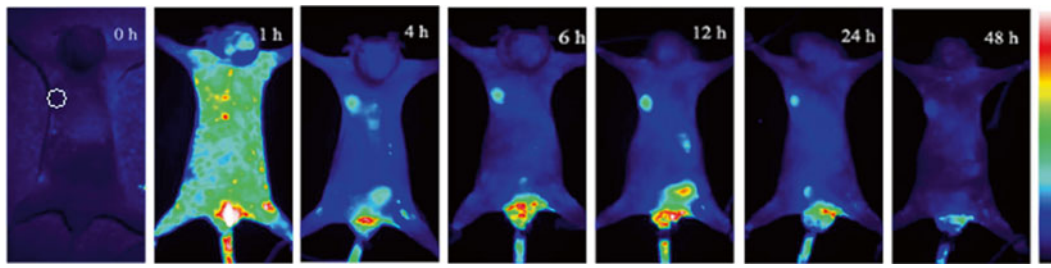

Fig. 3 NIR images of nude mice bearing MDA-MB-231 tumor xenograft after intravenous injection of cRGD-ICG-Der-02 within 48 h. MDA-MB-231 tumor was implanted on the right axillary fossa (Reproduced from Ref. 17 with permission from Wiley)

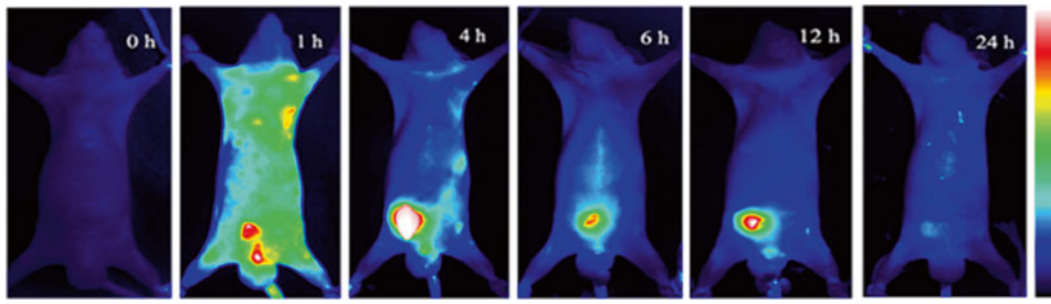

Fig. 4 NIR images of normal nude mice after intravenous injection of c(RGDyK)-ICG-Der-02 (Reproduced from Ref. 17 with permission from Wiley)

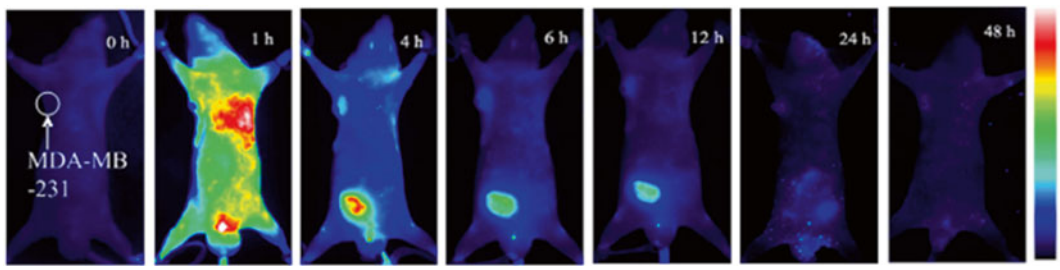

Fig. 5 NIR images of nude mice bearing MDA-MB-231 tumor xenograft after intravenous injection of ICG-Der-02 within 48 h. MDA-MB-231 tumor (0.5–0.7 cm) was implanted on the right axillary fossa (Reproduced from Ref. 17 with permission from Wiley)

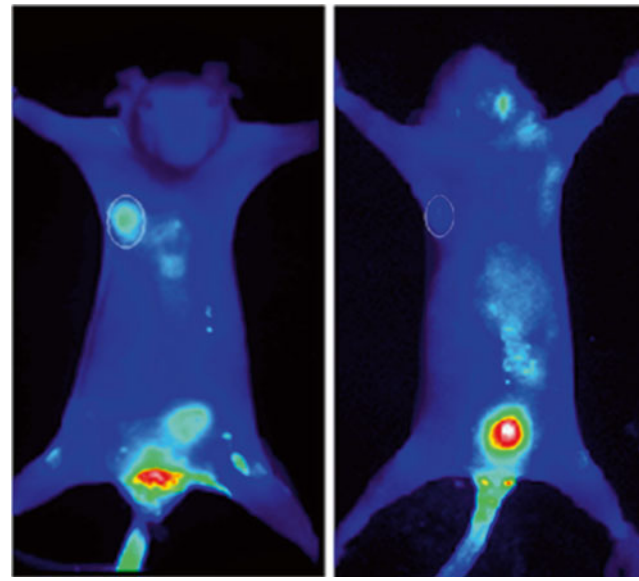

Fig. 6 NIR images of MDA-MB-231 tumor bearing mice at 4 h post injection of c(RGDyK)-ICG-Der-02 (*Left*) and c(RGDyK)-ICG-Der-02/c(RGDyK) (*Right*) (Reproduced from Ref. 17 with permission from Wiley)

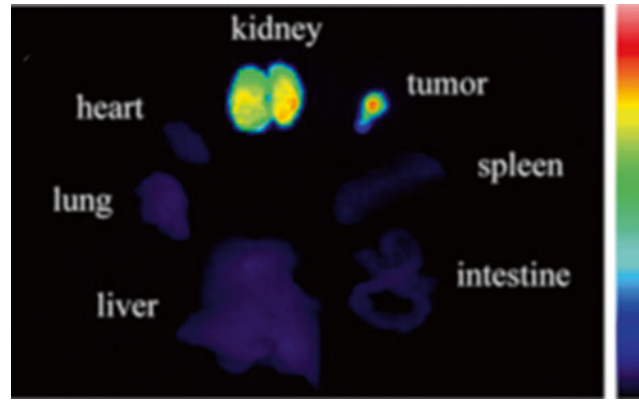

Fig. 7 NIR images of the MDA-MB-231 tumor and main organs excised from the tumor mice 12 h after intravenous injection of c(RGDyK)-ICG-Der-02 (Reproduced from Ref. 17 with permission from Wiley)

9. Receptor specificity of the NIR probe can be validated by a blocking experiment. Here, free cyclic RGD was used as the blocking agent (Fig. 6). A mixture of 5 $mg \cdot kg^{-1}$ of cyclic RGD and 2 nmol c(RGDyK)-ICG-Der-02 is intravenously injected into mouse. The fluorescence images are acquired using the same method as described above.
10. If needed, ex vivo fluorescence imaging (Fig. 7) can also be carried out to validate the in vivo imaging results. Euthanize

the mouse 12 h post injection and harvest the tumor and major organs and image them using the in vivo imaging system (*see* **Note 10**).

11. All experiments are carried out on five mice for statistical analysis (*see* **Note 11**).

4 Notes

1. The imaging system is easy to use once the user has gone through appropriate training of the system. The key issue is choosing the right excitation filter for in vivo imaging. The filter we used to acquire the images shown in this protocol is 765 nm.
2. A nude mouse lacks thymus, resulting in a suppressed immune system due to a greatly reduced number of T cells. Note that the number of T cells will increase with age and other factors (such as virus infection), and the appropriate age for tumor inoculation is 4–6 weeks. In addition, the immune-suppressed nude mice are susceptible to hepatitis and pneumonia; therefore, the hygiene standard is very high for their maintenance. To ensure long-term survival and reproduction of nude mice, specific pathogen free (SPF) environment is required and the cages, beddings, food, and water all need rigorous sterilization before use.
3. To ensure that the immunodeficient mice are not infected by cells contaminated with viruses, the cells should be tested.
4. The concentration of cancer cells injected into mouse is about 5×10^6 per mL of PBS.
5. To prepare for injection, the cell suspension need to be agitated to prevent the cells from settling and then withdrawn from the sterile tube into a 1-cc TB syringe without needle. After injection, place the mouse in a clean cage and observe for 10–15 min to ensure recovery from the anesthesia.
6. During the first week after the implantation, a small bump should be visible where the tumor cells were injected but this should vanish. After 2–3 weeks, a tumor should begin to be visible at the site of implantation and grow. Measure the tumor with vernier caliper, and the tumor size can be calculated using the follow formula: $V_{\text{tumor}} = a \times b^2/2$ (a is the longer dimension of the tumor and b the shorter dimension of the tumor).
7. Before injection, firstly make sure the sample was dissolved in PBS solution completely. Then, make sure the mouse was fixed and make the vessel dilated. The tail veins swell at higher temperature, simplifying the intravenous-injection procedure. It is better to immerse the tail into hot water until the tail becomes

red. However, the temperature of the hot water should not be too high in order to avoid scalding the tail. We also recommend injecting some PBS (about 50 μL) afterward to flush the tail vein.

8. To avoid interference of natural light, all the images should be taken under dark for tracing the fluorescence signal. Besides, to maximum reduce the interference of any other unrelated fluorescence, mice should be fed with food without fluorescence. Besides, the fluorescence imaging of the preinjection mouse was acquired and set as background imaging.
9. Images were collected from different angles, including abdomen and back. Make sure the excitation intensity is fixed for every image, and pesto color mode is chosen for image acquisition.
10. Ex vivo imaging of the tumor and main organs was performed to confirm the signal biodistribution and the selective tumor targeting of the probe. The tissue–background ratio (T/B ratio) was calculated as follows: T/B ratio = (tissue signal – background signal)/background signal.
11. Data are expressed as means ± standard deviation. Statistical analysis was performed using Student's *t*-test with statistical significance assigned for a *p*-value of <0.05.

References

1. Frangioni JV (2003) *In vivo* near-infrared fluorescence imaging. Curr Opin Chem Biol 7:626–634
2. Ballou B, Emst LA, Waggoner AS (2005) Fluorescence imaging of tumors *in vivo*. Curr Med Chem 12:795–805
3. Rao J, Dragulescu-Andrasi A, Yao H (2007) Fluorescence imaging *in vivo*: recent advances. Curr Opin Biotechnol 18:17–25
4. Wu WT, Aiello M, Zhou T, Berliner A, Banerjee P, Zhou SQ (2010) In-situ immobilization of quantum dots in polysaccharide-based nanogels for integration of optical pH-sensing, tumor cell imaging, and drug delivery. Biomaterials 31:3023–3031
5. Zhang J, Deng DW, Qian ZY, Liu F, Chen XY, An LX, Gu YQ (2010) The targeting behavior of folate-nanohydrogel evaluated by near infrared imaging system in tumor-bearing mouse model. Pharm Res 27:46–55
6. Aswendt M, Adamczak J, Tennstaedt A (2014) A review of novel optical imaging strategies of the stroke pathology and stem cell therapy in stroke. Front Cell Neurosci 8:226
7. Morgan N, English S, Chen W, Chernomordik V, Gandjbakhche A, Russo A, Smith P (2005) Real time *in vivo* non-invasive optical imaging using a near-infrared fluorescent quantum dots. Acad Radiol 12:313–323
8. Torchilin VP (2007) Micellar nanocarriers: pharmaceutical perspectives. Pharm Res 24:1–16
9. Zhang C, Liu T, Su YP, Luo SL, Zhu Y, Tan X, Fan S, Zhang LL, Zhou Y, Cheng TM, Shi CM (2010) A near-infrared fluorescent heptamethine indocyanine dye with preferential tumor accumulation for *in vivo* imaging. Biomaterials 31:6612–6617
10. Escobedo JO, Rusin O, Lim S, Strongin RM (2010) NIR dyes for bioimaging applications. Curr Opin Chem Biol 14:64–70
11. Zhu Y, Hong H, Xu ZP, Li Z, Cai W (2013) Quantum dot-based nanoprobes for *in vivo* targeted imaging. Curr Mol Med 13:1549–1567
12. Conconi MT, Ghezzo F, Dettin M, Urbani L, Grandi C, Guidolin D, Nico B, Di Bello C, Ribatti D, Parnigotto PP (2010) Effects on

in vitro and *in vivo* angiogenesis induced by small peptides carrying adhesion sequences. J Pept Sci 16:349–357

13. Mather S (2009) Molecular imaging with bioconjugates in mouse models of cancer. Bioconjug Chem 20:631–643
14. Huveneers S, Truong H, Danen HJ (2007) Integrins: signaling, disease, and therapy. Int J Radiat Biol 83:743–751
15. Lee S, Xie J, Chen XY (2010) Peptide-based probes for targeted molecular imaging. Biochemistry 49:1364–1376
16. Wu Y, Cai WB, Chen XY (2006) Near-infrared fluorescence imaging of tumor integrin $\alpha_v\beta_3$ expression with cy7-labeled RGD multimers. Mol Imaging Biol 8:226–236
17. Cao J, Wan S, Tian J, Li S, Deng D, Qian Z, Gu Y (2012) Fast clearing RGD-based near-infrared fluorescent probes for *in vivo* tumor diagnosis. Contrast Media Mol Imaging 7:390–402
18. Gu Y, Liu F, Fang C, Qian Z, Achilefu S (2010) In vivo investigation of pharmacokinetics of model drug: comparison of near infrared technique with high-performance liquid chromatography. Proc SPIE 7576:75760A-1–75760A-8
19. Morton CL, Houghton PJ (2007) Establishment of human tumor xenografts in immunodeficient mice. Nat Protoc 2:247–250

Chapter 4

FRET Imaging of Enzymatic Activities Using Smart Probes

Jinbo Li, Yan Zhang, and Zhen Cheng

Abstract

Tumor-related enzymes are extensively involved in the occurrence, development, invasion, and metastasis of tumors, indicating they hold the potential to serve as biomarkers for tumor diagnosis and treatment. Smart probes based on characteristic activities of these enzymes and fluorescence resonance energy transfer (FRET) have been widely developed for fluorescent imaging of enzymatic activities. Here, we describe the detailed chemical strategies for construction of smart probe and its application for FRET imaging of fibroblast activation protein alpha in vitro and in vivo.

Key words Enzyme, Fluorescence resonance energy transfer, Peptide, Fluorescent imaging, Smart probe

1 Introduction

Tumor occurrence is often accompanied by the over-expression of tumor-related enzymes, e.g., fibroblast activation protein alpha (FAPα), matrix metalloproteinases (MMPs), and cathepsins, which in turn will also promote the development, invasion, and metastasis of tumor [1–3]. The unique properties of tumor-related enzymes make them as potential and promising biological targets for tumor diagnosis and treatment [4–6]. Therefore, direct in situ imaging of these enzymes is beneficial to early detection, surgical therapy, and prognosis of tumors [4, 7, 8]. Activatable fluorescent probes, which usually consist of a fluorophore, a specific peptide substrate of target enzyme, and a quencher corresponding to the fluorophore, have widely served as smart probes for fluorescent imaging of tumor-related enzymes [9, 10]. The short distance between the fluorophore and quencher enables the fluorescence resonance energy transfer (FRET) effects, causing quenching of the fluorescent signals from fluorophore. Upon interaction with the target enzymes in tumor sites, the peptide substrate will be digested into fragments and the dissociation between the fluorophore and the

Mingfeng Bai (ed.), *In Vivo Fluorescence Imaging: Methods and Protocols*, Methods in Molecular Biology, vol. 1444,
DOI 10.1007/978-1-4939-3721-9_4,

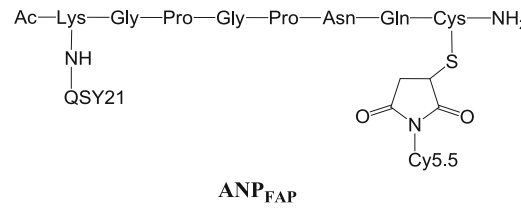

ANP_{FAP}

Fig. 1 Chemical structure of ANP_{FAP}

quencher will induce the recovery of the fluorescent signals, realizing FRET imaging of enzymatic activities.

In previous systematic protocols for construction of a smart fluorescent probe, an activatable near-infrared (NIR) fluorescent probe (ANP_{FAP}, Fig. 1) was reported for FRET imaging of FAPα [11], which is a member of the serine protease family and highly expressed in most epithelial cancers [12–14]. The specific peptide substrate of FAPα, Lys-Gly-Pro-Gly-Pro-Asn-Gln-Cys (KGPGPNQC), was selected as the backbone for construction of the smart probe and synthesized using the standard solid phase peptide synthetic protocols [15]. With the insertion of lysine and cysteine into each end of the peptide substrate, we were able to further functionalize the peptide backbone with the NIR fluorophore Cy5.5 and its quencher QSY21 through unique chemical strategies, which are amine-NHS and thiol-maleimide reactions, respectively. The resulted smart probes were obtained in moderate yield and stable in aqueous solution. Furthermore, with the smart probe, successful in vitro and in vivo FRET imaging of FAPα was also realized.

Here, we systematically summarize the chemical methods and protocols used in our previous studies for construction of ANP_{FAP} and its application for FRET imaging of FAPα. Our bioconjugation strategies is applicable to a wide range of smart probes and should benefit scientists interested in further developing smart probes for FRET imaging of enzymatic activities.

2 Materials

All aqueous solutions were prepared using ultrapure water, and all organic solvents are analytical grade reagents. Unless specifically indicated otherwise, all the reagents and solutions are prepared and stored at room temperature.

2.1 Peptide Synthesis

1. Automatic peptide synthesizer.
2. Rink amide MBHA resin.
3. N-Fmoc-protected amino acids.
4. *N*,*N*-Dimethylformamide (DMF).
5. Hydroxybenzotriazole (HOBt).
6. Pyridine.

7. Diisopropylethylamine (DIPEA).
8. Anhydrous acetic anhydride.
9. Trifluoroacetic acid (TFA).
10. Triisopropylsilane.
11. Ethanedithiol.
12. Acetonitrile.
13. Dichloromethane (DCM).
14. Methanol.
15. Diethyl ether.
16. Solvent A, 0.1 % TFA in water.
17. Solvent B, 0.1 % TFA in acetonitrile.
18. Reversed-phase high-performance liquid chromatography (RP-HPLC).

2.2 Probe Synthesis

1. Cy5.5-maleimide. Store at −20 °C (*see* **Note 1**).
2. QSY21-NHS. Store at −20 °C (*see* **Note 1**).
3. Phosphate buffered saline (PBS): 0.137 M NaCl, 0.003 M KCl, 0.01 M Na_2HPO_4, 0.002 M KH_2PO_4, pH = 7.4.
4. Dimethyl sulfoxide (DMSO).
5. Agilent UV-visible ChemStation.

2.3 Enzymatic Assay

1. Recombinant FAPα. Store at −70 °C (*see* **Note 2**).
2. Recombinant dipeptidyl peptidase-IV (DPPIV). Store at −70 °C (*see* **Note 2**).
3. Recombinant metallopeptidase-2 (MMP-2). Store at −70 °C (*see* **Note 2**).
4. Inifite M1000 spectrofluorometer.

2.4 In Vivo Assay

1. C6 rat glioma cells.
2. U87MG human glioma cells.
3. Female athymic nude mice.
4. IVIS200 small animal imaging system.

3 Methods

Unless specifically indicated otherwise, all procedures are carried out at room temperature.

3.1 Peptide Synthesis

1. Synthesize the peptide Ac-Lys-Gly-Pro-Gly-Pro-Asn-Gln-Cys-NH_2 on the automatic peptide synthesizer by using standard solid-phase peptide synthetic protocols. Specifically, use 0.2 mmol rink amide MBHA resin (1 equivalent) and 1 mmol Fmoc-protected amino acid (5 equivalents) for peptide synthesis.

2. Use filter to wash the resin with 10 mL of DMF, DCM, and methanol respectively for three times.
3. Mix the resin with 50 mL of DMF in a 100 mL conical flask. Add 1 mmol anhydrous acetic anhydride, 1 mmol HOBt, and 100 μL of DIPEA into the flask. Cover the lid and mix the mixture with stirring bar for 30 min (*see* **Note 3**).
4. After removing the solvents, wash the resin with 10 mL of DMF, DCM, and methanol respectively for three times.
5. Prepare the cleavage solution in a 20 mL flask by mixing 9.25 mL of TFA, 0.25 mL of triisopropylsilane, 0.25 mL of ethanedithiol, and 0.25 mL of H_2O (*see* **Note 4**).
6. Pour the resin into the cleavage solution and mix the mixture with stirring bar for 2 h (*see* **Note 5**).
7. Prepare 50 mL of cold anhydrous diethyl ether ahead by using dry ice.
8. Collect the supernatant from **step 6** by using filter. Pour the supernatant into cold anhydrous diethyl ether from **step 7** (*see* **Note 6**).
9. Collect the precipitates by centrifugation (4000 rpm (~2500 × *g*), 5 min).
10. After discarding the supernatant, dry the precipitates with Argon (*see* **Note 7**).
11. Purify the peptide with a semi-preparative reversed-phase high-performance liquid chromatography (RP-HPLC). Set the flow rate to 4 mL/min, with the mobile phase starting from 95% solvent A and 5% solvent B (0–3 min) to 35% solvent A and 65% solvent B at 33 min.
12. Collect and lyophilize the product (*see* **Note 8**).

3.2 Probe Synthesis

1. Mix 300 μg Cy5.5-maleimide (1 equivalent) with 450 μg peptide (2 equivalents) in 300 μL of PBS (pH = 7.4) in a 1.5 mL centrifuge tube (*see* **Note 9**).
2. Keep the tube in dark and shake for 2 h (*see* **Note 10**).
3. Purify the Cy5.5-labeled peptide with RP-HPLC. Set the flow rate to 4 mL/min, with the mobile phase starting from 95% solvent A and 5% solvent B (0–3 min) to 35% solvent A and 65% solvent B at 33 min.
4. Collect and lyophilize the product.
5. Mix the Cy5.5-labeled peptide, 440 μg QSY21-NHS (1 equivalent) with 2 μL DIPEA in 100 μL DMSO in a 1.5 mL centrifuge tube.
6. Keep the tube in dark and shake for 2–6 h (*see* **Note 10**).
7. Purify ANP_{FAP} with RP-HPLC. Set the flow rate to 4 mL/min, with the mobile phase starting from 95% solvent A and 5% solvent B (0–3 min) to 35% solvent A and 65% solvent B at 33 min.

8. Collect and lyophilize the product.
9. Prepare a stock solution of ANP_{FAP} (1 mM) in water and characterize by measuring the absorption and fluorescence spectra (*see* **Note 11**).

3.3 Enzymatic Assay

1. Pre-warm the spectrofluorometer to let the inside temperature reach 37 °C.
2. Mix 1 μL of ANP_{FAP} with 0.25, 0.5, and 1 μL of FAPα (100 μg/mL) or 1 μL of DPPIV or MMP-2 (100 μg/mL) in 100 μL of PBS in a 96-well plate (*see* **Note 12**).
3. Cover the plate with lid and put it into the pre-warmed spectrofluorometer.
4. Set the excitation wavelength at 675 nm and record the emission spectra from 680 to 800 nm every 10 min.
5. Image the samples directly by the IVIS200 imaging system after 1 h incubation for phantom study (*see* **Note 13**).

3.4 In Vivo Assay

1. Prepare 5 C6 (FAPα negative) and 5 U87MG (FAPα negative) tumor bearing mice by subcutaneously injecting three million C6 cells and five million U87MG cells into the right shoulder of female athymic nude mice (*see* **Note 14**).
2. Dilute 10 nmol ANP_{FAP} in 1.5 mL of PBS.
3. Inject each mouse with 1 nmol ANP_{FAP} in 150 μL of PBS via tail-vein injection.
4. Perform in vivo fluorescent imaging at 0.5, 1, 2, 3, and 4 h after injection by IVIS200 small animal imaging system. Use Cy5.5 filter (excitation 615–665 nm; emission 695–770 nm) and Cy5.5 background filter (580–610 nm) (*see* **Note 15**).

4 Notes

1. These dyes are quite sensitive to moisture and light, so dissolve them in anhydrous DMSO and make aliquots upon arrival. Store the aliquots in dark at −20 °C.
2. Repeated freeze–thaw will induce degradation of these recombinant proteins. Upon arrival, make aliquots of these recombinant proteins and store the aliquots at −70 °C.
3. Perform Kasier test [15] to make sure the reaction is finished even though it usually takes 30 min for the acetylation of the peptide to complete.
4. Prepare the cleavage solution in a fume hood. As TFA and ethanedithiol are toxic and smelly, wear goggles and mask to prepare the solution. Ethanedithiol was added to protect thiol groups of cysteine from cross-linking.

5. It usually takes 2 h to cleave peptides from the resin, while longer reaction time (e.g., 3–4 h) is also acceptable.
6. Do this in the fume hood. Mix the solution by vortex to allow complete precipitation of peptides.
7. Do not use air to dry the peptides, since the thiol group of cysteine is prone to rapid cross-linking.
8. Use the peptide immediately or store it under argon and away from moisture.
9. An alternative approach for functionalization of peptide with Cy5.5 is to mix peptide (2 equivalents) and Cy5.5-maleimide (1 equivalent) with 2 μL of DIPEA in 100 μL of anhydrous DMF. Under this condition, this reaction usually takes 30 min.
10. Run analytic RP-HPLC to monitor the reaction progress.
11. Store the stock solution in dark and at 4 °C. The probe is stable for several months.
12. Add each component into the 96-well plate quickly, as the enzymatic cleavage starts immediately once the recombinant protein and probe were mixed together.
13. Phantom study means samples were directly viewed under the IVIS200 imaging system to mimic fluorescent imaging of smart probes in living mice.
14. Because C6 tumor grows much faster than U87MG tumor, less C6 cells are used to ensure that these two types of tumors are ready for imaging at the same time. These tumors grow to the appropriate sizes for imaging in about 3 weeks post-injection of tumor cells.
15. The background filter is used to eliminate the interference signal from tissue autofluorescence.

Acknowledgement

This work was supported in part by National Cancer Institute (NCI) 5R01 CA119053 (Z.C.) and the National Basic Research Program of China (No. 2011CB935800).

References

1. Nelson AR, Fingleton B, Rothenberg ML, Matrisian LM (2000) Matrix metalloproteinases: biologic activity and clinical implications. J Clin Oncol 18(5):1135–1149
2. Tan GJ, Peng ZK, Lu JP, Tang FQ (2013) Cathepsins mediate tumor metastasis. World J Biol Chem 4(4):91–101
3. Liu R, Li H, Liu L, Yu J, Ren X (2012) Fibroblast activation protein: a potential therapeutic target in cancer. Cancer Biol Ther 13(3): 123–129
4. Bu L, Shen B, Cheng Z (2014) Fluorescent imaging of cancerous tissues for targeted surgery. Adv Drug Deliv Rev 76C:21–38

5. Choi KY, Swierczewska M, Lee S, Chen X (2012) Protease-activated drug development. Theranostics 2(2):156–178
6. Wu Y, Zhang W, Li J, Zhang Y (2013) Optical imaging of tumor microenvironment. Am J Nucl Med Mol Imaging 3(1):1–15
7. Bu L, Ma X, Tu Y, Shen B, Cheng Z (2014) Optical image-guided cancer therapy. Curr Pharm Biotechnol 14(8):723–732
8. Orbay H, Bean J, Zhang Y, Cai W (2014) Intraoperative targeted optical imaging: a guide towards tumor-free margins in cancer surgery. Curr Pharm Biotechnol 14(8):733–742
9. Razgulin A, Ma N, Rao J (2011) Strategies for in vivo imaging of enzyme activity: an overview and recent advances. Chem Soc Rev 40(7):4186–4216
10. Lacivita E, Leopoldo M, Berardi F, Colabufo NA, Perrone R (2012) Activatable fluorescent probes: a new concept in optical molecular imaging. Curr Med Chem 19(28):4731–4741
11. Li J, Chen K, Liu H, Cheng K, Yang M, Zhang J, Cheng JD, Zhang Y, Cheng Z (2012) Activatable near-infrared fluorescent probe for in vivo imaging of fibroblast activation protein-alpha. Bioconjug Chem 23(8):1704–1711
12. Rettig WJ, Garin-Chesa P, Beresford HR, Oettgen HF, Melamed MR, Old LJ (1988) Cell-surface glycoproteins of human sarcomas: differential expression in normal and malignant tissues and cultured cells. Proc Natl Acad Sci U S A 85(9):3110–3114
13. Garin-Chesa P, Old LJ, Rettig WJ (1990) Cell surface glycoprotein of reactive stromal fibroblasts as a potential antibody target in human epithelial cancers. Proc Natl Acad Sci U S A 87(18):7235–7239
14. Scanlan MJ, Raj BK, Calvo B, Garin-Chesa P, Sanz-Moncasi MP, Healey JH, Old LJ, Rettig WJ (1994) Molecular cloning of fibroblast activation protein alpha, a member of the serine protease family selectively expressed in stromal fibroblasts of epithelial cancers. Proc Natl Acad Sci U S A 91(12):5657–5661
15. Shelton PT, Jensen KJ (2013) Linkers, resins, and general procedures for solid-phase peptide synthesis. Methods Mol Biol 1047:23–41

Chapter 5

Fluorescence Imaging of Inflammation in Live Animals

Mingzhou Zhou, Jie Cao, and Walter J. Akers

Abstract

Inflammation is associated with many diseases, such as stroke, cancer, and atherosclerosis. Noninvasive in vivo monitoring of inflammation can provide deeper understanding of such diseases, which might help to develop better treatment. Inflammation normally causes neutrophils and macrophages to generate reactive oxygen species (ROS) as the destruction tool, which can be used as a biomarker for inflammation. Near-infrared (NIR) window is optimal for in vivo fluorescence imaging owing to the reduced autofluorescence and low attenuation of light in biological tissues. Among NIR fluorescent probes, activatable probes have the promise of achieving high imaging contrast. In this chapter, we describe the method for in vivo fluorescence imaging of inflammation using a ROS-activatable NIR probe.

Key words Inflammation, ROS, In vivo, Near infrared fluorescence imaging, Activatable probe

1 Introduction

Inflammation is our body's nonspecific protective immune response to eliminate injury and initiate the repairing process [1]. Inflammation is involved in many disease processes, such as stroke [2] and cancer [3]. Chronic inflammation also causes diseases such as atherosclerosis [4]. Monitoring and understanding inflammation can contribute to a better understanding of those diseases and develop treatments. There are primarily two types of inflammation, infection inflammation and sterile inflammation [5]. Infection inflammation is caused by the microorganisms intrusion; sterile inflammation, on the other hand, is normally caused by trauma, ischemia–reperfusion injury, or chemically induced injury [5]. Both types of inflammation have similar mechanism. When an injury is detected, immune cells, mainly neutrophils and macrophages, will infiltrate the site of the infection via chemotaxis. Besides phagocytosis, neutrophils and macrophages also produce reactive oxygen species (ROS) and reactive nitrogen species (RNS) to destroy the microorganisms and damaged tissues, as well as activate lymphocytes and adapt proper immune responses

Mingfeng Bai (ed.), *In Vivo Fluorescence Imaging: Methods and Protocols*, Methods in Molecular Biology, vol. 1444,
DOI 10.1007/978-1-4939-3721-9_5,

[5]. Here, we introduce ischemia to cause an inflammatory response [6] and image the generated ROS using fluorescence imaging.

Fluorescence imaging is a powerful tool to monitor and study biological processes at molecular level noninvasively with a high resolution in cells, tissues, and small animals [7]. Fluorescence imaging can also be used as a complementary technique to other imaging methods, such as X-ray computed tomography (CT), magnetic resonance imaging (MRI), and positron emission tomography (PET), and has started to be translated into clinical applications [8]. For deeper tissue and in vivo imaging, fluorescent dyes that are photoactive in the near-infrared (NIR) window, 650–900 nm, are preferred due to reduced autofluorescence and low attenuation of light in biological tissues [9].

The contrast of fluorescence imaging is typically achieved through two strategies. First, the dyes can be conjugated to targeting groups (e.g., antibodies [10] and peptides [11]) so that the fluorescence dyes accumulate at the region of interest. Second, the fluorescence of the probes is designed to be quenched initially, and then regenerated through certain activating processes (e.g., the cleavage of the fluorescent dye from its quencher dye by enzymes associated with diseases [12] and the regeneration of an interrupted conjugation system through oxidation process [13, 14]). The second type of the fluorescence probes is called the activatable probes. Compared to the "always on" probes of the first type, activatable probes are not highly fluorescent until reaching the target sites, thus offering high imaging contrast. Here, we describe the detailed protocol for performing in vivo fluorescence imaging of inflammation using a ROS-activatable probe [14]. As a reduced product of a cyanine dye, this probe is nonfluorescent because the reduction disrupted the sp^2 conjugation system essential to achieve NIR fluorescence. ROS subsequently oxidize the probe to regenerate the sp^2 conjugation system, making the oxidation product fluorescent in the NIR window. Base on this design, reduced cyanine dyes can act as ROS sensors to image inflammation in vivo.

2 Materials

2.1 Instrumentation

The in vivo images were captured with the Pearl Impulse Small Animal Imaging system (LiCor Biosciences, Lincoln, NE).

2.2 Fluorescence Imaging Agent

Currently, there is no commercially available NIR contrast agent to image inflammation. Such contrast agent, however, can be readily synthesized through a one-step $NaBH_4$ reduction from commercially available dyes [13, 14].

2.2.1 Inflammation Imaging Contrast Agent Synthesis General Strategy

A variety of NIR dyes, including the commercially available Cy7, are suitable to be used as the precursor to synthesize ROS-sensitive contrast agents [13]. We used a Cy7 analog developed by Dr.

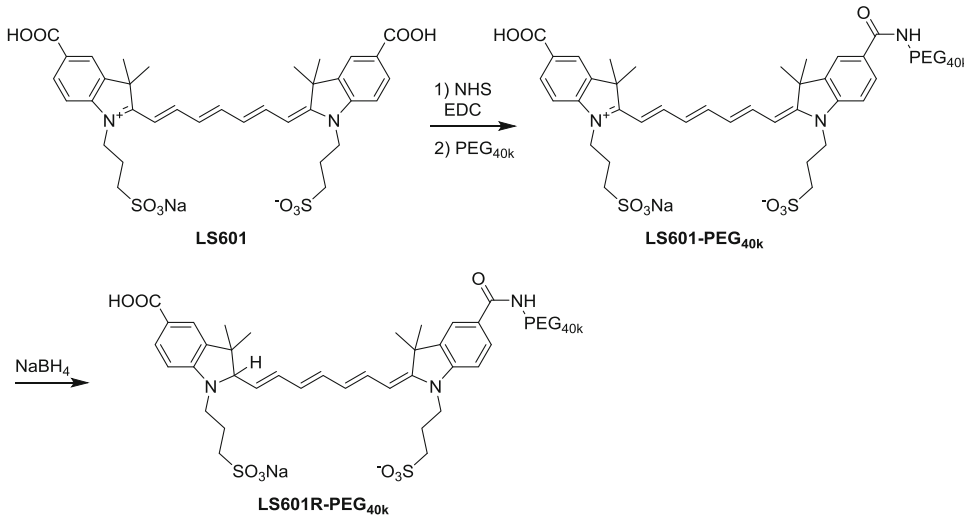

Scheme 1 Preparation of ROS sensitive probe **LS601R**-PEG_{40k} from **LS601**. (Reprinted from Ref. 14 with permission from Publisher)

Mikhail Berezin, **LS601** (Scheme 1), as the dye of choice [15]. **LS601**, which has its absorption and emission peaks at 769 nm 800 nm in DMSO, respectively, is a functionalizable NIR dye with high brightness.

2.2.2 Conjugation of LS601 to a 40 kDa PEG (PEG40k) (See Note 1)

Although not required, we found that **LS601** showed better contrast when conjugated to a PEG_{40k} molecule. This PEGylation increased **LS601**'s blood circulation time, reduced its albumin binding and nonspecific protein interaction [16]. A standard NHS ester–amine conjugation was applied here (Scheme 1):

1. **LS601** (56 mmol) is dissolved in DMF (2 mL).
2. To the above solution is added N-hydroxysuccinimide (NHS, 120 mmol) and *N*-(3-Dimethylaminopropyl)-*N'*-ethylcarbodiimide hydrochloride (EDC, 120 mmol).
3. The reaction mixture is stirred overnight in the dark.
4. The product is precipitated out from the solution by adding diethyl ether (10 mL) to the reaction mixture (*see* **Note 2**).
5. Recrystallization of the intermediate is done by redissolving the precipitate in a minimal amount of methanol (*see* **Note 3**) followed by adding excess amount of diethyl ether to precipitate out the product (*see* **Note 4**), which is filtered and dried.
6. The intermediate **LS601**-NHS ester (5 μmol) is redissolved in DMSO (100 μL).
7. To a solution of methoxy-PEG-amine 40 kDa (PEG_{40k}, 2.5 μmol) in $NaHCO_3$ buffer (0.1 M, 1 mL) is added the above solution.

8. The reaction mixture is shaken for 3 h in the dark.
9. The product, **LS601**-PEG_{40k}, is purified with a Sephadex G-25 column eluted with water (*see* **Note 5**).

2.2.3 Characterization of the LS601-PEG_{40k} Compound

SDS-PAGE is used to quantitatively characterize **LS601**-PEG_{40k}. Bio-Rad Any KD or 4–20% Mini-PROTEAN TGXTM Gel is used to characterize **LS601**-PEG_{40k} and manufacturer's protocol is followed. A Precision Plus Protein All Blue Standard (Bio-Rad Laboratories, fluorescent at 710 nm) is used as the ladder. After development, the gel is imaged using the Pearl Impulse Small Animal Imaging system (LiCor Biosciences, Lincoln, NE), where the probe is imaged using the 785 nm/810 nm channel; the ladder is imaged using the 685 nm/710 nm channel (*see* **Note 6**). The quantitative analysis is done using the Pearl Cam Software (LiCor Biosciences, Lincoln, NE). An equal size region of interest (ROI) is drawn at all the bands on the gel in both channels. The fluorescence intensity of each ROI is determined by subtracting the background fluorescence from the mean intensity of that ROI. The relative distribution of each band is then calculated through dividing each band's fluorescence intensity by the sum of all bands' fluorescence intensity (*see* **Note 7**). For this **LS601**-PEG_{40k} conjugation, ~70% of the product is the mono-PEGylated **LS601**, ~22.5% is the di-PEGylated **LS601**, and there is about ~7.5% of **LS601** that has not been conjugated to PEG_{40k} (*see* **Note 8**).

2.2.4 Reduction of the Dyes to ROS Sensors

The fluorescent dyes need to be reduced prior to ROS sensing imaging. The reduction of the dyes followed a general $NaBH_4$ reduction procedure.

1. **LS601**-PEG_{40k} (0.28 μmol) is dissolved in deionized (DI) water (1 mL) and then cooled to 0 °C.
2. To the above solution at 0 °C is added 20 μL $NaBH_4$ (1 mg/mL) in DI water in four portions (*see* **Note 9**). UV–Vis absorption is used to check the completion of this reaction by monitoring the disappearance of the 770 nm peak.
3. The reaction is then left overnight in the dark before the in vivo use.

2.2.5 Probe Evaluation

The probes from the $NaBH_4$-reduction can be tested for the ROS sensitivity before in vivo application (*see* **Note 10**). The procedure below is followed.

1. A quartz cuvette filled with methanol (2 mL) and a stirring bar is placed in a fluorometer, whose excitation wavelength is set at 720 nm and emission range is set between 735 and 950 nm.
2. To this cuvette is added 5 μL of the reduced **LS601** (1 mg/mL in DMSO).

3. H_2O_2 is then added to the above solution immediately followed by ferrous sulfate (10 mM, 15 μL).
4. The emission is monitored (*see* **Note 11**).

2.3 Animal Models

Animal studies are performed in accordance to protocols approved by Washington University School of Medicine in St. Louis Animal Studies Committee for humane care and use of laboratory animals.

2.3.1 Animals

6–10-week-old C57B16 black male mice (Harlan Laboratories, Indianapolis, IN) are used in this study.

2.3.2 Surgical Procedure to Induce Ischemia

Ischemia was introduced at the lower thigh and lower limb.

1. Buprenorphine (0.1 mg/g) is administered subcutaneously before surgery and 12 h post-surgery.
2. Mice are anesthetized by isoflurane (2%, 1 L/min) (*see* **Note 12**).
3. The hair of the lower abdomen and the ventral surface of both hindlimbs is removed using electric clipping followed by cream depilatory.
4. The shaved mice are placed supinely on a covered heating pad with limbs secured.
5. The right hindlimb is prepared for the aseptic surgery using betadine and ethanol on cotton swabs (3×).
6. In the inguinal area, parallel to the body wall, a 1-cm skin incision is made using fine forceps and surgical scissors (*see* **Note 13**).
7. 7-0 silk ligatures is placed around the artery and vein bundle (*see* **Note 14**) after dissecting the subcutaneous fat pad from the femoral sheath.
8. Finally, the blood flow is occluded from the segment of the femoral artery and vein between the distal and the 7-0 silk knots by resecting the femoral artery within the ligatures.
9. After the surgery, the skin is closed by 6-0 nylon sutures in a simple interrupted pattern.
10. 0.5 mL saline is administered subcutaneously.
11. The anesthesia is then removed.
12. The mouse's recovery is monitored on the heating pad.

3 In Vivo Imaging

Imaging studies are carried out 3 days post-surgery. All procedures are done at room temperature unless otherwise specified.

1. The mice are anesthetized by isoflurane (2%, 1 L/min) pre-injection.
2. Turn on the imager.

3. Open the drawer to ensure the machine is connected (*see* **Note 15**).
4. Wait for the machine to warm up (*see* **Note 16**).
5. Click the camera icon (*see* **Note 17**).
6. The mice are administered with **LS601R**-PEG_{40k} intravenously via the tail vein.
7. Turn on the isoflurane for the imager and place the mouse on the imaging bed.
8. Start the imaging process by pushing the start button (*see* **Note 18**).
9. Images are acquired at immediately, 1, 4, and 24 h post-injection.

4 Control Studies and Imaging Evaluation

4.1 Control Study

Two control studies are applied: (1) Imaging of injured limb vs. uninjured limb by **LS601R**-PEG_{40k}, and (2) imaging of injured limb using **LS601R**-PEG_{40k} vs. unreduced dye (**LS601**-PEG_{40k}). As shown in Fig. 1, the limb that was induced with ischemia (left) showed higher contrast than the intact limb (right) when imaged by **LS601R**-PEG_{40k}. In addition, when both **LS601R**-PEG_{40k} and **LS601**-PEG_{40k} were studied under the same imaging study condition, the reduced form, **LS601R**-PEG_{40k} showed much higher contrast than the unreduced form (Fig. 2).

4.2 Ex Vivo Study Sample Preparation

The anesthetized mice are euthanized immediately after the last scan via cervical dislocation. Thigh and calf muscles are collected, snap-frozen in Optimal Cutting Temperature compound (OCT), and stored at −80 °C for further analysis.

4.3 Histology Analysis

Oxidation stress caused by ROS at the injury site is evaluated by immunohistochemistry. ROS could cause the oxidation of DNA and RNA's deoxyguanosine to form 8-oxidized guanosine (8-OHG) [17]. Under the same condition, tyrosine could also be oxidized to nitrotyrosine [18]. Both 8-OHG and nitrotyrosine antibodies are readily available and are applied here for the immunohistochemistry stain. Normal uninjured muscle is used as the control.

1. The mouse muscle specimens are first fixed with 4% paraformaldehyde (Fig. 3).
2. The muscle is then embedded in paraffin.
3. The muscle is cut into 5 μm sections using cryostat.
4. 8-OHG and nitrotyrosine antibodies are used to stain the muscle.

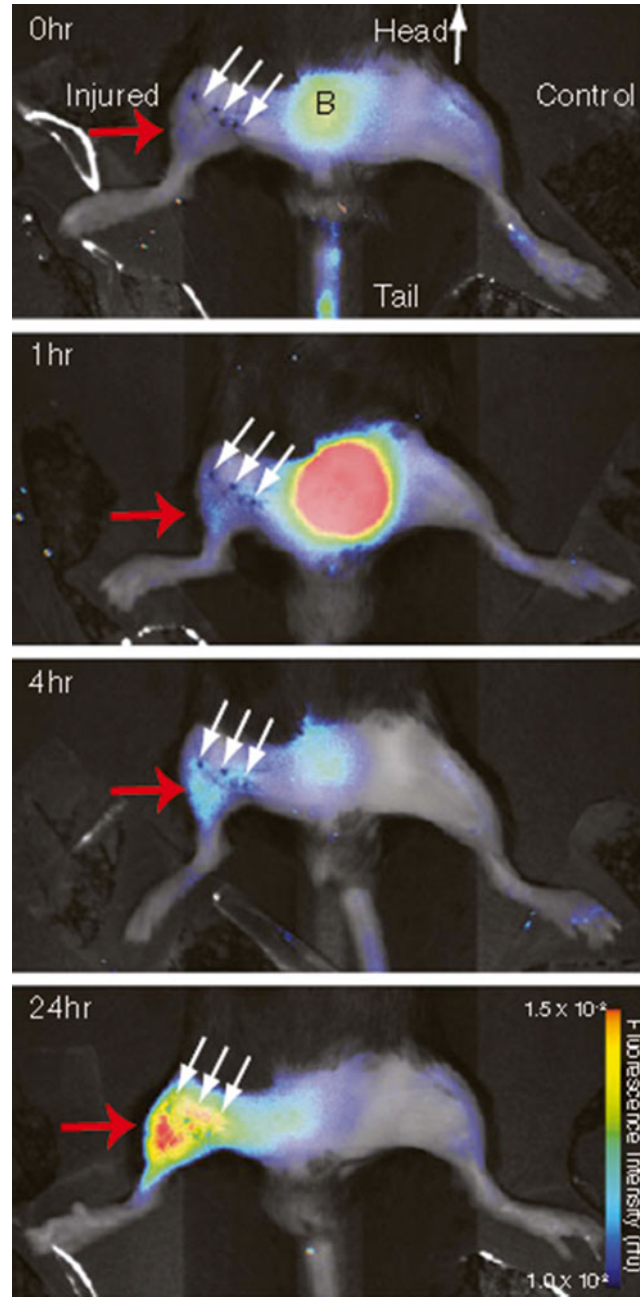

Fig. 1 Fluorescence imaging at immediately, 1, 4 and 24 h post-injection of **LS601R**-PEG_{40k} (785 nm/810 nm channel). The *white arrows* show the surgical site and the *red arrow* shows the fluorescence increase. Fluorescence of the uninjured limb did not increase significantly. (Reprinted from Ref. 14 with permission from Publisher)

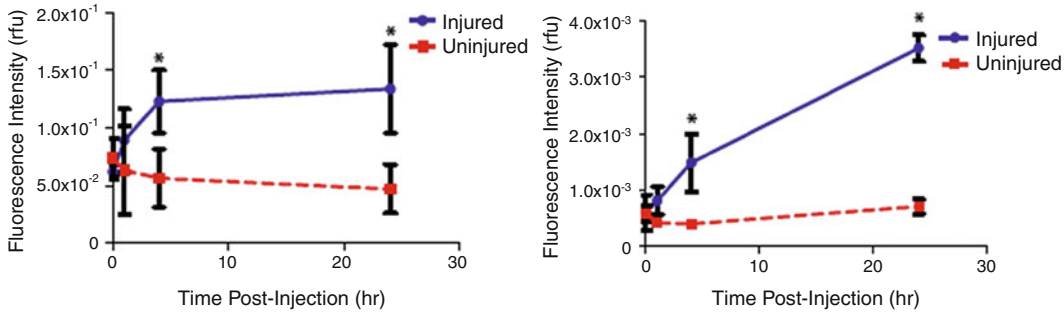

Fig. 2 Left, fluorescence intensity change at the ROIs selected around the surgical site at different time points after injecting **LS601**-PEG_{40k} ($n=3$); *right*, fluorescence intensity change at the ROIs selected around the surgical site at different time points after injecting **LS601R**-PEG_{40k} ($n=3$). **LS601R**-PEG_{40k} caused a 5.8× increase at the ROI. (Reprinted from Ref. 14 with permission from Publisher)

5 Imaging Process

The Quantitative post imaging analysis is done using Pearl Cam Software (LiCor Biosciences, Lincoln, NE). A thigh region distal to the surgical incision is selected as the ROI, whose mean intensity is determined using the Pearl Cam Software. Student's t test is used to compare the injured and uninjured limbs with $\alpha=0.01$. Graphpad Prism 5.0 is then used for the statistical analysis of the imaging data.

6 Notes

1. Conjugation to a PEG molecule is not essential for the inflammation imaging, but is important to extend circulation time in vivo for adequate contrast in this model [13].
2. 10–50× volume of diethyl ether is needed to fully precipitate the product.
3. Minimal amount of methanol used here is critical to obtain higher yield of the reaction.
4. Repeat the recrystallization step if necessary.
5. The product should show a green band on the column.
6. Those channels are the default setting of the Pearl Imager. Other fluorescence imaging systems may also be used to match the fluorescence emissions of other dyes.
7. This calculation is based on the fact that all the fluorescent bands carry the same fluorophore.
8. The mixture of mono- and di-PEGylation did not affect **LS601**'s ability to image inflammation.
9. UV–Vis absorption is measured after adding each portion. More portions of $NaBH_4$ can be added if necessary.

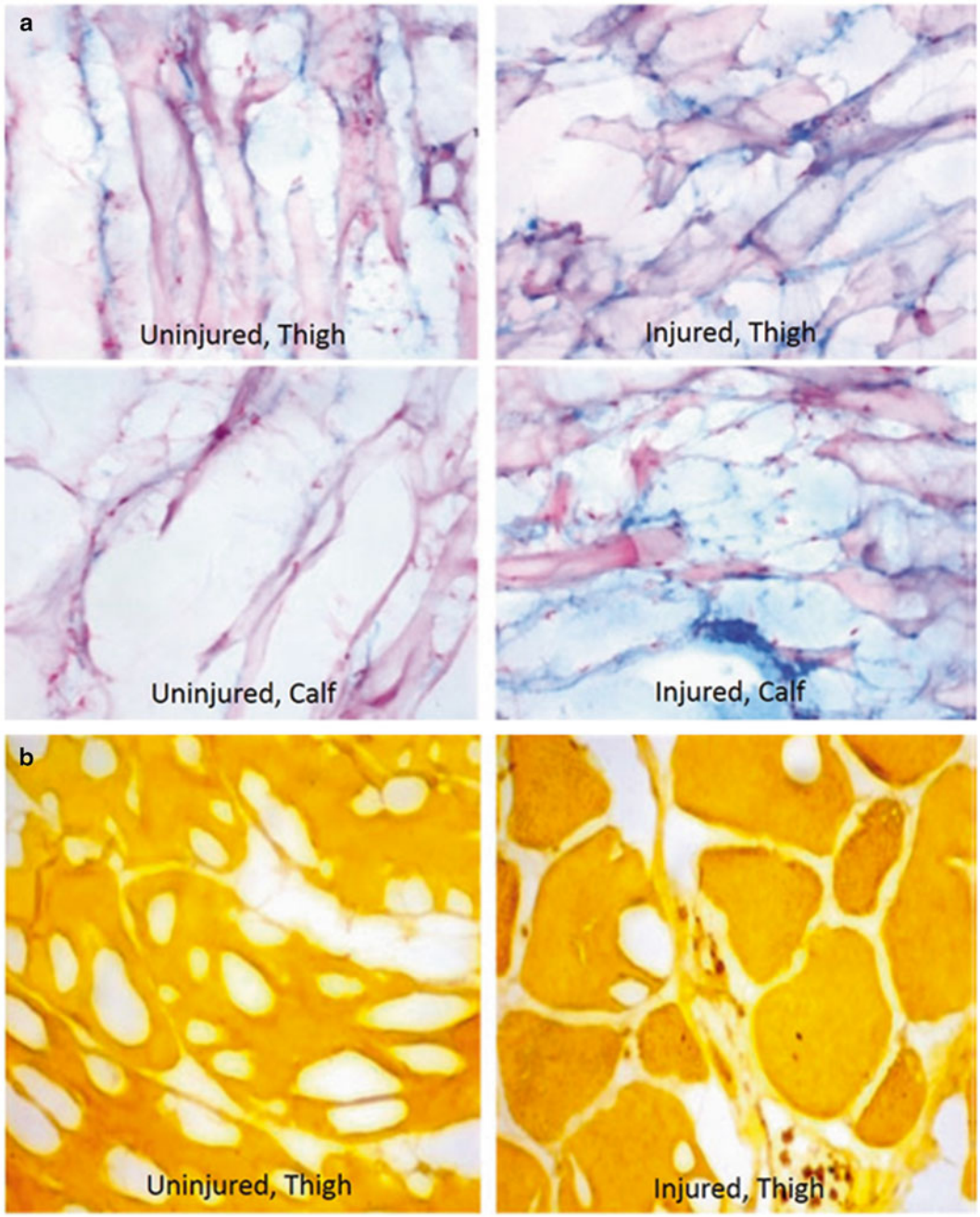

Fig. 3 (**a**) There is a mild increase of 8-OHG stain (*blue*) in the injured muscle compared to the uninjured muscle; (**b**) There is mild increase of nitrotyrosine stain (*brown*) in the injured muscle compared to the uninjured muscle. (Reprinted from Ref. 14 with permission from Publisher)

10. We only test LS601's ability for ROS sensing since PEGylation should not affect the fluorophore.
11. As a result of the oxidation, the absorption peak at ~770 nm was regenerated.

12. This is verified by the absence of the toe pinch reflex.
13. The surgery is performed under a stereomicroscope (3–4×).
14. Femoral nerve should be carefully avoided at the distal femoral, perforating artery, epigastric artery and proximal femoral.
15. One easy way to check if the machine is connected is to turn the temperature off. An error message will show if the machine is not connected.
16. The camera icon will change from gray to clickable when the machine is warmed up.
17. Add animal IDs; change the camera settings: channels, resolution, and focal plane.
18. The images will be saved automatically.

References

1. Ferrero-Miliani L, Nielsen OH, Andersen PS, Girardin SE (2007) Chronic inflammation: importance of NOD2 and NALP3 in interleukin-1beta generation. Clin Exp Immunol 147:227–235
2. Huang J, Upadhyay UM, Tamargo RJ (2006) Inflammation in stroke and focal cerebral ischemia. Surg Neurol 66:232–245
3. Coussens LM, Werb Z (2002) Inflammation and cancer. Nature 420:860–867
4. Libby P, Ridker PM, Maseri A (2002) Inflammation and atherosclerosis. Nature 420: 868–874
5. Chen GY, Nuñez G (2010) Sterile inflammation: sensing and reacting to damage. Nat Rev Immunol 10:826–837
6. Benjelloun N, Renolleau S, Represa A, Ben-Ari Y, Charriaut-Marlangue C (1999) Inflammatory responses in the cerebral cortex after ischemia in the P7 neonatal Rat. Stroke 30:1916–1923
7. Solomon M, Liu Y, Berezin MY, Achilefu S (2011) Optical imaging in cancer research: basic principles, tumor detection, and therapeutic monitoring. Med Princ Pract 20:397–415
8. Liu Y, Zhao YM, Akers W, Tang ZY, Fan J, Sun HC, Ye QH, Wang L, Achilefu S (2013) First in-human intraoperative imaging of HCC using the fluorescence goggle system and transarterial delivery of near-infrared fluorescent imaging agent: a pilot study. Transl Res 162:324–331
9. Weissleder R (2001) A clearer vision for in vivo imaging. Nat Biotechnol 19:316–317
10. Kaur S, Venktaraman G, Jain M, Senapati S, Garg PK, Batra SK (2012) Recent trends in antibody-based oncologic imaging. Cancer Lett 315:97–111
11. Bai M, Bornhop DJ (2012) Recent advances in receptor-targeted fluorescent probes for in vivo cancer imaging. Curr Med Chem 19:4742–4758
12. Akers WJ, Xu B, Lee H, Sudlow GP, Fields GB, Achilefu S, Edwards WB (2012) Detection of MMP-2 and MMP-9 activity in vivo with a triple-helical peptide optical probe. Bioconjug Chem 23:656–663
13. Kundu K, Knight SF, Lee S, Taylor WR, Murthy N (2010) A significant improvement of the efficacy of radical oxidant probes by the kinetic isotope effect. Angew Chem Int Ed Engl 49:6134–6138
14. Magalotti S, Gustafson TP, Cao Q, Abendschein DR, Pierce RA, Berezin MY, Akers WJ (2013) Evaluation of inflammatory response to acute ischemia using near-infrared fluorescent reactive oxygen sensors. Mol Imaging Biol 15:423–430
15. Gustafson TP, Cao Q, Achilefu S, Berezin MY (2012) Defining a polymethine dye for fluorescence anisotropy applications in the near-infrared spectral range. ChemPhysChem 13(3): 716–723
16. He Q, Zhang J, Shi J, Zhu Z, Zhang L, Bu W, Guo L, Chen Y (2010) The effect of PEGylation of mesoporous silica nanoparticles on nonspecific binding of serum proteins and cellular responses. Biomaterials 31:1085–1092
17. Wu LL, Chiou CC, Chang PY, Wu JT (2004) Urinary 8-OHdG: a marker of oxidative stress to DNA and a risk factor for cancer, atherosclerosis and diabetics. Clin Chim Acta 339:1–9
18. Dijkstra G, Moshage H, van Dullemen HM, de Jager-Krikken A, Tiebosch AT, Kleibeuker JH, Jansen PL, van Goor H (1998) Expression of nitric oxide synthases and formation of nitrotyrosine and reactive oxygen species in inflammatory bowel disease. J Pathol 186:416–421

Chapter 6

Fluorescence Lifetime Imaging of Cancer In Vivo

Owen Peng and Walter J. Akers

Abstract

Optical imaging of fluorescent reporters in animal models of cancer has become a common tool in oncologic research. Fluorescent reporters including fluorescent proteins, organic dyes, and inorganic photonic materials are used in fluorescence spectroscopy, microscopy, and whole body preclinical imaging. Fluorescence lifetime imaging provides additional, quantitative information beyond that of conventional fluorescence intensity signals, enabling signal multiplexing, background separation, and biological sensing unique to fluorescent materials.

Key words Molecular imaging, Microenvironment, Drug delivery, Oncology, Animal model, Time-domain, Diffuse spectroscopy, Optical, Preclinical

1 Introduction

Fluorescence lifetime (FLT) is an intrinsic property of fluorescent compounds (fluorophores) that emit light after absorbing higher energy photons. The measured FLT corresponds to the average amount of time a population of fluorescent molecules spends in the excited state prior to photon emission. FLT measurements represent a population effect rather than direct measurement of individual fluorophores. Unlike fluorescence intensity, FLT is a quantitative measurement directly related to the quantum yield of a dye, not its concentration.

This property of fluorophores has been used extensively in microscopy (fluorescence lifetime imaging microscopy, FLIM) to detect protein–protein interactions, fluorescence resonance energy transfer (FRET), and changes in local pH (Fig. 1). FLT imaging microscopy and FLT endoscopy have utilized intrinsic tissue FLT data to assess differences in distribution of factors such as NADH and FADH and their oxidation state to correlate with pathologic changes or other biological processes [1]. FRET occurs when fluorophores with similar spectral characteristics are in close proximity, and absorbed energy is transferred from the donor fluorophore to

Mingfeng Bai (ed.), *In Vivo Fluorescence Imaging: Methods and Protocols*, Methods in Molecular Biology, vol. 1444,
DOI 10.1007/978-1-4939-3721-9_6,

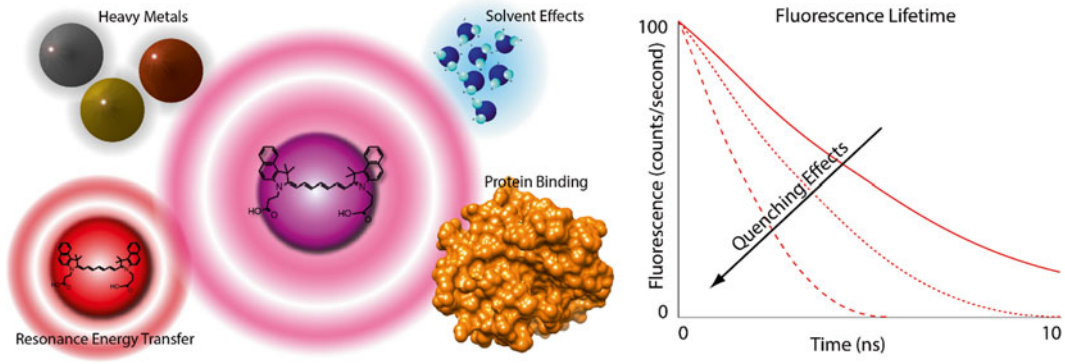

Fig. 1 Depiction of quenching sources and energy transfer mechanisms that can affect the measured fluorescence lifetime of fluorophores in biological tissues. Physical and chemical characteristics of the fluorophore environment can affect the excited state dye, reducing its quantum yield and therefore fluorescence lifetime

the acceptor. Microscopy applications of fluorescent protein FRET pairs have demonstrated very effective strategies for investigating protein–protein interactions. Initial methods for measuring FRET required measuring the fluorescence of each fluorophore, calibrating signals with individual control measurements, improving the accuracy of energy transfer calculations. After implementation of fluorescence lifetime imaging microscopy (FLIM), it has been shown that FLT measurements are more accurate in measuring FRET by measuring a single emission channel [2].

Two methods are available for FLT measurement, frequency domain and time domain. Time domain fluorescence lifetime measurements in deep tissue have been shown to be superior to frequency domain methods due to the quality of information detected [3]. Time domain measurements require pulsed laser excitation on the order of nanosecond pulse width and time-gated detection. Collected time-domain fluorescence measurements are typically presented as a temporal point spread function (TPSF), a statistical representation of the counted photons relative to the time after excitation. Time correlated single photon counting detectors are the most accurate and reliable for this purpose. Another method uses gated image intensifiers, measuring fluorescence emission at discrete time intervals after excitation [4]. This method can be much faster, binning a given range of time after excitation into gates to cover an expected FLT range with temporal resolution dependent on the number of gatings acquired.

Translating FLT imaging to preclinical and clinical arenas introduces challenges due to nonlinear absorption and scattering properties of biological tissues. Nonetheless, FLT measurements can significantly enhance the amount of information gained from near infrared (NIR) optical imaging.

At this time, there has been only one preclinical FLT imaging system available for purchase, the Optix systems from Advanced

Research Technologies, which is no longer in business. Regardless, FLT imaging continues to be explored and the same principles apply to any time-domain imaging system, only varying by the specific method of data acquisition and analysis software capabilities. In fact, 3D FLT imaging has been reported for whole body imaging of organic fluorophores [4, 5] and fluorescent proteins [6, 7] in murine models.

Cancer represents an important application for diagnostic imaging with many challenges. In general, cancer tissue is very similar to normal, healthy tissue, particularly at early stages. Differences that distinguish cancer from noncancerous tissues can include increased expression and activity of growth receptors and remodeling enzymes, altered pH and increased metabolism. Molecular imaging methods have gained significant ground in detecting increased metabolism, cell proliferation, and cell-surface receptor expression, but measuring enzyme activity and pH has proved elusive [8].

Our lab and others have demonstrated the potential of FLT imaging using near infrared (NIR) molecular probes in whole-animal optical imaging [4, 9–14]. The independence of FLT from dye concentration minimizes the detrimental effects of concentration artifacts, including photobleaching and dye decomposition. In addition, the FLT is less perturbed by light scattering [15, 16], excitation intensity, or sample turbidity [17]. FLT imaging allows multiplex resolution of probes that exhibit the same steady state optical properties (absorption and emission) with different FLT characteristics [9]. We have shown that NIR fluorescent reporters that clear through the kidneys have significantly lower fluorescence lifetime in the bladder, likely due to low amounts of protein in the urine [18, 19]. More recently, we demonstrated that FLT imaging can improve detection of enzyme-mediated hydrolysis of FRET-based NIR fluorescent probes in vivo [20]. Current instrumentation allows FLT resolution of 0.2 ns or less, which favors detection of small FLT changes.

Future applications: Fluorescence lifetime imaging has great potential for noninvasive sensing when paired with advanced fluorescent molecules. We and others have worked to develop sensing fluorescent dyes for detecting tumor-specific characteristics such as pH [21, 22], enzyme activity [20, 23–25], and molecular radicals [26]. While many of these sensing dyes rely on spectral changes of absorbance and/or fluorescence emission, others act by changes in quantum yield (seen as intensity), which is directly related to the fluorescence lifetime. These include dyes sensitive to pH [21, 27], selective protein binding [28, 29], and ion concentration [30].

In scattering media, including biological tissues, fluorescence intensity is generally not quantitative due to surface enhancement of signals. Fluorescence lifetime on the other hand is not as sensitive to scattering and therefore represents a quantitative method for

noninvasive sensing. We have recently shown that fluorescence lifetime imaging can independently quantify changes in fluorescence signals due to differences in pH [22], enzyme activity [20], and biodegradation of nanoparticles [31]. In these cases, fluorescence intensity alone would not have provided reliable measurements of these events. As more of these sensing dyes are developed, fluorescence lifetime imaging will gain utility and potential for diagnostic use.

2 Materials

1. Appropriate animal model. All animal studies must be approved by your institutional animal care and use committee and follow guidelines specified by the granting agency such as the *Guide for the Care and Use of Laboratory Animals* [32].
2. Anesthesia such as ketamine–xylazine cocktail for injection or isoflurane with precision vaporizer for inhalation delivery.
3. Hair remover cream such as Gel Hair Remover Cream (Veet)
4. Low fluorescence rodent chow such as #D10001 (OpenSource Diets), TD.97184 (Envigo), or 5V75 (LabDiet) fed for at least 3 days prior to imaging to reduce fluorescence from digesta in gastrointestinal tract.
5. Fluorescent contrast agent with optical properties matching excitation source and emission filters of the instrument to be used.
6. Fluorescence lifetime imaging system, computer, and software for acquiring and analyzing time-domain fluorescence data.

3 Methods

Optical imaging can be performed in three basic geometries: reflectance, diffuse reflectance, and transillumination (Fig. 2).

3.1 Animal Handling

As with most preclinical imaging procedures, mice must be anesthetized to prevent corruption of data by movement during scanning. Anesthesia can be performed using injectable (e.g., ketamine–xylazine) or inhaled (e.g., isoflurane) methods. Injectable anesthesia gives greater flexibility in manipulation and positioning, but has a lower safety threshold and may not last as long as needed. Gas anesthesia is rapidly induced, safe and recovery is quick but requires strict positioning of the nose and mouth for delivery. The Optix MX3 is equipped for gas anesthesia with nose cone to facilitate scanning a single mouse from head to tail.

1. Animals should be anesthetized for all procedures including imaging. If not completely anesthetized, mice may move during the scan or result in poor positioning. Use ketamine

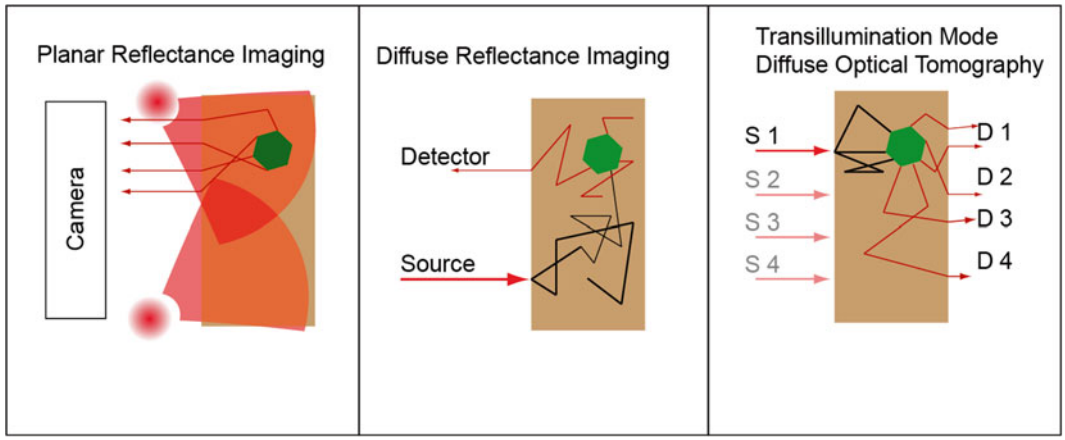

Fig. 2 Cartoons of geometries for preclinical optical imaging of fluorescent molecules. Photons are scattered in biological tissues, traveling a random, nonlinear path. The Optix MX3 uses laser excitation for diffuse reflectance imaging in a raster scanning technique to measure fluorescence intensity and fluorescence lifetime several millimeters below the skin surface

and xylazine cocktail (80–100 mg/kg ketamine and 10–15 mg/kg xylazine) for intraperitoneal (IP) injection. Ketamine is a controlled drug, requiring appropriate individual or institutional licenses for purchase and use. Isoflurane is usually delivered using a precision vaporizer with appropriate pressure-regulated gas source (e.g., 30–100% oxygen). Typically, 2–3% isoflurane is sufficient for anesthetizing mice in an induction chamber followed by maintenance anesthesia at 2% via nose cone.

2. If using haired mice, hair must be removed by gentle clipping and chemical depilatory prior to imaging. We have had success with several cream agents that are applied for about 3 min, then rinsed away. It is important to carefully follow instructions to prevent skin damage as these can cause burns if left on for too long. Animal temperature should be maintained using heated pad as heat loss occurs quickly, particularly when wet.
3. Position animals as flat as possible with relation to the scanning head on the heated imaging platform (Fig. 3b). Best data collection will occur from surfaces normal to the excitation source and detector (*see* **Note 1**).
4. Once animal placement is satisfactory, close the instrument door and begin scanning.

3.2 Performing the Scan

1. First turn on the system and wait for the detector to warm up. This process can take up to 15 min as the system must adjust the chamber to the proper temperature and the laser must warm-up.
2. Choose a Laser Preset. The excitation wavelength must be chosen based on the optimal detection characteristics of the fluorescent reporter. As the Optix system utilizes laser excitation,

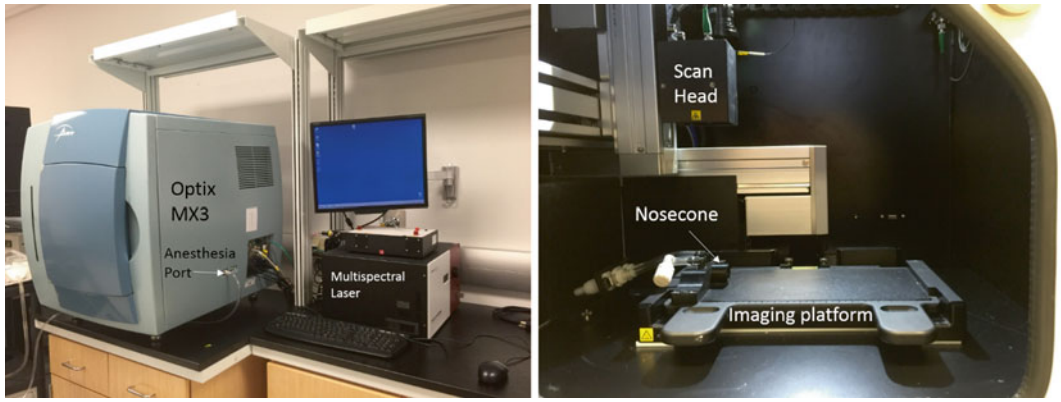

Fig. 3 Optix MX3 time domain diffuse optical imaging system equipped with supercontinuum white light laser, gas anesthesia, and heated imaging platform for imaging mouse models of cancer

which is essentially monochromatic, emission filters can be used that better fit the maximum emission range of the dye relative to lamp and light emitting diode (LED) sources used by many imaging systems. That being said, preselected settings for commonly used fluorescent reporters cover the majority of fluorescent proteins and dyes used for in vivo imaging. In the upper left corner you can adjust the wavelength emitted by the laser. There are many presets, but you can also create custom presets. There are three variables that go into each preset, the wavelength of the laser that hits the specimen, the time window, or the amount of time photons are collected, and the collection filter. The collection filter specifies for the system which photons to collect and analyze. For example, if the collection filter is set at 530 nm, the system will only collect photons that are 530 nm. The preset chosen is very important and should be tailored to the specific dye that is used in the system (*see* **Note 2**).

3. After the detector and laser are warmed up, a small icon in the lower left corner of the screen will appear that shows a lock. If this lock is "locked" and the background is yellow, the system is closed and specimens cannot be placed inside. After the system has warmed up, the icon will be green and "unlocked".
4. Place your mouse in the chamber on the imaging platform.
5. Next, press the scan icon in the upper left hand corner of the screen. It has a beaker, a flask, and a graduated cylinder on it. This is the first scan that will be done. This scan recognizes the sample that will be scanned on camera. You should see a picture of the sample in black and white on the computer screen.
6. Input the study name and location to save. Click "Next."
7. You will be brought to another screen. Here you will be able to choose between in vivo and in vitro scanning. In vivo is

used for 3D objects while in vitro is used for flat solutions. Depending on the settings the information collected will be different. Also name the specimen appropriately. Press "Next".

8. A profilometry scan of the specimen will occur to measure the height of the object and for 3D representation. This process takes about 1 minute. A sound from the system will indicate completion of the scan.
9. The next step is to select the region in which you will do the scan. You can choose the shape of the region of interest. Often times the basic rectangle is sufficient to the experiment. Using the "paintbrush" option, you can create your own region of interest. Within this region of interest you will see a series of horizontal and vertical lines. The frequency of these lines is related to the resolution chosen. Each intersection is a point that will be scanned. The region of interest should be large enough to encompass the entire sample, but at the same time should have minimal excess space, as this area will only increase the scanning time.
10. Next, choose an appropriate scanning resolution. By choosing a scan resolution, you are selecting the frequency of points of interest within the region of interest. For example, a scan resolution of 1 mm will place scanning points every 1 mm throughout the entire region of interest. While ideally all scans would be done in the highest resolution of 0.5 mm, this is not possible, because of time restraints. Since the system is rather slow, and even at low resolutions such as 3.0 mm time spent on higher resolutions is often not worth the increased detail of the scan. Most of the time a 3.0 mm resolution is used even for a relatively small area, as even that type of scan may take upwards of 15 min. Sometimes a higher resolution is needed, but a preliminary 3.0 mm scan should be done first in order to gauge the necessity of further scans.
11. After choosing the appropriate region of interest and the appropriate resolution press the scan button. This button will start an intensity scan that measures the intensity of emission at each point in the region of interest. The system uses the intensity information for planning the quantitative scan in which the laser power and detector integration time will be optimized pixel-by-pixel to ensure adequate photon counts without saturating the detector.
12. The initial scan is performed to evaluate fluorescence intensity at each pixel that will be used to plan the subsequent quantitative scan. For the quantitative scan, the system uses the intensity information to adjust the laser power and detector integration time for each pixel to obtain sufficient photon counts for accurate fluorescence lifetime determinations.

13. This next page is the start screen for a full quantitative scan. An important option to select is the "reject low quality points" option. This option eliminates points with low photon counts from the quantitative scan in order to save time. From the starting 100, press the down arrow and see on screen how the system blacks out the low intensity areas. Black out as much as possible to save the most time, while also not blacking out any regions that contain high intensities as they may contain important information. Then press next to start the scan. This is the longest scan of the process taking from 2 to 20 min, depending on the signal intensity and number of points measured.
14. When the scan is done press the "view results" button and then the "finish" button. The view results option opens up Optiview analysis software for data analysis.

3.3 Data Analysis

3.3.1 Fluorescence Intensity Analysis

1. An Intensity Plot is shown when Optiview is first opened. The intensity plot shows the amount of scattered photons collected by the system at each individual point and is determined as the integral of the TPSF curve.
2. The intensity scale can be adjusted with sliding bar in the top center of the analysis window.
3. Image zoom and intensity scales can be equalized across all images in the window for direct comparison.
4. Region of interest analysis can be performed to evaluate fluorescence intensity values for specific locations as desired.

3.3.2 Fluorescence Lifetime Analysis

1. The TPSF fit tool is located in the top left corner of the screen. There are three graph icons in that area and the left-most icon is the Fit Tool.
2. After clicking on the icon, your mouse will turn into an arrow. With the arrow, click on a point of interest on the intensity scan.
3. A new screen will appear showing the temporal point spread function representing the detected photons over time at the specified point (Fig. 4c). A nonlinear, exponential fit of the TPSF will also appear as a red line over the tail of the TPSF. Fitting of the TPSF from near the peak to the tail will be automatically performed and initial fluorescence lifetime calculated (*see* **Note 3**). The chi squared error of the fit will be plotted below the TPSF showing the goodness of fit (Fig. 4d).

3.3.3 Interpreting Fluorescence Lifetime

1. Fluorescence lifetime is a specific property of each fluorescent material that measures the amount of time a dye will remain in the excited state before releasing its energy as a photon. Since lifetime is specific to each dye it is a very important measurement to have.

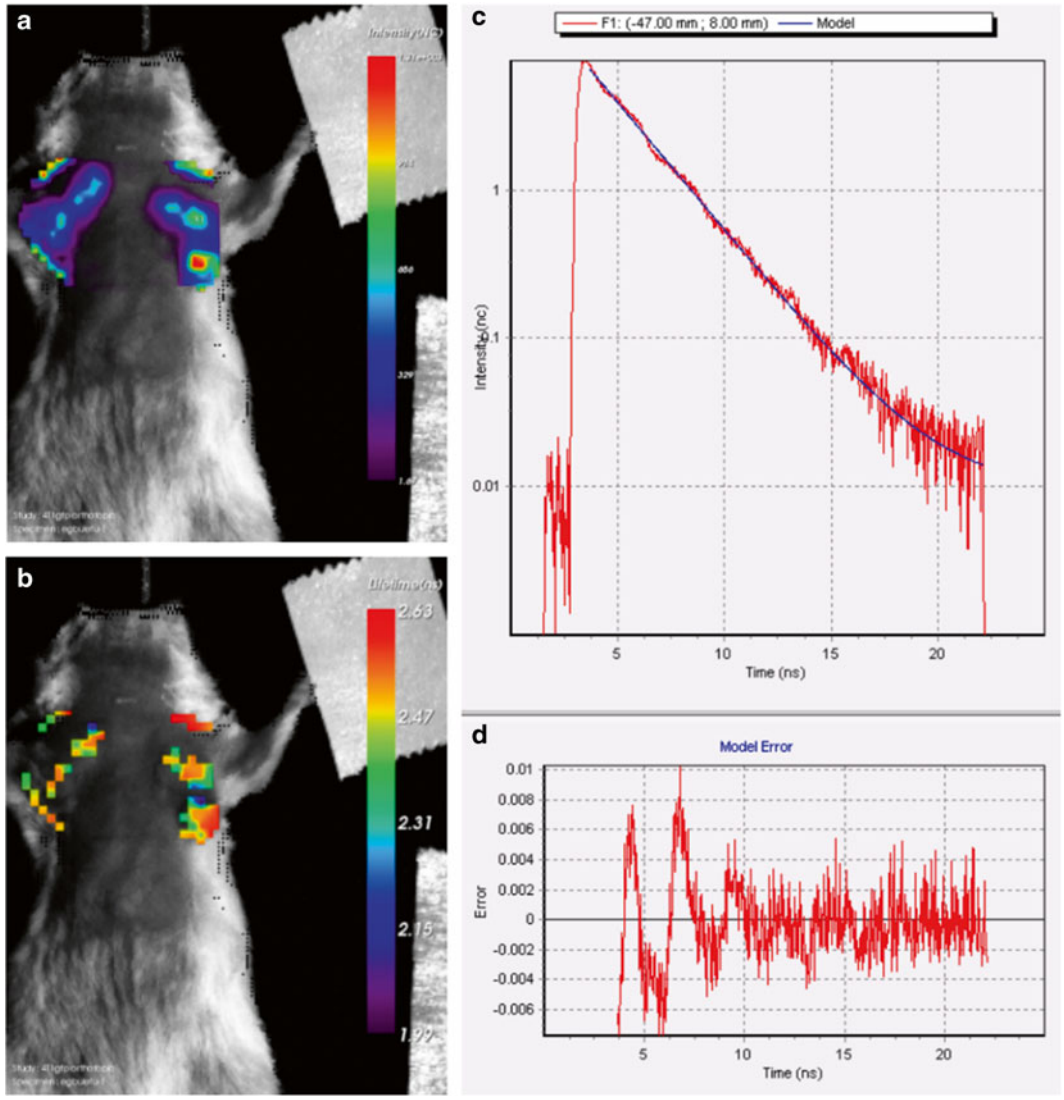

Fig. 4 Fluorescence intensity (**a**) and lifetime (**b**) maps from orthotopic tumors from murine mammary carcinoma cells expressing green fluorescent protein (excitation 470 nm, emission 500 nm). The fluorescence TPSF (**c**) shows a linear fit of logarithmic plot with minimal fitting error (**d**). The FLT map demonstrates contamination of GFP signal with autofluorescence in areas adjacent to tumor tissues

2. The TPS Fit Tool shows the lifetime at a single point, but the intensity scan can be converted into a lifetime plot. To do this under "Tasks" select lifetime analysis. Afterwards a lifetime plot will be produced.
3. As opposed to the intensity graph, interpretation of the fluorescence lifetime map is not straightforward. This makes sense, because it means that almost all the fluorescence present is a result of the specific dye used.
4. Fluorescence lifetime is a very useful tool in fluorescence imaging, because oftentimes it is not clear whether the source

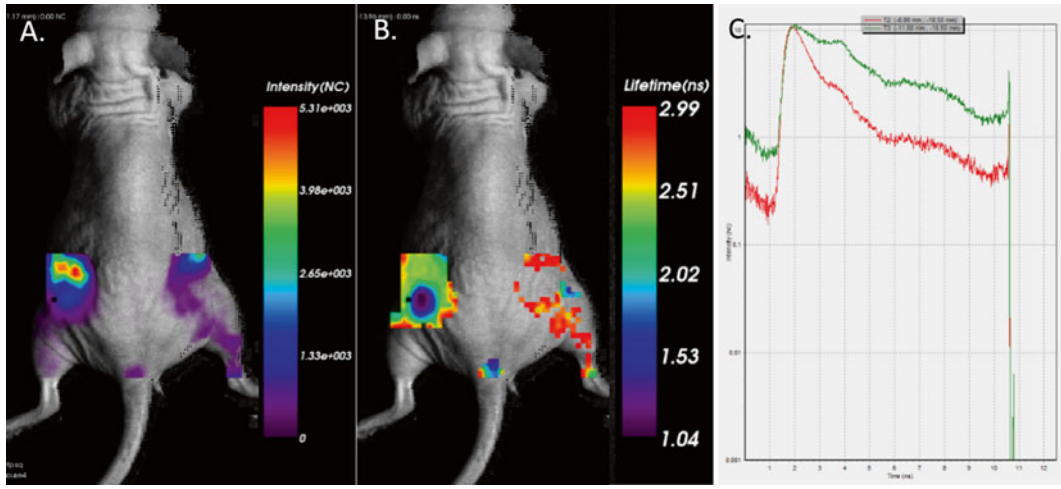

Fig. 5 Fluorescence intensity (**a**) and lifetime (**b**) maps of mouse with subcutaneous tumor xenograft of ovarian carcinoma cells transfected with infrared fluorescent protein. FLT information enables discrimination of IFP signal (~0.9 ns) from adjacent signal originating from gastrointestinal contents (>2 ns). The TPSFs (**c**) for tumor (*red*) and GI (*green*) show distinct differences in fluorescence decays

of fluorescence is actually the used dye or another source. Since fluorescence lifetime is specific to each particular dye despite the intensity, it is a good diagnostic to see for sure that the intensity is actually from dye (Fig. 5).

4 Notes

1. How the specimen is positioned in the chamber initially is very important to the results of your study. If the specimen is flat, it will be difficult for the laser to penetrate the sample and produce any significant scattering. In this case, it would be important to place some type of backing underneath the sample to promote scattering of the photons. With transparent specimens, oftentimes the system will not detect the sample very well. To fix this problem, a white sheet of paper can be placed underneath the sample in order for the machine to detect it.
2. Fluorescence signals can be overwhelmed by excitation light if not sufficiently blocked by the emission filter. A way to correct for this problem is to adjust the wavelength of the excitation light. If the wavelength of the collection filter is too similar to the wavelength of the laser excitation the likelihood of misattribution of intensity is higher. This is because the wavelength of the laser stays relatively constant from emission to collection. For example, a 730 nm laser when reabsorbed will still be at 730 nm. Contrast this with the scattered photons from fluorescence. When the fluorescent subject absorbs the

photons of the laser, it absorbs and releases the photons, but releases them at a variety of wavelengths. Each different wavelength is emitted at varying frequencies, and when graphed these emitted photons create an emission spectrum. While a high intensity may be assumed to be good, this is not always the case. It is important to know where these photons are coming from. Ideally, only photons scattered by the subject will be collected and analyzed by the machine, but this is not the case. Oftentimes, the machine will be collecting photons that come directly from the laser in addition to the photons scattered by the subject, and this can heavily skew results. The laser is a direct stream of photons whereas the scattered photons are very dispersed; as a result, the photons coming from the laser will be represented significantly more in the intensity count than the scattered photons. Therefore, it is good to see a high intensity, because it shows evidence of fluorescence, but it is more important that the photons collected are a result of actual scattering rather than laser reflection.

3. Ideally the line will show a straight steady decay with relatively little noise and a lack of artifacts. Noise is the random fluctuations of the TPSF. Artifacts are a large irregularity in the general slope of the graph and may be due to reflected excitation light that bleeds through the emission filter in low fluorescence areas.

References

1. Lakowicz JR, Szmacinski H, Nowaczyk K, Johnson ML (1992) Fluorescence lifetime imaging of free and protein-bound NADH. Proc Natl Acad Sci U S A 89(4):1271–1275
2. Zhong W, Wu M, Chang CW, Merrick KA, Merajver SD, Mycek MA (2007) Picosecond-resolution fluorescence lifetime imaging microscopy: a useful tool for sensing molecular interactions in vivo via FRET. Opt Express 15(26):18220–18235
3. Kumar AT, Raymond SB, Bacskai BJ, Boas DA (2008) Comparison of frequency-domain and time-domain fluorescence lifetime tomography. Opt Lett 33(5):470–472
4. Nothdurft RE, Patwardhan SV, Akers W, Ye Y, Achilefu S, Culver JP (2009) In vivo fluorescence lifetime tomography. J Biomed Opt 14(2):024004
5. Kumar AT, Raymond SB, Dunn AK, Bacskai BJ, Boas DA (2008) A time domain fluorescence tomography system for small animal imaging. IEEE Trans Med Imaging 27(8):1152–1163
6. Rice WL, Kumar AT (2014) Preclinical whole body time domain fluorescence lifetime multiplexing of fluorescent proteins. J Biomed Opt 19(4):046005
7. Kumar AT, Chung E, Raymond SB, Van de Water JA, Shah K, Fukumura D, Jain RK, Bacskai BJ, Boas DA (2009) Feasibility of in vivo imaging of fluorescent proteins using lifetime contrast. Opt Lett 34(13):2066–2068
8. Zhang X, Bloch S, Akers W, Achilefu S (2012) Near-infrared molecular probes for in vivo imaging. Curr Protoc Cytom Chapter 12: Unit12 27
9. Akers W, Lesage F, Holten D, Achilefu S (2007) In vivo resolution of multiexponential decays of multiple near-infrared molecular probes by fluorescence lifetime-gated whole-body time-resolved diffuse optical imaging. Mol Imaging 6(4):237–246
10. Bloch S, Lesage F, McIntosh L, Gandjbakhche A, Liang K, Achilefu S (2005) Whole-body fluorescence lifetime imaging of a tumor-targeted near-infrared molecular probe in mice. J Biomed Opt 10(5):54003
11. Godavarty A, Sevick-Muraca EM, Eppstein MJ (2005) Three-dimensional fluorescence lifetime tomography. Med Phys 32(4): 992–1000
12. Hassan M, Riley J, Chernomordik V, Smith P, Pursley R, Lee SB, Capala J, Gandjbakhche AH

(2007) Fluorescence lifetime imaging system for in vivo studies. Mol Imaging 6(4):229–236

13. Abulrob A, Brunette E, Slinn J, Baumann E, Stanimirovic D (2007) In vivo time domain optical imaging of renal ischemia-reperfusion injury: discrimination based on fluorescence lifetime. Mol Imaging 6(5):304–314
14. Gurfinkel M, Thompson AB, Ralston W, Troy TL, Moore AL, Moore TA, Gust JD, Tatman D, Reynolds JS, Muggenburg B, Nikula K, Pandey R, Mayer RH, Hawrysz DJ, Sevick-Muraca EM (2000) Pharmacokinetics of ICG and HPPH-car for the detection of normal and tumor tissue using fluorescence, near-infrared reflectance imaging: a case study. Photochem Photobiol 72(1):94–102
15. Cerussi AE, Maier JS, Fantini S, Franceschini MA, Mantulin WW, Gratton E (1997) Experimental verification of a theory for the time-resolved fluorescence spectroscopy of thick tissues. Appl Opt 36(1):116–124
16. Kuwana E, Sevick-Muraca EM (2002) Fluorescence lifetime spectroscopy in multiply scattering media with dyes exhibiting multiexponential decay kinetics. Biophys J 83(2):1165–1176
17. Ntziachristos V, Ripoll J, Weissleder R (2002) Would near-infrared fluorescence signals propagate through large human organs for clinical studies? Opt Lett 27(5):333–335
18. Goiffon RJ, Akers WJ, Berezin MY, Lee H, Achilefu S (2009) Dynamic noninvasive monitoring of renal function in vivo by fluorescence lifetime imaging. J Biomed Opt 14(2):020501
19. Akers WJ, Berezin MY, Lee H, Achilefu S (2008) Predicting in vivo fluorescence lifetime behavior of near-infrared fluorescent contrast agents using in vitro measurements. J Biomed Opt 13(5):054042
20. Solomon M, Guo K, Sudlow GP, Berezin MY, Edwards WB, Achilefu S, Akers WJ (2011) Detection of enzyme activity in orthotopic murine breast cancer by fluorescence lifetime imaging using a fluorescence resonance energy transfer-based molecular probe. J Biomed Opt 16(6):066019
21. Lee H, Akers W, Bhushan K, Bloch S, Sudlow G, Tang R, Achilefu S (2011) Near-infrared pH-activatable fluorescent probes for imaging primary and metastatic breast tumors. Bioconjug Chem 22(4):777–784
22. Berezin MY, Guo K, Akers W, Northdurft RE, Culver JP, Teng B, Vasalatiy O, Barbacow K, Gandjbakhche A, Griffiths GL, Achilefu S (2011) Near-infrared fluorescence lifetime pH-sensitive probes. Biophys J 100(8):2063–2072
23. Akers WJ, Xu B, Lee H, Sudlow GP, Fields GB, Achilefu S, Edwards WB (2012) Detection of MMP-2 and MMP-9 activity in vivo with a triple-helical peptide optical probe. Bioconjug Chem 23(3):656–663
24. Zhang Z, Fan J, Cheney PP, Berezin MY, Edwards WB, Akers WJ, Shen D, Liang K, Culver JP, Achilefu S (2009) Activatable molecular systems using homologous near-infrared fluorescent probes for monitoring enzyme activities in vitro, in cellulo, and in vivo. Mol Pharm 6(2):416–427
25. Lee H, Akers WJ, Cheney PP, Edwards WB, Liang K, Culver JP, Achilefu S (2009) Complementary optical and nuclear imaging of caspase-3 activity using combined activatable and radio-labeled multimodality molecular probe. J Biomed Opt 14(4):040507
26. Magalotti S, Gustafson TP, Cao Q, Abendschein DR, Pierce RA, Berezin MY, Akers WJ (2013) Evaluation of inflammatory response to acute ischemia using near-infrared fluorescent reactive oxygen sensors. Mol Imaging Biol 15(4):423–430
27. Hayashi A, Asanuma D, Kamiya M, Urano Y, Okabe S (2016) High affinity receptor labeling based on basic leucine zipper domain peptides conjugated with pH-sensitive fluorescent dye: visualization of AMPA-type glutamate receptor endocytosis in living neurons. Neuropharmacology 100:66–75
28. Sundaram GS, Garai K, Rath NP, Yan P, Cirrito JR, Cairns NJ, Lee JM, Sharma V (2014) Characterization of a brain permeant fluorescent molecule and visualization of Abeta parenchymal plaques, using real-time multiphoton imaging in transgenic mice. Org Lett 16(14):3640–3643
29. Zhang X, Tian Y, Zhang C, Tian X, Ross AW, Moir RD, Sun H, Tanzi RE, Moore A, Ran C (2015) Near-infrared fluorescence molecular imaging of amyloid beta species and monitoring therapy in animal models of Alzheimer's disease. Proc Natl Acad Sci U S A 112(31):9734–9739
30. Kikuchi K (2010) Design, synthesis and biological application of chemical probes for bioimaging. Chem Soc Rev 39(6):2048–2053
31. Almutairi A, Akers WJ, Berezin MY, Achilefu S, Frechet JM (2008) Monitoring the biodegradation of dendritic near-infrared nanoprobes by in vivo fluorescence imaging. Mol Pharm 5(6):1103–1110
32. National Research Council (U.S.). Committee for the Update of the Guide for the Care and Use of Laboratory Animals., Institute for Laboratory Animal Research (U.S.), National Academies Press (U.S.) (2011) Guide for the care and use of laboratory animals, 8th edn. National Academies Press, Washington, D.C.

Chapter 7

Noninvasive Imaging of Fluorescent Reporters in Small Rodent Models Using Fluorescence Molecular Tomography

Weizhou Hou and Steve H. Thorne

Abstract

The capacity to combine noninvasive whole animal imaging of genetic reporters and exogenously added probes in a single animal makes fluorescence imaging a powerful tool for investigating molecular events in live animals in preclinical research. However, the adsorption and diffraction properties of light passing through tissues mean that the choice of reporters, models, and imaging systems needs to be carefully considered. Here, we describe approaches to design and run experiments incorporating noninvasive whole animal fluorescence imaging into small animal imaging studies.

Key words Optical, Fluorescence, Whole animal, Molecular imaging, Noninvasive, Reporters

1 Introduction

The use of optical imaging to rapidly and inexpensively interrogate molecular events in whole animal models has revolutionized the way small animals are used in research [1–3]. This has been primarily driven by the use of luciferase reporters for bioluminescence imaging. However limits in the number of available reporters and the primarily two-dimensional nature of this modality have meant that many investigators have begun to increasingly incorporate whole animal fluorescent reporter imaging into small animal experiments. The potential to repeatedly image and co-register multiple reporters imaged in distinct channels in a single animal makes this approach appealing, but issues related to sensitivity and background autofluorescence have historically limited its application. Over the last 5–10 years many of these issues have been overcome, primarily through the development and commercialization of instrumentation that makes use of trans-illumination with laser light sources, raster scanning of the subject and multiple detectors suitable for tomographic imaging. In addition, software has been developed that is capable of reconstructing images with better sensitivity and resolution and more accurate quantification. Finally the

Mingfeng Bai (ed.), *In Vivo Fluorescence Imaging: Methods and Protocols*, Methods in Molecular Biology, vol. 1444,
DOI 10.1007/978-1-4939-3721-9_7,

engineering of genetically encoded fluorescent reporters with excitation and emission spectra in the far-red range (that is most suitable for whole animal imaging studies) have further helped fluorescence whole animal imaging to become a viable alternative to the more commonly used bioluminescence imaging approaches.

Although whole animal fluorescence imaging has the potential to bring much of the power of flow cytometry or confocal microscopy to the field of small animal research, careful consideration needs to be given to the choice of reporters and instrumentation when designing new models. These are covered, along with basic protocols for imaging small animals, focusing on use of the FMT2500 system (PerkinElmer).

2 Materials

1. Reagent or reporter to be imaged (*see* **Notes 1** and **2**).
2. Mice, typically obtained from commercial vendors (e.g., Jackson Laboratories or Charles River) (*see* **Note 3**).
3. Anesthetic (ideally inhaled, such as isoflurane, but injectable anesthetic can be used).
4. Ultrapure water (ideally deionized water).
5. 70% ethanol.
6. 3D Fluorescence tomography imaging system (e.g., FMT2500, PerkinElmer) with appropriate image analysis software (e.g., TruQuant, PerkinElmer) (*see* **Note 4**).
7. Imaging diet (alfalfa free).
8. Nair (or equivalent depilatory) (*see* **Note 5**).

3 Methods

1. Pre-preparation of the mice. Due to issues relating to autofluorescence of the regular diet (primarily caused by chlorophyll in alfalfa), an alfalfa-free imaging diet should be provided to the mice for at least 2 days in advance of the first imaging time point. In addition, mouse fur can absorb and diffract excitation and emission light meaning that Nair (or equivalent depilatory) should be used to remove fur from around areas to be imaged in mice approximately 24 h in advance of the first imaging (*see* **Note 5**).
2. Labeling of cells or macromolecules. Depending on the events that are to be imaged it may be necessary to label cells or macromolecules prior to delivery. Many commercial probes are available to image structural components in vivo (e.g., vasculature), that are sensitive to local environmental conditions

within the host (such as hypoxia, glycolysis, and apoptosis) or that are activated by local enzymatic conditions (such as protease activated probes). However, if a genetic (reporter gene) is to be imaged, then a suitable fluorescent protein (ideally iRFP or FP-650, not GFP or RFP) needs to be expressed from within the host. This may involve ex vivo lentiviral labeling of a cell line (such as a tumor cell line), or genetic engineering of a pathogen, construction of a transgenic animal or adoptive transfer of a cell type, or transplant of a tissue or organ from a labeled transgenic animal. Alternatively, some fluorophore labeling kits are available, such that an appropriate fluorophore (such as Cy5.5) can be covalently attached to surface proteins on a cell. This will only allow short-term imaging of initial trafficking. Finally, many macromolecules (such as DNA, proteins, or peptides (such as antibodies) or liposomes) may be labeled prior to delivery (*see* **Notes 1** and **2**).

3. Inject engineered or tagged macromolecules, cells or virus or other imaging agents into mice. Timing of delivery prior to imaging will depend on the events to be imaged and may require initial pilot experiments to determine ideal time frames (for example, for viral or DNA delivery of reporter genes it may be necessary to initially determine the time needed for these to be expressed to sufficient levels for imaging). Many commercial probes will have manufacturer's guidelines for timing of injection prior to imaging, and some are available in different forms that may have shorter or longer times to clearance depending on how often imaging is needed.
4. Anesthetize the mice. Choice and level of anesthetic will need to be approved by Institutional Animal Care and Use Committee (IACUC) (*see* **Note 6**) and may also require special permits depending on the state or country.
5. Image the mice. Imaging parameters, including exposure times, resolution, filter sets and regions of interest are usually set through the software associated with imaging instrumentation and the available settings varies from device to device, such that careful study of the manufacturer's instructions and, ideally prior training is recommended. Although often more detailed than bioluminescence imaging, fluorescence imaging devices are typically straightforward and do not require specialized trained operators as with many clinical imaging modalities. An example of the imaging steps for use of the FMT2500 system (Perkin Elmer) would involve;
   (a) Place one mouse face down in the removable imaging cassette. Make sure the target area to be imaged is located in the center of the glass plate.
   (b) Place the top plate over the subject and tighten the height adjustment knobs by turning them clockwise.

(c) Insert the imaging cassette into the internal docking station.

(d) Choose the subject you want to image from the Select Subject tree using the TruQuant software.

(e) Choose the laser channel, based on the fluorescent agent injected into the mouse. Choose the agent you want to image from the drop-down list—the selection defaults to the agent selected for the subject's group at the time of the group's creation.

(f) Scan the mouse.

(g) Analyze the image according to TruQuant operator manual.

(h) For quantitation in pmol fluorescence, use the same threshold for all the groups.

6. Clean and disinfect apparatus. This should again be done in consultation with the guidelines recommended by the manufacturer (as some disinfectants, even 70% ethanol, may damage the equipment) and ensure disinfectant is used as required by local IACUC guidelines.
7. Image analysis. This is typically performed on software associated with different imaging devices and has capabilities for altering thresholds and quantifying data (Fig. 1).
8. Verify the imaging results. It is important to verify and validate the imaging results. This may involve ex vivo analysis of fluorescence in different organs or tissues post mortem for a subset of the animals.

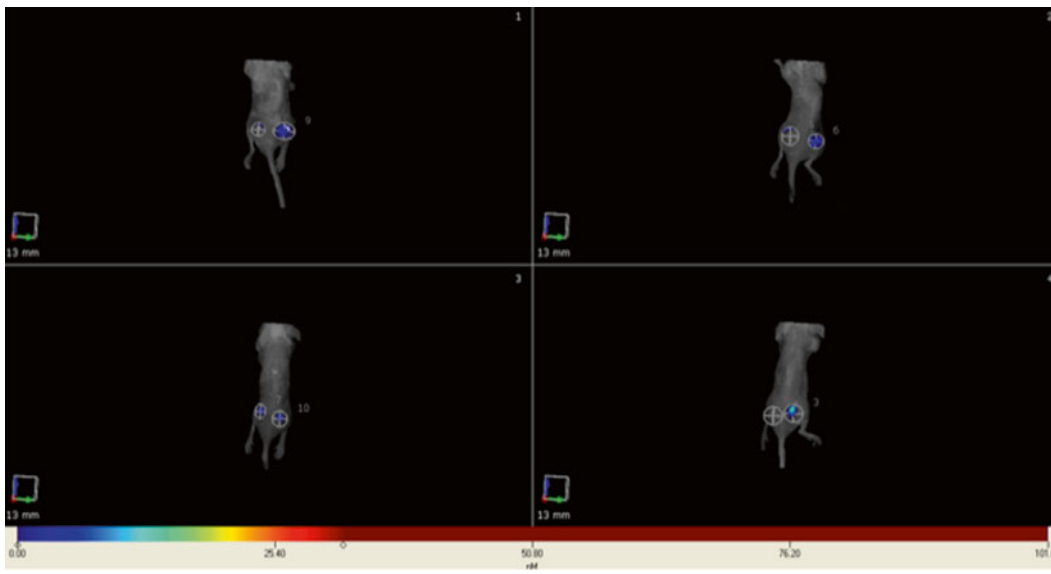

Fig 1 Screenshot from TruQuant software. Images from four animals imaged from the same group and analyzed in parallel. Conversion of raw data to pmol of fluorophore is used to quantify data

4 Notes

1. The choice of reagents to be imaged. Depending on the model and event to be examined, a variety of biological agents might be labeled (such as peptides, antibodies, DNA, sugars, small molecules, or cells). Fluorophore binding to these agents can require some complex chemistry, or might be possible through simple one step procedures with commercially available kits (such as *N*-hydroxysuccinimide (NHS) esterification of Cy dyes to cysteine residues). Consideration should be given to any possible changes to the physical properties of the reagents as a result of fluorophore labeling (including increases in size or changes in charge or hydrophobicity). Cells can be labeled in a variety of different ways, such as loading with fluorescently labeled quantum dots, membrane labeling, peptide labeling, or through expression of fluorescent proteins. Issues to be considered, include the reduction in fluorophore concentration after cell division; processing or metabolizing of fluorophore, or uptake into other cell types such as macrophages after cell death; effects of cellular manipulation on cellular viability or function; length of time needed to follow imaging of cell tracking after transfer should be considered when choosing a labeling protocol. In addition, although multiple fluorescent proteins are available, only a small number have the required spectral properties that make them suitable for whole animal imaging (*see* below) [4]. However, cells labeled with appropriate fluorescent proteins can be treated in a similar way as luciferase labeled cells (with the exceptions that (1) there is usually no need for exogenous addition of substrate; (2) ATP is not required for fluorescence, so fluorescence will be possible outside of the cell or after a cell has lost viability; and (3) fluorescent proteins tend to be more stable than luciferase, and therefore may be less useful as a means to follow gene expression profiles unless they have been modified).
2. Choice of fluorophore(s). One of the major advantages of fluorescence imaging is that multiple (up to four) channels can be imaged in the same animal. Different instrumentation from different vendors offers different fluorophore channels, but the key consideration is the wavelength of light needed to pass through tissue. This applies both to excitation and emission, with wavelengths between 650 and 950 nm providing the greatest tissue penetration properties. This means that fluorophores in the far red and near infrared range are the most suited to whole animal imaging. The high level of autofluorescence at lower wavelengths also complicates imaging in this range. This wavelength recommendation does reduce the number of fluorescent proteins that can be readily imaged at any depth in living animals; however, several recently described

proteins do have adsorption and emission spectra in the appropriate wavelength ranges.

3. Choice of mouse strain. This will again primarily depend on the events to be studied, and in some cases availability of transgenics. In general, because of the need to remove fur, nude mouse strains are preferred if possible. When immunocompetent animals are needed, white mouse strains are preferable to black strains (again due to the ease of light traveling through the skin pigmentation), but some black strains, including C57/BL6, are commercially available in albino form at slightly more cost than the wild type strain.
4. Choice of Imaging Apparatus. Novel imaging devices are being introduced to the market at a rapid rate, while some investigators have chosen to build their own custom models. This means a large range of technical approaches to image collection have been incorporated. The most effective devices typically use trans-illumination of the subjects and will utilize laser excitation light, raster scanning and multiple detectors. The imaging device incorporated will therefore further determine the limits of sensitivity and quantification available to investigators.
5. Fur removal. Although Nair is recommended, other depilatory creams are available. These should be verified for a lack of autofluorescence before being used. Alternatively, animals may be shaved; however, this tends to provide less even fur removal and increases the possibility of nicking the skin that may interfere with events to be imaged. The fur will also regrow, so removal may need to be repeated for longer term imaging studies. The choice to remove all or only a region of the fur will also be a consideration.
6. Institutional Animal Care and Use Committee. As with all animal studies, IACUC approval will be required for all animal strains and species, reagents and procedures used in the process of the studies.

References

1. Contag CH, Contag PR, Mullins JI, Spilman SD, Stevenson DK, Benaron DA (1995) Photonic detection of bacterial pathogens in living hosts. Mol Microbiol 18(4):593–603
2. Thorne SH, Contag CH (2005) Using *in vivo* bioluminescence imaging to shed light on cancer biology. Proc IEEE 93(4):750–762
3. Weissleder R, Pittet MJ (2008) Imaging in the era of molecular oncology. Nature 452(7187): 580–589
4. Shaner NC, Steinbach PA, Tsien RY (2005) A guide to choosing fluorescent proteins. Nat Methods 2(12):905–909

Chapter 8

In Vivo Tumor Angiogenesis Imaging Using Peptide-Based Near-Infrared Fluorescent Probes

Rui Huang, Peter S. Conti, and Kai Chen

Abstract

Near-infrared fluorescence (NIRF) imaging is an emerging imaging technique for studying diseases at the molecular level. Optical imaging with a near-infrared emitting fluorophore for targeting tumor angiogenesis offers a noninvasive method for early tumor detection and efficient monitoring of tumor response to anti-angiogenesis therapy. CD13 receptor, a zinc-dependent membrane-bound ectopeptidase, plays important roles in regulating tumor angiogenesis and the growth of new blood vessels. In this chapter, we use CD13 receptor as an example to demonstrate how to construct CD13-specific NGR-containing peptides via bioorthogonal click chemistry for visualizing and quantifying the CD13 receptor expression in vivo by means of NIRF optical imaging.

Key words Tumor angiogenesis, Near-infrared fluorescence imaging, Peptide-based probes, Molecular imaging, Cancer

1 Introduction

Near-infrared fluorescence (NIRF) imaging is an excellent noninvasive technique for studying diseases at the molecular level in living subjects [1–4]. As an excellent complement to nuclear imaging techniques, such as positron emission tomography (PET) and single-photon emission computed tomography (SPECT), NIRF imaging does not employ ionizing radiation or radioactive materials, rendering it cost-effective, robust, sensitive, and straightforward over other imaging modalities [3, 5, 6]. Although absorption and scattering from biological tissues may limit penetration of light through the body, photon penetration into and out of tissue can be more efficient in the near-infrared window (650–900 nm) with minimal intra-tissue scattering. Recent research advances have demonstrated that NIRF imaging is playing a valuable role in better understanding of biology, early diagnosis of diseases, and effective assessment of treatment [7–9].

Mingfeng Bai (ed.), *In Vivo Fluorescence Imaging: Methods and Protocols*, Methods in Molecular Biology, vol. 1444,
DOI 10.1007/978-1-4939-3721-9_8,

Angiogenesis, the formation of new blood vessels from pre-existing vasculature, is a fundamental process occurring during tumor progression [10–13]. A sizable body of evidence suggests that the formation of tumor angiogenesis is a complex multi-step process that follows a characteristic sequence of events mediated and controlled by growth factors, cellular receptors, and adhesion molecules [14–16]. Therefore, biomarkers exclusively expressed in tumor angiogenesis can be recognized as potential targets for cancer diagnosis and therapy. Numerous studies have proved that CD13 receptor is an important regulator of endothelial morphogenesis during tumor angiogenesis [17]. CD13 receptor, also known as aminopeptidase N (APN), is a zinc-dependent membrane-bound ectopeptidase that degrades preferentially proteins and peptides with an *N*-terminal neutral amino acid [18]. Research results suggest that overexpression of CD13 is associated with the progression of many tumors, such as prostate, colon, and pancreatic cancer [19–21]. Through in vivo screening of a phage-displayed peptide library, a tumor vasculature homing phage carrying sequence CNGRCVSGCAGRC was selected by using human breast carcinoma xenografts [22]. Later, the molecular basis behind NGR tumor-homing properties was revealed, and NGR-containing peptide was identified as a specific ligand for CD13 receptor [23]. Consequently, a number of NGR-containing derivatives have been developed for both CD13-targeted tumor imaging and therapy [6, 24–30].

Click chemistry offers chemists a platform for modular and high-yielding synthetic transformations for constructing highly diverse molecules [31]. The Huisgen 1,3-dipolar cycloaddition reaction, which fuses an azide and an alkyne together, and provides access to a variety of five-membered heterocycles, has become of great use in the development of new molecular probes [32]. Based on our previous experience [33], a catalyst-free click chemistry system using the ligation of dibenzocyclooctyne and azide was chosen to prepare peptide-based near-infrared fluorescent probes (Fig. 1) [34, 35]. To this end, the dimeric NGR peptide (NGR2) was conjugated with an azide-terminated Cy5.5 fluorophore (Cy5.5-N_3) to rapidly afford Cy5.5-NGR2 in a quantitative yield. The Cy5.5-NGR2 peptide provided highly sensitive and target-specific imaging of CD13 receptor expression in tumors. The excellent tumor-to-normal tissue ratio and fast

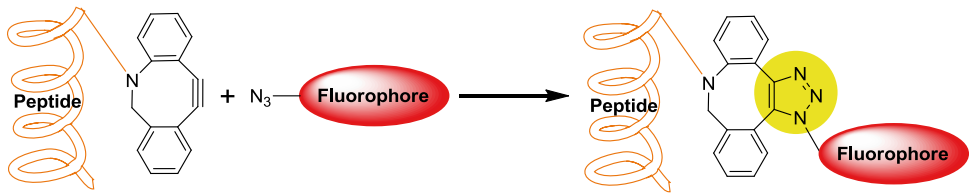

Fig. 1 Schematic representation of the construction of peptide-based near-infrared fluorescent probe via bioorthogonal click chemistry for in vivo tumor angiogenesis imaging

tumor targeting ability of Cy5.5-NGR2 have proved it a promising molecular probe, not only allowing the NIRF imaging of CD13 overexpressed tumor angiogenesis, but also having the potential to facilitate noninvasive monitoring of CD13-targeted anti-angiogenesis therapy.

2 Materials

Prepare all solutions using ultrapure water (prepared by purifying deionized water) and analytical grade reagents. Prepare and store all reagents at room temperature (unless indicated otherwise). Diligently follow all waste disposal regulations when disposing waste materials.

1. Monomeric NGR peptide [GGGCNGRC; disulfide Cys:Cys = 4 – 8] (C S Bio, Inc., Menlo Park, CA, USA).
2. Dimeric NGR peptide (NGR2) is prepared using the reported procedure [30].
3. Cy5.5 azide (Cy5.5-N_3) (Lumiprobe, Hallandale Beach, FL, USA).
4. DBCO-PEG_4-NHS ester (Click Chemistry Tools, Inc., Scottsdale, AZ, USA).
5. Sodium borate buffer (pH 8.5).
6. Phosphate-buffered saline (PBS).
7. 0.1% TFA in water (Solution A, which has been rigorously degassed for high-performance liquid chromatography [HPLC] use).
8. 0.1% TFA in acetonitrile (Solution B, which has been rigorously degassed for HPLC use).
9. Luna C18 reversed phase column (5 μm, 250 × 4.6 mm) (Phenomenex, Torrance, CA, USA).
10. Chamber slides (VWR Corporate, Radnor, PA, USA).
11. Dulbecco's modified Eagle's medium (DMEM) (USC Cell Culture Core, Los Angeles, CA, USA).
12. HT-1080 human fibrosarcoma cell line (ATCC, Manassas, VA, USA).
13. MCF-7 human breast cancer cell line (ATCC, Manassas, VA, USA).
14. Fetal bovine serum (FBS).
15. Paraformaldehyde (PFA).
16. Matrigel (BD Biosciences, San Jose, CA, USA).
17. Female athymic nude mice (Harlan Laboratories, Livermore, CA, USA).

3 Methods

3.1 Preparation of DBCO-Conjugated NGR2 Peptide

1. Dissolve the dimeric NGR peptide (NGR2) (2.6 μmol) in 200 μL of sodium borate buffer (pH = 8.5).
2. Add DBCO-PEG_4-NHS ester (3.1 μmol) dissolved in 20 μL of DMSO.
3. Adjust the mixture to pH 8.5 (*see* **Note 1**).
4. Sonicate at room temperature for 1 h.
5. Purify the crude peptide by HPLC (*see* **Note 2**).
6. Collect the peak containing the desired product.
7. Lyophilize to afford a fluffy white powder (*see* **Note 3**).

3.2 Preparation of Cy5.5-NGR2 Peptide

1. Dissolve the DBCO-conjugated NGR2 peptide (0.48 μmol) in 100 μL of PBS.
2. Add Cy5.5-N_3 (0.53 μmol) in 10 μL of DMSO and 100 μL of acetonitrile (*see* **Note 4**).
3. Shake the mixture in the dark at room temperature for 15 min.
4. Purify the crude peptide by HPLC (*see* **Note 5**).
5. Collect the peak containing the desired product.
6. Lyophilize to afford Cy5.5-NGR2 peptide (*see* **Note 6**).

The chemical structure of Cy5.5-NGR2 peptide is illustrated in Fig. 2.

3.3 Absorption and Emission Spectra of Cy5.5-NGR2 Peptide

1. The absorption spectrum of Cy5.5-NGR2 peptide is recorded on a Cary 14 UV-Vis spectrometer (Bogart, GA, USA). The spectrum is scanned from 550 to 800 nm with an increment of 1 nm.
2. The fluorescence emission of Cy5.5-NGR2 peptide is measured using a Shimadzu RF-5301PC spectrofluorophotometer (Columbia, MD, USA), and the spectrum is scanned from 550 to 800 nm with an increment of 1 nm. The wavelength of excitation light is set at 650 nm.

The absorption and emission fluorescence spectra of Cy5.5-NGR2 peptide in deionized water are illustrated in Fig. 3.

3.4 Binding Specificity of Cy5.5-NGR2 to CD13 Receptor

1. HT-1080 and MCF-7 cells are grown in DMEM supplemented with 10% FBS at 37 °C in humidified atmosphere containing 5% CO_2.
2. HT-1080 and MCF-7 cells are grown in chamber slides with a density of 2×10^4/well for 24 h.
3. Wash cells with serum-free DMEM medium for 3 min, fix cells in each well with 2% PFA for 10 min, and then wash cells with serum-free DMEM medium (three times, 3 min/wash).

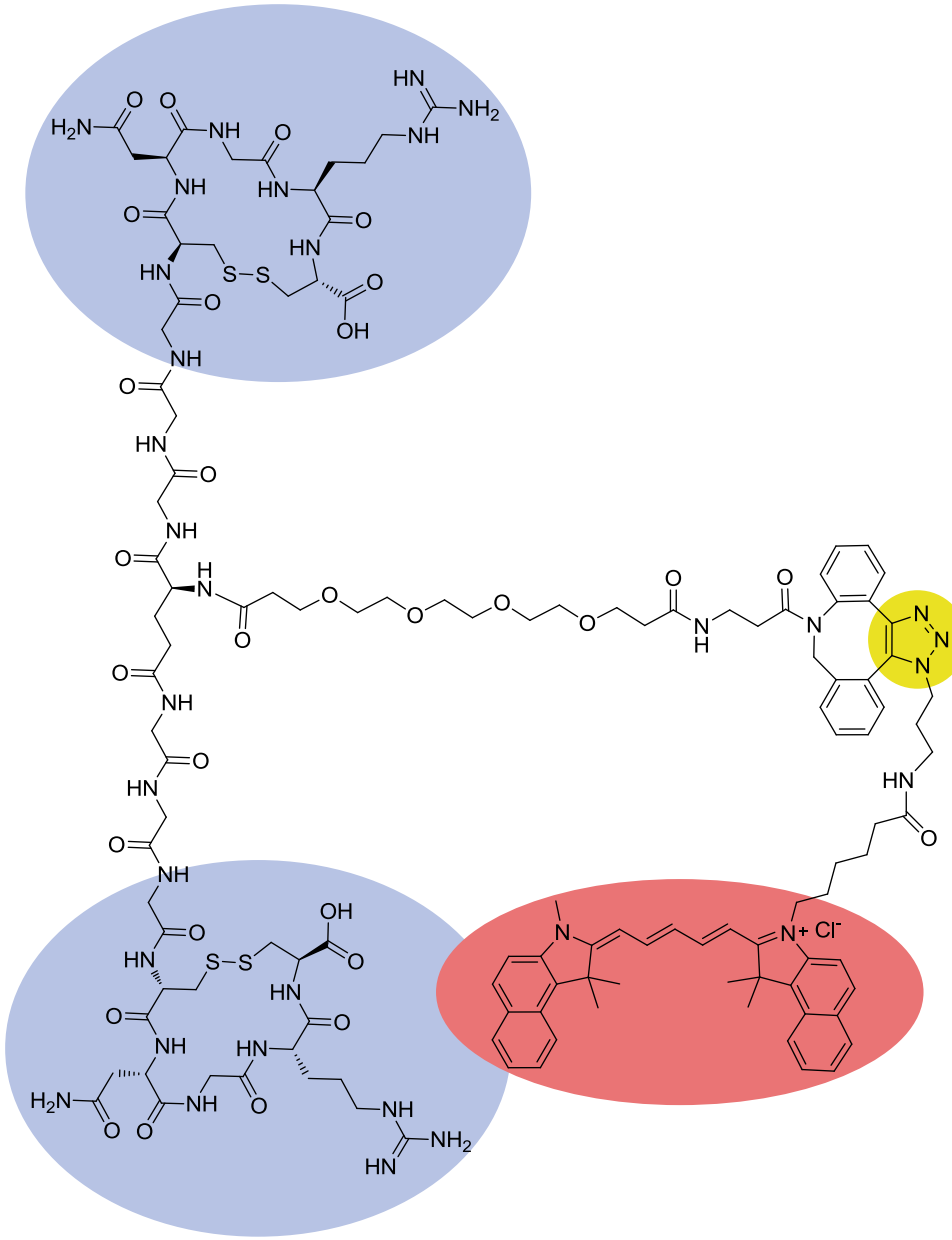

Fig. 2 Schematic structure of Cy5.5-NGR2 peptide. *Blue*: NGR peptide; *red*: Cy5.5 dye. Reproduced from Ref. 6 with permission from Springer

4. Add 20 nM of Cy5.5-NGR2 peptide in 200 μL of serum-free DMEM medium to the HT-1080 or MCF-7 cells.
5. Incubate at 37 °C in the dark for 15 min.
6. Wash cells with PBS (three times, 5 min/wash).
7. For the blocking group, the HT-1080 cells are co-incubated with 20 nM of Cy5.5-NGR2 peptide and 50 μM of non-labeled monomeric NGR peptide (*see* **Note** 7).

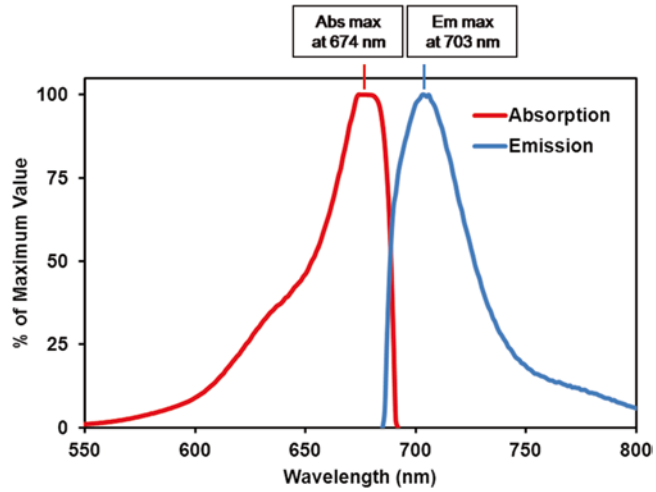

Fig. 3 Absorption and emission fluorescence spectra of Cy5.5-NGR2 peptide. Reproduced from Ref. 6 with permission from Springer

8. Mount the chamber slides with a 4′,6-diamidino-2-phenylindole (DAPI)-containing mounting medium.
9. Place the slides under a Zeiss LSM 510 confocal laser scanning microscope (Carl Zeiss Microscopy, LLC, Thornwood, NY, USA) with a Cy5 filer and record the images at 633 nm excitation wavelength.

It is critical that the CD13-binding specificity is maintained after chemical modification of NGR peptides (*see* **Note 8**). A representative result is shown in Fig. 4.

3.5 In Vivo NIRF Optical Imaging

1. Generate the tumor xenografts by subcutaneous injection of five million HT-1080 cells suspended in 50 μL of cell culture media and 50 μL of BD Matrigel into the right shoulder of female athymic nude mice (Harlan Laboratories, Livermore, CA, USA) (*see* **Note 9**). The mice are subjected to in vivo NIRF imaging studies when the tumor volume reaches 200–300 mm^3 (about 2 weeks after inoculation). Monitor the tumor volume every other day using a caliper following the formula $V = (witdth)^2 \times length / 2$.
2. Set up the IVIS Imaging System 200 Series (PerkinElmer Inc., Alameda, CA, USA). A Cy5.5 filter set is used to acquire the fluorescent signals.
3. Obtain the fluorescent signals by scanning a tumor-bearing mouse before the injection of Cy5.5-NGR2.
4. Inject 1.5 nmol of Cy5.5-NGR2 into a tumor-bearing mouse via the tail vein while the mouse is under isoflurane anesthesia.
5. For the blocking experiment, inject 1.5 nmol of Cy5.5-NGR2 with a non-labeled monomeric NGR peptide (20 mg/kg) into a tumor-bearing mouse via the tail vein.

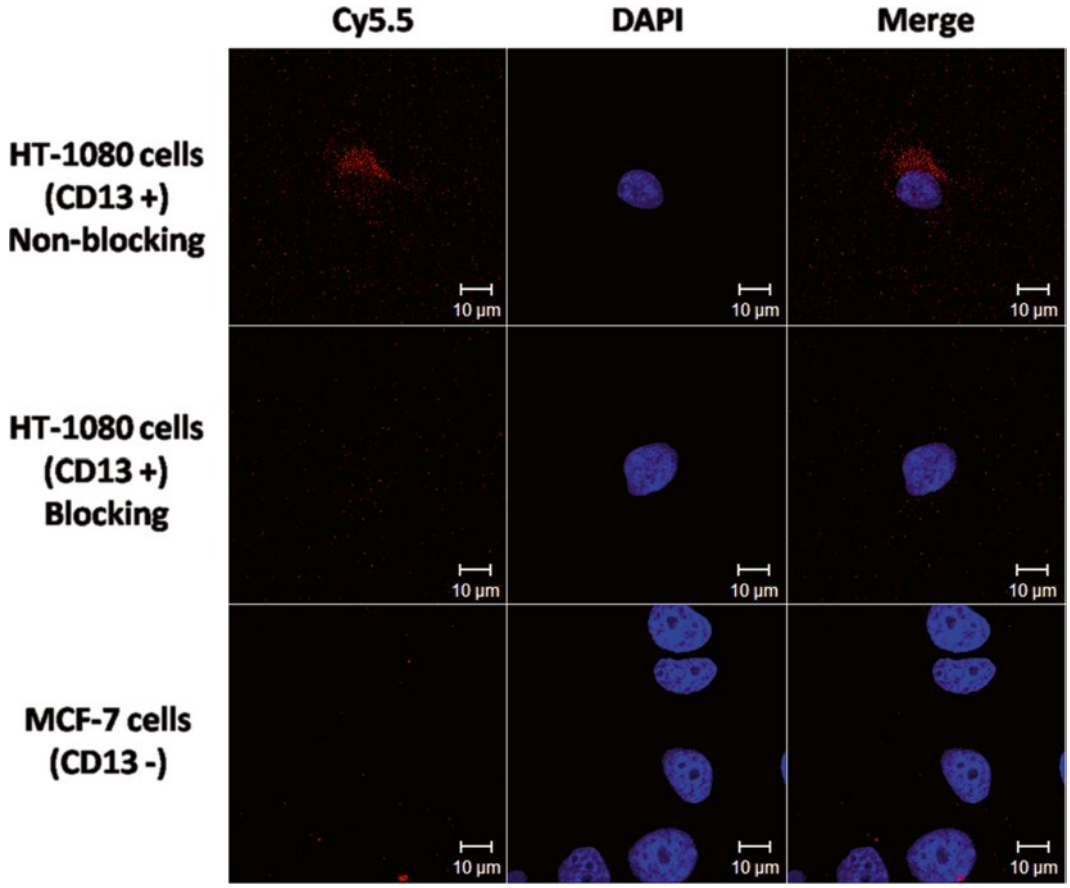

Fig. 4 Confocal microscopy results of Cy5.5-NGR2 with HT-1080 cells (CD13 positive) and MCF-7 cells (CD13 negative) (magnification: 100×). The blocking study is achieved by adding unlabeled monomeric NGR peptide. *Top*: Incubation of Cy5.5-NGR2 (20 nM) with CD13-positive HT-1080 cells; *middle*: incubation of Cy5.5-NGR2 (20 nM) with CD13-positive HT-1080 cells blocked by a non-labeled monomeric NGR peptide (50 μM); *bottom*: incubation of Cy5.5-NGR2 (20 nM) with CD13-negative MCF-7 cells. Reproduced from Ref. 6 with permission from Springer

6. Scan the animal at 0.5, 1, 2, 3, and 4 h (*see* **Note 10**). The identical illumination settings (lamp voltage, filters, f/stop, field of views, binning) are used to acquire all images. All NIRF images are acquired using 1-s exposure time (f/stop = 4). Fluorescence emission images are normalized and reported as photons per second per centimeter squared per steradian (p/s/cm^2/sr) (*see* **Note 11**).

Representative NIRF images are shown in Fig. 5 after HT-1080 tumor-bearing mice are injected with 1.5 nmol of Cy5.5-NGR2. To determine tumor contrast, mean fluorescence intensities of the tumor area at the right shoulder of the animal and of the normal tissue at the surrounding tissue are calculated using the region-of-interest (ROI)

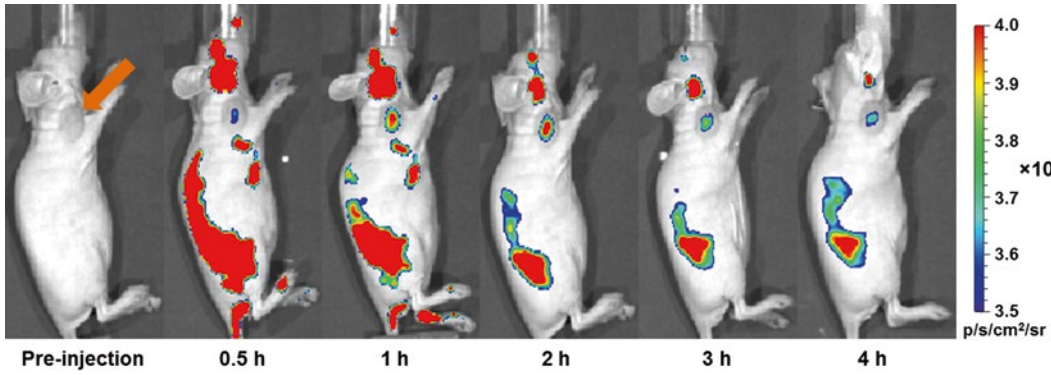

Fig. 5 Time-course fluorescence imaging of subcutaneous HT-1080 tumor-bearing nude mice after intravenous injection of 1.5 nmol of Cy5.5-NGR2. The tumors are clearly visualized as indicated by an *arrow* from 0.5 to 4 h pi. The fluorescence intensity is recorded as per second per centimeter squared per steradian (p/s/cm^2/sr). Reproduced from Ref. 6 with permission from Springer

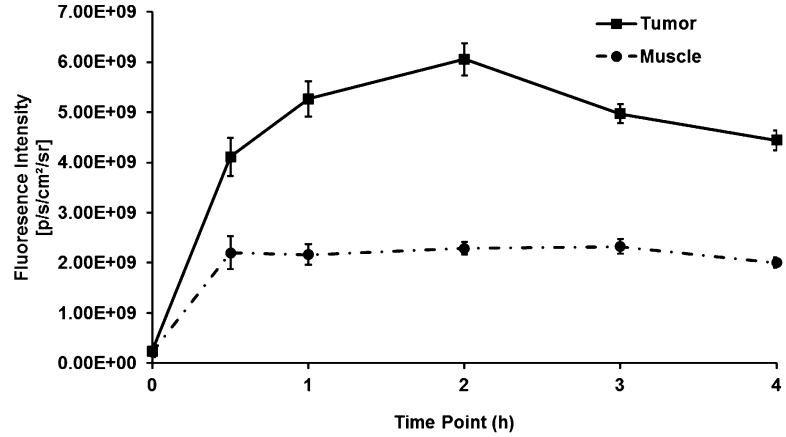

Fig. 6 Quantification and kinetics of in vivo targeting character of Cy5.5-NGR2 in the HT-1080 tumor vs. muscle. The Cy5.5-NGR2 uptake in HT-1080 tumor at various time points is significantly higher than that in muscle. *Error bar* is calculated as the standard deviation ($n=3$). Reproduced from Ref. 6 with permission from Springer

function of the IVIS Living Image 4.4 software (PerkinElmer Inc., Alameda, CA, USA). The fluorescence signal resulting from Cy5.5-NGR2 is clearly visible and the tumor fluorescence intensity reaches maximum at 2 h post-injection (Fig. 6). The NIRF images of HT-1080 tumor-bearing mice at 2 h pi from the non-blocking and blocking group are presented in Fig. 7. Tumor contrast as quantified by the ROI analysis of images shows that the tumor-to-muscle value at 2 h pi is reduced from 2.65 ± 0.13 to 1.05 ± 0.06 ($P<0.05$) by blocking CD13 receptor with a non-labeled NGR peptide (Fig. 8) (*see* **Note 12**).

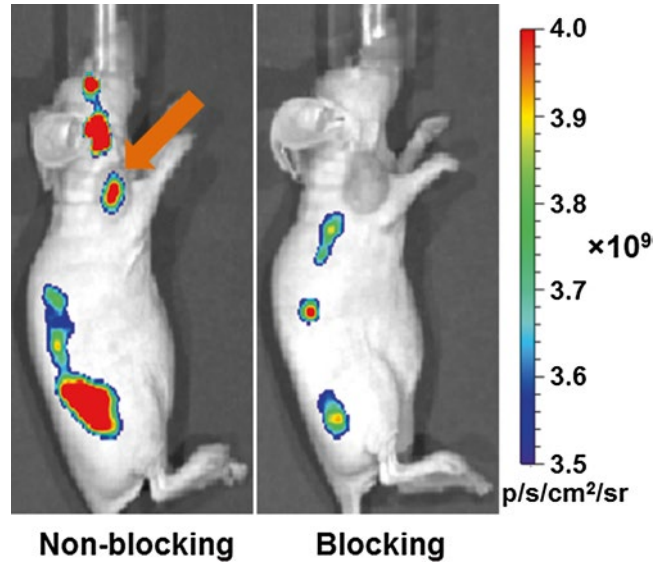

Fig. 7 Representative optical imaging (at 2 h pi) of mice bearing HT-1080 tumor on the right shoulder demonstrating blocking of Cy5.5-NGR2 (1.5 nmol) uptake by co-injection with a non-labeled monomeric NGR peptide (20 mg/kg). Reproduced from Ref. 6 with permission from Springer

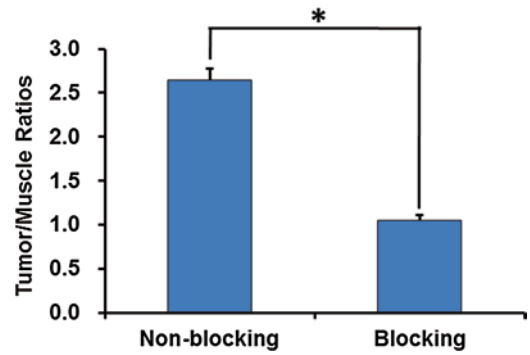

Fig. 8 Fluorescence intensity ratio of tumor to muscle based on the ROI analysis of Cy5.5-NGR2 uptake at 2 h pi in HT-1080 tumors without (non-blocking) or with (blocking) co-injection of a non-labeled monomeric NGR peptide (20 mg/kg). *Error bar* is calculated as the standard deviation ($n = 3$). Reproduced from Ref. 6 with permission from Springer

4 Notes

1. It is critical to adjust the pH value of mixture to 8.5 for amide bond formation between a succinimide ester and an amino group.
2. The flow rate is 1 mL/min with the mobile phase starting from 100% solvent A (0.1% TFA in water) to 40% solvent A and 60% solvent B (0.1% TFA in acetonitrile) at 22.5 min.

3. A typical yield is between 70 and 80%.
4. The selection of NIR optical dyes for in vivo cancer imaging is referred to the literature [36].
5. The flow rate is 1 mL/min with the mobile phase starting from 100% solvent A (0.1% TFA in water) to 5% solvent A and 95% solvent B (0.1% TFA in acetonitrile) at 30 min.
6. A typical yield is between 90 and 95%. The fluorescent peptide is stored as a dry powder in the dark at −20 °C until use.
7. To achieve the blocking experiment, various concentrations of non-labeled NGR peptide are tested. However, if the concentration of blocking NGR peptide is too high, the cells may detach from the chamber slide.
8. The receptor binding affinity of fluorescent probe can also be determined by cell-based receptor-binding assay.
9. Animals are fed with alfalfa-free diet, such as 2018 Teklad global 18% protein rodent diet (Harlan Laboratories, Livermore, CA, USA) for 2 weeks prior to tumor implantation and maintained on the same diet throughout the study to minimize autofluorescence and improve imaging clarity.
10. Based on the pharmacokinetics of fluorescent probe, the imaging time points can be varied.
11. To investigate the biodistribution of fluorescent probe, ex vivo NIRF imaging can be performed. After injection of fluorescent probe at a certain time point, tumors, tissues, and organs are dissected and subjected to ex vivo NIRF imaging. The uptake of fluorescent probe can be quantified by the ROI analysis of images.
12. Statistical analysis is performed with a Student's *t* test. Statistical significance is assigned for P values < 0.05.

Acknowledgments

This work was supported by the American Cancer Society (#IRG-58-007-51), the Robert E. and May R. Wright Foundation, and the USC Department of Radiology.

References

1. Weissleder R, Tung CH, Mahmood U, Bogdanov A Jr (1999) In vivo imaging of tumors with protease-activated near-infrared fluorescent probes. Nat Biotechnol 17(4):375–378
2. Tung CH (2004) Fluorescent peptide probes for in vivo diagnostic imaging. Biopolymers 76(5):391–403
3. Chen X, Conti PS, Moats RA (2004) In vivo near-infrared fluorescence imaging of integrin alphavbeta3 in brain tumor xenografts. Cancer Res 64(21):8009–8014
4. Kobayashi H, Ogawa M, Alford R, Choyke PL, Urano Y (2010) New strategies for fluorescent probe design in medical diagnostic imaging. Chem Rev 110(5):2620–2640
5. Chen K, Yap LP, Park R, Hui X, Wu K, Fan D, Chen X, Conti PS (2012) A Cy5.5-labeled phage-displayed peptide probe for near-infrared

fluorescence imaging of tumor vasculature in living mice. Amino Acids 42(4):1329–1337

6. Li G, Xing Y, Wang J, Conti PS, Chen K (2014) Near-infrared fluorescence imaging of CD13 receptor expression using a novel Cy5.5-labeled dimeric NGR peptide. Amino Acids 46(6):1547–1556
7. Raymond SB, Skoch J, Hills ID, Nesterov EE, Swager TM, Bacskai BJ (2008) Smart optical probes for near-infrared fluorescence imaging of Alzheimer's disease pathology. Eur J Nucl Med Mol Imaging 35(Suppl 1):S93–S98
8. Wunderbaldinger P, Turetschek K, Bremer C (2003) Near-infrared fluorescence imaging of lymph nodes using a new enzyme sensing activatable macromolecular optical probe. Eur Radiol 13(9):2206–2211
9. Sakatani K, Kashiwasake-Jibu M, Taka Y, Wang S, Zuo H, Yamamoto K, Shimizu K (1997) Noninvasive optical imaging of the subarachnoid space and cerebrospinal fluid pathways based on near-infrared fluorescence. J Neurosurg 87(5):738–745
10. Chen K, Chen X (2011) Positron emission tomography imaging of cancer biology: current status and future prospects. Semin Oncol 38(1):70–86
11. Chen K, Conti PS (2010) Target-specific delivery of peptide-based probes for PET imaging. Adv Drug Deliv Rev 62(11):1005–1022
12. Cai W, Gambhir SS, Chen X (2008) Chapter 7. Molecular imaging of tumor vasculature. Methods Enzymol 445:141–176
13. Huang R, Wang M, Zhu Y, Conti PS, Chen K (2015) Development of PET probes for cancer imaging. Curr Top Med Chem 15(8):795–819
14. Ellis LM, Liu W, Ahmad SA, Fan F, Jung YD, Shaheen RM, Reinmuth N (2001) Overview of angiogenesis: biologic implications for antiangiogenic therapy. Semin Oncol 28(5 Suppl 16):94–104
15. Kuwano M, Fukushi J, Okamoto M, Nishie A, Goto H, Ishibashi T, Ono M (2001) Angiogenesis factors. Intern Med 40(7):565–572
16. Yancopoulos GD, Davis S, Gale NW, Rudge JS, Wiegand SJ, Holash J (2000) Vascular-specific growth factors and blood vessel formation. Nature 407(6801):242–248
17. Bhagwat SV, Lahdenranta J, Giordano R, Arap W, Pasqualini R, Shapiro LH (2001) CD13/APN is activated by angiogenic signals and is essential for capillary tube formation. Blood 97(3):652–659
18. Guzman-Rojas L, Rangel R, Salameh A, Edwards JK, Dondossola E, Kim YG, Saghatelian A, Giordano RJ, Kolonin MG, Staquicini FI, Koivunen E, Sidman RL, Arap W, Pasqualini R (2012) Cooperative effects of aminopeptidase N (CD13) expressed by nonmalignant and cancer cells within the tumor microenvironment. Proc Natl Acad Sci U S A 109(5):1637–1642
19. Teranishi J, Ishiguro H, Hoshino K, Noguchi K, Kubota Y, Uemura H (2008) Evaluation of role of angiotensin III and aminopeptidases in prostate cancer cells. Prostate 68(15):1666–1673
20. Ikeda N, Nakajima Y, Tokuhara T, Hattori N, Sho M, Kanehiro H, Miyake M (2003) Clinical significance of aminopeptidase N/CD13 expression in human pancreatic carcinoma. Clin Cancer Res 9(4):1503–1508
21. Hashida H, Takabayashi A, Kanai M, Adachi M, Kondo K, Kohno N, Yamaoka Y, Miyake M (2002) Aminopeptidase N is involved in cell motility and angiogenesis: its clinical significance in human colon cancer. Gastroenterology 122(2):376–386
22. Arap W, Pasqualini R, Ruoslahti E (1998) Cancer treatment by targeted drug delivery to tumor vasculature in a mouse model. Science 279(5349):377–380
23. Pasqualini R, Koivunen E, Kain R, Lahdenranta J, Sakamoto M, Stryhn A, Ashmun RA, Shapiro LH, Arap W, Ruoslahti E (2000) Aminopeptidase N is a receptor for tumor-homing peptides and a target for inhibiting angiogenesis. Cancer Res 60(3):722–727
24. von Wallbrunn A, Waldeck J, Holtke C, Zuhlsdorf M, Mesters R, Heindel W, Schafers M, Bremer C (2008) In vivo optical imaging of CD13/APN-expression in tumor xenografts. J Biomed Opt 13(1):011007
25. Negussie AH, Miller JL, Reddy G, Drake SK, Wood BJ, Dreher MR (2010) Synthesis and in vitro evaluation of cyclic NGR peptide targeted thermally sensitive liposome. J Control Release 143(2):265–273
26. Wang RE, Niu Y, Wu H, Amin MN, Cai J (2011) Development of NGR peptide-based agents for tumor imaging. Am J Nucl Med Mol Imaging 1(1):36–46
27. Shao Y, Liang W, Kang F, Yang W, Ma X, Li G, Zong S, Chen K, Wang J (2014) 68Ga-labeled cyclic NGR peptide for MicroPET imaging of CD13 receptor expression. Molecules 19(8): 11600–11612
28. Li G, Wang X, Zong S, Wang J, Conti PS, Chen K (2014) MicroPET imaging of CD13 expression using a ^{64}Cu-labeled dimeric NGR peptide based on sarcophagine cage. Mol Pharm 11(11):3938–3946
29. Ma W, Kang F, Wang Z, Yang W, Li G, Ma X, Li G, Chen K, Zhang Y, Wang J (2013) ^{99m}Tc-labeled monomeric and dimeric NGR peptides for SPECT imaging of CD13 receptor in tumor-bearing mice. Amino Acids 44(5):1337–1345
30. Chen K, Ma W, Li G, Wang J, Yang W, Yap LP, Hughes LD, Park R, Conti PS (2013) Synthesis

and evaluation of ^{64}Cu-labeled monomeric and dimeric NGR peptides for microPET imaging of CD13 receptor expression. Mol Pharm 10(1):417–427

31. Kolb HC, Sharpless KB (2003) The growing impact of click chemistry on drug discovery. Drug Discov Today 8(24):1128–1137
32. Nwe K, Brechbiel MW (2009) Growing applications of "click chemistry" for bioconjugation in contemporary biomedical research. Cancer Biother Radiopharm 24(3):289–302
33. Chen K, Wang X, Lin W, Shen K-F, Yap LP, Hughes LD, Conti PS (2012) Strain-promoted catalyst-free click chemistry for rapid construction of ^{64}Cu-labeled PET imaging probes. ACS Med Chem Lett 3(12):1019–1023
34. Debets MF, van Berkel SS, Schoffelen S, Rutjes FP, van Hest JC, van Delft FL (2010) Aza-dibenzocyclooctynes for fast and efficient enzyme PEGylation via copper-free (3+2) cycloaddition. Chem Commun 46(1):97–99
35. Debets MF, van Berkel SS, Dommerholt J, Dirks AT, Rutjes FP, van Delft FL (2011) Bioconjugation with strained alkenes and alkynes. Acc Chem Res 44(9):805–815
36. Luo S, Zhang E, Su Y, Cheng T, Shi C (2011) A review of NIR dyes in cancer targeting and imaging. Biomaterials 32(29):7127–7138

Chapter 9

Intraoperative Fluorescence Imaging and Multimodal Surgical Navigation Using Goggle System

Christopher A. Mela, Francis A. Papay, and Yang Liu

Abstract

Intraoperative imaging is an invaluable tool in many surgical procedures. We have developed a wearable stereoscopic imaging and display system entitled Integrated Imaging Goggle, which can provide real-time multimodal image guidance. With the Integrated Imaging Goggle, wide field-of-view fluorescence imaging is tracked and registered with intraoperative ultrasound imaging and preoperative tomography-based surgical navigation, to provide integrated multimodal imaging capabilities in real-time. Herein we describe the system instrumentation and the methods of using the Integrated Imaging Goggle to guide surgeries.

Key words Fluorescence imaging, Stereoscopic imaging, Multimodal imaging, 3D imaging, Image-guided surgery, Surgical navigation

1 Introduction

When resecting a cancerous lesion, surgeons need to accurately distinguish between tumors and healthy tissues. This is sometimes achieved by natural sight and palpation alone [1]. Unfortunately, the cancerous tissues can be easily mistaken for healthy tissues, making a complete resection difficult to achieve [2]. This can result in residual tumors remaining inside the body postoperation at the margins of the surgical site. Imaging of surgical margins is a field that has emerged to determine whether a cancerous mass has been completely removed by analyzing the excised healthy tissue margins postoperation [3–5]. If a positive margin is found, the odds of a local cancer recurrence are high; for example in laryngeal cancer the odds of recurrence go up from 32 to 80% when a positive margin is found [6]. Unfortunately, imaging of margins is typically conducted after the primary surgery has been completed. Therefore, if a positive margin is found, the doctor is likely to recommend a second surgery. The field of intraoperative imaging was developed to mitigate the need of additional surgeries by, in

Mingfeng Bai (ed.), *In Vivo Fluorescence Imaging: Methods and Protocols*, Methods in Molecular Biology, vol. 1444,
DOI 10.1007/978-1-4939-3721-9_9,

the case of cancer resections, localizing the tumors during the operation and offering better surgical margin control.

Moreover, the ability to image vasculature, lymphatics, and bile ducts in real-time can aid in a number of surgeries. Due to anatomical variations, unintended nicks and cuts in an artery can occur, potentially resulting in patient death or other serious surgical complications [7–9]. Also, imaging of the arteries and bile ducts can aid in their repair. Sentinel lymph node (SLN) mapping is another application of this category. SLN mapping is the standard staging method for breast cancer and melanoma [10].

Currently, surgeons rely on imaging systems to help guide surgical interventions as well as to evaluate the efficacy of the procedure when determining whether a follow-up surgery will be required. Preoperative modalities often utilized include magnetic resonance imaging (MRI), X-ray computed tomography (CT), and ultrasound among others [11–18]. In many instances, these modalities are used in conjunction to improve their efficacy; however difficulties remain. Due to their relative specificity, complexity, large size, and potential risk associated with long-term use, these technologies can be difficult to implement intraoperatively. Also, it can be difficult to correlate the surgical landscape with preoperative images during a surgery [17, 18]. To overcome these challenges, intraoperative imaging systems have been developed to offer real-time guidance. Most intraoperative imaging systems, such as fluoroscopy and ultrasound, only offer contrast based on functional information. Moreover, most systems rely on 2D imagery, which fails to provide crucial depth and 3D structural information to the surgeons. In addition, many techniques display the imagery on a free-standing display screen or monitor which requires the surgeon to continuously look away from the surgical site. This can be distracting and can make it difficult for the surgeon to correlate the surgical landscape with the imaging data.

To overcome these limitations, pioneering work has been conducted at the University of Akron and the Cleveland Clinic. We have developed a wearable stereoscopic multimodal imaging and display system entitled Integrated Imaging Goggle to provide surgical guidance in real-time [19, 20]. This system can offer the advantages of multimodal imaging, improved correlation of preoperative, and intraoperative images with the surgical landscape, as well as a user-friendly interface and real-time functionality. Herein we discuss the system instrumentation and the usage of the goggle for guiding surgical procedures. Our Integrated Imaging Goggle is a compact, wearable imaging and display system, which leverages on the principles of stereoscopic vision to present both depth and lateral spatial information to the physician (Fig. 1). We incorporate stereoscopic fluorescence imaging capability with real-time 2D ultrasound imaging and preoperative 3D MRI or CT data. The system aligns the point of view of the imaging system with that of

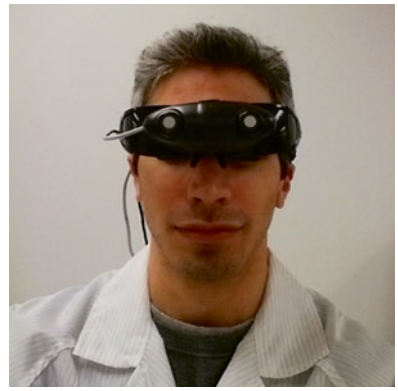

Fig. 1 Color photo of integrated imaging goggle

the surgeon. This makes the system easy to use and comprehend as looking through a pair of glasses. We will discuss the functionality of our system as applied to image-guided tumor resections and SLN mapping.

2 Materials

2.1 Integrated Imaging Goggle

The Integrated Imaging Goggle is composed of multiple modules, including two imaging sensors for stereoscopic imaging and a stereoscopic wearable display for fluorescence 3D imaging, a computational module, an adjustable optical illumination source, and an additional optional module including an intraoperative ultrasound module. The imaging sensors utilize CMOS technology, with adjustable lenses and 832 nm band-pass filters (Edmunds Optics, NJ) for fluorescent emission detection. When worn on the head, each display screen is centered over one eye. The stereoscopic imaging sensors are affixed to the front of the wearable display, directly over the display screens, providing for an imaging system from the true point of view of the surgeon (*see* **Note 1**). The imaging sensors and the wearable display are connected to a laptop or PC through USB, which provides the computational processing power for operating the system. In addition, the acquired medical images from our system can be transferred over a network connection to a remote PC for telemedical advising. The illumination module is provided for supplying intensity adjustable filtered diffused light for fluorescence excitation (*see* **Note 2**). The ultrasound module has a transducer capable of B-mode scanning, which is connected to the wearable imaging and display system via USB, and provides additional subsurface depth and anatomical data to the surgeon. Ultrasound images are processed via the computational module and registered onto the fluorescence images.

2.2 Preoperative MRI/CT

In addition to the given modules, which physically form the Integrated Imaging Goggle, preoperative MRI or CT can be incorporated into the system digitally. The sagittal, coronal, or transverse slices of an MRI or CT scan of a patient taken prior to the operation can be segmented and then formed together into a 3D volume. This volume is then registered to the stereoscopic images captured by the two CMOS sensors, and displayed through the wearable display to the surgeon.

2.3 Fluorescence Tracers

Near-infrared (NIR) light is used often for surgical fluorescence imaging due to its enhanced ability to penetrate through tissue with minimal absorption (*see* **Note 3**). To this end, we have utilized FDA-approved indocyanine green (ICG) for conducting fluorescence imaging. A reagent grade of ICG can be obtained from Sigma Aldrich (St. Louis, MO). This dye is excited optimally at 775 nm and has peak emissions at 830 nm. The dye is often procured in a more stable powdered form for long-term storage, and can be dissolved in a saline solution, at various dye concentrations, for surgical applications. Alternatively, newly emerging NIR targeting molecular tracers may be used in preclinical settings.

2.4 Animal and Human Requirements

Animal testing protocols must be approved by the Institutional Animal Care and Use Committee (IACUC), for federally funded research, and the Institutional Review Board (IRB) for any human testing. Protocol subject to review may include anesthetic methods, surgical methods including the participation of a board-certified surgeon, housing and nutritional supply for the animals prior to testing, pain management, and humane euthanization for animals after testing. In addition, written informed consent must be given by all human patients.

Additional requirements for animals include scissors, razors, and hair removal cream to prepare the animals for surgical procedures. Additional requirement for human study is based on specific clinical studies and clinicians' inputs.

3 Methods

3.1 Preclinical SLN Surgical Guidance

Small-animal goggle-aided surgical studies have been conducted in rodents and rabbits [21–23]. Procedures varied depending on the type of operation, either SLN mapping or image-guided tumor resection. The primary areas of difference were the administration of fluorescent dye, preparation of the animal for surgery, and the surgical methods involved. The procedure followed the methods listed below:

1. The procedure begins by anesthetizing the animal using an anesthesia cocktail such as ketamine and xylazine.

2. Next, any hair covering the surgical area is clipped and either shaven or removed using a topical cream.
3. For SLN mapping, a phosphate-buffered saline solution containing ICG is injected either peritumorally or intradermally.
4. Activate the goggle and the computational software to begin intraoperative imaging.
5. Activate the illumination module, and place the anesthetized animal in the center of the illuminated area where the light is uniform.
6. Wear the goggle to examine for fluorescence under image guidance. SLNs have higher fluorescence intensity than the surrounding tissue under excitation from the illumination module.
7. Surgically expose the region with high-level fluorescence signal by cutting and folding back the skin and muscles, to expose the SLNs. The bright fluorescent lymph nodes can be excised or biopsied (*see* **Note 4**).
8. The excised region can be further examined with the goggle to look for remaining lymph nodes.
9. If control lymph nodes are needed, ischiatic lymph nodes may also be excised for comparison with fluorescent SLNs.

3.2 Preclinical Image-Guided Tumor Resection

For preclinical image-guided tumor resections, animals were anesthetized and their hair removed using the same methods discussed above. NIR contrast agents should be administered, such as the intravenous injection of ICG at a dose of 0.5 mg per kg body weight. Alternatively, preclinical targeting molecular tracers may be administered. The preclinical image-guided tumor resection followed the methods listed below:

1. Activate the goggle and the computational software.
2. Activate the illumination module, and place the anesthetized animal in the center of the illuminated area where the light is uniform.
3. For abdominal oncologic surgeries, a midline incision is made from the sternum to the chest. The organs of interest such as the liver are exposed by a lateral reflection of the dissected tissue.
4. Wear the goggle to inspect the organ of interest for tissues with elevated fluorescence level. The fluorescence intensity from cancerous tissues is higher than the surrounding healthy tissue under excitation from the illumination module (*see* **Note 4**).
5. Resect the fluorescent tissue under image guidance from the goggle.
6. Reexamine the surgical bed and surrounding tissues for remaining fluorescent tissue.

7. If healthy tissues are needed as a control, resect some tissues with lower fluorescence levels to compare with the excised cancerous tissues.

3.3 Goggle-Aided Intraoperative Imaging in Human Patients

Previous studies were conducted using an earlier version of the goggle system that is 2D based (without stereoscopic imaging), for the intraoperative guidance of hepatocellular carcinoma (HCC) resections [2]. Either intravenous injection or transarterial hepatic (TAH) delivery of an ICG saline solution was conducted (*see* **Note 5**). For future clinical studies, intraoperative imaging aided by the new 3D stereoscopic goggle would follow the methods listed below, upon approval by the IRB:

1. The patient will be anesthetized.
2. Activate the goggle and the computational software.
3. Activate the illumination module, and place the surgical region of interest (ROI) of the anesthetized patient in the center of the illumination beam where the light is uniform.
4. The surgeon will perform the laparotomy per standard clinical guidelines, to expose the liver.
5. After liver exposure and subsequent immobilization, the liver may be assessed by naked-eye visual inspection and palpation prior to imaging guidance.
6. The surgeon will wear the goggle to inspect the fluorescent lesion from various angles to obtain an accurate assessment of tumor size and location (*see* **Note 4**). The pathophysiology of liver cancer favors the accumulation of ICG in the tumors 12–24 h after i.v. injection of ICG, providing a higher fluorescence signal than healthy liver tissues.
7. The surgeon will perform the tumor resection.
8. Following the primary resection, the surgical margins may be analyzed using the goggle to look for residual tissues with high level of fluorescence.
9. A secondary resection may be conducted if residual cancerous tissues are found.
10. The resected tissues are sent to pathology department for further analysis.

3.4 Fluorescence-Ultrasound Multimodal Intraoperative Imaging

The Integrated Imaging Goggle, recently developed at the University of Akron and the Cleveland Clinic, has the capability to guide surgeries with both intraoperative fluorescence imaging and ultrasound imaging (*see* **Note 6**). The ultrasound images were registered directly to the transducer, as seen through the goggles, using three LED markers on the transducer and a point-based image registration algorithm, to generate stereoscopic composite images in real-time. Three virtual points were defined on a transparent tab added to the bottom of the image read into the

computer from the ultrasound. When all three LEDs were detected by either camera, the registration algorithm was activated and the virtual points on the images were aligned with the center points of the detected LEDs. The LED centers were detected by first thresholding the camera images to eliminate the background, leaving only the bright LED dots. For this to be successful, the LEDs were adjusted to be brighter than any other point on the image. To ensure that this was consistently the case, the LED intensity was set to the point of sensor saturation. Then, the camera images, minus the saturated LED dots, were scaled so that none of the fluorescence emissions would also reach saturation. The dots were then fitted with circular shapes using a contour fitting algorithm, from which the center points could be defined and passed to the registration algorithm. Either a rigid transform or an affine transform was implemented upon user's command. The methods of multimodal intraoperative imaging using the Integrated Imaging Goggle proceed as follows:

1. Activate the Integrated Imaging Goggle and the computational software.
2. Activate the illumination module, and place the anesthetized animal in the center of the illuminated area where the excitation light is uniform.
3. Connect the ultrasound module with a 2D transducer to the system.
4. Wear the Integrated Imaging Goggle to inspect the area of interest under fluorescence imaging and ultrasound imaging simultaneously.
5. The overlaid intraoperative fluorescence and ultrasound images are displayed by the Integrated Imaging Goggle to the user in real-time, as shown in Fig. 2a.
6. The high level of NIR fluorescence indicates the presence of lesions.
7. The ultrasound data provides further information on the size and depth of the lesion.
8. Resect the lesion under image guidance provided by the Integrated Imaging Goggle.
9. Reexamine the surgical bed for remaining lesions under multimodal imaging, as needed.

3.5 Intraoperative Fluorescence Imaging Integrated with Preoperative Tomography-Based Surgical Navigation

The Integrated Imaging Goggle that we developed can provide integrated guidance based on intraoperative stereoscopic fluorescence imaging and surgical navigation based on preoperative MRI or CT data (*see* **Note 6**). Preoperative MRI or CT scans may be acquired according to standard clinical practice, where a series of 2D MRI or CT slices are taken for the ROI on the patient. The preoperative images are read into the computational module of our

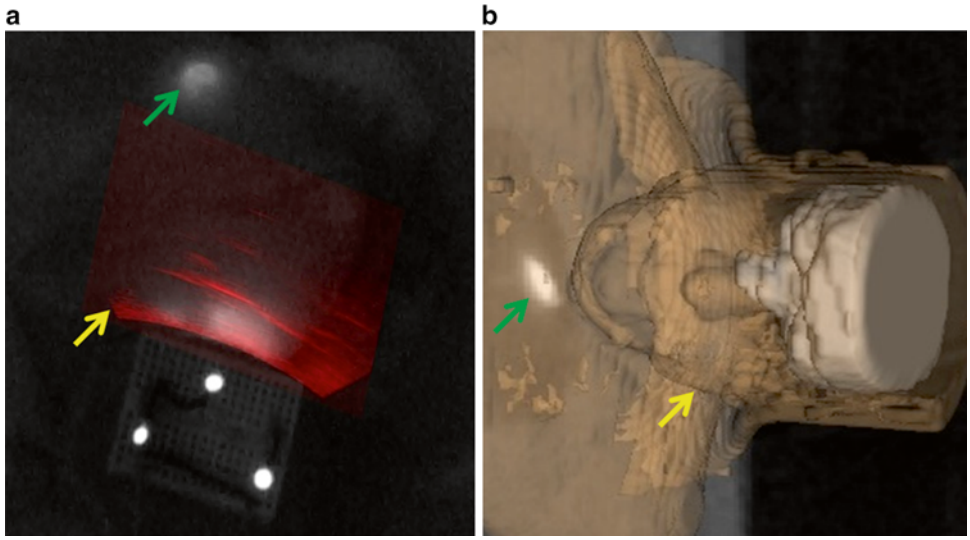

Fig. 2 Integrated Imaging goggle enables multimodal imaging and intraoperative fluorescence imaging registered with preoperative tomography-based surgical navigation. (**a**) Overlaid image of intraoperative ultrasound data registered with intraoperative fluorescence imaging data in preclinical studies is shown. *Yellow arrow* indicates B-mode ultrasound data; *green arrow* indicates lesions with high fluorescence intensity. (**b**) Overlaid image of preoperative MRI data registered with intraoperative fluorescence imaging data in proof-of-concept studies is shown. *Yellow arrow* indicates preoperative MRI surgical navigation data; *green arrow* indicates lesions with high fluorescence intensity from tissues

system, segmented, processed into a 3D model, and registered with the intraoperative fluorescence images (Fig. 2b).

For data processing, segmentation, and registration, we used the following methods. In brief, we utilized an intensity-based k-means algorithm to segment our sample MRI images. The segmented images were then combined sequentially into a single three-dimensional matrix, where each image corresponding to a single MRI slice was placed at the same coordinates in the x–y plane at a different z-axis value (*see* **Note** 7). Subsequently, the 3D MRI data was registered with intraoperative fluorescence images. The orientation of the 3D MRI object was specified to the desired direction, facing the goggle detector, and the center point of the projection was also specified. So far we have demonstrated the feasibility of integrating intraoperative fluorescence imaging and preoperative MRI-based surgical navigation in proof-of-concept studies. In the future we will improve and optimize the system performance, and conduct more preclinical studies as well as translational studies.

The methods of using integrated fluorescence imaging and MRI-based surgical navigation, offered by the Integrated Imaging Goggle, proceed as follows:

1. Load the segmented preoperative MRI data into the system.
2. Activate the Integrated Imaging Goggle and the computational software.

3. Activate the illumination module, and place the region of interest in the center of the illuminated area where the excitation light is uniform.
4. Wear the Integrated Imaging Goggle to inspect the area of interest under fluorescence imaging and MRI-based surgical navigation.
5. The overlaid intraoperative fluorescence and preoperative MRI images are displayed by the Integrated Imaging Goggle to the user in real-time, as shown in Fig. 2b.
6. The high level of NIR fluorescence indicates the presence of lesions.
7. The preoperative MRI data provides further information on the size and depth of the lesion, as well as a global anatomical reference.
8. Resect the lesion under image guidance provided by the Integrated Imaging Goggle.
9. Reexamine the surgical bed for remaining lesions under intraoperative fluorescence imaging and MRI-based surgical navigation, as needed.

3.6 Conclusions

In conclusion, we have developed a real-time stereoscopic imaging and display system entitled Integrated Imaging Goggle. The Integrated Imaging Goggle can simultaneously provide intraoperative fluorescence imaging, intraoperative ultrasound imaging, and preoperative MRI-based surgical navigation capabilities. Various image-guided surgeries such as sentinel lymph mapping and tumor resection can be aided by the goggle in preclinical, translational, and clinical settings.

4 Notes

1. The stereoscopic imaging capability, offered by the Integrated Imaging Goggle, provides surgeons with depth perception, which is crucial for guiding surgeries accurately. For clinical translation, stereoscopic imaging is desirable for accurate intraoperative image guidance.
2. The intensity of illumination should be adjusted based on the concentration and quantum yield of the fluorescent tracers. A higher level of illumination facilitates the detection of lesions.
3. An appropriate concentration of fluorescent tracers will prove beneficial to visibility. Fluorescence signal from the tracers should not saturate the detectors or cause self-quenching.
4. Observing the lesions from all sides through the Integrated Imaging Goggle will provide the surgeon with an excellent estimate of the depth of the object, improving surgical accuracy.

5. ICG can be administered within 12–48 h prior to the liver cancer surgery. This will provide adequate time for the liver to clear excess ICG which has not been deposited in the tumor.
6. The Integrated Imaging Goggle is the first system that simultaneously offers intraoperative fluorescence imaging, intraoperative ultrasound, and preoperative MRI-based surgical navigation. The ability to seamlessly integrate, track, and register preoperative tomographic data, intraoperative fluorescence imaging data, and intraoperative ultrasound data can multiplex the information and provide better image guidance in the operating room.
7. The segmented regions, colors, texture, and transparency of the 3D MRI object can be adjusted to fit the preferences of the user. Increasing the transparency may allow the surgeon to better visualize the intraoperative fluorescence in diseased tissues based on the registered image.

References

1. Kelderhouse LE, Chelvam V, Wayua C, Mahalingam S, Poh S, Kularatne SA, Low PS (2013) Development of tumor-targeted near infrared probes for fluorescence guided surgery. Bioconjug Chem 24:1075–1080
2. Liu Y, Zhao Y-M, Akers W, Tang Z-Y, Fan J, Sun H-C, Ye Q-H, Wang L, Achilefu S (2013) First in-human intraoperative imaging of HCC using the fluorescence goggle system and transarterial delivery of near-infrared fluorescence imaging agent: a pilot study. Transl Res 162:324–331
3. Wilke LG, Brown JQ, Bydlon TM, Kennedy SA, Richards LM, Junker MK, Gallagher J, Barry WT, Geradts J, Ramanujam N (2009) Rapid noninvasive optical imaging of tissue composition in breast tumor margins. Am J Surg 198:566–574
4. Keller MD, Majumder SK, Kelley MC, Meszoely IM, Boulos FI, Olivares GM, Mahadevan-Jansen A (2010) Autofluorescence and diffuse reflectance spectroscopy and spectral imaging for breast surgical margin analysis. Lasers Surg Med 42:15–23
5. Sasaki K, Matsuda M, Ohkura Y, Kawamura Y, Hashimoto M, Ikeda K, Kumada H, Watanabe G (2013) Minimum resection margin should be based on tumor size in hepatectomy for hepatocellular carcinoma in hepatoviral infection patients. Hepatol Res 43:1295–1303
6. Hughes OR, Stone N, Kraft M, Arens C, Birchall MA (2010) Optical and molecular techniques to identify tumor margins within the larynx. Head Neck 32:1544–1553
7. Garcia-Allende PB, Glatz J, Koch M, Ntziachristos V (2013) Enriching the interventional vision of cancer with fluorescence and optoacoustic imaging. J Nucl Med 54:664–667
8. Ashitate Y (2012) Real-time simultaneous near-infrared fluorescence imaging of bile duct and arterial anatomy. J Surg Res 176:7–13
9. Matsui A, Tanaka E, Choi HS, Winer JH, Kianzad V, Gioux S, Laurence RG, Frangioni JV (2010) Real-time intra-operative near-infrared fluorescence identification of the extrahepatic bile ducts using clinically available contrast agents. Surgery 148:87–95
10. Jain V, Phillips BT, Conkling N, Pameijer C (2013) Sentinel lymph node detection using laser-assisted indocyanine green dye lymphangiography in patients with melanoma. Int J Surg Oncol. doi:10.1155/2013/904214
11. Houssami N, Turner R, Morrow M (2013) Preoperative magnetic resonance imaging in breast cancer: meta-analysis of surgical outcomes. Ann Surg 257:249–255
12. Aukema TS, Olmos RAV, Wouters MWJM, Klop WMC, Kroon BBR, Vogel WV, Nieweg OE (2010) Utility of preoperative 18F-FDG PET/CT and brain MRI in melanoma patients with palpable lymph node metastases. Ann Surg Oncol 17:2773–2778
13. Hinz T, Voth H, Ahmadzadehfar H, Hoeller T, Wenzel J, Bieber T, Schmid-Wendtner M-H (2013) Role of high-resolution ultrasound and PET/CT imaging for preoperative characterization of sentinel lymph nodes in cutaneous melanoma. Ultrasound Med Biol 39:30–36

14. Pallone MJ, Poplack SP, Avutu HBR, Paulsen KD, Barth RJ Jr (2014) Supine breast MRI and 3D optical scanning: A novel approach to improve tumor localization for breast conserving surgery. Ann Surg Oncol 21: 2203–2208
15. Lam DL, Mitsumori LM, Neligan PC, Warren BH, Shuman WP, Dubinsky TJ (2012) Preoperative CT angiography and three-dimensional image post processing for deep inferior epigastric perforator flap breast reconstructive surgery. Br J Radiol 85:1293–1297
16. Nam WH, Kang D-G, Lee D, Lee JY, Ra JB (2012) Automatic registration between 3D intra-operative ultrasound and pre-operative CT images of the liver based on robust edge matching. Phys Med Biol 57:69–91
17. Kingham TP, Jayaraman S, Clements LW, Scherer MA, Stefansic JD, Jarnagin WR (2013) Evolution of image-guided liver surgery: transition from open to laparoscopic procedures. J Gastrointest Surg 17:1274–1282
18. van der Vorst JR, Schaafsma BE, Verbeek FPR, Keereweer S, Jansen JC, van der Velden L-A, Langeveld APM, Hutteman M, Löwik CWGM, van de Velde CJH, Frangioni JV, Vahrmeijer AL (2013) Near-infrared fluorescence sentinel lymph node mapping of the oral cavity in head and neck cancer patients. Oral Oncol 49: 15–19
19. Mela CA, Patterson CL, Liu Y (2015) A miniature wearable optical imaging system for guiding surgeries. Proc SPIE 93110Z. doi: 10.1117/12.2076226
20. Mela CA, Patterson C, Thompson WK, Papay F, Liu Y (2015) Stereoscopic Integrated imaging goggles for multimodal intraoperative image guidance. PLoS One. doi:10.1371/journal.pone.0141956
21. Liu Y, Njuguna R, Matthews T, Akers WJ, Sudlow GP, Mondal S, Tang R, Gruev V, Achilefu S (2013) Near-infrared fluorescence goggle system with complementary metal-oxide-semiconductor imaging sensor and see-through display. J Biomed Opt. doi:10.1117/1.JBO.18.10.101303
22. Liu Y, Bauer AQ, Akers WJ, Sudlow G, Liang K, Shen D, Berezin MY, Culver JP, Achilefu S (2011) Hands-free, wireless goggles for near-infrared fluorescence and real-time image-guided surgery. Surgery 149:689–698
23. Liu Y, Akers WJ, Bauer AQ, Mondal S, Gullicksrud K, Sudlow G, Culver JP, Achilefu S (2013) Intraoperative detection of liver tumors aided by fluorescence goggle system and multimodal imaging. Analyst 138:2254–2257

Chapter 10

Utilization of Near-Infrared Fluorescent Imaging for Pharmaceutically Relevant Applications

Jelena M. Janjic, Sravan Kumar Patel, and Christina Bagia

Abstract

Optical imaging can be utilized for several pharmaceutical applications involving near-infrared fluorescent (NIRF) dyes or NIRF moiety-containing products. Especially during the early phases of product development, NIRF dyes can be used as surrogates for drugs and optical imaging methods can be utilized to optimize the pharmaceutical product properties based on dye entrapment efficiency, in vitro dye release, cellular uptake, and in vivo biodistribution. Based on in vivo accumulation, product efficacy and toxicity can be evaluated in the early development stage. Compared to visible fluorescent dyes, NIRF offers advantages such as low background from formulation excipients as well as biological components.

In this chapter, the utility of NIRF imaging methods for in vitro characterization (in vitro release and cellular uptake) and in vivo/ex vivo applicability of pharmaceutically relevant products is presented in detail. Specifically, the application of fluorescence imaging to characterize perfluorocarbon-based formulations for dye loading, in vitro release, cellular uptake, and in vivo imaging to assess target accumulation and biodistribution is discussed. These methods are widely applicable to other nanoparticle-based products involved in inflammation/cancer imaging and therapy. Overall, NIRF-based techniques are indispensible because they are relatively easy, fast, and cost effective to characterize and optimize pharmaceutical products at different stages of product development.

Key words NIRF, Nanoemulsions, Hydrogels, Biodistribution, Inflammation

1 Introduction

In this chapter we describe utility of in vitro and in vivo near-infrared fluorescence (NIRF) imaging applied to quality evaluations of nanoemulsion and gel formulations designed for anti-inflammatory drug delivery. Nanoemulsions are kinetically stable emulsions with a droplet size typically between 100 and 500 nm, high oil content, and low amounts of surfactant [1]. Nanoemulsions have wide applications in pharmaceutical industry where they are typically used to increase tissue penetration of poorly soluble drugs (transdermal), and improve drug solubility and bioavailability (injectables) [2–6]. They are also easily incorporated into other dosage forms such as capsules and gels and can be produced on

Mingfeng Bai (ed.), *In Vivo Fluorescence Imaging: Methods and Protocols*, Methods in Molecular Biology, vol. 1444,
DOI 10.1007/978-1-4939-3721-9_10,

industrial scale [6–8]. Protocols described in this chapter use perfluorocarbon (PFC) nanoemulsions reported earlier [9–14] as example nanomedicines. Passive targeting to circulating inflammatory cells by PFC nanoemulsions has been extensively investigated for the purpose of ^{19}F magnetic resonance imaging (MRI) of inflammation [12, 15–17]. As imaging agents, PFC nanoemulsions are easily combined with NIRF dyes for dual-mode, ^{19}F MRI/NIRF, imaging. Janjic et al. [18] reported in 2008 perfluoropolyether (PFPE) conjugation to several fluorescent dyes. PFC nanoemulsions can also be labeled with NIR dyes by entrapment during nanoemulsification in the lipid or surfactant layer [12–14]. Additionally, PFC nanoemulsions designed as dual-mode imaging agents were utilized for optical and photoacoustic imaging by Akers et al. [19] and they were also investigated as ultrasound imaging contrast agents in preclinical models [20]. As a theranostic platform, PFC nanoemulsions have attracted increasing interest over the past 5 years. In one example, Wickline and co-workers incorporated a cytolytic peptide (melittin), an anticancer agent, into the lipid layer of a PFC nanoemulsion droplet [21]. They showed that favorable pharmacokinetics and tumor targeting of melittin were successfully achieved with dramatic reduction of tumor size [22]. At the same time the nanoemulsion provided tumor-specific ^{19}F MRI in a mouse model. Further, paclitaxel was formulated in a block-polymer-stabilized perfluoropentane nanoemulsion for image-guided delivery using ultrasound and MRI in a mouse tumor model [20]. Recent study used PFC nanoemulsions to deliver antigen to dendritic cells with the goal of boosting the immune response in DC-based vaccines [23]. For active targeting strategies in nanoemulsion-based theranostics, the targeting agent is attached to the droplet surface by covalent conjugation. For example, PFC nanoemulsions targeted to $\alpha_v\beta_3$ integrins for atherosclerosis imaging have been developed [24]. In an earlier study, Lanza et al. reported targeted delivery of antiproliferative drugs to smooth muscle cells using perfluorooctyl bromide (PFOB) nanoemulsions [25]. All together, these reports strongly suggest that PFC nanoemulsions are attractive technology for development of imaging and drug delivery agents.

In this chapter, we discuss application of NIRF imaging to PFC nanoemulsions' quality assessment. Further, we also discuss utilization of NIRF imaging for evaluating drug incorporation and drug release from hydrogels where the incorporated therapeutic payload can be detected by NIRF.

NIRF can be utilized to assay the NIRF dye concentration in pharmaceutical formulations, and assess release profile in relevant media and optical stability upon storage. It can also be employed to evaluate the dose- and time-dependent uptake kinetics in cells. Several techniques are reported in the literature to assess uptake such as flow cytometry, plate readers, and fluorescence/confocal imaging.

The method reported here is significantly faster and requires less resources and experimental steps. These protocols however can be widely applied to other nanosystems labeled with NIRF dyes or inherently fluorescent in the near-infrared (NIR) range. In addition to cellular uptake of NIRF-labeled nanoemulsions in vitro, we can determine biodistribution of nanoemulsions by imaging harvested organs from animals. This method can be used early in the development process to optimize the formulation for effective target accumulation or changes in organ distribution.

When the therapeutic payload is NIRF visible, optical imaging can be used for incorporation and release analysis in vitro. Recently Berlec et al. [26] reported new probiotic designed to inhibit tumor necrosis factor alpha (TNFα) in inflammatory bowel disease. The probiotic is formed by genetically engineering L. Lactis to express TNFα-binding motif (*L. Lactis*-TNFα) on its surface and effectively neutralize TNF in the gastrointestinal tract upon oral delivery. To facilitate better understanding of the probiotic effects on inflammation in vivo, we reengineered the bacteria to express NIR-visible protein tag, infrared fluorescent protein (IRFP) [27]. When the NIRF-visible probiotic (*L. Lactis*-TNFα/IRFP) is incorporated into a hydrogel, in vitro NIRF imaging can be used to monitor its stability and release from the gel. The gel is designed to serve as a vehicle for sustained release of therapeutic bacteria in the lower colon and rectum [27]. Here the gel is discussed as a model pharmaceutical preparation for biologic material delivery and NIR imaging applied to study the formulation behavior in vitro. The presented protocols can be further optimized to varied pharmaceutical formulations that incorporate either NIRF dyes or are designed for multimodal imaging.

2 Materials

2.1 Materials Used for NIR Imaging of Nanoemulsions

DiR dye (a commercially available NIR fluorescent dye) dissolved in ethanol is used for nanoemulsion preparations. For the NIR fluorescence standard curve DiR dye is dissolved directly in Miglyol 812 N oil. All DiR-labeled nanoemulsions were prepared as reported earlier [9, 11, 13].

2.2 Materials for Biologic Material Quantification and Release Studies in Hydrogels Using NIR Imaging

All samples for NIR imaging must be freshly prepared. As the model NIR-visible biologics, we used *L. Lactis*-IRFP and *L. Lactis*-TNFα/IRFP samples lyophilized in sucrose. Although both bacteria samples are fluorescent (IRFP), *L. Lactis*-TNFα/IRFP is also engineered to produce TNFα-binding motif on their surface. Bacteria suspensions were prepared in Dulbecco's phosphate-buffered saline (DPBS) 1× without calcium chloride and magnesium chloride. Handle the samples with care and clean the surfaces and glassware with isopropanol after use.

2.3 Materials Needed for NIR Assessment of Cellular Uptake of Fluorescent Nanoemulsions

1. NIR-labeled PFC nanoemulsions are prepared as previously reported [9, 11].
2. RAW 264.7 macrophage-like cells (ATCC).
3. Dulbecco's modified Eagle medium (DMEM)-based complete cell culture medium supplemented with fetal bovine serum (FBS) at 10%.

2.4 Materials Needed for In Vivo and Ex Vivo Assessment of Nanoemulsions in a Mouse Inflammation Model

Detailed description of the mouse model and reagents used for this example is available elsewhere [28].

1. Anesthesia setup (isoflurane/oxygen).
2. Black cloth.
3. IVIS Lumina® XR imaging station.

3 Methods

3.1 Methods for Imaging Nanoemulsions

3.1.1 Standard Calibration Curve

1. Stock solution 1: 10 mg of DiR is dissolved in 2 mL ethanol (4.934 mM).
2. Stock solution 2: 5 μL of stock 1 is transferred in a 5 mL volumetric flask filled with Miglyol 812 N (5 μM).
3. Stock solution 3: 100 μL of stock 2 is transferred in a 2 mL volumetric flask filled with Miglyol 812 N (0.5 μM).
4. The theoretical concentration of DiR in the nanoemulsion that corresponds to 100% loading is 0.5 μM (*see* **Note 1**).
5. Build calibration curve at levels from 10 to 120% (from 0.05 to 0.6 μM).
6. For all dilutions use two stock solutions (stocks 2 and 3) (*see* **Note 1**).
7. Dilutions:

   120% (0.6 μM): 120 μL of stock 2 + 880 μL Miglyol 812 N.

   100% (0.5 μM): 100 μL of stock 2 + 900 μL Miglyol 812 N.

   80% (0.4 μM): 80 μL of stock 2 + 920 μL Miglyol 812 N.

   60% (0.3 μM): 60 μL of stock 2 + 940 μL Miglyol 812 N.

   40% (0.2 μM): 40 μL of stock 2 + 960 μL Miglyol 812 N.

   20% (0.1 μM): 20 μL of stock 2 + 980 μL Miglyol 812 N.

   10% (0.05 μM): 100 μL of stock 3 + 900 μL Miglyol 812.

3.1.2 Sample Preparation for Nanoemulsions

1. 25 μL of nanoemulsion (20 μM of DiR) is diluted by adding 975 μL of DI–H_2O (0.5 μM of DiR). Prepare samples in triplicates.
2. Vortex gently until it becomes homogeneous.

3.1.3 Method for Imaging of NIR Dye-Loaded Nanoemulsions

1. From prepared standards and nanoemulsion dilutions transfer 100 μL of all the solutions from the calibration curve and the sample solutions into a 96-well plate in triplicates (*see* **Notes 1** and **2**).
2. Clean the surface of LiCOR Odyssey imaging system with isopropanol before placing the 96-well plate (*see* **Note 3**).
3. Record fluorescence images using a LiCOR Odyssey system.
4. LiCOR Odyssey setup: preset: Microplate 2, resolution: 169 μm, quality: lowest, focus offset: 3.0 mm, channel: 800 nm, intensity: 2.5.
5. LiCOR Odyssey analysis: Using instrument software, draw regions of interest (ROI) for fluorescence quantification. Specifically, grid size: rows 8 and columns 12, spacing between grid lines 9.0×9.0 mm, well space and size: circle and 6.7×6.7 mm. Make sure that the samples are within the circle.
6. Correct with the background (empty well).

3.2 Methods for Biologic Material Quantification and Release Studies in Hydrogels Using NIR Imaging

3.2.1 Standard NIR Imaging Calibration Curve for Bacteria

1. Stock solution: Weigh 10 mg of *L. Lactis*-IRFP bacteria and disperse in 10 mL DPBS (1.0 mg/mL bacteria) (*see* **Notes 1**, **2**, and **4**).
2. The theoretical concentration of bacteria in the gel that corresponds to 100% loading is 0.376 mg/mL.
3. Build calibration curve at levels from 10 to 120% (from 0.0376 to 0.4512 mg/mL).
4. For all dilutions use the stock solution 1.
5. Dilutions:

   120% (0.4512 mg/mL): 451 μL of stock 1 + 549 μL DPBS.
   100% (0.3760 mg/mL): 376 μL of stock 1 + 624 μL DPBS.
   80% (0.3008 mg/mL): 301 μL of stock 1 + 699 μL DPBS.
   65% (0.2444 mg/mL): 244 μL of stock 1 + 756 μL DPBS.
   50% (0.1880 mg/mL): 188 μL of stock 1 + 812 μL DPBS.
   30% (0.1128 mg/mL): 113 μL of stock 1 + 887 μL DPBS.
   10% (0.0376 mg/mL): 37.6 μL of stock 1 + 962.4 μL DPBS.

3.2.2 Sample Preparation for Bacteria Quantification

1. Weigh 100 mg of bacteria hydrogel (3.76 mg/mL of bacteria) and add 900 μL of DPBS 1× (0.376 mg/mL bacteria). Prepare samples in triplicates.
2. Let the solution sit for 30 min and then vortex gently until it becomes homogeneous.

3.2.3 Sample Preparation for Bacteria Release Studies

1. Weigh 500 mg of bacteria hydrogel (3.76 mg/mL of bacteria) and add 5 mL of DPBS (0.376 mg/mL bacteria). Prepare six samples for release studies.

2. Release conditions: Temperature: 25 °C, platform shaker, sampling volume: 100 μL.

3.2.4 Quantification by NIR Imaging of Bacteria Content and Release

1. For bacteria quantification: Transfer 500 μL of all the solutions from the calibration curve and the sample solutions into a 24-well plate clear flat-bottom plate.
2. For bacteria release studies: Transfer 100 μL of all the solutions from the calibration curve and the sample solutions in a 96-well plate.
3. Avoid bubbles in the wells containing samples and standards.
4. Clean the surface of LiCOR with isopropanol before placing the 24-well plate or the 96-well plate (*see* **Note 3**).
5. Measure fluorescence using a LiCOR Odyssey system.
6. LiCOR Odyssey setup for quantification: preset: Microplate 2, resolution: 169 μm, quality: lowest, focus offset: 3.0 mm, channel: 700 nm, intensity: 4.0.
7. LiCOR Odyssey setup for release studies: preset: Microplate 2; resolution: 169 μm, quality: lowest, focus offset: 3.0 mm, channel: 700 nm, intensity: 6.5.
8. LiCOR Odyssey grid analysis for quantification: Using instrument software, draw regions of interest (ROI) for fluorescence quantification. Specifically, grid size: rows 4 and columns 6, spacing between grid lines 19 × 19 mm, well space and size: circle and 17 × 17 mm. Make sure that the samples are within the circle.
9. LiCOR Odyssey grid analysis for release studies: grid size: rows 8 and columns 12, spacing between grid lines 9.0 × 9.0 mm, well space and size: circle and 6.7 × 6.7 mm. Make sure that the samples are within the circle.
10. Correct with the background (empty well).
11. Example NIRF images of samples and standards prepared obtained on LiCOR Odyssey and used for above-described quantification are shown in Fig. 1.

3.3 Methods for Assessment of Cellular Uptake of Fluorescent Nanoemulsions by NIR Imaging

1. Plate cells at 0.3 million/well in 6-well plates in 2 mL cell culture medium of choice (e.g., DMEM supplemented with 10% FBS, *see* Subheading 2.3).
2. After overnight incubation (18–20 h) at 5% CO_2 and 37 °C, remove the media and wash 2× DPBS.
3. Prepare serial dilutions of nanoemulsion in complete cell culture medium. Perform this step prior to washing cells in **step 2** to avoid leaving the cells in DPBS or to get dry for longer times.

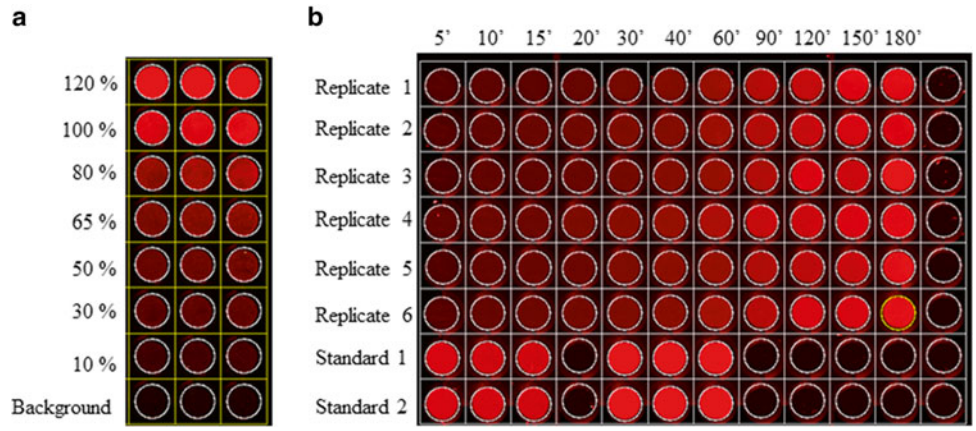

Fig. 1 (**a**) Calibration curve of bacteria *L. Lactis*-IRFP. (**b**) Release studies of bacteria L. Lactis-IRFP/TNFα from hydrogels (six replicates at different time points). At the same plate we measured bacteria standard at one level (100 %) in duplicate (C. Bagia, 2014 unpublished)

4. Add these dispersions to cells and incubate for required amount of time (e.g., 24 h).
5. After incubation, remove the dispersion from plates by aspiration and wash the cells 2× with DPBS.
6. Add 0.5 mL trypsin–EDTA (0.05 %), incubate at 37 °C and 5 % CO_2 for 2 min, followed by addition of 1.5 mL medium and collection of cells by repeated pipetting.
7. Centrifuge the cells at 300 × *g*, 5 min, and remove the supernatant.
8. Add 2 mL of cell culture medium to the cell pellet, disperse evenly, count the cells from each dilution using trypan blue exclusion assay, and record the cell number (for alternative to cell counting *see* **Note 5**).
9. Centrifuge the cells at 550 × *g* for 10 min to form a tight pellet (*see* **Note 4**).
10. Remove the supernatant and add 180 μL of DI.H_2O and 200 μL of TFA (0.02 % v/v) containing aqueous solution.
11. Transfer this dispersion to 5 mm NMR tubes.
12. Before imaging, clean the Odyssey glass bed with isopropanol (*see* **Note 2**).
13. Place the tubes in an increasing concentration (dilution), starting at the lower left corner of the flat bed.
14. LiCOR Odyssey setup: preset: Microplate 2, resolution: 169 μm, quality: lowest, focus offset: 2.5 mm, channel: 700 nm, intensity: 5.0.

15. Record the images. If the images show white spots, change the intensity setting below five and record the images.
16. LiCOR Odyssey analysis for quantification: Adjust the image curves to see the edges of the NMR tube of lower concentration or control (no nanoemulsion) dilution. Remove automatic background correction and manually draw rectangles on the highest concentration NMR tube. Leave spaces on the left/right, lower/upper edges. Copy the rectangle and place it on all the NMR tube images. Make sure that the sample is within the rectangle (*see* **Note 6**).
17. From the software, select export excel file for shapes to obtain an Excel sheet with fluorescence data for the drawn shapes.
18. Divide the integrated intensity values with cell number obtained in **step 8**.
19. Plot the data with nanoemulsion dilution on *x*-axis and corresponding integrated fluorescence/cell on *y*-axis to obtain dose-dependent uptake.
20. These samples can be assessed for ^{19}F content using NMR. Data from step 19 can be used to establish correlation between the two imaging methods, NIRF and ^{19}F NMR [13].

3.4 Methods for In Vivo and Ex Vivo Assessment of Nanoemulsions in a Mouse Inflammation Model by NIR Imaging

3.4.1 Animal Treatment and Preparation for Imaging

1. In this experiment, animals are injected with fluorescent PFC nanoemulsions, followed by subcutaneous injection of complete Freund's adjuvant in the mouse foot pad to induce inflammation. X-ray/fluorescence images are collected at different time points to assess changes in inflammation based on macrophage infiltration, which are labeled with fluorescent PFC nanoemulsions.
2. Before starting the experiment, turn on IVIS imaging station and open the IVIS software in the connected computer. Wait till the instrument is initialized.
3. Set the parameters such as field of view (C), exposure (1 s), lamp level (high), F/stop (2), binning (medium), and excitation (640 nm) and emission (700 nm) wavelengths. Check the boxes for X-ray and white light image [28].
4. Anesthetize the animals in a closed chamber connected with isoflurane/oxygen flow.
5. Place the animal inside the imaging station bed, which is maintained at 37 °C. Place the animal in the dorsal position with anesthesia port connected. Spread the fore and hind limbs apart.
6. In order to avoid signal from tail, bladder, and abdominal region, which can saturate the detector, place a black cloth on these areas (Fig. 2a).

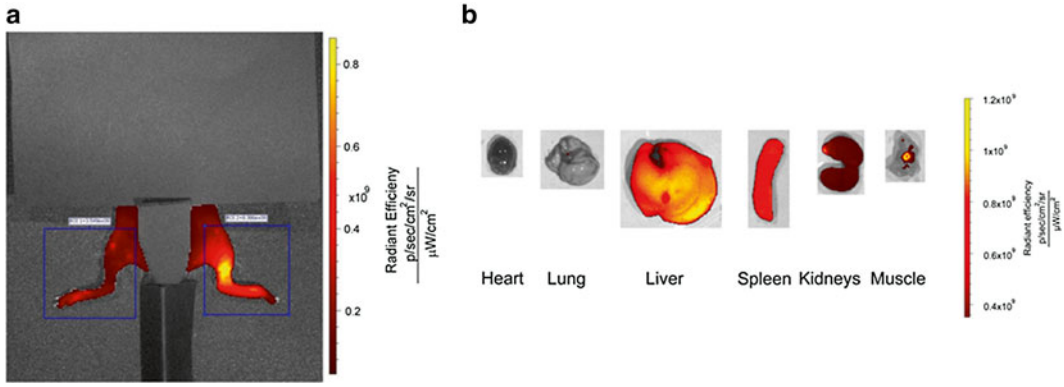

Fig. 2 (**a**) Image showing placement of black cloth to avoid fluorescence from tail, bladder, and abdominal region of the mouse. (**b**) Fluorescence/white light composite image showing alignment of different tissues for biodistribution analysis (reproduced from Ref. 28 with permission)

7. Close the imaging station door and collect the images.
8. Return the mouse to the cage and start imaging the next animal with same imaging parameters. Continue recording images with the same procedure and settings at each imaging time point till the end of the study.
9. For biodistribution study, anesthetize the animals and euthanize them by cervical dislocation.
10. Collect liver, spleen, kidneys, heart, lungs, and muscle.
11. Line the organs on a paper as shown in Fig. 2b and place them in the imaging station.
12. Collect the images and adjust settings if necessary [28] (*see* **Notes 6**, 7, and **8**).
13. After imaging, record the weights of organs/tissues on a digital weighing balance.

3.4.2 Image Analysis for Quantification of Signal in Animals

1. Open all the images to be analyzed using IVIS software.
2. Select X-ray and fluorescence to obtain an overlay image. Adjust X-ray and fluorescence settings to obtain an image showing concentrated fluorescence in the inflamed paw region. Make all the images background subtracted.
3. Draw ROI for the control paw in such a way that it covers the whole paw and half of femur (thigh bone) (Fig. 2a). Bones can be visualized based on anatomical X-ray image. Place another ROI similarly on the inflamed paw region. Repeat this for all the images and obtain quantification data for all the images.
4. From the obtained images, use total radiant efficiency values for data analysis.

5. Divide the total radiant efficiency of inflamed paw with respective control paw for each animal and calculate the average and standard deviation. Plot the values for different treatment groups with ratio on *y*-axis and imaging time points on *x*-axis.
6. For biodistribution images, draw separate ROIs on the background-subtracted images (see Subheading 3.4.2) and obtain total radiant efficiency values. Divide these values with tissue weight and report results with normalized total efficiency on *y*-axis and organ/tissue name on *x*-axis (*see* **Notes** 7 and 9).

4 Notes

1. When measuring test samples always prepare fresh standard and compare within the same plate. It is recommended to build a fresh calibration curve each time new analysis is performed. Select one level from the curve and then do the calculations accordingly. Inter-day validations can be performed on the calibration curve beforehand to determine appropriate time interval needed for retesting full calibration range and ensuring proper functioning of the calibration.
2. All samples must be protected from light.
3. If the surface of the instrument is not cleaned with isopropanol the obtained images are not uniform and can show variation in fluorescence uniformity. Impurities depending on composition may appear on the images or contribute to high fluorescence background. So it is highly recommended to clean the surface of LiCOR and the bottom of the plate.
4. Samples should be analyzed immediately after preparation in order to minimize fluorescence degradation in lysed cell components. If storage is required, store the samples at 4 °C away from light. DO NOT FREEZE.
5. If there are many samples, cell counting could be tedious. Alternate methods such as protein assay or cell viability assays (CellTiter-Glo®) can be utilized to obtain information regarding cell number. If the integrated intensity is not normalized to cell number or protein content, erroneous results can be obtained as the cell collection after trypsinization may not be able to collect all the cells from the plate. This is particularly a problem for highly adherent activated macrophages.
6. The size of the rectangle during data analysis should be the same for all the tubes in order to account for equal background.
7. Optimize the imaging parameters based on whether the detector shows signal saturation for fluorescence. For example, increasing the exposure time and binning to high could lead to

detector saturation. Similarly, the excitation and emission wavelengths should be adjusted based on the fluorescence spectra of the utilized nanoemulsions. It is not necessary that use of excitation and emission maximum will provide with optimum images. Adjust these wavelengths using the in-built excitation and emission filters, yet remaining within the near-infrared range of the nanoemulsions' fluorescence spectra to obtain optimum images. Adjust all the parameters individually, collect images, and select the settings that provide optimum results.

8. While optimizing the parameters, image more than one mouse from each group to make sure that the obtained images remain optimum (no detector saturation). Once the parameters are optimized, make sure to use the same settings for all the imaging sessions for an experiment.
9. Rely on quantification (ratio) data rather than visual fluorescence inspection to arrive at any conclusions.

References

1. McClements DJ (2012) Nanoemulsions versus microemulsions: terminology, differences, and similarities. Soft Matter 8(6):1719–1729
2. Shakeel F, Shafiq S, Haq N, Alanazi FK, Alsarra IA (2012) Nanoemulsions as potential vehicles for transdermal and dermal delivery of hydrophobic compounds: an overview. Expert Opin Drug Deliv 9(8):953–974
3. Kotta S, Khan AW, Pramod K, Ansari SH, Sharma RK, Ali J (2012) Exploring oral nanoemulsions for bioavailability enhancement of poorly water-soluble drugs. Expert Opin Drug Deliv 9(5):585–598
4. McClements DJ, Rao J (2011) Food-grade nanoemulsions: formulation, fabrication, properties, performance, biological fate, and potential toxicity. Crit Rev Food Sci Nutr 51(4):285–330
5. Rajpoot P, Pathak K, Bali V (2011) Therapeutic applications of nanoemulsion based drug delivery systems: a review of patents in last two decades. Recent Pat Drug Deliv Formul 5(2):163–172
6. Sarker DK (2005) Engineering of nanoemulsions for drug delivery. Curr Drug Deliv 2(4):297–310
7. Mitri K, Vauthier C, Huang N, Menas A, Ringard-Lefebvre C, Anselmi C, Stambouli M, Rosilio V, Vachon JJ, Bouchemal K (2012) Scale-up of nanoemulsion produced by emulsification and solvent diffusion. J Pharm Sci 101(11):4240–4247
8. Muller RH, Harden D, Keck CM (2012) Development of industrially feasible concentrated 30% and 40% nanoemulsions for intravenous drug delivery. Drug Dev Ind Pharm 38(4):420–430
9. Janjic JM, Shao P, Zhang S, Yang X, Patel SK, Bai M (2014) Perfluorocarbon nanoemulsions with fluorescent, colloidal and magnetic properties. Biomaterials 35(18):4958–4968
10. Vasudeva K, Andersen K, Zeyzus-Johns B, Hitchens TK, Patel SK, Balducci A, Janjic JM, Pollock JA (2014) Imaging neuroinflammation in vivo in a neuropathic pain rat model with near-infrared fluorescence and (1)(9)F magnetic resonance. PLoS One 9(2):e90589
11. Patel SK, Patrick MJ, Pollock JA, Janjic JM (2013) Two-color fluorescent (near-infrared and visible) triphasic perfluorocarbon nanoemuslions. J Biomed Opt 18(10):101312
12. Balducci A, Wen Y, Zhang Y, Helfer BM, Hitchens TK, Meng WS, Wesa AK, Janjic JM (2013) A novel probe for the non-invasive detection of tumor-associated inflammation. Oncoimmunology 2(2):e23034
13. Patel SK, Zhang Y, Pollock JA, Janjic JM (2013) Cyclooxgenase-2 inhibiting perfluoropoly (ethylene glycol) ether theranostic nanoemulsions-in vitro study. PLoS One 8(2):e55802
14. O'Hanlon CE, Amede KG, O'Hear MR, Janjic JM (2012) NIR-labeled perfluoropolyether nanoemulsions for drug delivery and imaging. J Fluor Chem 137:27–33
15. Stoll G, Basse-Lusebrink T, Weise G, Jakob P (2012) Visualization of inflammation using (19) F-magnetic resonance imaging and perfluorocarbons. Wiley interdiscip Rev Nanomed Nanobiotechnol 4(4):438–447

16. Kadayakkara DK, Beatty PL, Turner MS, Janjic JM, Ahrens ET, Finn OJ (2010) Inflammation driven by overexpression of the hypoglycosylated abnormal mucin 1 (MUC1) links inflammatory bowel disease and pancreatitis. Pancreas 39(4):510–515
17. Weise G, Basse-Luesebrink TC, Wessig C, Jakob PM, Stoll G (2011) In vivo imaging of inflammation in the peripheral nervous system by (19)F MRI. Exp Neurol 229(2):494–501
18. Janjic JM, Srinivas M, Kadayakkara DK, Ahrens ET (2008) Self-delivering nanoemulsions for dual fluorine-19 MRI and fluorescence detection. J Am Chem Soc 130(9): 2832–2841
19. Akers WJ, Kim C, Berezin M, Guo K, Fuhrhop R, Lanza GM, Fischer GM, Daltrozzo E, Zumbusch A, Cai X, Wang LV, Achilefu S (2011) Noninvasive photoacoustic and fluorescence sentinel lymph node identification using dye-loaded perfluorocarbon nanoparticles. ACS Nano 5(1):173–182
20. Rapoport N, Nam KH, Gupta R, Gao Z, Mohan P, Payne A, Todd N, Liu X, Kim T, Shea J, Scaife C, Parker DL, Jeong EK, Kennedy AM (2011) Ultrasound-mediated tumor imaging and nanotherapy using drug loaded, block copolymer stabilized perfluorocarbon nanoemulsions. J Control Release 153(1):4–15
21. Soman NR, Lanza GM, Heuser JM, Schlesinger PH, Wickline SA (2008) Synthesis and characterization of stable fluorocarbon nanostructures as drug delivery vehicles for cytolytic peptides. Nano Lett 8(4):1131–1136
22. Soman NR, Baldwin SL, Hu G, Marsh JN, Lanza GM, Heuser JE, Arbeit JM, Wickline SA, Schlesinger PH (2009) Molecularly targeted nanocarriers deliver the cytolytic peptide melittin specifically to tumor cells in mice, reducing tumor growth. J Clin Invest 119(9): 2830–2842
23. Dewitte H, Geers B, Liang S, Himmelreich U, Demeester J, De Smedt SC, Lentacker I (2013) Design and evaluation of theranostic perfluorocarbon particles for simultaneous antigen-loading and (19)F-MRI tracking of dendritic cells. J Control Release 169(1-2): 141–149
24. Caruthers SD, Cyrus T, Winter PM, Wickline SA, Lanza GM (2009) Anti-angiogenic perfluorocarbon nanoparticles for diagnosis and treatment of atherosclerosis. Wiley Interdiscip Rev Nanomed Nanobiotechnol 1(3):311–323
25. Lanza GM, Yu X, Winter PM, Abendschein DR, Karukstis KK, Scott MJ, Chinen LK, Fuhrhop RW, Scherrer DE, Wickline SA (2002) Targeted antiproliferative drug delivery to vascular smooth muscle cells with a magnetic resonance imaging nanoparticle contrast agent: implications for rational therapy of restenosis. Circulation 106(22):2842–2847
26. Ravnikar M, Strukelj B, Obermajer N, Lunder M, Berlec A (2010) Engineered lactic acid bacterium Lactococcus lactis capable of binding antibodies and tumor necrosis factor alpha. Appl Environ Microbiol 76(20):6928–6932
27. Janjic JM, Berlec A, Bagia C, Liu LS, Jeric I, Gach M, Janjic BM, Strukelj B (2016) NIR and MR imaging supported hydrogel based delivery system for anti-TNF alpha probiotic therapy of IBD. SPIE BiOS, 972309–972309-10
28. Patel SK, Beano W, Anderson C, Janjic JM (2015) Theranostic nanoemulsions for macrophage COX-2 inhibition in a murine inflammation model. 160 (1): 59–70

Chapter 11

In Vivo Cell Tracking Using Two-Photon Microscopy

Daniela Malide

Abstract

Recently we have explored and developed approaches imaging using confocal/two-photon microscopy, which enables simultaneous high-resolution assessment of specifically fluorescently marked cells in conjunction with structural components of the tissues visualized via harmonic generated signals. This approach uses commercially available confocal and two-photon laser microscope and automated user-interactive image analysis methods based on commercially available software packages allowing easy implementation in usual microscopy facilities.

Key words Fluorescent proteins, Multiphoton microscopy, Adipose tissue, Lymph node, Cell tracking, Second harmonic generation, Third harmonic generation

1 Introduction

Fluorescent compounds and genetically encoded fluorescent proteins (FPs) have emerged as invaluable tools to mark cells and structures of interest providing contrast for confocal and two-photon microscopy imaging [1, 2]. Recent advances in the pulsed near-infrared lasers and microscope technological improvements have enabled the combination of fluorescence and nonlinear image contrast modalities in a single turnkey instrument. These have allowed combining the use for microscopy imaging, of second-order processes such as second harmonic generation (SHG) [3], third-order processes such as third-harmonic generation (THG), and two-photon excited fluorescence (TPEF) [4, 5]. In the last few years, we have explored these capabilities and developed approaches imaging using confocal/two-photon hybrid microscopy which enables simultaneous high-resolution assessment of specifically marked cells in conjunction with structural components of the tissues. Specifically, complementary information about the structure and function of the tissues and individual cells of live biological specimens can be monitored with high spatial resolution, over large areas, for extensive periods of time. To do this, we employed

Mingfeng Bai (ed.), *In Vivo Fluorescence Imaging: Methods and Protocols*, Methods in Molecular Biology, vol. 1444,
DOI 10.1007/978-1-4939-3721-9_11,

a series of strategies based on ex vivo fluorescent vital-dye labeling, transgenic mouse models expressing cytoplasmic EGFP, or DsRed, and marking hematopoietic progenitor and stem cells using cotransduction with lentiviral vectors encoding up to five fluorescent proteins [6–9]. As the lentiviral approach was covered extensively elsewhere [7, 8], we reviewed here the other approaches. We showed that this methodology facilitates cell tracking in various tissues including adipose tissue, bone marrow, spleen, thymus, lymph nodes, spleen, liver, lung, heart, skin, skeletal muscle, pancreas, and kidney as well. Moreover the 3D images can be assessed qualitatively and quantitatively to appreciate the distribution of cells with minimal perturbations of the tissues. The goal of this chapter is to provide investigators interested in tracking cells in various tissues with a set of basic protocols that will enable investigating cell fate in vivo. Finally these procedures can be easily adapted to imaging various tissues of interest for biologists.

2 Materials

2.1 Animals

Control C57Bl/6 mice, 6–12 weeks old, and EGFP and DsRed mice (Jackson Laboratories) were provided by Dr. Xingmin Feng (Hematology Branch, NHLBI). The B6/EGFP transgenic mice carry an enhanced green fluorescent protein (EGFP) cDNA under the control of a chicken β-actin promoter and a cytomegalovirus enhancer in all of the tissues, except for erythrocytes and hair and the DsRed mice express the red fluorescent protein variant DsRed. MST under the control of the chicken beta actin promoter coupled with the cytomegalovirus (CMV) immediate early enhancer for widespread fluorescent protein expression. All mice were housed and handled in accordance with the Guide for the Care and Use of Laboratory Animals of the National Institutes of Health, and enrolled in NHLBI Animal Care and Use Committee-approved protocols. Aplastic anemia mouse model was generated as previously described [10, 11]. Lineage $(Lin)^-$ stem cell antigen 1 $(SCA1)^+cKit^+$ cells (known as LSK cells) (an enriched population of hematopoietic stem cells (HSCs)) were obtained as previously described [12].

2.2 Reagents

1. Fluorescent dyes: LipidTOX Red, Cell Mask Deep Red, and Hoechst 33342 (Life Technologies, Grand Island, NY).
2. Phosphate-buffered saline (PBS): 210.0 mg/L KH_2PO_4, 9000 mg/L NaCl, 726.0 mg/L $Na_2HPO_4 -7H_2O$.

2.3 Equipment

1. 35 mm Culture dishes with number 0 cover glass bottom (MatTek Corporation, Ashland, MA) (*see* **Note 1**).
2. Glass cover slips, 12 mm diameter, #1 and #2 thickness (Corning, Corning, NY).

3. Surgical instruments: Operating scissors (11.5 cm straight); #7 curved-tip tweezers (one with blunt and one with sharper tips), 25 cm curved-tip forceps, microscissors, scalpel blades.
4. 50, 10 mL Conical tubes, 6-well plastic plates, 96-multi-well plates (Corning).
5. Microscopy: We perform microscopy imaging using an inverted Leica SP5 five-channel confocal and multiphoton system (Leica Microsystems, Mannheim, Germany) (Fig 1)

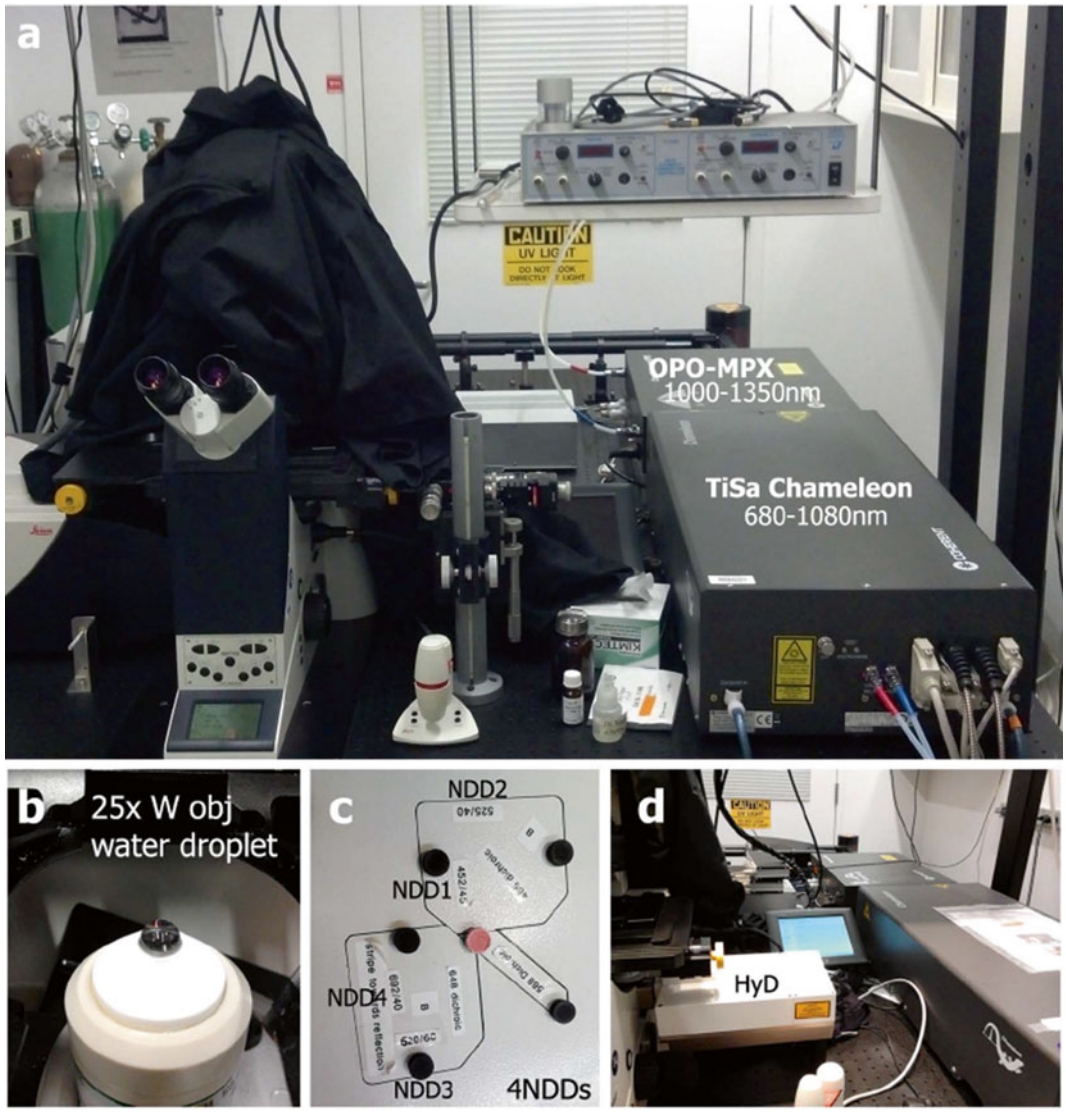

Fig. 1 General layout of the two-photon-OPO microscope system. Overall front view (**a**, top) and specific views (**b**–**d**) of major components referred in the text including the microscope, two-photon TiSa and OPO lasers, water dipping 25× objective, four non-descanned detector module (NDDs), and two-hybrid detector module (HyDs)

equipped with multi-line argon, diode 561 nm, HeNe 594 nm, and HeNe 633 nm visible lasers. We use in two-photon mode a pulsed femtosecond titanium:sapphire (Ti-Sa) laser (Chameleon Vision II, Coherent, Santa Clara, CA) tunable for excitation from 680 to 1080 nm with dispersion correction. We use in experiments involving red-shifted fluorescent dyes FPs (DsRed) and THG and an optical parametric oscillator (OPO) laser (Chameleon Compact OPO, or Chameleon MPX, Coherent, Glasgow, UK) to extend the output wavelength range as far as 1000–1300 nm, alone, sequentially, or simultaneously with the Ti-Sa laser (Fig. 1a).

Image various tissues using Leica HCX-IRAPO-L 25×/0.95 NA water dipping objective (WD = 2.5 mm) (Fig. 1b), or HC-PL-IRAPO 40×/1.1 NA water immersion objective (WD = 0.6 mm).

Separate fluorescence emission, in two-photon mode, by high-efficiency custom dichroic mirrors and collect with a fiber-coupled four-channel nondescanned (external) detector (NDDs) (Fig. 1c) as follows: a dichroic mirror at 568 nm followed by a dichroic mirror at 465 nm, followed by a 452/45 nm emission filter for SHG, or autofluorescence, and Cerulean or Hoechst with NDD1, or a 413/17 nm emission filter for THG with NDD1, a 525/40 nm emission filter for EGFP or Venus with NDD2, and a 648 nm dichroic mirror and 620/60 nm emission filter for tdTomato or mCherry with NDD3, and a 692/40 nm emission filter for Cell Mask Deep Red, or other far-red dyes with NDD4 [7, 8]. We use highly sensitive directly coupled 2-external hybrid detectors (HyDs) module with a 495 nm dichroic mirror and 405/10 nm, or 413/17 nm emission filters as an alternative option suitable for detecting generally weak (THG) signals (Fig. 1d).

Reveal structural information by two-photon microscopy intrinsic contrast imaging (as described above) of tissue autofluorescence from elastin, NADH (excited with 780 nm), second harmonic generated signal (SHG) from fibrillar collagen (excited with 1200, 920, or 860 nm), and third harmonic generated signals (THG) excited with 1200 or 1300 nm, collected in a back-scattered epi-direction.

For 3D volume rendering, collect series of x-y-z images (typically $1 \times 1 \times 4$ μm^3 voxel size) along the *z*-axis at 5 μm intervals over a range of depths (150–300 μm) throughout various tissues, over large regions using the tile function of the Leica LAS-AF software to automatically generate stitched volumes comprising an entire lymph node, approximately 2.5×1.2 mm^2 (*x*–*y*) and 300 μm (*z*). For 3D renderings and quantitative image analyses, we use Imaris v 7.7.2 software (Bitplane, Zurich, Switzerland). Other comparable imaging systems and software packages may be used.

3 Methods

The procedures described here have been developed to (1) visualize fluorescently labeled cells in intact tissues without sectioning and further processing [6, 13], (2) track fluorescently marked cells in various organs following injecting of the cells in various mouse disease models including aplastic anemia and bone marrow transplantations experiments [7, 8], and (3) complement the fluorescence with structural and cellular information via harmonic non-fluorescent imaging of murine organs [14]. We relied on the use of fluorescent proteins that were either genetically expressed in adult animals or introduced in specific cell populations via viral (lentiviruses) methods [6–8].

3.1 Two-Photon Microscopy of Whole-Mount Tissues Containing Cells Labeled with Vital Fluorescent Dyes

The procedures to obtain different organs from the mice for live imaging, including anesthesia/euthanasia and surgical procedures, have been extensively described elsewhere [7, 8]. We perform labeling of various tissues with vital dyes by bathing the whole or piece of the tissue in a solution containing the fluorescent dyes at the appropriate concentration. Here we are showing examples for visualization of the large lipid droplets of the adipose cells in the intact tissue (Fig. 2) and for visualization of plasma membrane outlining cells in the pancreas (Fig. 3). These procedures can be easily adapted to other tissues and other dyes.

1. Place a piece of freshly excised abdominal unfixed adipose tissue in the plastic cover of a 35 mm chamber containing a solution of LipidTOX Red for staining neutral lipids of the large adipose cells diluted 1:100 (from the stock solution) in PBS for 20–30 min at room temperature [13].
2. Wash with PBS 3 × 5 min and place the tissue in PBS in the 35 mm chamber for microscopy imaging right away using the 25× water dipping objective (*see* **Note 1**) and Fig. 1b. Place gently a cover slip #1 on top to weigh down and to avoid movement of the tissue.
3. In this example we imaged an experiment labeling adipose cells (LipidTOX Red) in a mouse ubiquitously expressing EGFP fluorescence, predominantly visible in the blood vessels throughout the adipose tissue (Fig. 2a). Use the TiSa laser tuned at 860 nm excitation and collect harmonic signals and emitted fluorescence with NDDs 1–3 as described in the previous section (Subheading 2.3, **item 5**): split emission first through a 568 nm dichroic mirror and then again through a 465 nm dichroic directing the SHG from collagen via 452/45 nm emission filter on NDD1 and the green (EGFP) fluorescence via 525/40 nm emission filter on NDD2. Separate emission in 568–648 nm range, directing red (LipidTOX Red) fluorescence via 620/60 nm emission filter on NDD3 (*see* **Note 2** and Fig. 1c).

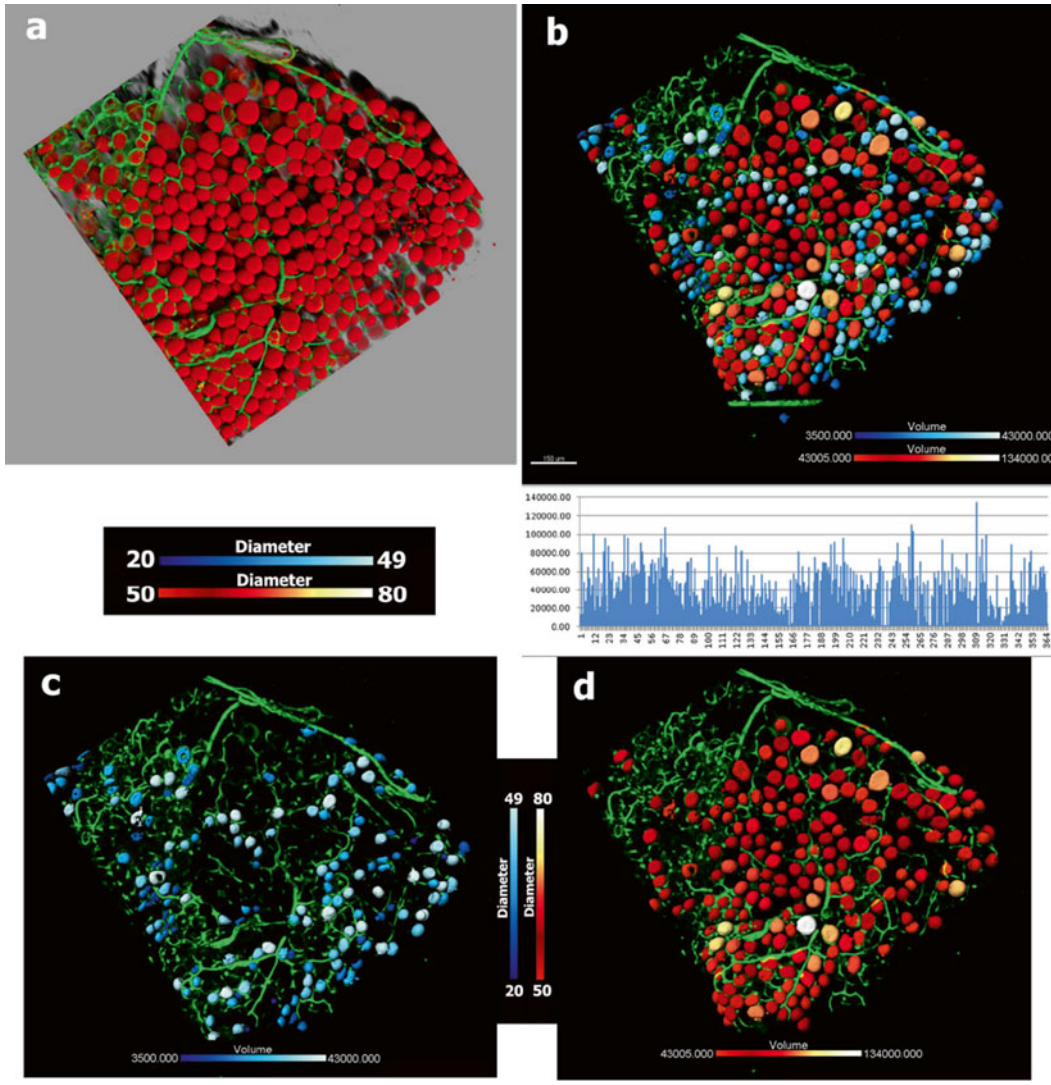

Fig. 2 3D architecture of adipose for tissue qualitative and quantitative analyses. (**a**) 3D volume rendering of TPEF (using Imaris shadow projection) reveals adipose cells (*red*, LipidTOX Red) and blood vessels (*green*, EGFP). (**b**) Quantitative analysis of adipose cell size (volume) in intact tissue. Color-mapped sizes are displayed using *blue* and *red hue* for cells with diameters <50 μm and >50 μm, respectively. Diameter scale *color bar* and a *histogram plot* of individual cell volume distribution are shown in the *middle row*. Size-based color-coded images extracted from TPEF images suggest that small (**c**) and large (**d**) adipose cells localize near and away from blood vasculature, respectively. Scale bar, 150 μm

4. Acquire tiled-*z*-stacks of images over large areas using the tile function of the Leica LAS-AF software for qualitatively and quantitatively accurate assessment. Approximately 200 images were computationally stitched to reconstruct ~1 mm^3 adipose tissue.

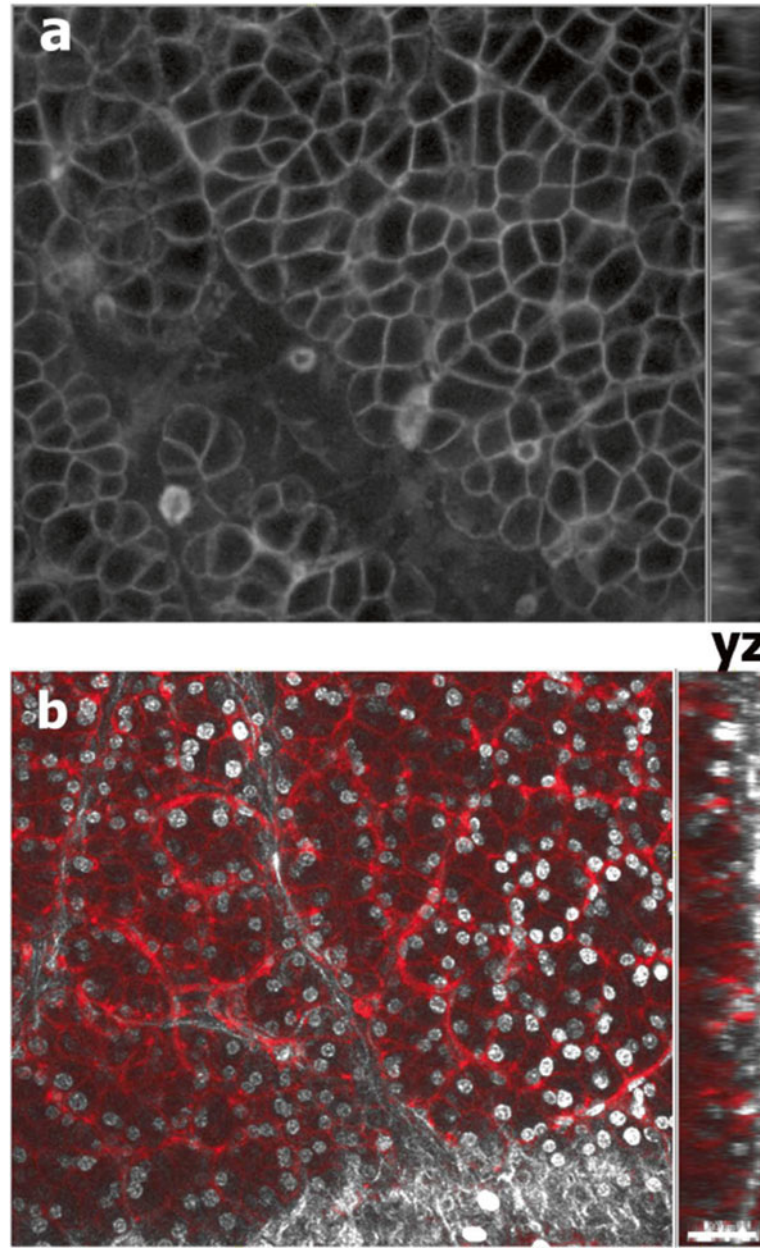

Fig. 3 (**a**) Pancreatic acinar cells outlined by plasma membrane labeling with Cell Mask Deep Red imaged with 1200 nm wavelength via the OPO. (**b**) Pancreatic acinar cells revealed by Cell Mask Deep Red (*red*) same as described in (**a**) with nuclei labeled by Hoechst (*white*) and collagen SHG (*white*). Scale bar, 30 μm

5. Import raw images in Imaris software and visually explore the data. From the TPEF create a 3D volume-rendered image (Fig. 2a) (with Surpass volume rendering as a shadow projection) illustrating the architecture of the adipose cells (red) and their relation with the blood vessels (green).

6. For quantitative analyses of the adipose cell sizes in intact tissue, use software (Imaris) automatic object surface segmentation, with user-enabled editing for accuracy, to individually separate the adipose cells. Thus obtain total number of cells, and their detailed statistics including individual cell volume (μm^3). Plot a cell volume distribution histogram and use a color-coded lookup table to extract a statistics-mapped (volume) color image (Fig. 2b–d). For convenient evaluations translate the volume data into diameter values (assuming spherical cell shapes). This analysis reveals two populations of adipose cells: one comprising smaller cells with diameters < 50 μm (displayed pseudo-colored in blue hues) and the other of cells larger than the average >50 μm (pseudo-colored in red hues) (Fig. 2b–d). Examine adipose cell size and relationship to blood vessels in intact tissue showing smaller cells near the blood vessels (Fig. 2c) outlining the periphery of clusters of internally located larger adipose cells (Fig. 2d).
7. Light scattering, autofluorescence, and absorption by tissue are reduced at longer wavelengths, driving the development of red dyes and red-shifted FPs for in vivo use [15, 16]. Two-photon excitation wavelengths of far red-emitting dyes lie beyond the range of typical TiSa lasers but can be generated by OPO lasers. As an example of a plasma membrane far-red staining, place a piece of freshly excised unfixed mouse pancreas in a solution of Cell Mask Deep Red (labeling plasma membrane) 1:500 from the 5 mg/ml stock, for 5–10 min at 37 °C, wash 3 × 5 min with PBS, place in 35 mm cover glass chamber, lay gently a cover slip #1, and image immediately (*see* **Note 3**). Use the OPO laser tuned at 1200 nm to excite far-red dye and detect far-red fluorescence via 692/40 nm emission filter with NDD4 (*see* **Notes 4**–7). Use optimally infrared-corrected 40× W objective (*see* **Note 8**), collect *z*-stacks of images, import them in Imaris software, and display the 3D rendering or xy, xz, yz orthogonal views (Fig. 3a). Use the sample just described to perform a double labeling to reveal also cell nuclei: incubate with Hoechst 33342 dilution 1:500 from the 10 mg/ml stock solution for 2–3 min at 37 °C. Use the same imaging setup as just described, i.e., OPO laser tuned at 1200 nm for Hoechst excitation, and collect emission in conjunction with collagen SHG with NDD1 via 413/17 nm emission filter (Fig. 3b) (*see* **Note 9**).

3.2 Two-Photon Microscopy of Whole-Mount Tissues Containing Cells Genetically Marked by Fluorescent Proteins

During our studies of hematopoiesis using cells marked by lentiviral encoded FPs and confocal and two-photon microscopy, we observed serendipitously that 1010 nm excitation wavelength is suitable for imaging combinations of up to three FPs (Cerulean, Venus, mCherry) (unpublished). This wavelength can be accomplished via TiSa laser or the OPO laser, providing ~640 mW and

1 W output peak power, respectively. Moreover, 1010 nm also allowed two-photon excitation of DAPI (Hoechst), EGFP, and DsRed. As an example, we illustrate detecting EGFP- and DsRed-marked cells together with collagen SHG in a popliteal lymph node from an aplastic anemia mouse model (Fig. 4).

1. Place a freshly excised popliteal lymph node in the 35 mm glass chamber in 50–100 μL PBS, and lay gently a cover slip on the top as described before.
2. Use 1010 nm wavelength either from the TiSa or the OPO lasers.
3. Image large regions using the tile and *z*-stack functions of the software, and computationally stitch the images as previously described, reconstructing the entire lymph node. Examine orthogonal *xy*, *xz*, *yz* views (Fig. 4a, b). Employing 1010 nm from the OPO, we observed higher efficiency in exciting red-shifted FPs, less harm, and deeper penetration of live tissue (*see* **Note 10**).

3.3 In Vivo Tracking of Label-Free Resident Cells in Murine Tissues via Third Harmonic Generation Microscopy (THG)

We developed and validated a methodology for high-resolution 3D harmonic imaging of intact murine tissues that requires no fluorescent labeling, based on epi- third harmonic generation (THG) imaging by pulsed near-infrared light in the 1200–1300 nm range available from the OPO. Visualizing THG in the epi- (back-scattered) direction enabled high-resolution depth-resolved imaging of whole-mount, intact tissues without the need for physical sectioning [14]. We illustrated intrinsic THG interface signals, outlining cell membranes and tissue inhomogeneities, revealing subcellular resolution of 3D architecture in various murine tissues and organs, including the subcutaneous and perivisceral white and brown adipose tissue, with clearly demarcated lipid droplets, blood vessels and cells, and myelinated peripheral nerves (Fig. 5).

1. For THG use sample illumination from the OPO laser tuned at 1200 or 1300 nm and collect emission at 1/3 of the incident wavelengths, 405/10 nm and 413/17 nm, respectively, using either NDD1 or directly epi-mounted 2-HyDs module (s*ee* **Note 11**).
2. Combine multiharmonic, THG and SHG images assessing qualitatively and quantitatively 3D distribution of the cells, blood vessels, peripheral nerves via THG, and collagen fibers via SHG, in label-free adipose tissue (Fig. 5a–c).
3. For multimodal imaging in adipose tissue combine sequentially OPO-excited THG signals (from multilocular lipid droplets of brown adipose cells) with OPO fluorescence-excitation by 1200 nm wavelength of red-shifted fluorescent proteins (DsRed) expressed in the blood vessels (Fig. 5d).

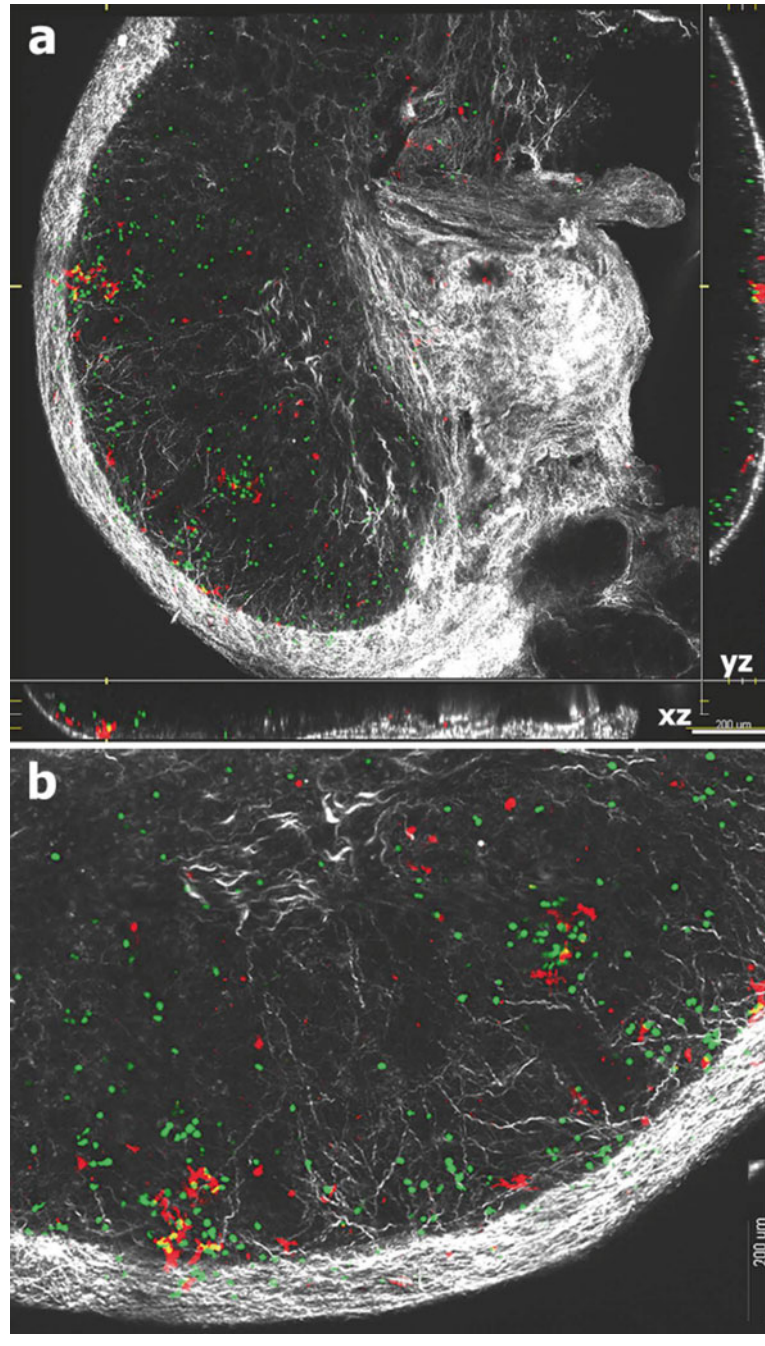

Fig. 4 Popliteal lymph node EGFP-regulatory T cells and DsRed-marked LSK cells imaged in conjunction with SHG of collagen fibers via the OPO laser excitation with 1010 nm; (**a**) *xy*, and *xz* and *yz* side views are shown. (**b**) Enlarged area of the lymph node shows better resolved clusters of interacting EGFP (*green*) and dsRed (*red*) cells along collagen fiber network. Scale bar, 200 μm

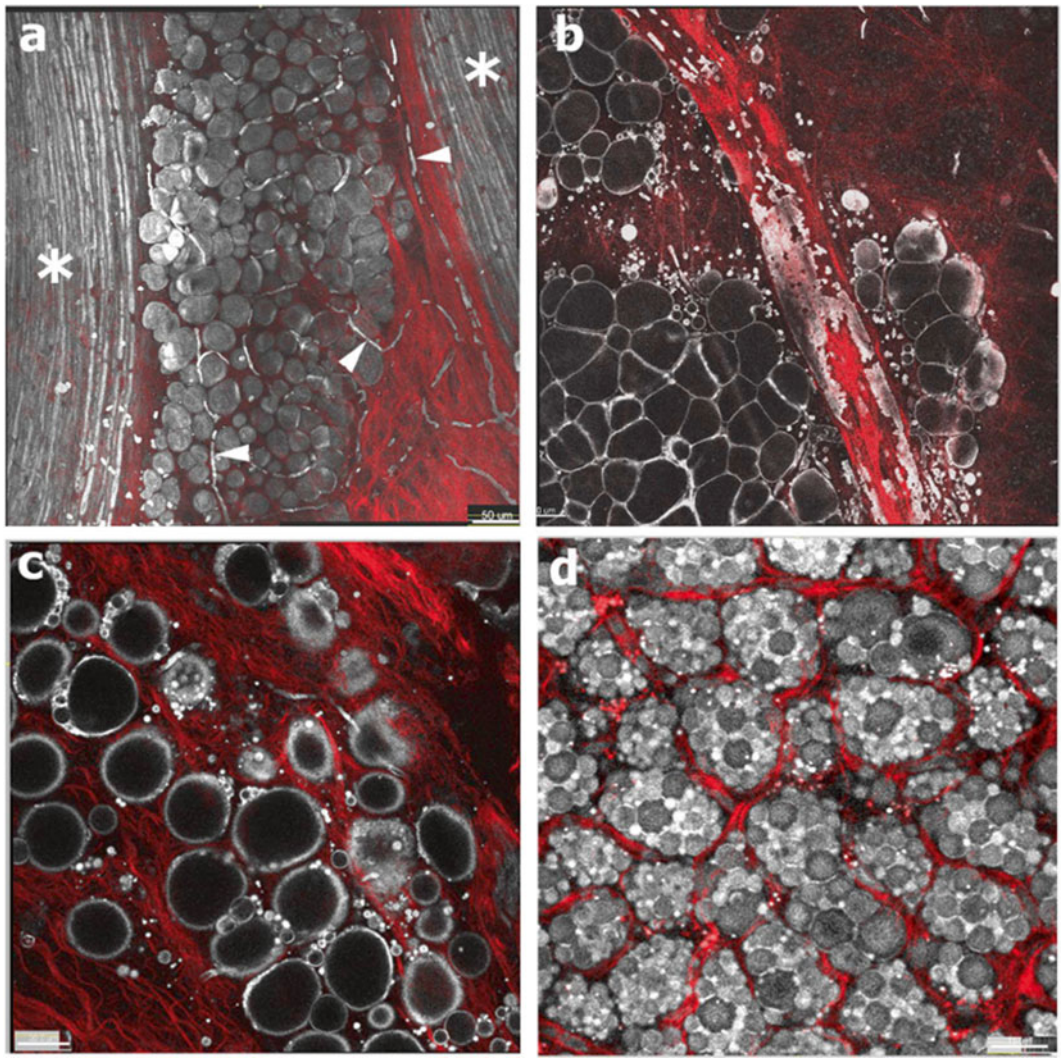

Fig. 5 THG imaging of adipose tissue. (**a**) THG (*white*) reveals white adipose cell boundaries, myelinated sheets of large peripheral nerves (indicated by *asterisk*), and discontinuous blood vessels (*arrowheads*) in conjunction with SHG (*red*) of collagen fibers imaged using NDD1-2. (**b**) THG (*white*) reveals white adipose cell outlines, large blood vessel with cells in the lumen; SHG (*red*) collagen layers of the vessel wall, and dispersed collagen fibers imaged using NDD1-2. (**c**) THG (*white*) demarcates clearly large white adipose cells imaged in conjunction with SHG (*red*) using two-channel HyD module. (**d**) THG (*white*) delineates each brown adipose cell with multiple round, grape-like, lipid droplets; individual cells are surrounded by blood vessels (*red*) in a mouse expressing dsRed in the blood vasculature; imaging using OPO 1200 nm excitation and two-channel HyDs detection. 3D reconstruction of *z*-stacks through the depth of intracapsular brown adipose tissue. Scale bars, 50 μm (**a**, **b**), 30 μm (**c**), and 15 μm (**d**), respectively

4 Notes

1. We recommend using no. 0 cover glass bottom chambers when imaging with the 25× water dipping objective. Practice is necessary to deposit a large (~30 μL) water droplet on the objective without spilling over (Fig. 1b). When focusing, bring gently the objective to the cover glass of the imaging chamber without squeezing the droplet. These conditions (no. 0 cover slip and the large water droplet) result in optimally focusing and obtaining high-contrast images throughout the depth of most tissues.
2. White adipose tissue is extremely fragile and cells can break easily in contact with glass surfaces. We recommend performing vital dye labeling procedures using plastic dishes; handle tissue extremely gently avoiding squeezing the lipid droplets and transfer tissue only for imaging without delay in the cover glass bottom chambers [13, 17]. Keep the liquid (PBS) around the tissue to a minimum (~50–100 μL) to avoid sample drying, and gently place a cover slip (use lighter weight #1) on the top to prevent adipose tissue tendency to float.
3. When using vital fluorescent dyes to label intact, unfixed organs and tissues, the optimal concentration and time need to be determined empirically. A good starting point is approximately five- to tenfold higher than the concentration recommended for labeling isolated or cultured cells.
4. Cell Mask vital dye-labeled tissues need to be imaged immediately to visualize plasma membrane effectively, as over time the dye disappears from the plasma membrane due to internalization.
5. When reagents are precious, it is advisable to perform labeling and washing steps in 96-well plastic plates to minimize agent volumes.
6. When imaging on external NDDs and particularly on HyDs, we drape black fabric around the microscope, thus avoiding external stray light leakage into the detectors.
7. A good alignment of TiSa and OPO lasers is essential for accurate imaging and a bead sample is necessary for periodically checking the lasers overlap, especially if the temperature fluctuates. To prevent undesirable effects of thermal drift we monitor the room temperature using a USB device in order to ensure that temperature is within specifications.
8. When imaging with the OPO, particular care should be given to use an objective that is corrected for transmission in the 1000–1300 nm range.

9. When imaging with TiSa or OPO, we use calibrated curves of pre-compensation (built into the software) to restore the pulse width at the sample. This results in increased excitation efficiency and tissue imaging depth (~30–40 % deeper).
10. Illuminating at 1010 nm enables excitation of three FPs (dyes) at once, allowing simultaneous tracking of three cell populations using only one laser and suitable detectors.
11. For generally weak THG signals, maximizing detection efficiency using directly coupled HyDs is critical in achieving acceptable signal-to-noise ratio in most samples.

Acknowledgements

This work was supported by intramural funding of the Division of Intramural Research, National Heart, Lung, and Blood Institute, NIH. We thank Dr. Xingmin Feng (Hematology Branch, NHLBI) for providing the mice, Dr. Christian A. Combs for the overall support of NHLBI light microscopy core facility, and Brent Nettrour, Peter Pecoraro, for the technical support of the microscope.

References

1. Livet J, Weissman TA, Kang H, Draft RW, Lu J, Bennis RA, Sanes JR, Lichtman JW (2007) Transgenic strategies for combinatorial expression of fluorescent proteins in the nervous system. Nature 450(7166):56–62
2. Snippert HJ, van der Flier LG, Sato T, van Es JH, van den Born M, Kroon-Veenboer C, Barker N, Klein AM, van Rheenen J, Simons BD, Clevers H (2010) Intestinal crypt homeostasis results from neutral competition between symmetrically dividing Lgr5 stem cells. Cell 143(1):134–144
3. Campagnola PJ, Millard AC, Terasaki M, Hoppe PE, Malone CJ, Mohler WA (2002) Three-dimensional high-resolution second-harmonic generation imaging of endogenous structural proteins in biological tissues. Biophys J 82(1 Pt 1):493–508
4. Friedl P, Wolf K, von Andrian UH, Harms G (2007) Biological second and third harmonic generation microscopy. Curr Protoc Cell Biol Chapter 4: Unit 4 15
5. Debarre D, Supatto W, Pena AM, Fabre A, Tordjmann T, Combettes L, Schanne-Klein MC, Beaurepaire E (2006) Imaging lipid bodies in cells and tissues using third-harmonic generation microscopy. Nat Methods 3(1):47–53
6. Takaku T, Malide D, Chen J, Calado RT, Kajigaya S, Young NS (2010) Hematopoiesis in 3 dimensions: human and murine bone marrow architecture visualized by confocal microscopy. Blood 116(15):e41–e55
7. Malide D, Metais JY, Dunbar CE (2014) In vivo clonal tracking of hematopoietic stem and progenitor cells marked by five fluorescent proteins using confocal and multiphoton microscopy. J Vis Exp 90:e51669
8. Malide D, Metais JY, Dunbar CE (2012) Dynamic clonal analysis of murine hematopoietic stem and progenitor cells marked by 5 fluorescent proteins using confocal and multiphoton microscopy. Blood 120(26): e105–e116
9. Weber K, Thomaschewski M, Warlich M, Volz T, Cornils K, Niebuhr B, Tager M, Lutgehetmann M, Pollok JM, Stocking C, Dandri M, Benten D, Fehse B (2011) RGB marking facilitates multicolor clonal cell tracking. Nat Med 17(4):504–509
10. Chen J, Brandt JS, Ellison FM, Calado RT, Young NS (2005) Defective stromal cell function in a mouse model of infusion-induced bone marrow failure. Exp Hematol 33(8): 901–908

11. Chen J, Ellison FM, Eckhaus MA, Smith AL, Keyvanfar K, Calado RT, Young NS (2007) Minor antigen h60-mediated aplastic anemia is ameliorated by immunosuppression and the infusion of regulatory T cells. J Immunol 178(7):4159–4168
12. Bloom ML, Wolk AG, Simon-Stoos KL, Bard JS, Chen J, Young NS (2004) A mouse model of lymphocyte infusion-induced bone marrow failure. Exp Hematol 32(12):1163–1172
13. Malide D (2008) Application of immunocytochemistry and immunofluorescence techniques to adipose tissue and cell cultures. Methods Mol Biol 456:285–297
14. Malide D (2014) In vivo tracking of label-free resident cells in murine tissues via third harmonic generation microscopy. Poster presented at the ASCB annual meeting. Philadelphia, PA
15. Miyawaki A, Shcherbakova DM, Verkhusha VV (2012) Red fluorescent proteins: chromophore formation and cellular applications. Curr Opin Struct Biol 22(5):679–688
16. Hense A, Nienhaus K, Nienhaus GU (2015) Exploring color tuning strategies in red fluorescent proteins. Photochem Photobiol Sci 14(2):200–212
17. Malide D (2001) Confocal microscopy of adipocytes. Methods Mol Biol 155:53–64

Chapter 12

Small-Animal Imaging Using Diffuse Fluorescence Tomography

Scott C. Davis and Kenneth M. Tichauer

Abstract

Diffuse fluorescence tomography (DFT) has been developed to image the spatial distribution of fluorescence-tagged tracers in living tissue. This capability facilitates the recovery of any number of functional parameters, including enzymatic activity, receptor density, blood flow, and gene expression. However, deploying DFT effectively is complex and often requires years of know-how, especially for newer mutlimodal systems that combine DFT with conventional imaging systems. In this chapter, we step through the process of using MRI-DFT imaging of a receptor-targeted tracer in small animals.

Key words Molecular imaging, Fluorescence, Cancer, Mutlimodal imaging, Anatomical priors, MRI, Diffuse optics, NIRFAST, Image reconstruction

1 Introduction

Diffuse fluorescence tomography (DFT) is a molecular imaging modality that leverages the principles of tissue optics to recover volumetric distributions of fluorescence activity in cm-scale tissue volumes. The DFT imaging protocol generally involves measuring light projections through tissue volumes, and then fitting the measured boundary data to the diffusion approximation of light propagation in tissue. While examples of DFT in humans have been reported [1], the modality is more commonly applied to small-animal imaging, primarily owing to the small tissue volumes and flexibility in choosing fluorescent tracers.

Compared to other molecular imaging modalities, such as single-photon emission tomography (SPECT) and positron emission tomography (PET), DFT generally benefits from higher signal-to-noise ratio characteristics and eliminates the need to handle radioactive tracers (the use of which presents safety concerns as well as signal loss over time). Importantly, DFT also enables simultaneous imaging of multiple tracers, which can be leveraged

Mingfeng Bai (ed.), *In Vivo Fluorescence Imaging: Methods and Protocols*, Methods in Molecular Biology, vol. 1444,
DOI 10.1007/978-1-4939-3721-9_12,

to reveal additional functional information about tissue status. While these benefits represent important advantages for DFT technology, the major challenge for the modality is photon scatter in tissue, which impacts image resolution, contrast recovery, and the ability to provide quantitative information. Recent comprehensive classifications of the optical properties of different tissues and organs can certainly help improve the accuracy of DFT image reconstruction [2]; however, even with exact knowledge of the tissue optical properties, the ill-conditioned and often underdetermined nature of the DFT reconstruction problem still limit spatial resolution [3].

To help address these challenges, much of the field has moved towards developing dual-modality systems which couple MRI/CT/ultrasound scanners with DFT instruments [4–14]. Data from the two systems can be merged in a number of ways, including incorporating the conventional modality images into the image reconstruction algorithms, to help reduce the DFT parameter space and improve imaging accuracy. While CT-coupled DFT systems offer high-resolution anatomical templates for DFT reconstruction and interpretation, small-animal CT is notorious for insensitivity to tumors, even with high-dose CT-contrast. MRI-based hybrid systems, on the other hand, are more difficult to implement; however, they are well suited for DFT studies in tumor due to the high soft-tissue contrast and ability to image MRI contrast agents, such as Gd-DTPA [5]. Identifying tumor tissue with Gd-MR images allows the optical data to be used to quantify functional parameters (such as receptor activity).

A less investigated limitation of molecular imaging approaches in general is the variability in the relationship between molecular-targeted tracer distribution and the biological distribution of the molecule being targeted [15]. The ability of DFT to image multiple tracers simultaneously can be used to account for nonspecific uptake and this is a clear advantage that other small-animal molecular imaging modalities cannot easily replicate. In this implementation, multiple tracers can be discriminated based on spectral differences in the light absorption and fluorescence properties of different commercially available fluorophores. Such multiplexing can be used to administer an untargeted tracer, in concert with a targeted tracer, to account for nonspecific effects [16–18].

Considering the numerous idiosyncrasies of DFT data collection and image reconstruction, care is required in all facets of the DFT process. Thus, we present the following illustrative example of a typical imaging protocol used in our lab for MRI-DFT of a glioblastoma model in athymic mice. The guidance provided herein can be adapted to other tumor models provided that appropriate expertise in the specific model is available.

2 Materials

2.1 MRI-DFT Imaging system

The imaging system consists of a diffuse fluorescence tomography instrument coupled to a clinical MRI scanner (Philips 3 T Achieva). This system has been detailed extensively in the literature [19–21], and is briefly described here. The optical detection subsystem consists of 16 Acton Research Insight spectrometers (though only 8 are used for small-animal studies), each with a Pixis CCD cooled to –70 °C. Each spectrograph contains a motorized turret with two gratings: a 1200 and 300 lp/mm, the latter of which is used most frequently. Light is coupled from the tissue in the bore of the magnet to the optical instruments via 13 m long bifurcated fiber bundles that pass through wall ports. The source branch of each fiber consists of a single 400 μm fiber that couples to a motorized rotating stage aligning a source fiber from the excitation laser to each fiber channel sequentially. While the fiber channel under illumination is not used for detection, light transmitted through the tissue is coupled to the remaining fiber channels. The detection branch of the bundles contains six 400 μm fibers that surround the source fiber. On the spectrometer end, these six fibers are arranged in a line to align with the slit. Before entering the spectrograph, light passes through custom-designed entrance optics units in which the light is collimated, passes through a motorized filter wheel, and is focused on the spectrograph slit. As with any spectrometer, care must be taken to align and focus the image of the fiber onto the sensor before use, which can be achieved by manipulating the focusing optics and fiber position while running the sensor in focus mode. This must be repeated for all detection channels. Note that slits are generally kept open for fluorescence imaging to increase light collection.

The animal interface consists of a rodent coil modified to accommodate the optical fibers in a circular array surrounding the tissue. Fiber terminals that contact the tissue in the MRI bore need to be nonmagnetic and therefore are made of black Delrin. A black Delrin cylindrical insert with a mouse bed fits concentrically in the coil and is designed to position the mouse head near the radial center of the coil. Finally, a custom-designed sliding bite-bar system allows the animal's teeth to be attached to the bar and the animal pulled into the cylinder for positioning, as seen in Fig. 1.

2.2 Reagents

1. IRDye 800CW-EGF (LI-COR Biosciences, Lincoln, NE): Epidermal growth factor (EGF) labeled with a fluorescent tracer having a maximum light absorption around 775 nm and maximum fluorescence emission around 800 nm.
2. Alexa Fluor 750 (Life Technologies): An "untargeted" fluorescent tracer with maximum light absorption around 750 nm and maximum fluorescence emission around 775 nm.
3. Gadolinium diethylene triamine pentaacetic acid (Gd-DTPA): Standard clinical Gd preparation such as Magnevist or Omniscan.

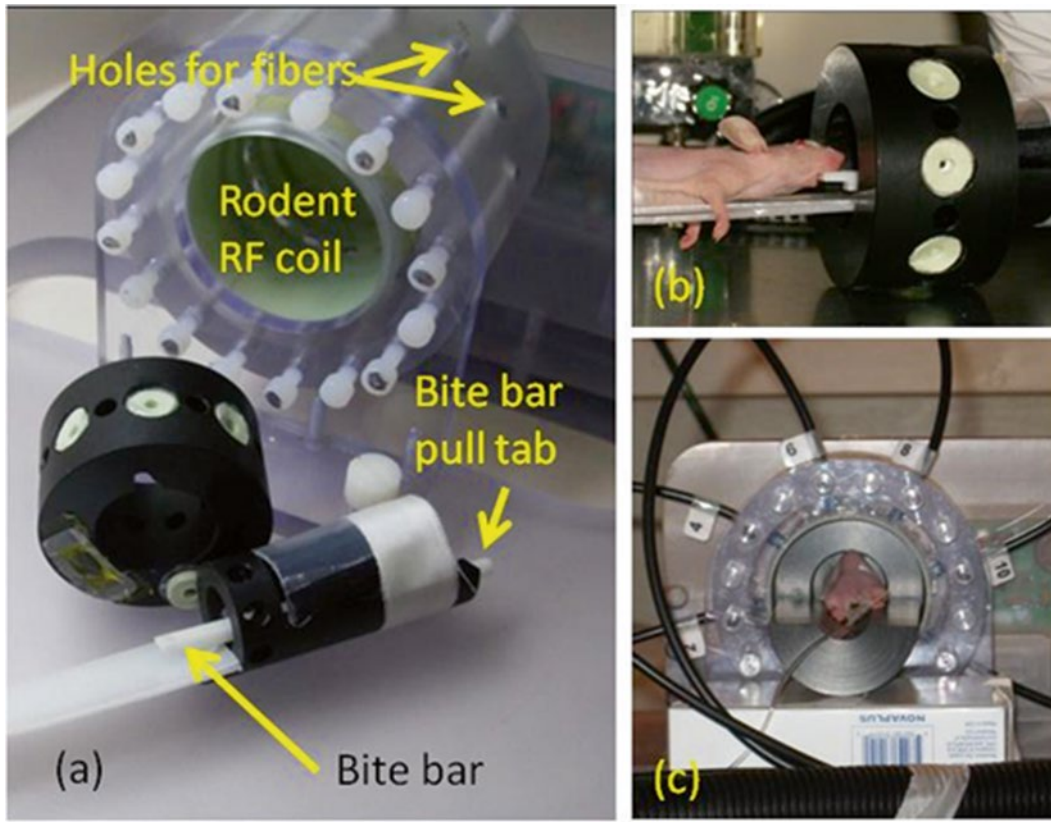

Fig. 1 MRI-DFT animal interface. (**a**) Rodent RF coil with holes drilled to accommodate optical fibers. The black Delrin cylinders position the mouse inside the coil. The larger Delrin cylinder holds MRI fiducial markers (*toroidal shaped* markers). The bite-bar mouse positioning system is also shown in (**a**) and holding a mouse in (**b**). A nose cone for isoflurane/oxygen gas (not shown) attaches to the pull-tab side of the unit. (**c**) Panel (**c**) reproduced from Acad. Rad. 2010 with permission from Elsevier [25]. A mouse positioned in the coil on the MRI scanner bed with fibers placed in contact with the head

2.3 Software

1. NIRFAST: Before beginning, be sure to download and install NIRFAST (www.nirfast.org; also download NirView), an open-source software package for multimodal diffuse optical imaging distributed for free by the Optics in Medicine lab at Dartmouth College.
2. MATLAB (Mathworks, Natick, MA).

3 Methods

3.1 Animal Preparation

1. Isolate 1×10^6 U-251 human glioblastoma cells (Sigma-Aldrich, St. Louis, MO) and mix with 5 μL of phosphate buffer solution to prepare for cell implantation into left cerebrum of athymic mice by stereotactic frame [22]. After tumor cells have been implanted, switch the animal to a non-chlorophyll

diet to reduce the normally high autofluorescence found in immunocompromised mice.

2. Two days before MRI-DFT imaging, acquire gadolinium-enhanced MRI images to confirm the presence of visible tumors in the brain.
3. The choice of a time delay between administering the fluorescent tracer and imaging depends on many factors, including the intended target, type of tracer, disease type, and whether tracer kinetics are important for the study. In some cases, the tracer is administered days prior to imaging to allow the unbound probe to clear while in others imaging is performed dynamically immediately after administration. For this example protocol, assume administration of 1 nmol Li-COR IRDye800CW-EGF 48 h prior to imaging. This must be done in the tail vein, and a skilled animal researcher will know whether the injection is successful by "feel." If the vein is missed, that animal is not used in the rest of the study.

3.2 MRI-DFT Imaging Protocol (48 h After Injection as Per Above)

3.2.1 Positioning and System Calibration

1. Set up optically-coupled small-animal imaging coil on the MRI scanner bed. Insert fibers in marked positions. Replace all fiducial markers that may have dried out. These will be used to identify fiber positions in the MR images. Initialize the optical imaging system and turn on excitation laser. Check the power output of the laser.
2. Prepare a syringe connected to a short catheter tube with a butterfly needle containing several milliliters of clinical Gd-DTPA solution. Anesthetize animal with constant-flow isoflurane. Once asleep, insert needle intraperitoneally and tape in place. Do not administer Gd at this point.
3. Position animal in the MRI-DFT array on the scanner's bed, ensuring that the Gd-syringe lies outside the coil and thus is accessible after the animal has been moved into the bore. Ensure that isoflurane/oxygen flows through the interface to keep the animal asleep. Use best estimates to align the fiber plane to cross the tumor location (usually just anterior of the ears). Push the fibers in to contact the head of the mouse using light-to-moderate compression.
4. Align coil with bore per standard MR protocol and move subject into the bore.
5. Acquire a scout image series and locate the mouse brain and fiducial markers. Change MR slice orientation and position such that slices are parallel and aligned with the plane of the fibers (*see* **Note 1**). Confirm whether the fiber plane intersects the tumor (*see* **Note 2**). If the mouse is not positioned properly, repeat **steps 3–5**.

3.2.2 Imaging

1. Once the animal is positioned properly, acquire a full series of T1-weighted MR images. These are pre-Gd contrast images.
2. Enter the MRI room and without moving the animal find the Gd-loaded syringe and administer 0.03 mL. Leave the room and turn off all lights. Black out windows if necessary.
3. Start the optical acquisition. This process illuminates each optical fiber and measures the transmitted light at all other positions. For an array of eight optical fibers, 56 projections are used. The system acquires all fluorescence measurements (filtered) and then a corresponding set of excitation measurements.
4. While the system is acquiring optical data, the remainder of the MR sequence can be completed. This includes another T1-weighted series (post Gd-contrast) and a T2-weighted series (*see* **Note 3**).
5. Imaging for this subject is complete once both systems have finished.

3.3 MRI and Optical Data Processing

The image protocol produces two main data streams: (a) MR image stacks and (b) optical spectra of tracer fluorescence emission and corresponding excitation source spectra for 56 projections. The objective is to merge these data sets and recover images of fluorescence yield (product of the quantum yield and the absorption coefficient of the fluorophore at the excitation wavelength) in the tissue volume. Initially, MRI and optical data are processed separately and merged in the reconstruction steps.

3.3.1 MRI Image Processing

The objective of the MRI image processing step is twofold: to produce a finite element method (FEM) mesh of the tissue volume containing regions tagged based on tissue type, and to locate the positions of the optical fibers on the FEM mesh to serve as sources and detectors in the image reconstruction algorithm. Historically, we have used only the T1-weighted post-Gd contrast image series for MRI-DFT image reconstruction in this animal model. Begin by importing this image series in NirView.

1. Using the segmentation (threshold, dilation, and erosion) and manual paintbrush tools, segment the tissue into three regions: brain, tumor tissue (based on Gd-contrast), and the rest of the head. An example is shown in Fig. 2 (c) (*see* **Notes 4–7**).
2. Now use the fiducial markers in the image to triangulate the contact points of the optical fibers on the tissue (*see* **Note 8**).
3. Save the NirView session before proceeding. You may also save an "*.mha" file under File > Save Volume which can be used to display MRI-DFT image overlays once reconstruction has completed.

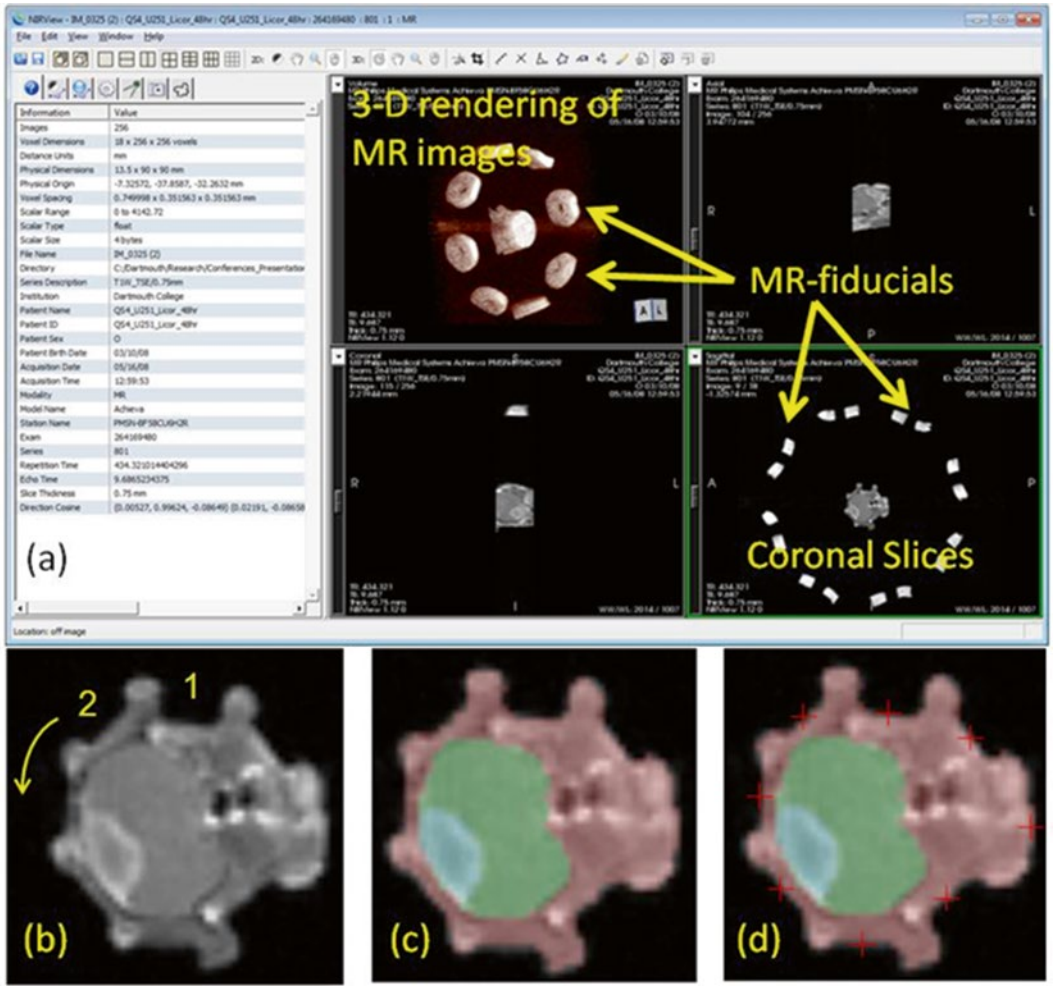

Fig. 2 Processing MRI data for MRI-DFT. (**a**) The NirView interface showing a T1-weighted Gd-enhanced image stack just after it has been imported. *Axial*, *sagittal*, and *coronal* views are presented, as well as a 3-D rendering based on intensity values. It is easiest to process images in the coronal plane. (**b**) A zoomed-in view of a coronal slice showing indents where the fibers contacted the tissue. The user must keep track of the order of the fiber channels. (**c**) Semi-opaque overlay of a segmentation mask (aka "label map") after the images were segmented into three tissue regions (*cyan* = tumor, *green* = brain, and *red* = the rest of the tissue). (**d**) Same as (**c**) with markers added to mark fiber positions. Ensure that markers are added in the order corresponding to the fiber channel numbers (i.e., first marker corresponds to fiber 1, second to fiber 2)

4. Select File > Create Mesh. This will launch a Matlab window to generate a 3-D FEM mesh compatible with the optical image reconstruction algorithms. Change the NIRFAST mesh type field to "Fluorescence" (*see* **Note 9**).
5. A volumetric mesh should be displayed with a window asking the user to place sources and detectors. These coordinates should already be populated. NIRFAST automatically moves

sources one scatter distance inside the tissue surface and detectors position just inside the surface based on surface normals (*see* **Note 10**).

6. Once the mesh has been finalized and saved, assign optical properties to each region (*see* **Note 11**).

3.3.2 Optical Data Processing

Optical spectra need to be processed and calibrated for use in the image reconstruction algorithms. For each spectrum measured (56 fluorescence and 56 excitation measurements), the following procedures are followed.

1. Subtract dark noise baseline offset of CCD or CMOS sensors (*see* **Note 12** for suggested methods of acquisition). However it is obtained, subtract the background offset from each of the 112 (56 fluorescence and 56 excitation measurements) spectra.
2. Correct for exposure time to obtain counts/s.
3. Correct for inter-system variance using correction factors measured a priori as a calibration standard.
4. For fluorescence spectra only: To decouple the LICOR tracer fluorescence signal from contaminating background autofluorescence, a linear least squares spectral fitting algorithm is used, as reported previously [19, 23]. For single-tracer imaging, we use two basis spectra—one for background autofluorescence acquired either on an animal without tracer injected or a tissue phantom, and the pure tracer fluorescence which is recorded using a liquid phantom with 1 % intralipid and a high concentration of fluorophore. These two basis spectra should be acquired for each spectrometer and can be used for all animals using this tracer. An example of the spectral fitting process for a single projection is shown in Fig. 3.
5. Once the tracer-specific fluorescence shape has been extracted from the spectra, the shape is integrated to provide a single measure of fluorescence intensity for each projection.
6. Calibrated excitation peaks are also integrated.

3.4 Combining Data to Reconstruct MRI-DFT Images

The procedures described above have produced the following: a volumetric FEM mesh model of the animal's head with tagged tissue regions and source-detector positions, 56 fluorescence intensity measurements from the optical projections through the head, and 56 corresponding excitation intensity measurements. The optical data should be saved as columns in a NIRFAST-compatible data file ("*.paa") as described in the NIRFAST documentation. The NIRFAST software package contains light propagation models that allow data to be processed into images of optical parameters (such as fluorescence yield).

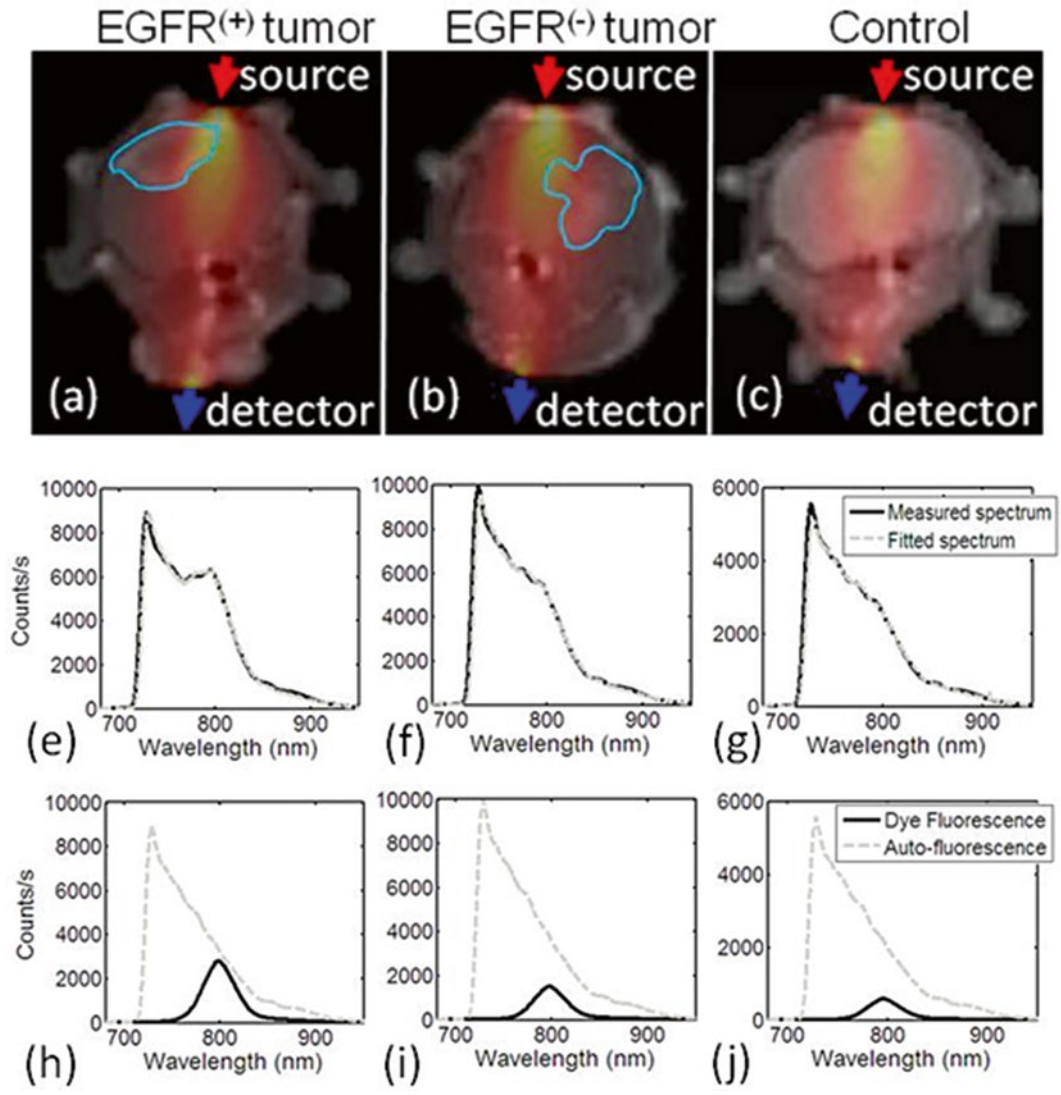

Fig. 3 Raw optical spectra measured with the MRI-FMT are pre-processed using a simple spectral fitting algorithm. Examples of measured fluorescence spectra are shown in (**d**) through (**f**) for U251, 9 L and control mice, respectively. These spectra correspond to a signal detection channel directly opposite to a source at the top of the head, as shown in (**a**) through (**c**). For illustrative purposes, the sensitivity values between the source and detector are plotted on the corresponding MR images and an outline of the tumor region as defined by the gadolinium contrast enhancement is included to demonstrate the extent to which the tumor lies in the sensitivity field. Pre-recorded spectra of the fluorescent probe and tissue autofluorescence from mice are used to decouple the signals originating from tissue autofluorescence and the optical probe itself. The results of this process are shown in (**g**) through (**i**) and the fitted spectra are compared to the measured spectra in (**d**) through (**f**). Figure and caption reproduced from JBO 2010 with permission from Society of Photo Optical Instrumentation Engineers [23]

3.4.1 Data Calibration

Before images are recovered, the data need to be further calibrated and scaled to the numerical model in NIRFAST. This program calibrates the fluorescence data to the model by calculating a modeled excitation field based on the optical properties provided, and then calculating:

$$I_{calibratedfluorescence} = I_{measuredfluorescence}(I_{modelexcitation}/I_{measuredexcitation})$$

Once calibrated, the program then performs a homogenous fit to estimate the value of fluorescence yield that best fits the data assuming that the fluorescence intensity in the volume is homogeneous. The following information is called on by the fluorescence calibration script:

In NIRFAST, select Data > Calibrate > Fluorescence. Input the following:

1. Input Mesh: The mesh created in Subheading 3.3.1, **step 4**.
2. Data: Excitation and fluorescence emission data saved in one file as per above.
3. Save Data To (Optional): Using this field is recommended to save a fully calibrated version of the data, which will be only fluorescence emission data (since excitation data are used in the calibration).
4. Save Mesh To (Optional): Using this field is recommended as this will be the mesh input in the reconstruction program. It contains the results of the homogeneous fitting routine and is also termed as the "Initial guess mesh."

3.4.2 Reconstruct Images

The fluorescence reconstruction algorithm in NIRFAST uses the mesh and calibrated data to recover images of fluorescence yield in the tissue volume. This is done by adjusting the fluorescence yield throughout the volume to best fit the calculated light fields (diffusion-based modeling) to match the calibrated measured data on the surface (projection data).

In NIRFAST, select Reconstruct > Fluorescence. Input the following:

1. Input Mesh: The "Initial guess mesh."
2. Input Data: The fully calibrated data from above.
3. Save Solution To: Enter a file name (no extension) for the solution files that will be saved during reconstruction.
4. Prior information: There are several options for enforcing the boundaries of the internal tissue types (encoded in the mesh) in the image reconstruction process (*see* **Note 13**).
5. Initial Regularization: The choice of regularization is often system and case specific and is often chosen based on extensive phantom studies (*see* **Note 14**).
6. Use defaults for all the other parameters.

7. Run the reconstruction program, which may take several minutes for this 3-D mesh. Expect between 15 and 40 iterations before convergence (defined as a 2% or less change in the L2 norm error between iterations).

3.4.3 Visualization and Image Processing

1. Once reconstructed, volume rendered and 3-axis slices of the results may be viewed by selecting Solution > View Solution in NIRFAST and browsing to the solution files (as well as the mesh).
2. Once loaded, use the drop-down menu in the viewer window to select the parameter to view—be sure to select "etamuaf" as this is the only parameter that was reconstructed—the rest were pulled from the mesh itself.
3. To view the solution overlaid on the MRI, select File > Open Dicoms and browse to the "*.mha" file you saved during image segmentation in NirView. Use Thresholding to view co-registered fused MRI and DFT images.
4. "Read Solution" also loads the recovered fluorescence yield (etamuaf) values into the Matlab workspace. These values can be used for statistical analysis, assessment of diagnostic performance, etc.

3.5 Advanced MRI-DFT Imaging Techniques

An advanced implementation of MRI-DFT introduces dynamic multi-tracer imaging to the experimental protocol. This approach provides a rich data set, which can be leveraged to extract additional, and more quantitative, information about tissue status.

In this example, the quantitative value of cell surface receptor molecular imaging in DFT can be enhanced by so-called dual-tracer or paired-label kinetic modeling strategies [18], which account for delivery variability and nonspecific binding and retention of a targeted tracer using the uptake dynamics of a second "untargeted" tracer. Adoption of these approaches to DFT is described below [22]:

1. Inject an equimolar concentration of an untargeted fluorescence tracer along with the targeted imaging tracer. The fluorescence emitted from the untargeted tracer must be distinguishable from the targeted so that the respective signals can be separated prior to data analysis. Here, Alexa Fluor 750 is proposed as an untargeted imaging tracer pair for IRDye-800CW-EGF. The two molecules absorb and emit light at similar wavelengths allowing a single laser to be used to excite them both; yet the emission spectra are different enough to allow spectral decomposition approaches to separate the signals (*see* **Note 15**).
2. Selection of a suitable untargeted tracer partner for the targeted tracer is critical (*see* **Note 16**).

3. Upon injection of the two tracers, dynamic DFT imaging is carried out with the aim of acquiring full projection data sets at least every 2 min, up to 60 min, to describe the temporal dynamics of imaging tracer uptake and binding.
4. If the emission spectra of the two tracers are collected spectroscopically, spectral decomposition can be applied by least square optimization to separate the imaging tracer signals from each other and from background autofluorescence.
5. Using the principles described previously, concentration maps of each tracer in brain, tumor, and non-brain can then be reconstructed at each frame of the serial imaging protocol.
6. Average targeted receptor concentrations can then be calculated in each region of interest by using the dual-tracer kinetic model (Eq. 1) [18, 22], which allows the binding potential (*BP*), a parameter proportional to receptor concentration, to be estimated:

$$F_{\mathrm{T}}(r,t) = R_1 F_{\mathrm{UT}}(r,t) + \left(k_2 - \frac{R_1 k_2}{1+BP}\right) F_{\mathrm{UT}}(r,t) * e^{-\frac{k_2 t}{1+BP}}, \qquad (1)$$

where F_{T} and F_{UT} represent the fluorescence activity of the targeted and untargeted tracers, respectively, at region, r, and time, t. R_1 represents the ratio of blood to tissue extraction efficiencies of the two tracers, k_2 represents the rate constant governing tissue to blood efflux, and * is the convolution operator.

4 Notes

1. We typically acquire between 20 and 30 coronal slices at 0.75 mm/slice to cover the head from the nose to behind the ears.
2. It may be necessary to acquire a few T1-weighted slices to confirm.
3. We suggest waiting for about 5 min after administering Gd before acquiring the follow-up T1-weighted images.
4. The segmentation mask should be continuous in all dimensions (no "islands" outside the tissue region due to image artifacts or fiducial markers; cropping can help with this, as can the paintbrush-erase function).
5. It is important to fill in any "holes" in the segmentation mask.
6. Small complex shapes on the boundary (such as the ears) should be smoothed or removed as this will add unnecessary complexity to the mesh.
7. Manually check each slice to ensure that it is smooth with no holes before proceeding.

8. In many cases, an indent caused by each fiber is visible in the images, making locating fibers straightforward; however, the proper orientation and registration with each physical channel must be worked out by the user. In our protocol, we use the "marker/seed" tool in NirView to mark the positions of the fibers in ascending order. In other words, the first fiber marked in NirView corresponds to fiber 1, the second marker corresponds to fiber 2, etc., for a total of eight markers. These markers should be just on the surface of the tissue, as shown in Fig. 2d.
9. The "Size" field under "Surface Facet Settings" may also be adjusted to change the average size of elements (aim for just under 1 mm). We generally aim for a mesh in the 10,000–20,000 node range, and facet size may need to be adjusted to achieve this. All other input fields can be left as default.
10. For small, complex shapes, it is often advisable to write a script to do this in a more controlled manner (based on absolute directions vs. surface normals). These scripts can be added as plug-ins, which appear in the "Create Source Detectors from Fiducials" field.
11. As reported previously [23], we have used the following values estimated from reports in the literature [24]: the brain and suspected tumor regions $ax = 0.03\ \mathrm{mm}^{-1}$, $sx' = 2.25\ \mathrm{mm}^{-1}$ at the excitation wavelength and $am = 0.03\ \mathrm{mm}^{-1}$, $sm' = 2.75\ \mathrm{mm}^{-1}$ at the emission wavelength. All other tissue types were assumed homogenous and assigned ax, $m = 0.01\ \mathrm{mm}^{-1}$ and sx, $m' = 1\ \mathrm{mm}^{-1}$ at the exciting and emitting wavelengths.
12. This can be measured a priori or between measurements. Alternatively, a fully filtered dark region of the spectrum can be used to estimate the offset across the whole spectrum.
13. We typically use the "hard priors" implementation, which assumes that each tissue region has homogeneous fluorophore distribution. Thus, the reconstruction process becomes a three-parameter problem.
14. For consistency, this value should be kept the same for all subjects if running an animal study. Much of the data we have reported used a value of 10 (default).
15. By employing a single-laser excitation with spectral decomposition of the emission spectra, the tissue optical property differences experienced by the signals from each tracer are kept to a minimum, allowing a single light-propagation model to be employed for both tracers in the image reconstruction.
16. Suitability entails that the blood plasma kinetics of the two tracers are roughly equivalent, the vascular permeability of the two tracers is similar, and nonspecific binding of the tracers is similar and preferably negligible.

Acknowledgment

This work was funded by National Institutes of Health Grants R01CA184354, R01CA109558, R01CA156177, and U54CA151662 as well as Department of Defense Award W81XWH-09-1-0661.

References

1. Corlu A, Choe R, Durduran T, Rosen MA, Schweiger M, Arridge SR, Schnall MD, Yodh AG (2007) Three-dimensional in vivo fluorescence diffuse optical tomography of breast cancer in humans. Opt Express 15(11):6696–6716
2. Jacques SL (2013) Optical properties of biological tissues: a review. Phys Med Biol 58(11): R37–R61. doi:10.1088/0031-9155/58/11/R37
3. Ntziachristos V, Ripoll J, Wang LV, Weissleder R (2005) Looking and listening to light: the evolution of whole-body photonic imaging. Nat Biotechnol 23(3):313–320. doi:10.1038/nbt1074
4. Da Silva A, Leabad M, Driol C, Bordy T, Debourdeau M, Dinten JM, Peltie P, Rizo P (2009) Optical calibration protocol for an x-ray and optical multimodality tomography system dedicated to small-animal examination. Appl Opt 48(10):D151–D162. doi:10.1364/Ao.48.00d151
5. Davis SC, Pogue BW, Springett R, Leussler C, Mazurkewitz P, Tuttle SB, Gibbs-Strauss SL, Jiang SS, Dehghani H, Paulsen KD (2008) Magnetic resonance-coupled fluorescence tomography scanner for molecular imaging of tissue. Rev Sci Instrum 79(6), doi: 10.1063/1.2919131; Artn 064302
6. Gruber JD, Paliwal A, Krishnaswamy V, Ghadyani H, Jermyn M, O'Hara JA, Davis SC, Kerley-Hamilton JS, Shworak NW, Maytin EV, Hasan T, Pogue BW (2010) System development for high frequency ultrasound-guided fluorescence quantification of skin layers. J Biomed Opt 15(2), doi: 10.1117/1.3374040; Artn 026028
7. Guo X, Liu X, Wang X, Tian F, Liu F, Zhang B, Hu G, Bai J (2010) A combined fluorescence and microcomputed tomography system for small animal imaging. IEEE Trans Biomed Eng 57(12):2876–2883. doi:10.1109/TBME.2010.2073468
8. Kepshire D, Mincu N, Hutchins M, Gruber J, Dehghani H, Hypnarowski J, Leblond F, Khayat M, Pogue BW (2009) A microcomputed tomography guided fluorescence tomography system for small animal molecular imaging. Rev Sci Instrum 80(4), doi: 10.1063/1.3109903; Artn 043701
9. Lin Y, Barber WC, Iwanczyk JS, Roeck W, Nalcioglu O, Gulsen G (2010) Quantitative fluorescence tomography using a combined tri-modality FT/DOT/XCT system. Opt Express 18(8):7835–7850. doi:10.1364/OE.18.007835
10. Lin Y, Ghijsen MT, Gao H, Liu N, Nalcioglu O, Gulsen G (2011) A photo-multiplier tube-based hybrid MRI and frequency domain fluorescence tomography system for small animal imaging. Phys Med Biol 56(15):4731–4747. doi:10.1088/0031-9155/56/15/007
11. Schulz RB, Ale A, Sarantopoulos A, Freyer M, Soehngen E, Zientkowska M, Ntziachristos V (2010) Hybrid system for simultaneous fluorescence and x-ray computed tomography. IEEE Trans Med Imaging 29(2):465–473. doi:10.1109/TMI.2009.2035310
12. Stuker F, Baltes C, Dikaiou K, Vats D, Carrara L, Charbon E, Ripoll J, Rudin M (2011) Hybrid small animal imaging system combining magnetic resonance imaging with fluorescence tomography using single photon avalanche diode detectors. IEEE Trans Med Imaging 30(6):1265–1273. doi:10.1109/TMI.2011.2112669
13. Yang X, Gong H, Quan G, Deng Y, Luo Q (2010) Combined system of fluorescence diffuse optical tomography and microcomputed tomography for small animal imaging. Rev Sci Instrum 81(5):054304. doi:10.1063/1.3422252
14. Zhang X, Badea C, Hood G, Wetzel A, Qi Y, Stiles J, Johnson GA (2011) High-resolution reconstruction of fluorescent inclusions in mouse thorax using anatomically guided sampling and parallel Monte Carlo computing. Biomed Opt Express 2(9):2449–2460. doi:10.1364/BOE.2.002449
15. Pressman D, Day ED, Blau M (1957) The use of paired labeling in the determination of tumor-localizing antibodies. Cancer Res 17(9): 845–850

16. Baeten J, Haller J, Shih H, Ntziachristos V (2009) In vivo investigation of breast cancer progression by use of an internal control. Neoplasia 11(3):220–227
17. Liu JT, Helms MW, Mandella MJ, Crawford JM, Kino GS, Contag CH (2009) Quantifying cell-surface biomarker expression in thick tissues with ratiometric three-dimensional microscopy. Biophys J 96(6):2405–2414. doi:10.1016/j.bpj.2008.12.3908
18. Tichauer KM, Samkoe KS, Sexton KJ, Hextrum SK, Yang HH, Klubben WS, Gunn JR, Hasan T, Pogue BW (2012) In vivo quantification of tumor receptor binding potential with dual-reporter molecular imaging. Mol Imaging Biol 14(5):584–592. doi:10.1007/s11307-011-0534-y
19. Davis SC, Dehghani H, Wang J, Jiang S, Pogue BW, Paulsen KD (2007) Image-guided diffuse optical fluorescence tomography implemented with Laplacian-type regularization. Opt Express 15(7):4066–4082
20. Davis SC, Gibbs-Strauss SL, Tuttle SB, Jiang S, Springett R, Dehghani H, Pogue BW, Paulsen KD (2008) MRI-coupled spectrally-resolved fluorescence tomography for in vivo imaging – art. no. 68500K. SPIE 6850:K8500. doi:10.1117/12.764252
21. Davis SC, Pogue BW, Springett R, Leussler C, Mazurkewitz P, Tuttle SB, Gibbs-Strauss SL, Jiang SS, Dehghani H, Paulsen KD (2008) Magnetic resonance-coupled fluorescence tomography scanner for molecular imaging of tissue. Rev Sci Instr 79(6):064302-064301–064302-064310
22. Davis SC, Samkoe KS, Tichauer KM, Sexton KJ, Gunn JR, Deharvengt SJ, Hasan T, Pogue BW (2013) Dynamic dual-tracer MRI-guided fluorescence tomography to quantify receptor density in vivo. Proc Natl Acad Sci U S A 110(22):9025–9030. doi:10.1073/pnas.1213490110
23. Davis SC, Samkoe KS, O'Hara JA, Gibbs-Strauss SL, Paulsen KD, Pogue BW (2010) Comparing implementations of magnetic-resonance-guided fluorescence molecular tomography for diagnostic classification of brain tumors. J Biomed Opt 15(5):051602–051610
24. Pvd Z (1992) Measurment and modeling of the optical properties of human tissue in the near infrared. University College London, London, UK
25. Davis SC, Samkoe KS, O'Hara JA, Gibbs-Strauss SL, Payne HL, Hoopes PJ, Paulsen KD, Pogue BW (2010) MRI-coupled fluorescence tomography quantifies EGFR activity in brain tumors. Acad Radiol 17(3):271–276

Chapter 13

In Vivo Metal Ion Imaging Using Fluorescent Sensors

Genevieve C. Van de Bittner and Tasuku Hirayama

Abstract

In vivo imaging in living animals provides the ability to monitor alterations of signaling molecules, ions, and other biological components during various life stages and in disease. The data gained from in vivo imaging can be used for biological discovery or to determine elements of disease progression and can inform the development and translation of therapeutics. Herein, we present theories behind small-molecule, fluorescent, metal ion sensors as well as the methods for their successful application to in vivo metal ion imaging, including ex vivo validation.

Key words Fluorescence, Near-infrared, Copper, In vivo imaging, IVIS spectrum, Wilson's disease, Metal, Ion

1 Introduction

Fluorescence-based metal imaging has been widely developed for the detection of biologically relevant metal ions in biological samples and for live-cell imaging [1–5]. Given the importance of metal ions for biological regulation, particularly with regard to enzyme activation/deactivation and enzyme catalysis, a goal of the fluorescence imaging community has been the development of sensors for in vivo metal ion imaging. One method is use of chelation-based, small-molecule, "turn-on" fluorescent sensors that are low- or non-fluorescent in the absence of the metal ion and highly fluorescent upon metal coordination (Fig. 1a) [1, 5].

Development of these fluorescent sensors has relied heavily on two photophysical phenomena, photo-induced electron transfer (PET) and internal charge transfer (ICT), which are discussed in detail in several reviews [6, 7]. Briefly, design of these sensors requires tuning the electron density of the chelating moiety so that metal ion coordination modulates the PET and/or ICT efficiency. Coordination with a cationic metal ion, such as Ca^{2+}, Zn^{2+}, Cu^{+}, or

Author contributed equally with all other contributors.

Mingfeng Bai (ed.), *In Vivo Fluorescence Imaging: Methods and Protocols*, Methods in Molecular Biology, vol. 1444,
DOI 10.1007/978-1-4939-3721-9_13,

Cu^{2+}, decreases the electron-donating property of the coordinating nitrogen and oxygen atoms, leading to an increase in intensity or wavelength shift of the sensor fluorescence (Fig. 1a). The electron-donating properties of aromatic nitrogen atoms are particularly affected upon metal coordination, making them a key modulator of the PET/ICT phenomena and ultimately the sensor fluorescence. The large change in fluorescence properties of these "turn-on" sensors provides a low background and large dynamic range, making them especially useful for in vivo imaging.

Many of the initial metal ion sensors relied on excitation and emission wavelengths in the visible region, frequently relegating them to in vitro and live-cell imaging applications. Due to the improved tissue penetration of near-infrared (NIR) light [8–10], many researchers have adopted NIR fluorescent sensors for in vivo imaging applications, particularly for small animals, such as mice [11]. In the past decade, many reports have featured NIR fluorescent sensors for biological metal ions such as calcium, zinc, and copper. Only a few sensors, ZPP1, CaSiR-1, CS790AM, and CTMPA, have been applied to in vivo imaging of living, adult organisms [5, 11]. Of these sensors, ZPP1, CaSiR-1, and CS790AM are PET-type sensors that show enhanced fluorescence upon metal binding, and CTMPA is an ICT-type sensor that has a shifted emission wavelength upon metal coordination.

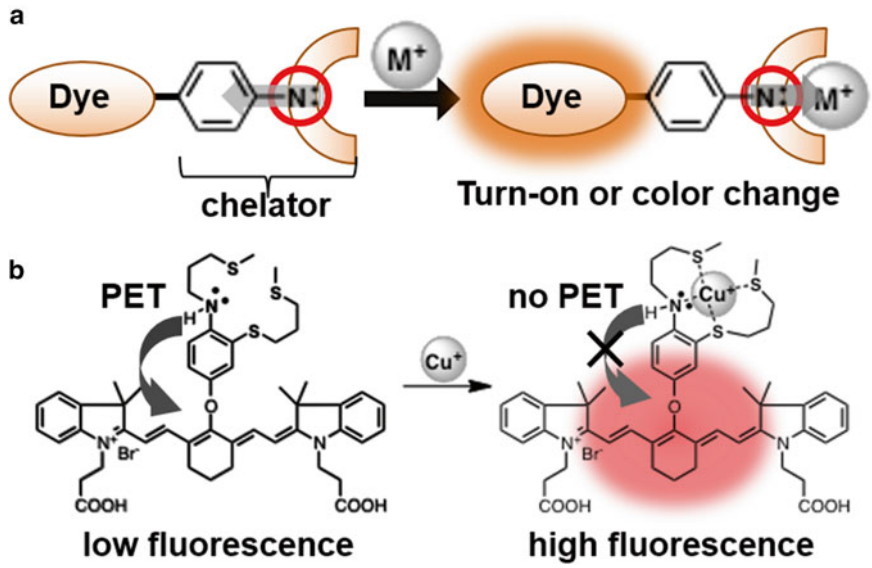

Fig. 1 (**a**) Schematic representation of chelation-based fluorescent sensor mechanism. The aromatic nitrogen atom of the chelator increases the electron density of the aromatic ring in the absence of metal ion chelation. Upon chelation, the nitrogen lone pair becomes occupied by metal coordination, reducing the electron density of the aromatic ring and inducing fluorescence turn-on and/or color change. (**b**) Cu^{+} detection mechanism of CS790 (de-esterified CS790AM), a PET-based NIR sensor

ZPP1, although it has excitation and emission wavelengths in the visible region, was successfully applied to in vivo imaging of Zn^{2+} in a murine model of prostate cancer [12]. CaSiR-1 was used to study Ca^{2+} in cerebral cortical neurons of a living mouse [13], and CTMPA successfully sensed Zn^{2+} in zebrafish [14]. Our own contribution, CS790AM, is an NIR fluorescent Cu^{+} sensor (Fig. 1b) that was used to detect Cu^{+} fluctuations in living mice, including a murine model of Wilson's disease [15].

Herein, we provide a protocol for in vivo Cu^{+} imaging with CS790AM that can be applied generally to the development of fluorescent sensors for in vivo metal ion detection. Special attention is given to sensor validation, as it is of paramount importance that in vivo fluorescent signals reliably report the in vivo metal ion concentration. Main validation steps included in this chapter are (1) demonstration of exogenous and endogenous in vivo metal ion sensing, (2) confirmation of in vivo imaging results through organ harvesting and fluorescence analysis, and (3) verification of the in vivo association of the fluorescent sensor and the targeted metal ion. All three validation steps were used in the development of CS790AM and are covered in the proceeding protocol for easy application to any existing or newly developed metal ion sensor. These techniques have been applied to murine disease models for monitoring therapeutic efficacy [15] and have potential applications in selecting therapeutic dosing in clinical trials.

2 Materials

2.1 CS790AM Purity Analysis

1. CS790AM or other metal ion sensor.
2. Glass-backed 60 F254 silica gel plates.
3. TLC plate cutter.
4. TLC capillary tubes.
5. TLC chamber.
6. Dichloromethane.
7. Methanol.
8. Chloroform-d (D=99.8%, +0.03% v/v tetramethylsilane).
9. NMR tube (5 or 7 mm diameter).

2.2 CS790AM Aliquoting

1. CS790AM or other metal ion sensor.
2. Methanol (spectrophotometric grade ≥99.8%).
3. 0.2 mL PCR microtubes with attached caps.
4. 1 Dram scintillation vial.
5. Pipettors: 20–200 µL and 200–1000 µL.
6. Pipet tips (pipettor-brand dependent).

7. 50 mL Conical tubes.
8. Nitrogen gas.
9. Parafilm®.

2.3 Animals and Animal Preparation

1. Mice: SKH1 (nude, immunocompetent; Charles River Laboratories, Wilmington, MA, USA) (recommended).
   Wild-type or genetic model with fur (requires fur removal).
2. Fur removal (if necessary): Nair hair removal cream, 1 L water, paper towels or gauze, timer.

2.4 Injection

1. Phosphate-buffered saline (PBS, USP grade): MilliQ water, 137 mM NaCl, 2.7 mM KCl, 10 mM Na_2HPO_4, 1.8 mM KH_2PO_4, pH 7.4.
2. DMSO (USP grade).
3. CS790AM aliquot.
4. $CuCl_2$.
5. ATN-224 (copper chelator, kindly provided by Andrew Mazar, Northwestern University, Evanston, IL).
6. 1.5 mL Eppendorf tubes.
7. 1 mL Syringes.
8. 0.2 μm Filters (sterile).
9. Syringe with attached needle (sterile, Cat. No. 309300, BD Biosciences).

2.5 Imaging

1. IVIS Spectrum with filter sets in the near-infrared region and Living Image software.
2. Inhaled anesthesia system with induction chamber for mice.
3. Isoflurane (USP grade).
4. Compressed oxygen.
5. 70% Ethanol.
6. Black paper.

2.6 Blood Collection, Perfusion, and Organ Harvesting

1. Isoflurane, ketamine/xylazine, pentobarbital, or pentobarbital/phenytoin (USP grade).
2. PBS (USP grade).
3. 8″ × 8″ Styrofoam square.
4. Push pins.
5. 24 G Needle(s).
6. 20 mL Syringe(s).
7. 1.5 mL Eppendorf.
8. 20–60 mm Petri dishes.
9. Forceps.

10. Dissecting scissors.
11. Clamp forceps.
12. Ice.

2.7 Blood Analysis

1. Microcentrifuge with temperature control, 1.5 mL sample size.
2. HPLC with automated fraction collector.
3. Gel filtration (size exclusion) column: Phenomenex Bio-Sep S-2000; 7.5 × 200, 10 μm.
4. 50 mM Sodium phosphate buffer, pH 7.5.
5. Fluorescence plate reader with NIR filters.
6. Black, clear-bottom 96-well plate.
7. Shimadzu 6650 graphite furnace atomic absorption spectrophotometer with an ASC-6100 autosampler.
8. MilliQ or deionized water.

3 Methods

3.1 CS70AM Quality Control (See Note 1)

3.1.1 TLC Purity Analysis

1. Cut TLC plate into 1 × 5 cm sections. Select one piece and use a pencil to mark the location where the sensor will be spotted, 0.5 cm from a 1 cm edge (Fig. 2).
2. Dissolve a 0.1 mg sample of CS790AM in 100 μL dichloromethane, spot it on TLC plate with a capillary tube, and let dry for 30 s.
3. Place the TLC plate into a TLC chamber containing ~2 mm mobile phase (dichloromethane:methanol = 8:1). Remove TLC plate when solvent front is 0.5 cm from the top of the plate (Fig. 2, *see* **Note 2**).

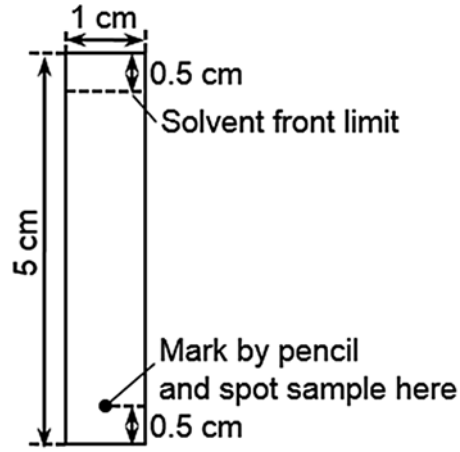

Fig. 2 Layout of a typical TLC plate used to test fluorescent sensor purity

3.1.2 ^{1}H-NMR Purity Analysis

1. Weigh 5 mg of CS790AM and dissolve it in chloroform-d (600 μL); transfer the solution to a standard NMR tube, and acquire ^{1}H-NMR spectrum with an NMR spectrometer.

3.2 CS790AM Aliquots (See Note 3)

1. Weigh 5.0 mg (4.5 μmol) of CS790AM in the 1 dram vial and add 450 μL methanol to make a 10 mM solution.
2. Aliquot 20 μL of the stock solution to each microtube, keeping the caps open. Cover the tubes with aluminum foil to protect from light, and place in a vacuum desiccator (without desiccant), equipped with a vacuum pump or a diaphragm pump.
3. Evaporate the methanol in vacuo until it is removed, at least 2 h.
4. Remove samples from the desiccator, close the caps, and place tubes into 50 mL conical tubes (or other sealable container). After purging with nitrogen gas, seal the containers with Parafilm®, and store in a −20 or −80 °C freezer.

3.3 Fur Removal (If Necessary)

1. Anesthetize mice with 3% isoflurane and 1.5 L/min O_2 flow rate for 5 min, and then reduce isoflurane to 1.5%.
2. While mice are under anesthesia, place a small amount of Nair cream on the area of the body that will be imaged and analyzed. Gently rub Nair into the fur, so that it reaches the hair follicles.
3. After about 30 s (*see* **Note 4**), wipe off Nair cream with paper towels or gauze wetted with water. Rinse skin repeatedly with DI water to ensure removal of all Nair cream (*see* **Note 5**).

3.4 Preparation of Injectables

1. Prepare a $CuCl_2$ solution in PBS for a final injection volume of 50 μL per animal and a maximum dose of 5 mg/kg. $CuCl_2$ should be injected 2 h prior to the injection of the fluorescent sensor to provide time for the Cu^{2+} to be converted to Cu^{+} in vivo.
2. Prepare an ATN-224 solution in PBS for a final injection volume of 50 μL per animal and a maximum dose of 5 mg/kg. ATN-224 should be injected 2 h prior to CS790AM for optimal copper chelation.
3. Prepare a 0.1 mM CS790AM solution in DMSO:PBS (7:3) for a final injection volume of 50 μL per animal (*see* **Note 6**). An uptake period of at least 5 min after CS790AM injection should be given prior to imaging (*see* **Note 7**).
4. Aseptic technique should be used to prepare all doses. Don sterile gloves, draw solutions into a 1 mL syringe, and filter into a sterile Eppendorf. Draw injection dose into a sterile syringe with attached needle, and inject shortly after preparation.

Table 1
Animal treatments for validating exogenous and endogenous Cu^+ imaging in vivo

Animal	$CuCl_2$ or vehicle	ATN-224 or vehicle	CS790AM or vehicle
1	Vehicle	Vehicle	Vehicle
2	Vehicle	Vehicle	CS790AM
3	$CuCl_2$	Vehicle	CS790AM
4	$CuCl_2$	ATN-224	CS790AM
5	Vehicle	ATN-224	CS790AM

3.5 Intraperitoneal Injection Procedure

For each imaging session, animals with five different treatments are included, as outlined in Table 1. Animal 1, which is only injected with vehicles, serves as a crucial control for monitoring autofluorescence.

1. Anesthetize the mouse in an isoflurane chamber with 3% isoflurane and 1.5 L/min O_2 flow rate. Ensure that the mouse has reached deep anesthesia by performing a toe/tail pinch (*see* **Note 8**).
2. Lift mouse out of the chamber by the tail and place mouse in supine position in one hand (usually the non-dominant hand). With thumb and index/middle fingers, grab the fur/skin of the mouse to make skin over the abdomen taut. Use the ring or pinkie finger to pin down the tail of the mouse.
3. Tilt the head of the mouse slightly downward, so that the organs move toward the diaphragm and away from the injection site.
4. Slowly insert syringe needle at a 30–45° angle (relative to the surface of the abdomen) near the bottom left or right side of the abdominal cavity. Gently pull back on the syringe plunger and make sure that no fluid/blood enters the needle. Push down gently on plunger to inject contents of the syringe (*see* **Notes 9** and **10**).
5. If imaging immediately, place mouse in IVIS Spectrum instrument and maintain anesthetic state with isoflurane at 1.25–1.75%.

3.6 Imaging Procedure and Image Analysis

1. Prior to CS790AM injection, open the Living Image program on the IVIS Spectrum and press the initialize button to reset the camera. Create a new folder for the data and go to the acquisition tab and select the "auto save to …" button to save the data to the newly created folder.

2. Click on the temperature window and set the stage temperature to 37 °C. Sanitize stage with 70% ethanol and cover with black paper for stage protection and easy cleanup.
3. Click on the Imaging Wizard button, choose fluorescence, and then select epi-illumination (*see* **Note 11**).
4. Select the appropriate wavelength pair for the sensor or input the wavelengths by selecting Input Ex/Em. For CS790AM the wavelengths are 745 nm (Ex) and 800 nm (Em) (*see* **Note 12**).
5. On the last page, select Manual Settings and choose Fstop 2, Binning 8, and 1 s exposure (*see* **Notes 13** and **14**). Also select the appropriate Field of View (i.e., choose D for imaging five mice) and enter a subject height (typically 1.5 cm for mice).
6. Mice should be lying prone or supine (*see* **Note 15**) inside the camera with noses in the isoflurane-delivering nose cones, and completely inside the outermost grid lines (green laser lines) projected on the imaging surface. Place black plastic dividers between the animals to prevent fluorescent signal bleed-over.
7. Press the acquire button 5 min after CS790AM injection to acquire imaging data (Fig. 3). Images containing saturated areas should be retaken with a shorter exposure or lower sensor dose (*see* **Note 16**).
8. If several imaging time points are needed, re-image mice as necessary (*see* **Note 17**).

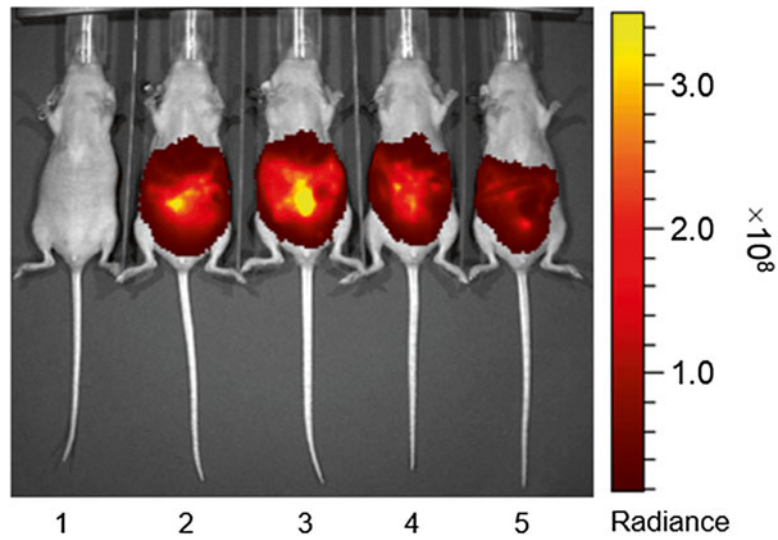

Fig. 3 Representative image of exogenous and endogenous in vivo fluorescent Cu^{+} sensing with CS790AM. Treatments for animals 1–5 correspond to those listed in Table 1. Increases in in vivo fluorescence are seen after $CuCl_2$ injection (animal 3), and decreases are seen following ATN-224 administration (animals 4 and 5). Animals are in supine position for optimal abdominal organ imaging. Adapted from Hirayama et al. [15]

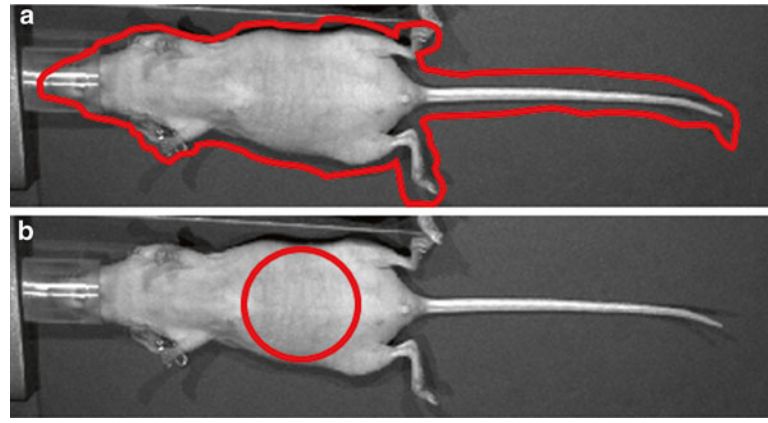

Fig. 4 Examples of ROIs for image analysis. (**a**) Whole-body ROI for total fluorescence comparison. (**b**) Abdominal ROI for abdominal fluorescence comparison. The type of ROI used will depend on the study, but consistency in ROI size is crucial. For best comparisons, animals should be of similar size and weight

9. To analyze a particular image in the Living Image software, open and double-click the image.
10. Go to the Tool Palette window to adjust the minimum and maximum settings for the image under Image Adjust.
11. Select the units for data analysis from the drop-down menu on the upper left side of the selected image.
12. Under the ROI Tools menu, draw regions of interest (ROIs) on the selected image and measure the signal using the measurement tool (Fig. 4, *see* **Note 18**). The measured data can now be saved as a text file or copied into Excel for statistical analysis.

3.7 Blood Collection, Perfusion, Organ Harvesting, and Organ Imaging

1. Heavily anesthetize mouse with isoflurane, ketamine/xylazine, pentobarbital, or pentobarbital/phenytoin. Ensure that mouse has reached surgical plane of anesthesia by performing a toe/tail pinch. When using isoflurane, maintain anesthetic administration throughout the perfusion procedure.
2. Lay mouse supine on Styrofoam platform, and pin each limb to the Styrofoam board using a push pin.
3. Make a small incision into peritoneal cavity of the mouse using forceps and dissecting scissors. Starting with the initial incision, carefully make a vertical cut toward the head of the mouse to expose the abdominal cavity (*see* **Note 19**). Continue cutting towards the head of the mouse until you reach the sternum. At this point, cut through the diaphragm and cut through the ribcage on either side of the sternum.
4. Using clamp forceps, grab onto the bottom end of the sternum and pull it toward the head of the mouse to expose the heart.

Gently grab the heart with forceps, and make a small incision into the right atrium. Collect 200–300 μL blood into a 1.5 mL Eppendorf and store on ice.

5. Continue to hold the heart with the forceps. While keeping the heart in place, insert a needle (attached to a 20 mL syringe with PBS) into the left ventricle of the heart. Release the heart and begin to push the PBS into the heart, forcing blood and PBS out of the right atrium. There will be some back pressure, and it will take a few minutes to empty the syringe.
6. After the first few milliliters of PBS are pumped into the heart, the organs will begin to lose their color. If the organ of interest still retains color (blood) after the perfusion, this can sometimes be removed by injecting more PBS into the descending aorta/mesenteric artery or the vena cava.
7. Dissect the organ(s) of interest from the mouse and put into a small petri dish(es) on ice. Image the organs using an IVIS camera and imaging procedures outlined in Subheading 3.6 (Fig. 5, *see* **Note 20**).

3.8 Blood Analysis

When fluorescent sensors are used for in vivo imaging, they are added to a biological matrix much more complicated than the solutions used for in vitro sensor development. Upon injection, in vivo metabolism of a sensor may include polar oxidations, a key metabolic pathway for xenobiotics [16], which are known to influence the fluorescence of sensor-like molecules [17].

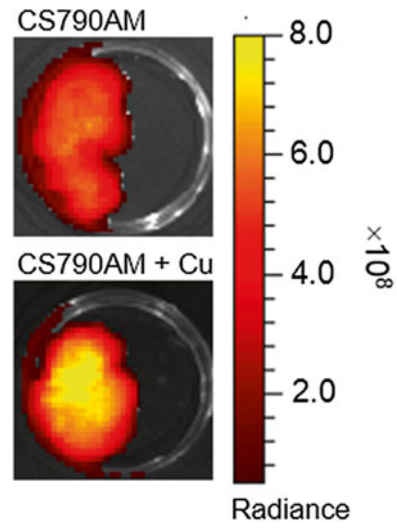

Fig. 5 Representative images of CS790AM fluorescence in livers from animals treated with vehicle or $CuCl_2$. Liver fluorescence increases following $CuCl_2$ treatment, validating the in vivo CS790AM fluorescence increase measured after $CuCl_2$ injection. Adapted from Hirayama et al. [15]

Sensor injection may also alter the sensor solvation, which has well-documented impacts on fluorescence [18], and the sensor will interact with biological molecules in vivo, whose sensor-fluorescence effects have not been tested. Thus, it is imperative to validate that the detected in vivo fluorescence is correlated with the metal ion of interest (*see* **Note 21**). In the case of CS790AM, a blood analysis consisting of gel filtration followed by fluorescence measurements and atomic absorption indicated that the detected fluorescent signal co-eluted (was associated) with copper [15].

1. Centrifuge collected blood at 4000 × *g* for 10 min at 4 °C to separate serum. The serum will be the top, clear layer following centrifugation.
2. Load 100 μL serum onto the size-exclusion column, pre-equilibrated with 50 mM sodium phosphate buffer, pH 7.5. Separate sample using 50 mM sodium phosphate buffer at a flow rate of 0.25 mL/min. Collect 0.25 mL samples over 80 min.
3. Transfer 0.25 mL samples to a black, clear-bottom 96-well plate and measure the fluorescence of the samples using a plate reader with NIR fluorescence filters (*see* **Note 22**). This measurement will indicate which fractions contain the fluorescent sensor.
4. Transfer samples to an atomic absorption spectrophotometer, ideally furnished with an autosampler. If the metal ion concentration in the samples is high, the samples can be diluted with MilliQ or deionized water. Create a calibration curve using a weighed sample of the metal ion.
5. Compare the fractions containing fluorescence to those containing the metal ion of interest. If the fluorescent signal is resulting from detection of the metal ion, these fractions should overlap (*see* **Note 23**).

4 Notes

1. Some decomposition products or impurities have fluorescence and/or absorbance in the visible to near-infrared region and may cause false-positive/negative signal in imaging experiments and make analysis of subtle changes in copper flux difficult.
2. Typically, a reddish brown spot appears when CS790AM is decomposed while a single green spot is observed for pure CS790AM.
3. Aliquoting produces more reproducible imaging over time for three reasons: (1) a more accurate weight for the sensor is obtained due to the larger sample size; (2) the same amount of

mass is added to small, individual-experiment samples; and (3) it reduces exposure of the sensor to light and oxygen, which can cause decomposition.

4. Nair can burn the mouse skin if it is left on for too long. Experiment with a shorter time on small areas of fur first and use nude, immunocompetent mice whenever possible.
5. Use liberal amounts of water to remove the Nair product; Nair that is not removed may burn the skin or be eaten after the animals wake up from anesthesia. To keep animals warm, heat water gently (~30 °C) before wiping off Nair.
6. DMSO should be added prior to PBS or the CS790AM will not dissolve. A higher amount of PBS will cause the CS790AM to precipitate. Make a fresh CS790AM solution prior to each imaging experiment as the compound can degrade in solution over time. CS790AM can be kept as a stock solution in DMSO without the PBS.
7. For new sensors, image animals after different uptake periods to determine the optimum timing for sensor-ion binding in vivo.
8. This will prevent waking/jerking away from the needle during the injection(s) and provides more precise and reproducible injections.
9. If a bubble forms under the skin, the injection was subcutaneous instead of intraperitoneal.
10. $CuCl_2$ and ATN-224 are injected 2 h before CS790AM.
11. Epi-illumination is used because it is fast and sufficient for many applications. Trans-illumination and structured light data can be used to do 3D diffuse fluorescence tomography.
12. The excitation and emission filters should be optimized for each sensor before injection by placing a sample of the dissolved sensor into the IVIS Spectrum and selecting different filter pairs.
13. Depending on the brightness of the sensor, these settings can be changed to increase/decrease the sensitivity and/or the resolution.
14. It is best to start with a short exposure (1 s) and increase gradually if the exposure period does not result in a measurable signal. Be careful not to expose the sensor too long to prevent photobleaching. Once an ideal exposure time is found for a sensor, keep it the same for all imaging experiments.
15. The position of the animals (prone or supine) will be determined by the region/organ of interest for the study. When imaging most abdominal or thoracic organs, the supine position is recommended. When imaging the brain, brown fat, or the spine, the prone position is recommended.

16. In the pull-down menu at the top of the image window there is an option to show a saturation map. Regions that are saturated will be shown in red.
17. Multiple images can result in photobleaching of the sensor. The amount of photobleaching can be estimated by repeatedly imaging a syringe or Eppendorf containing the dissolved sensor.
18. ROIs can be drawn around the whole animal when using nude mice. If a particular region is being analyzed, keep the ROI size the same for each animal (this can be done by copying and pasting the ROI, using a right click and selecting from the menu). The ROI placement should be consistent across animals.
19. It is important not to cut any organs; otherwise the perfusion solution will leak out of the organs, making the perfusion incomplete.
20. Place organs in similar orientations to ensure an impartial comparison.
21. PET/ICT-modulated sensors bearing a nitrogen atom can be affected by pH because protonation of the nitrogen atom induces a similar effect as metal coordination, resulting in false-positive signals. When using these types of sensors it is necessary to measure the effect of pH on fluorescence signal prior to in vivo application.
22. It is recommended to optimize the filter set used in the plate reader with a sample of the sensor dissolved in DMSO and diluted in PBS (1:100) prior to the blood analysis.
23. The fluorescent signal and metal ion may not elute with a retention time corresponding to small molecules, as the sensor may be associated with serum proteins, such as albumin.

References

1. Domaille DW, Que EL, Chang CJ (2008) Synthetic fluorescent sensors for studying the cell biology of metals. Nat Chem Biol 4:168–175
2. McRae R, Bagchi P, Sumalekshmy S et al (2009) In situ imaging of metals in cells and tissues. Chem Rev 109:4780–4827
3. Chan J, Dodani SC, Chang CJ (2012) Reaction-based small-molecule fluorescent probes for chemoselective bioimaging. Nat Chem 4:973–984
4. Terai T, Nagano T (2013) Small-molecule fluorophores and fluorescent probes for bioimaging. Pflugers Arch 465:347–359
5. Carter K, Young A, Palmer A (2014) Fluorescent sensors for measuring metal ions in living systems. Chem Rev 114:4564–4601
6. Lakowics JR (2006) Principles of fluorescence spectroscopy. Springer, New York, NY
7. Ueno T, Urano Y, Setsukinai K et al (2004) Rational principles for modulating fluorescence properties of fluorescein. J Am Chem Soc 126:14079–14085
8. Georgakoudi I, Mueller MG, Feld MS (2002) Intrinsic fluorescence spectroscopy of biological tissue, Fluorescence in Biomedicine. Marcel Dekker, New York, NY

9. Frangioni JV (2003) In vivo near-infrared fluorescence imaging. Curr Opin Chem Biol 7:626–634
10. Weissleder R, Ntziachristos V (2003) Shedding light onto live molecular targets. Nat Med 9:123–128
11. Guo Z, Park S, Yoon J et al (2014) Recent progress in the development of near-infrared fluorescent probes for bioimaging applications. Chem Soc Rev 43:16–29
12. Ghosh SK, Kim P, Zhang XA et al (2010) A novel imaging approach for early detection of prostate cancer based on endogenous zinc sensing. Cancer Res 70:6119–6127
13. Egawa T, Hanaoka K, Koide Y et al (2011) Development of a far-red to near-infrared fluorescence probe for calcium ion and its application to multicolor neuronal imaging. J Am Chem Soc 133:14157–14159
14. Guo Z, Kim GH, Shin I et al (2012) A cyanine-based fluorescent sensor for detecting endogenous zinc ions in live cells and organisms. Biomaterials 33:7818–7827
15. Hirayama T, Van de Bittner GC, Gray LW et al (2012) Near-infrared fluorescent sensor for in vivo copper imaging in a murine Wilson disease model. Proc Natl Acad Sci U S A 109:2228–2233
16. Ortiz de Montellano P (2005) Cytochrome P450: structure, mechanism, and biochemistry. Plenum, New York, NY
17. Cathcart R, Schwiers E, Ames BN (1983) Detection of picomole levels of hydroperoxides using a fluorescent dichlorofluorescein assay. Anal Biochem 134:111–116
18. Valeur B (2001) Effect of polarity on fluorescence emission. polarity probes, Molecular fluorescence: principles and applications. Wiley-VCH, Weinheim

Chapter 14

Using Fluorescence Imaging to Track Drug Delivery and Guide Treatment Planning In Vivo

Qiaoya Lin, Huang Huang, Juan Chen, and Gang Zheng

Abstract

Imaging has become an indispensable tool in both clinical medicine and preclinical sciences. It enables doctors to locate sites of cancer/disease, track drug delivery, and guide operative planning, thus enhancing the treatment efficacy. Recently, we developed a multimodal theranostic lipid nanoparticles, named HPPS(NIR)-chol-siRNA with its built-in near-infrared (NIR) fluorescent probe core as a useful surrogate for tracking small interfering RNA (siRNA) delivery. By using the image co-registration of computed tomography (CT) and fluorescence molecular tomography (FMT), we achieved noninvasive assessment and treatment planning of siRNA delivery into the orthotopic tumor, thus enabling efficacious RNA interference (RNAi) therapy. In this chapter, we introduce this method to illustrate the use of CT-FMT co-registration for tracking drug delivery and guiding treatment planning in vivo.

Key words Nanoparticles, Fluorescence imaging, Computed tomography, Fluorescence molecular tomography, HDL, siRNA delivery

1 Introduction

Personalized cancer medicine tailors medical treatments to the characteristics, needs, and preferences of individual cancer patients during all stages of care, from diagnosis and treatment to prognosis. Noninvasive imaging modalities such as fluorescence imaging (FI), photoacoustic imaging, magnetic resonance imaging (MRI), computed tomography (CT), ultrasound, and positron emission tomography (PET) are useful tools for diagnosing diseases, delineating tumors, monitoring physiological responses to therapy, and providing quantitative ways to assess the delivery of therapy in tumor region to finely tune the treatment process [1, 2].

RNA interference (RNAi) therapy holds enormous promise for personalized medicine as it could be designed to specifically knock down any disease-related gene to give a highly selective treatment [3]. However, RNAi therapy has encountered big

Mingfeng Bai (ed.), *In Vivo Fluorescence Imaging: Methods and Protocols*, Methods in Molecular Biology, vol. 1444,
DOI 10.1007/978-1-4939-3721-9_14,

challenges in both the systemic delivery of small interfering RNAs (siRNAs) into its intended action site and the accurate assessment of the delivery efficiency. Therefore, the combination of a good siRNA delivery system and an imaging modality that is able to quantitatively monitor the siRNA delivery both at the intended disease site and non-intended sites may provide solutions to these challenges [4–7]. Several imaging modalities have been reported for visualizing nanoparticle-based siRNA delivery in vivo, such as MRI [8], single-photon emission computed tomography (SPECT) [9], PET [10], and FI [11–13]. FI is a noninvasive, fast, cost-effective, highly sensitive, and multichannel imaging technique, which enables tracking fluorophore of interest from the anatomical to cellular level. Conventional in vivo FI systems such as fluorescence reflectance imaging provide 2D imaging, and the development of fluorescence molecular tomography (FMT) extends FI into quantitative 3D imaging [14, 15].

Exogenous fluorophores introduced into animals emit fluorescence when excited with light of appropriate wavelength generated by broad-spectrum sources or laser beams with appropriate bandpass filters. The fluorescence signals of interest are then captured by a high-sensitive and low-noise charge-coupled device (CCD) camera at the matched emission wavelength to generate images. In 2D imaging, the detector and the excitation light source are usually positioned on the same side of the animal (Fig. 1a). Although 2D imaging is useful for imaging the distribution and/or activation of fluorescent probes in living animals, it experiences some limitations such as superficial tissue penetration (only a few millimeters) due to photon scattering and attenuation in tissue, and poor quantification because of the nonlinear relationship between the signal strength and depth, compounded by the complicated tissue optical properties [2].

Unlike 2D imaging, in FMT, the light source and the detector are usually positioned on opposite sides of the animal, and the scanning is usually comprised of two steps. During the first scan, multiple points on the tissue boundary are illuminated in a sequential fashion (Fig. 1b) and diffuse light patterns are collected separately around the boundary (Fig. 1c) using photodetector sets or a CCD camera. This creates a mapping of the diffusive propagation patterns of photons in the animal/tissue being scanned. The second scan is the measurement of fluorescence using the same source-detector pairs as the first scan. The scanning time for FMT is relatively fast, and ranges between 3 and 5 min. Mathematical processing of the raw data using light propagation models yields 3D quantitative images of the fluorophore distribution in animal/tissue. Although still limited by photo scattering and attenuation in tissues, the FMT is able to reach depths of 3–6 cm in muscle or

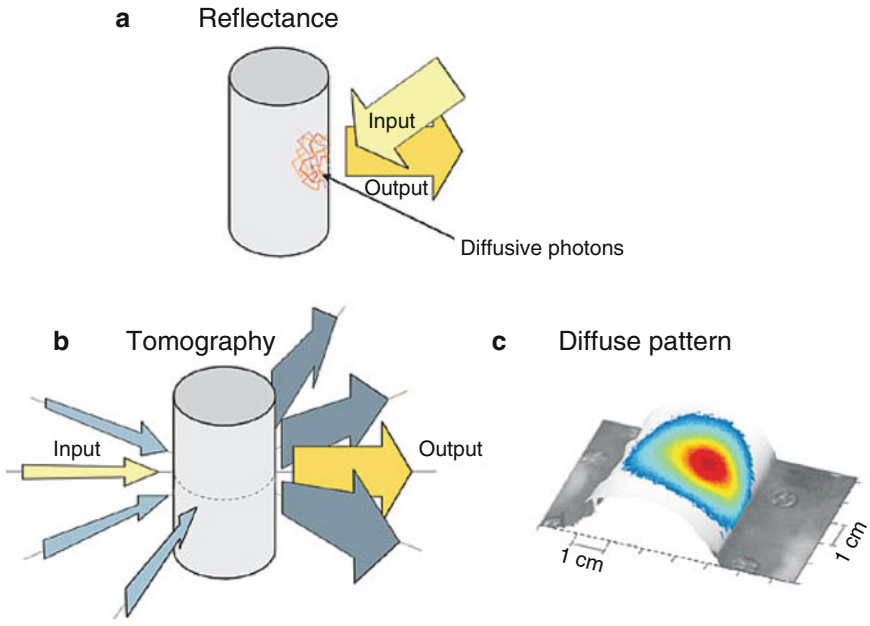

Fig. 1 Modes of data collection. (**a**) Fluorescence reflectance imaging. Excitation light (input) is expanded on the object surface and fluorescence light (output) collected from the same side of the object. Scattered photon trajectories are simplistically demonstrated with a few lines to demonstrate the typical volume sampling. (**b**) Tomography. Illustration of data collection where multiple point-source trans-illumination data are time-shared around a cylindrical geometry. Different geometries and the use of reflected data can also be used for tomographic purposes. The direction indicated by the *arrows* shows the general photon trajectory established. The pattern of data collected is, in fact, diffusive as is evident from the experimental measurements shown in (**c**) obtained from a trans-illuminated homogeneous diffusive cylinder. Reproduced with permission of Nature Publishing Group [2]

brain, or as far as 12 cm in less absorbing tissues such as the breast [16], showing a substantial improvement from 2D imaging. In addition, due to its 3D nature, FMT can be combined with anatomical imaging modalities such as CT or MRI to provide a high-resolution anatomical reference, leading to more accurate delineations of the tissues of interest.

In this chapter, we employed the FMT (co-registered to CT) to quantitatively track a novel multimodal theranostic lipid nanoparticle for target-specific RNAi therapeutics in a clinically relevant PC6-lu6 orthotopic prostate cancer model. We demonstrated that the nanoparticles enable in vivo noninvasive assessment of siRNA accumulation in orthotopic tumor by tracking the near-infrared (NIR) fluorescent surrogate using CT-FMT image co-registration, thus providing a useful means not only for real-time tracking of siRNA delivery, but also for rational dosimetry and the subsequent treatment planning, which directly impacts its therapeutic efficacy [17].

2 Materials

2.1 Nanoparticle Preparation and Characterization

1. 1, 2-Dimyristoyl-sn-glycero-3-phosphocholine (DMPC) was purchased from Avanti Polar Lipids Inc. (AL, USA). The DMPC was dissolved in chloroform at the concentration of 25 mg/mL (*see* **Note 1**).
2. Cholesteryl oleate (CO) was obtained from Sigma-Aldrich Co. (MO, USA). The CO was also dissolved in chloroform at the concentration of 25 mg/mL (*see* **Note 1**).
3. 1,1′-Dioctadecyl-3,3,3′,3′-tetramethylindotricarbocyanine iodide bis-oleate (DiR-BOA) was synthesized by the previously reported methods (MW 1013) [18]. 1 mg of DiR-BOA was dissolved in 100 μL chloroform (*see* **Note 2**).
4. The ApoA-1 mimetic peptide, Ac-FAEKFKEAVKDYFAKFWD, was purchased from GL Biochem Ltd. (Shanghai, China). The peptide (20 mg) was suspended in 5 mL PBS buffer (0.1 M NaCl, pH 7.5).
5. Tris–buffer saline (10 mM Tris–HCl, 0.15 M NaCl, 1 mM EDTA, pH 7.5) was prepared, filtered through 0.22 μm millipore filter, and then degassed under vacuum for at least 2 h.
6. All siRNAs were synthesized by Genepharma Co. (Shanghai, China). Cholesterol-conjugated siRNA-bcl-2 (chol-si-bcl-2) consisted of the sense strand 5′-chol-GfUGAAGfUfCAAfCAfUGfCfCfUGfC-dTsdTs-3′ and antisense strand 5′-GfCAGGfCAfUGfUfUGAfCfUfUfCAfC-dTsdT-3′. Cholesterol-conjugated siRNA bearing a scrambled sequence(chol-si-scramble) consisted of the sense strand 5′-Chol-GAfCGfUAAfCGGfCfCAfUAGfUfCfU-dTsdTs-3′ and the antisense strand 5′-AGAfCfUAfUGGfCfCGfUfUAfCGfUfC-dTsdT-3′. Abbreviations are as follows: chol, cholesterol; fC and fU, 2′-deoxy-2′-fluoro cytidine and uridine, respectively; "s," phosphorothioate linkage. Chol-siRNAs were dissolved in RNase-free water (Ambion, USA) (*see* **Note 3**).
7. A 15 mL round-bottom flask, parafilm.
8. High-purity nitrogen (>99%).
9. Branson 2510 water-bath sonicator (Thermo Fisher Scientific Inc., CA).
10. Centrifugal filter units (Amcon Ultra-15, 10 K, EMD Millipore, USA).
11. Akta fast protein liquid chromatography (FPLC) system (Amersham Biosciences, USA) equipped with a HiLoad 16/60 Superdex 200 pg column.
12. Agarose (electrophoresis grade) was obtained from BioShop Canada Inc. (Burlington, Canada). 2 g Agarose gel was dissolved

in 100 mL ddH2O, heated and cooled down, and then Gel red was added 0.002% (v/v).

13. Phosphotungstic acid solution (PTA) (Sigma Aldrich, CA).
14. Hitachi H-7000 transmission electron microscope (Hitachi Inc., Japan).
15. Zetasizer Nano-ZS90 (Malvern Instruments Ltd, UK).
16. Varian Cary 50 UV-visible spectrophotometer (Varian Inc., CA).

2.2 Four-Step Imaging to Track Drug Delivery

All animal studies were conducted in Animal Resource Center of University Health Network in accordance with protocols approved by the Animal Care Committee. Inhalation of isoflurane (2%) was given to mice via nose cone during the whole procedure of all in vivo animal experiments.

2.2.1 Establishing Orthotopic Prostate Cancer Model

1. Luciferase-transfected PC3-luc6 cell line was purchased from Caliper Life Sciences, Inc. (USA), and cell culture medium Eagle's minimum essential medium (EMEM) were obtained from the ATCC (American Type Culture Collection, VA, USA). Fetal bovine serum (FBS) and trypsin–ethylenediaminetetraacetic acid (EDTA) solutions were all purchased from Life Technologies Inc. (CA).
2. Adult male mice (athymic nude, Harlan, 6–8 weeks, 20–25 g average weight).
3. Microscope (Thermo Fisher Scientific Inc., CA).
4. Anesthetic machine with 2% isoflurane and oxygen supplier.
5. Buprenorphine (Comparative Medicine and Animal Resources Centre, CA).
6. Surgical tools included needle drivers, thumb forceps, surgical scissors, sterile gloves, mask, two types of suture (5–0, 18″, 19 mm 3/8c, Nylon suture-Black monofilament; 3–0, 18″, 19 mm 3/8c, Polyglactin 910-Undyed Braided-Synthetic absorbable suture), povidone iodine, isopropyl alcohol, syringe, cotton swab, and beaker.

2.2.2 Validation of Orthotopic Prostate Cancer Model and Quantification of Tumor Volume

1. D-Luciferin (PerkinElmer, CA).
2. Bioluminescence imaging system (planar imaging) (Xenogen, Caliper Life Sciences, USA).
3. MRI scanner (Bruker Icon 1 T Desktop MRI Scanner with a mouse body coil, Bruker BioSpin, USA).
4. MicroView v2.2 image analysis software (GE Healthcare, USA).

2.2.3 In Vivo Whole-Body Fluorescence Imaging (2D Imaging)

1. CRI Maestro™ imaging system (CRI, USA).
2. NIR filter (excitation filter: 725–755 nm, emission filter: 780 nm long pass).

2.2.4 CT-FMT Co-registration (3D Tomography Imaging)

1. Micro-CT scanner (GE Locus Ultra micro-CT, GE Healthcare, USA).
2. FMT system (PerkinElmer VisEn FMT 2500 LX Quantitative Tomography System, VisEn Medical Inc, USA).
3. FMT Animal Imaging Cassette inside Multi-Modality Adaptor.
4. Inveon™ Research Workplace 3.0 (IRW) image analysis software (Siemens, USA).

2.2.5 In Situ and Ex Vivo Fluorescence Imaging

1. CRI Maestro™ imaging system (CRI, USA).
2. NIR filter (excitation filter: 725–755 nm, emission filter: 780 nm long pass).
3. Surgical tools including thumb forceps, surgical scissors, sterile gloves, and mask.
4. Sterile PBS buffer (0.1 M NaCl, pH 7.5).
5. 12-Well cell culture plates.

2.2.6 Confocal Imaging of Frozen Tumor Tissue Slice

1. Liquid nitrogen.
2. Cryomold—standard size ($25 \times 20 \times 5$ mm).
3. Tissue Tek OCT-Somagen Diagnostic (Leica Biosystems, USA).
4. Leica CM3050S cryostat (Leica Microsystems Inc., USA).
5. DAPI containing mounting solution (Vector Laboratories, USA).
6. Olympus FV1000 laser confocal scanning microscopy (Olympus, Tokyo, Japan).

2.3 CT-FMT Co-registration Image-Guided Treatment Planning

1. Micro-CT scanner (GE Locus Ultra micro-CT, GE Healthcare, USA).
2. FMT system (PerkinElmer VisEn FMT 2500 LX Quantitative Tomography System, VisEn Medical Inc, USA).
3. FMT Animal Imaging Cassette inside Multi-Modality Adaptor.

2.4 In Vivo Therapeutic Efficacy Study

2.4.1 Polymerase Chain Reaction Assay

1. RNeasy Mini kit (Qiagen, CA).
2. qScript™ cDNA SuperMix (Quanta Biosciences, USA).
3. $2 \times$ Polymerase chain reaction (PCR) master mix (Thermo Scientific Fermentas, USA).

2.4.2 Terminal Deoxynucleotidyl Transferase dUTP Nick End Labeling Assay

1. 1% PFA in PBS, ethanol/acetic acid = 2:1; 3% aqueous hydrogen peroxide (Sigma-Aldrich, CA).
2. Avidin/biotin blocking kit (Lab VisionTM, CA).
3. Biotin-nucleotide cocktail.

4. Ultra Streptavidin Horseradish Peroxidase Labeling Reagent (ID Labs inc., USA).
5. DAB (Dako, CA).
6. Mayer's hematoxylin (Sigma-Aldrich, CA).
7. Aperio Whole Slide Scanner (Leica Biosystems, USA).

3 Methods

3.1 Nanoparticle Preparation and Characterization

1. A mixture of 30 μmol DMPC, 2.88 μmol CO, and 1 μmol NIR dye (DiR-BOA) in chloroform was dried under nitrogen in a 15 mL round-bottom flask, and connected with a high-vacuum system to dry continually for 1 h (*see* **Note 1**).
2. Then 10 mL of PBS buffer (0.1 M NaCl, pH 7.5) was added to the dried film and the mixture was vortexed intermittently for 5 min.
3. The turbid emulsion mixture was subsequently sonicated for 60 min at 48 °C (covered with aluminum foil to avoid light explosion) (*see* **Notes 2** and **4**).
4. ApoA-1 mimetic peptide (20 mg) suspended in 5 mL PBS buffer was then added dropwise into the emulsion mixture and the resulting mixture was stored at 4 °C overnight.
5. This complex was then filtered through a 0.22 μm millipore filter, concentrated with centrifugal filter units, and purified by gel filtration chromatography using FPLC system equipped with a HiLoad 16/60 Superdex 200 pg column and eluted with Tris-buffered saline at a flow rate of 1 mL min^{-1}. The fraction eluted at a retention time of 55–75 min was collected to acquire HPPS(NIR) nanoparticles.
6. Determination of the molar concentration of the nanoparticle: The molar concentration of DMPC (C_{DMPC}) in HPPS(NIR) nanoparticle sample was firstly determined using a phospholipid C assay kit (Wako Pure Chemical, USA). The number of DMPC molecules per HPPS(NIR) particle could be calculated using the known formula [19]: $2\pi[(d-20)/2]^2/70$, which gave the number of DMPC molecules in a HPPS(NIR) particle. In this formula, assumptions were made that the helix diameter and the surface area of DMPC were 10 Å and 70 $Å^2$, respectively; d was the diameter of HPPS(NIR) particles which could be determined by Zetasizer Nano-ZS90. Hence, the number of DMPC molecules per HPPS(NIR) particle can be calculated. The particle molar concentration ($C_{HPPS(NIR)}$) was then calculated by dividing the concentration of DMPC(C_{DMPC}) by the number of DMPC molecules per HPPS(NIR) particle.

7. Determination of the molar concentration of the NIR-core (C_{NIR}) in HPPS(NIR) particle: The nanoparticle samples were extracted with chloroform, vortexed for 3 min, and then centrifuged at 12 000 rpm for 10 min. The chloroform layer was collected and subjected to fluorescence measurement (excited at 748 nm and detected at 780 nm) to determine DiR-BOA concentration (C_{NIR}) based on the fluorescence standard curve of DiR-BOA generated in chloroform. The number of DiR-BOA molecules per HPPS nanoparticle was calculated by dividing C_{NIR} by $C_{HPPS(NIR)}$.
8. Determination of the molar concentration of Chol-siRNAs: Chol-siRNAs were dissolved in RNase-free water and the concentration of siRNA was quantified by measuring its absorbance at 260 nm using Varian Cary 50 UV-visible spectrophotometer.
9. Preparation of chol-siRNA-loaded HPPS(NIR) nanoparticle: The chol-siRNA and HPPS(NIR) solutions were mixed at a molar concentration ratio ranging from 1:5 to 1:20, and incubated for 1 h at room temperature. The resulting HPPS(NIR)-chol-siRNA was loaded in agarose gel electrophoresis to determine the particle's integrity and stability. The zeta-potential of HPPS(NIR)-chol-siRNA was measured by patented M3-PALS technology using Zetasizer Nano-ZS90 (*see* **Note 3**).

3.2 Four-Step Imaging to Track Drug Delivery

The surgery/injection was carried out using sterile technique and under pathogen-free condition in a biosafety hood with an operational microscope. For rodent surgeries, the surgeon must wear a cap and mask, clean lab coat or gown, and sterile gloves. All animals must have a full aseptic skin preparation prior to survival surgery.

3.2.1 Establishing Orthotopic Prostate Cancer Model

1. Preoperative analgesic buprenorphine (0.1 mg kg^{-1}) was subcutaneously injected to animals 30 min before the surgery. Preoperative antibiotic enrofloxacin (25 mg kg^{-1}) was given subcutaneously to mice 30 min before the operation.
2. Inhalation of isoflurane (1–2%) (within 100% oxygen) was given via a mask to anesthetize mice during the whole procedure. After the mice were placed on a supine position, the surgery area was scrubbed thoroughly three times with stepwise "10% Povidone Iodine Scrub" and 70% ethanol. When applying "10% Povidone Iodine Solution" and 70% ethanol to the surgical field, the solution-filled gauze was applied in a circular motion, from the center of the field towards the peripheral region.
3. A small midline incision was made in the lower abdomen passing through the skin layer, muscle layer, and the peritoneum into the abdominal cavity. Then, the bladder, seminal vesicles,

and prostate were partially moved out from the abdominal cavity to expose the dorsal prostate lobe.

4. Under an operating microscope, a total of 0.5×10^6 PC3-luc6 cells in 15 μL of saline (for orthotopic prostate model) or the same volume of cell-free saline (for sham-control) was injected in the dorsal prostate lobe using a 28 G insulin needle.
5. The organs were then returned into the body cavity, the muscle wall was closed with interrupted 4-0 absorbable sutures, and skin layer was closed with interrupted 5-0 nylon sutures.
6. Postoperatively, buprenorphine (0.1 mg kg^{-1}, administered subcutaneously and twice daily) was given to mice for 3 days. Saline solution (0.5 mL) was administered subcutaneously to mice immediately after the surgery to prevent dehydration. Postoperative antibiotic enrofloxacin was given to mice through drinking water (0.25 mg enrofloxacin/mL) for 7 days. After the completion of surgery, mice were transferred to a clean cage and allowed to wake up under observation.

3.2.2 Measurement of Tumor Volume Using MRI

MRI was used to confirm the presence of tumors and measure their volumes at various time points. Specifically, the animals were anesthetized using 2% isoflurane and placed in the body coil on the MRI scanner. MR images were acquired using a T2-weighted RARE sequence with a field of view (FOV) of 384×300 mm and a matrix size of 128 and 100 in the x and y directions, respectively. Tumor volumes were determined from the MR images using MicroView v2.2 (GE Healthcare, Waunakee, WI). Briefly, a 2D region of interest (ROI) was manually contoured around the tumor in each of the MR image slices. Integrating these ROIs generated a measurable 3D volume, which represented the tumor volume.

3.2.3 In Vivo Whole-Body Fluorescence Imaging (2D Imaging)

PC3-lu6 orthotopic prostate tumor-bearing and sham-control mice were intravenously injected with HPPS(NIR)-chol-siRNA, HPPS(NIR)-chol-si-scramble, or saline at various experimental concentrations. The in vivo whole-body fluorescence images were taken at various experimental time points by the CRI Maestro™ imaging system (CRI, USA) using an NIR filter (excitation filter: 725–755 nm, emission filter: 780 nm long pass, signal collection from 780 to 950 nm in 10 nm-step) with optimal exposure time to detect NIR signal (*see* **Note 5**).

3.2.4 CT-FMT Imaging and Image Co-registration

The in vivo tumor distribution of the chol-siRNA-loaded HPPS(NIR) was visualized using 3D imaging methods for small animals. Briefly, micro-CT was used to provide the anatomical reference and FMT was used to determine the 3D distribution of the chol-siRNA-loaded HPPS(NIR). Co-registration of CT and FMT images would provide a quantitative 3D visualization of the in vivo

distribution of the chol-siRNA-loaded HPPS(NIR) in tumor and surrounding tissues. Specifically, the animals were anesthetized using 2% isoflurane and stably immobilized in an FMT imaging cassette to prevent any movement of the animal during scanning and to provide a stable basis for CT-FMT image co-registration. The cassette was placed on the CT imaging bed and full-body 16-s anatomical micro-CT scans were performed. CT images were acquired at 80 kVp and 50 mA with a voxel size of 0.15 × 0.15 × 0.15 mm and a field of view of 15.7 cm (transaxial) and 10.2 cm (long). Immediately after each CT scan, the cassette was moved to the FMT chamber and secured in the FMT scanning stage. Using the vendor's software, the scan field was adjusted to cover the abdominal part of the animal, making sure that the prostate region was at the center of the field, to prevent border artifacts (*see* **Note 6**). The number of laser scanning points within the scan field was adjusted to approximately 128, the maximum allowed, ensuring high-quality imaging. FMT images were acquired at excitation and emission wavelengths of 745 nm and 770–800 nm, respectively, with a nominal voxel size of 1 mm^3. CT and FMT images were co-registered using the Inveon™ Research Workplace 3.0 (IRW) software (Siemens, USA). Specifically, there are four fiducial wells on the FMT imaging cassette as registration reference points, which were artificially placed on the exported FMT images by the vendor software. The imaging cassette was included in the CT scan, and thus the fiducial wells were present as well in the CT images. By matching these fiducial wells, CT and FMT images were co-registered.

3.2.5 *In Situ and Ex Vivo Fluorescence Imaging*

PC3-lu6 orthotopic prostate tumor-bearing and sham-control mice were intravenously injected with HPPS(NIR)-chol-siRNA, HPPS(NIR)-chol-si-scramble, or saline at various experimental concentrations. The whole-body, in situ, and ex vivo fluorescence images were taken at various experimental time points by the CRI Maestro™ imaging system using an NIR filter (excitation filter: 725–755 nm, emission filter: 780 nm long pass, signal collection from 780 to 950 nm in 10 nm-step) with exposure time of 10 ms to detect NIR signal (*see* **Note 5**).

3.2.6 *Confocal Imaging of Frozen Tumor Tissue Slice*

PC3-lu6 orthotopic prostate tumor-bearing mice were intravenously injected with HPPS-Cy5.5-chol-siRNA or Cy5.5-chol-siRNA at a Cy5.5-chol-siRNA dose of 1 mg kg^{-1}. After 24 h, the mice were sacrificed, and all tumors were subsequently frozen in liquid nitrogen and then cut into slides of 5 μm thickness using a Leica CM3050S cryostat. The frozen slides were mounted with DAPI containing mounting solution and imaged by Olympus FV1000 laser confocal scanning microscopy with excitation wavelengths of 405 nm (DAPI), and 633 nm (Cy5.5).

3.3 Using CT-FMT Co-registration Image to Guide Treatment Planning

3.3.1 FMT Quantification

With CT-FMT co-registration, the tumor was identified (Fig. 2a), a region of interest (ROI) was manually contoured around the tumor of the 3D FMT image (Fig. 2b), and the relative fluorescence intensity value of the region was quantified (images were normalized to background signal according to vendor instructions). For in vivo quantitative assessment of the HPPS(NIR)-chol-siRNA delivery in tumor, the fluorescence accumulation in mouse tumor was identified by CT-FMT co-registration and quantified by FMT fluorescence quantification every 24 h from immediately before the first dose to 48 h post the last dose

3.3.2 Assessment of Multiple-Dosing siRNA Delivery

Ten PC3-lu6 orthotopic prostate tumor-bearing mice were used in therapeutic study. Mice were subjected to treatment at day 7 after the tumor inoculation. They were randomly assigned to three treatment groups. Mice were administered intravenously with saline ($n=3$), HPPS(NIR)-chol-si-scramble ($n=3$), and HPPS(NIR)-chol-si-bcl-2 ($n=4$), respectively. They were given a treatment of six total doses with everyday injection of 200 μL saline or nanoparticles at the chol-siRNA dose of 10 mg kg^{-1}. All mice were sacrificed at 48 h post-last injection (day 14), and various organs and tumor tissues were excised for checking therapeutic response (Fig. 2c, d).

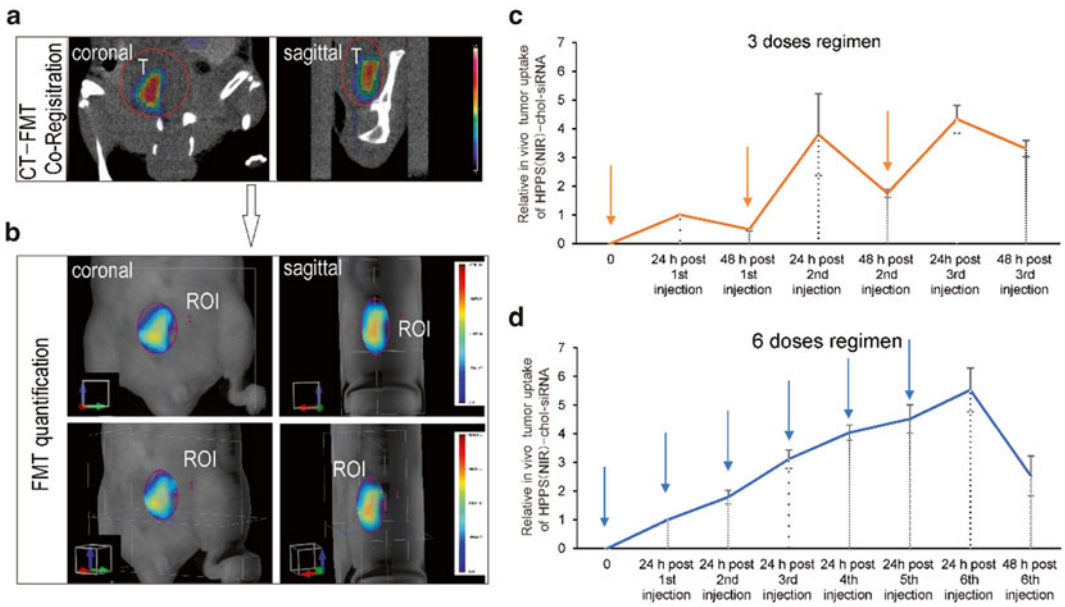

Fig. 2 CT-FMT image-guided assessment of multiple-dosing siRNA delivery. (**a**) The tumor margin was determined by CT-FMT co-registration imaging. (**b**) The relative accumulation of HPPS(NIR)-chol-siRNA in tumor was quantified by in vivo FMT fluorescence imaging. (**c**) The real-time fluorescence assessment of relative uptake of HPPS(NIR)-chol-siRNA in PC3-lu6 orthotropic tumor for the three-dose treatment regimen. (**d**) The real-time fluorescence assessment of relative uptake of HPPS(NIR)-chol-siRNA in PC3-lu6 orthotropic tumor for the six-dose treatment regimen. The *error bars* represent SEM and $n=3$ for each group. Reprinted with permission of John Wiley & Sons, Inc. [17]

3.4 In Vivo Therapeutic Efficacy Study

3.4.1 Polymerase Chain Reaction Assay

To observe bcl-2 gene expression, PCR was performed after treatment. Total RNA was isolated from each tumor tissue immediately after excision using an RNeasy Mini kit and quantified with Varian Cary 50 UV spectrophotometry. The amplification of cDNA was performed using qScript™ cDNA supermix kit according to vendor instructions. Amplification of the bcl-2 gene was conducted with a mixture of PCR master mix (12.5 μL, 2×), water (9.5 μL), oligonucleotide primer (1 μL), and cDNA (2 μL). 30 Cycles of amplification were run as follows: denaturation at 94 °C for 30 s, annealing at 57 °C for 30 s, and extension at 72 °C for 30 s using the primer: Bcl-2, sense 5′-TTCTTTGAGTTCGGTGGGGTC-3′, antisense 5′-GTGCTTGGCAATTAGTGGTCG-3′; beta 2-microglobulin (B2M), sense 5′-AGCAGAGAATGGAAAGTCAAA-3′, antisense 5′-TGTTGATGTTGGATAAGAGAA-3′. After amplification by PCR, samples were subjected to electrophoresis in 1% agarose gel containing 0.002% (v/v) Gel red. Gels were photographed with UV illumination and quantified by Image J software.

3.4.2 Terminal Deoxynucleotidyl Transferase dUTP Nick End Labeling Assay

Terminal deoxynucleotidyl transferase dUTP nick end labeling (TUNEL) assay was performed on frozen sections using in situ end-labeling technique for apoptosis.

1. Slides were fixed with 1% PFA in PBS, pH 7.4 preferably for 10 min at room temperature.
2. After draining off excess liquid and washing twice with PBS (5 min each), slides were post-fixed in precooled ethanol/acetic acid = 2:1 for 5 min at −20 °C. The ethanol:acetic acid mixture was removed and slides were washed with two changes of PBS.
3. Endogenous peroxidase activity was blocked using 3% aqueous hydrogen peroxide and endogenous biotin activity using avidin/biotin blocking kit.
4. Sections were treated with Buffer A (50 mM Tris–HCl (pH 7.5), 50 mM $MgCl_2$. 6 H_2O, 100 mM β-mercaptoethanol, and 0.005% BSA) for 5–10 min and then were incubated with a biotin-nucleotide cocktail in water bath at 37 °C for 1.5 h. After washing with PBS, slides were labeled with Ultra Streptavidin Horseradish Peroxidase Labeling Reagent (ID Labs inc.) for 30 min at room temperature.
5. The slides were then developed with freshly prepared DAB (Dako K3468) and counterstained with Mayer's hematoxylin. Lastly the slides were dehydrated and mounted.
6. Slides were scanned by Aperio Whole Slide Scanner and analyzed using Aperio ImageScope. Only DAB-positive staining apoptosis cells with the morphology of cytoplasmic condensation, loss of cell–cell contact, and cell shrinkage were counted as TUNEL-positive cells.

4 Notes

1. Chloroform is a flammable and hazardous solvent; thus all operation with the solvent must be done in a fume hood.
2. The DiR-BOA is a light-sensitive dye, and should be kept from light during the whole process.
3. RNase will degrade the siRNA, so all operations with siRNA involved should be kept RNase free. The working area should be cleaned up by RNaseZap solution to exclude any contamination.
4. As the sonication efficiency is critical to the nanoparticle preparation, such as its monodispersibility, yield, and reproducibility, keeping the consistent sonication setting is important. The water bath sonicator should be filled with water to the optimal level as marked inside the bath tank. The round-bottom flask should be positioned at the strongest sonication strength point inside the sonicator and kept at suitable depth, with the liquid level inside the flask at the same altitude level as the outside water of the water bath.
5. During fluorescence imaging, the exposure time is highly dependent on individual experiments and is usually adjusted to avoid overexposure while keeping significant signal-to-noise contrast.
6. The scan field must be appropriately sized around the site of interest to provide sufficient proximal and distal views for determining signal localization and quantification in 3D. Smaller anatomical sites such as paws, which present a challenge for optical tomography, can be imaged by placing them on an imaging block that mimics the density of normal tissue. This provides a robust means for trans-illuminating the paws and generating quantitative data.

Acknowledgements

The authors thank funding support from the China–Canada Joint Health Research Initiative (NSFC-30911120489, CIHR CCI-102936), the Natural Sciences and Engineering Research Council of Canada, the Canadian Institutes for Health Research, the Ontario Institute for Cancer Research, the Prostate Cancer Canada, the DLVR Therapeutics, the Canada Foundation for Innovation, the Princess Margaret Cancer Foundation, and the Joey and Toby Tanenbaum/Brazilian Ball Chair in Prostate Cancer Research.

References

1. Baker M (2010) Whole-animal imaging: the whole picture. Nature 463(7283):977–980
2. Ntziachristos V, Ripoll J, Wang LV, Weissleder R (2005) Looking and listening to light: the evolution of whole-body photonic imaging. Nat Biotechnol 23(3):313–320
3. Bumcrot D, Manoharan M, Koteliansky V, Sah DW (2006) RNAi therapeutics: a potential new class of pharmaceutical drugs. Nat Chem Biol 2(12):711–719
4. Whitehead KA, Langer R, Anderson DG (2009) Knocking down barriers: advances in siRNA delivery. Nat Rev Drug Discov 8(2): 129–138
5. Tandon P, Farahani K (2011) NCI image-guided drug delivery summit. Cancer Res 71(2):314–317
6. Lammers T, Kiessling F, Hennink WE, Storm G (2010) Nanotheranostics and image-guided drug delivery: current concepts and future directions. Mol Pharm 7(6):1899–1912
7. Mura S, Couvreur P (2012) Nanotheranostics for personalized medicine. Adv Drug Deliv Rev 64(13):1394–1416
8. Medarova Z, Pham W, Farrar C, Petkova V, Moore A (2007) In vivo imaging of siRNA delivery and silencing in tumors. Nat Med 13(3):372–377
9. Merkel OM, Librizzi D, Pfestroff A, Schurrat T, Buyens K, Sanders NN, De Smedt SC, Behe M, Kissel T (2009) Stability of siRNA polyplexes from poly(ethylenimine) and poly(ethylenimine)-g-poly(ethylene glycol) under in vivo conditions: effects on pharmacokinetics and biodistribution measured by Fluorescence Fluctuation Spectroscopy and Single Photon Emission Computed Tomography (SPECT) imaging. J Control Release 138(2):148–159
10. Bartlett DW, Su H, Hildebrandt IJ, Weber WA, Davis ME (2007) Impact of tumor-specific targeting on the biodistribution and efficacy of siRNA nanoparticles measured by multimodality in vivo imaging. Proc Natl Acad Sci U S A 104(39):15549–15554
11. Qi L, Gao X (2008) Quantum dot-amphipol nanocomplex for intracellular delivery and real-time imaging of siRNA. ACS Nano 2(7): 1403–1410
12. Tan WB, Jiang S, Zhang Y (2007) Quantum-dot based nanoparticles for targeted silencing of HER2/neu gene via RNA interference. Biomaterials 28(8):1565–1571
13. Cai W, Hsu AR, Li ZB, Chen X (2007) Are quantum dots ready for in vivo imaging in human subjects? Nanoscale Res Lett 2(6): 265–281
14. Weissleder R, Pittet MJ (2008) Imaging in the era of molecular oncology. Nature 452(7187): 580–589
15. Andreu N, Zelmer A, Wiles S (2011) Noninvasive biophotonic imaging for studies of infectious disease. FEMS Microbiol Rev 35(2):360–394
16. Ntziachristos V (2010) Going deeper than microscopy: the optical imaging frontier in biology. Nat Methods 7(8):603–614
17. Lin Q, Jin CS, Huang H, Ding L, Zhang Z, Chen J, Zheng G (2014) Nanoparticle-enabled, image-guided treatment planning of target specific RNAi therapeutics in an orthotopic prostate cancer model. Small 10(15):3072–3082
18. Zhang Z, Cao W, Jin H, Lovell JF, Yang M, Ding L, Chen J, Corbin I, Luo Q, Zheng G (2009) Biomimetic nanocarrier for direct cytosolic drug delivery. Angew Chem 48(48): 9171–9175
19. Mishra VK, Anantharamaiah GM, Segrest JP, Palgunachari MN, Chaddha M, Sham SW, Krishna NR (2006) Association of a model class A (apolipoprotein) amphipathic alpha helical peptide with lipid: high resolution NMR studies of peptide.lipid discoidal complexes. J Biol Chem 281(10):6511–6519

Chapter 15

In Vivo Fluorescence Imaging in the Second Near-Infrared Window Using Carbon Nanotubes

Guosong Hong and Hongjie Dai

Abstract

In vivo fluorescence imaging in the second near-infrared window (NIR-II window, 1000–1700 nm) is a powerful imaging technique that emerged in recent years. This imaging tool allows for noninvasive, deep-tissue visualization and interrogation of anatomical features and functions with improved imaging resolution and contrast at greater tissue penetration depths than traditional fluorescence imaging. Here, we present the detailed protocol for conducting NIR-II fluorescence imaging in live animals, including the procedures for preparation of biocompatible and NIR-II fluorescent carbon nanotube solution, live animal administration and NIR-II fluorescence image acquisition.

Key words Near-infrared II, Second near-infrared window, NIR-II fluorescence imaging, Carbon nanotubes, Tissue penetration, Photon scattering, Autofluorescence

1 Introduction

In vivo fluorescence imaging by detection of photons from fluorescent labels inside live animals under light excitation is a powerful and widely used technique that offers visualization of anatomical structures [1, 2], interrogation of functional biomolecules [3–5] and investigation of biochemical [6–8], physiological [9, 10], pharmacological [11, 12], and pathological processes [3, 13–15] in living organisms, owing to its high spatiotemporal resolution and sensitivity [16]. In vivo fluorescence imaging provides information that cannot be easily obtained from in vitro studies using cells and tissue sections, but in the meantime suffers from limited penetration depth that prevents high spatial resolution and sufficient signal-to-noise ratio (SNR) for deep tissue (beyond 100–200 μm) imaging in live experimental animals and human patients. The suboptimal penetration depth of conventional in vivo fluorescence imaging, which forms images by collecting fluorescence photons in the visible and near-infrared windows (400–1000 nm in wavelength), is the direct result of strong photon scattering and tissue

Mingfeng Bai (ed.), *In Vivo Fluorescence Imaging: Methods and Protocols*, Methods in Molecular Biology, vol. 1444,
DOI 10.1007/978-1-4939-3721-9_15,

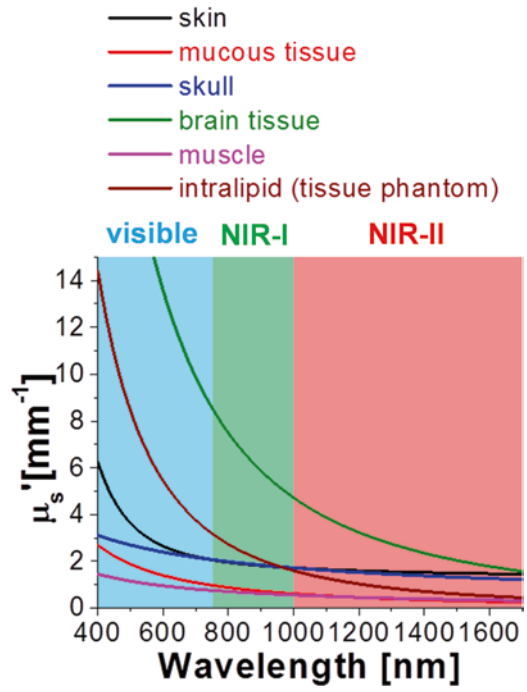

Fig. 1 Scattering coefficients of different biological tissues (skin: *black*; mucous tissue: *red*; skull: *blue*; brain tissue: *green*; muscle: *pink*) and tissue mimicking phantom (Intralipid: *brown*)

autofluorescence of thick biological tissues [17]. For most of the biological tissues such as the skin [18], mucous tissue [18], skull [19], brain tissue [20], and muscle [21], the amount of scattering of photons as they travel inside these tissues always scales inversely proportional to the photon wavelength, leading to significantly reduced amount of scattering with longer photon wavelengths (Fig. 1). On the other hand, it has been reported that tissue autofluorescence, which usually comes from endogenous chromophores inside the body, also decreases with increasing wavelengths, and becomes almost negligible beyond 1300 nm [22].

Therefore, in vivo fluorescence imaging should benefit from detection of fluorescence photons in the longer-wavelength, second near-infrared window (NIR-II window, 1000–1700 nm), owing to significantly reduced scattering and autofluorescence compared to the shorter-wavelength visible window (400–750 nm) and the traditional near-infrared window (NIR-I window, 750–1000 nm). Although longer wavelength photons in theory have lower diffraction-limited spatial resolution due to the linear dependence of diffraction limit on wavelength $\left(\sim \frac{0.61\lambda}{NA}\right)$, the dependence of scattering on wavelength scales exponentially $\left(\sim \lambda^{-\alpha}\right)$, suggesting as wavelength increases, the scattering-limited spatial resolution increases with a faster pace than the diffraction-

limited resolution decreases, in particular for thick and scattering biological samples. Since the first example demonstrating in vivo NIR-II fluorescence imaging of live animals in 2009 [23], our lab and others have established and improved the NIR-II imaging technique using a wide range of fluorophores with intrinsic photoluminescence in the NIR-II window, including single-walled carbon nanotubes [2, 23–33], chalcogenide quantum dots [34–43], rare-earth doped nanoparticles [22, 44–46], polymers [47], and organic molecules [48]. The crisp imaging resolution and sufficient signal contrast even at depths of several millimeters inside the tissue have allowed for anatomical and functional imaging of live experimental animals in a variety of disease models including cancer [24, 25, 33, 35], bacterial infection [32], cardiovascular [26, 30], and cerebrovascular diseases [29]. In this chapter, we will discuss the detailed protocol for performing in vivo NIR-II fluorescence imaging using single-walled carbon nanotubes (SWCNTs) as fluorescence labels in live animals.

2 Materials

All aqueous solutions should be prepared using deionized ultrafiltered (DIUF) water.

2.1 Preparation of Biocompatible SWCNT Solution

1. Raw HiPco single-walled carbon nanotube distributed in a wet, mud-like mixture with ethanol (Unidym).
2. Sodium deoxycholate (Sigma-Aldrich).
3. DSPE-mPEG (5 kDa) (1,2-distearoyl-sn-glycero-3--phosphoethanolamine-*N*-[methoxy(polyethyleneglycol, 5000)], Laysan Bio).
4. Regenerated cellulose dialysis tubing (3500 Da, Fisher Scientific).
5. Amicon® Ultra-4 Centrifugal Filter Units (30 kDa, Millipore).
6. Phosphate buffered saline, 10× Solution (Fisher).
7. Bath sonicator (Cole-Parmer, Model #08849-00).
8. 3.5 mL polycarbonate centrifuge tube and L8-60M ultracentrifuge (Beckman Coulter).

2.2 In Vivo SWCNT Administration

1. Experimental animals: athymic nude mice, Balb/c mice, and C57Bl/6 mice (*see* **Note 1** for more information).
2. 28 G insulin syringe (BD).
3. Hair removal gel (Nair).
4. Rodent gas (isoflurane) anesthesia system.
5. Clear Transpore Medical Tape (3 M).

2.3 In Vivo NIR-II Imaging System

1. Two-dimensional (2D) InGaAs detector array (2D OMA-V, Princeton Instruments).
2. 808-nm laser diode (RMPC lasers).
3. Optical fiber with a 4.5-mm focal length collimator (Thorlabs).
4. Achromatic doublet lenses with antireflective coating in the 1050–1620 nm range (Thorlabs). Three lenses with focal lengths of 75, 150, and 200 mm are needed.
5. Excitation filters including 850-nm shortpass and 1000-nm shortpass filters (Thorlabs).
6. Emission filters including 910-nm longpass, 1000-nm longpass, 1300-nm longpass and 1400-nm shortpass filters.
7. Silver-coated mirror with broad reflection band covering the NIR-II region (Thorlabs).

3 Methods

3.1 Preparation of Biocompatible SWCNT Solution for Injection

1. Raw HiPco SWCNTs from Unidym are mixed with ethanol in a slurry form to prevent aerosolization and inhalation. The slurry contains 12.3% raw HiPco SWCNTs by weight, therefore, to make an SWCNT solution solubilized by sodium deoxycholate with a SWCNT concentration of 0.25 mg/mL, 2 mg (0.25 mg/12.3% = 2.03 mg) of the SWCNT-containing slurry is weighed per millimeter of DIUF water. Weigh sodium deoxycholate to reach a concentration of 10 mg/mL. Mix the weighed SWCNT, sodium deoxycholate and DIUF in a 20 mL glass vial and make sure sodium deoxycholate dissolves in water.
2. Place the glass vial with well mixed chemicals in a bath sonicator and sonicate for 1 h. Pause sonication and replace the water bath every 20 min to avoid overheating of the solution (*see* **Notes 2** and **3** for more information).
3. After sonication the mixture inside the glass vial should look completely black with minimum amount of precipitates at the bottom. Carefully decant the suspension into the 3.5 mL polycarbonate centrifuge tubes and perform ultracentrifugation at 300,000 × *g* for 30 min to remove bundles and aggregates. Collect the supernatant, which should still look black after ultracentrifugation, into another 20 mL glass vial.
4. Add DSPE-mPEG (5 kDa) to the supernatant to reach a concentration of 1 mg/mL. Briefly sonicate the solution for 5 min to fully dissolve the DSPE-mPEG (5 kDa) powders. Load the suspension into the 3500 Da dialysis tubing and perform dialysis in a 1 L beaker containing 1× PBS solution, which is made by diluting the 10× buffer with water and used for pH control at 7.4 during the dialysis process (*see* **Note 4** for more information).

Keep the dialysis bath under vigorous stirring using a magnetic stir bar to speed up the dialysis process. It is recommended to change the 1× PBS dialysis buffer every 2 h for the first three bath changes, while the time interval for bath changes can increase as the bath gets less and less bubbly after multiple changes. A good end point for dialysis can be determined by leaving the dialysis bath unchanged for 12 h before taking some of the bath solution and checking for bubbliness. Usually it takes 6–8 bath changes with a total duration of 36–48 h to completely remove the small molecule surfactant (i.e., sodium deoxycholate) from the SWCNT suspension.

5. After dialysis is finished, carefully decant the SWCNT suspension into the 3.5 mL polycarbonate centrifuge tubes and perform ultracentrifugation at 300,000 × g for 30 min to remove bundles and aggregates that have formed during the dialysis process. Collect the supernatant.
6. Load the ultracentrifuged suspension of SWCNT, which should now be coated with the biocompatible polymeric surfactant, DSPE-mPEG, into 4 mL centrifugal filters with a cut-off size of 30 kDa (*see* **Note 5** for more information). Perform centrifugation at 4000 × g for 10 min to reduce the total volume of SWCNT solution to ≤400 μL. Resuspend the concentrated SWCNT solution to 4 mL with DIUF water, and repeat the above step for at least six times, which should reduce the concentration of free DSPE-mPEG molecules in the SWCNT suspension by one million times.
7. Collect the retentate from the centrifugal filter and add 10× PBS to this concentrated SWCNT suspension to make a final PBS concentration of 1×. Measure the UV–Vis-NIR absorption spectrum of this solution, and use the absorbance at 808 nm to compute the concentration of SWCNT according to the mass extinction coefficient of 46.0 L g^{-1} cm^{-1} [24, 49]. Adjust the concentration of SWCNT by either centrifugal filtration or dilution in 1× PBS to desired concentration. For in vivo mouse whole body imaging, the desired concentration is 0.085 g L^{-1} [2]. For in vivo mouse hind limb vascular imaging, the desired concentration is 0.10 g L^{-1} [26]. For in vivo mouse brain vascular imaging, the desired concentration is 0.43 g L^{-1} [29].

3.2 In Vivo NIR-II Fluorescence Imaging Setup

1. The in vivo NIR-II fluorescence imaging setup is assembled according to Fig. 2, which is comprised of a 256 × 320 pixel InGaAs camera, a pair of lenses for imaging formation (L*i* and L*j*, where *i*, *j* = 1,2,3), excitation and emission filters (F1 and F2), an animal platform (PF), a mirror (M), and a fiber-coupled 808-nm laser diode (LS). The 2D InGaAs camera (DT) should be placed at a distance of roughly 350 mm from the

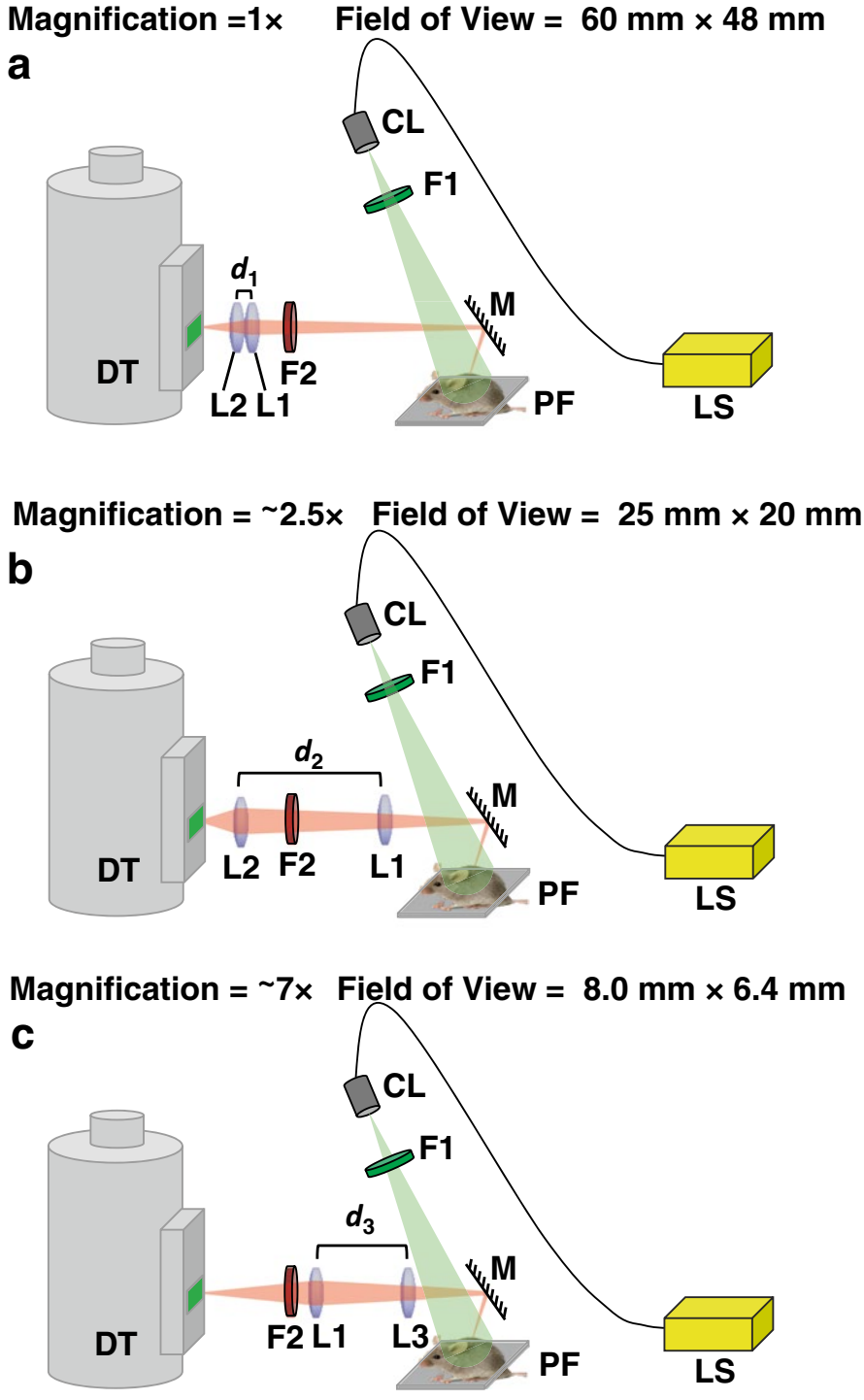

Fig. 2 Setups for in vivo NIR-II fluorescence imaging under different magnifications. (**a**) Optical diagram for in vivo NIR-II fluorescence imaging with a field of view of 60 × 48 mm that covers the entire mouse body, with $d_1 = 0$ mm. (**b**) Optical diagram for in vivo NIR-II fluorescence imaging with a field of view of 25 × 20 mm (~2.5× higher magnification than (**a**)) that covers one of the mouse hind limbs or the entire mouse head, with $d_2 = 200$ mm. (**c**) Optical diagram for in vivo NIR-II fluorescence imaging with a field of view of 8 × 6.4 mm (~7× higher magnification than (**a**)) that covers part of the mouse hind limb or part of the mouse brain, with $d_3 = 150$ mm. *CL:* collimator, *DT:* 2D InGaAs detector, *F1:* excitation filter set, *F2:* emission filter set, *L1*: 200-mm lens, *L2:* 75-mm lens, *L3:* 150-mm lens, *LS*: 808-nm laser diode, *M*: mirror, *PF*: animal platform

animal platform with its active area facing the platform. The InGaAs camera is mounted on a 2D translation stage allowing for fine position adjustment later during the experiment. A nose cone is mounted on the animal platform for inhalational anesthesia during the in vivo imaging experiment.

2. The magnification of the in vivo NIR-II fluorescence imaging can be adjusted by placing different lens sets between the InGaAs camera and the animal platform, and by changing the distance between the lenses. To achieve a field of view of 60 mm × 48 mm, that covers most of the mouse body, two touching NIR-II achromatic doublets ($d_1 = 0$ mm) with focal lengths of 75-mm (L2) and 200-mm (L1) are placed in front of the 2D InGaAs camera (DT) where the 75 mm lens, which is closer to the camera, is placed at a distance of ~40 mm from the camera (Fig. 2a). A field of view of 25 × 20 mm that covers one of the hind limbs or the entire head, can be achieved by placing the 75-mm lens (L2) at a distance of ~50 mm in front of the camera and the 200-mm lens (L1) at a distance of 200 mm ($d_2 = 200$ mm) from lens L2 (Fig. 2b). This should give a roughly 2.5-fold higher magnification than shown in Fig. 2a, and the magnification can be continuously adjusted from 1× to 2.5× by changing the distance between L1 and L2 from 0 mm (1×) to 200 mm (2.5×). An even higher magnification without using any microscopic objective can be achieved by using a 200-mm lens (L1) and a 150-mm lens (L3), with both the camera-L1 distance and the L1–L3 distance being roughly 150 mm ($d_3 = 150$ mm).
3. An excitation filter set comprised of an 850-nm shortpass and a 1000-nm shortpass filter is used to filter out the long-wavelength photons from the fiber-coupled 808-nm laser diode. An emission filter set comprised of a 910-nm longpass and a 1000-nm longpass filter is used to take in vivo fluorescence images in the entire NIR-II window (1000–1700 nm, with the upper bound determined by the responsivity cutoff of the 2D InGaAs camera), and an emission filter set comprised of a 1000-nm longpass, a 1300-nm longpass and a 1400-nm shortpass filter is used to take in vivo fluorescence images in the NIR-IIa window (1300–1400 nm) [29].
4. To adjust the focal plane of the in vivo NIR-II imaging setup, a 2D translation stage on which the 2D InGaAs camera is mounted can be adjusted along the optical axis of the imaging system to achieve the sharpest image. The location of the excitation beam should be aligned to the camera field of view of the animal platform, and the in-plane profile of the excitation power should be recorded using a sample with sufficient autofluorescence emission in the NIR-II window, such as a silicon wafer, and used later for flat-field correction. A typical power density of 808-nm laser excitation is 140 mW cm^{-2}, lower than the reported safe exposure limit of 329 mW cm^{-2} at 808 nm [50].

3.3 In Vivo Administration of SWCNT Solution and Image Acquisition

1. All animal experiments must be conducted in accordance with established animal care guidelines and protocols approved by the relevant authorities. Experimental animal is anesthetized inside an induction chamber using vaporized isoflurane gas before in vivo administration of the SWCNT solution. A gaseous mixture of O_2 at a flow rate of 2 L min^{-1} and 3% isoflurane is delivered into the induction chamber for inhalational anesthesia. After the mouse is anesthetized, the scalp skin is depilated (*see* **Note 6** for more information) and the animal is transferred to the imaging platform (Fig. 2) where a nose cone delivering 3% isoflurane mixed with 1.5 L min^{-1} O_2 flow is used throughout imaging. The mouse body is fixed onto the imaging platform with medical tapes to expose the area for imaging. Use the ambient room light to adjust the focus of the imaging system based on white-light optical images of the mouse (*see* **Note 7** for more information).
2. A 28 G insulin syringe is used to draw the SWCNT solution in 1× PBS with desired concentration. For intravenous administration of the SWCNT solution, the insulin syringe needle is inserted into the tail vein of the mouse, and the person performing injection should hold the syringe steadily inside the mouse tail vein until receiving a signal to start bolus injection in a synchronized manner with the dynamic image acquisition on the camera that collects NIR-II fluorescence under 808-nm excitation (*see* **Note 8** for more information).
3. The dynamic NIR-II video-rate recording can achieve a maximum frame rate of ~50 frames per second (fps), given an overhead time of 19 ms due to data readout on the 2D OMA-V InGaAs camera [47]. Depending on the exposure time for each frame, the actual frame rate will always be less than 50 fps, owing to an intrinsic tradeoff between SNR and temporal resolution. Static NIR-II fluorescence images can also be taken by capturing one image at a time in a noncontinuous acquisition mode, with a typical exposure time between 50 and 500 ms.

3.4 Post-acquisition Processing of In Vivo NIR-II Fluorescence Images

1. In Vivo NIR-II fluorescence images need to be flat-field corrected to account for the spatial nonuniformity of the excitation power in the imaging plane. Flat-field correction is typically achieved by dividing the original raw image by the flat-field correction file pixel by pixel (*see* **Note 9** for more information).
2. Static NIR-II fluorescence images can be plotted directly in common image analysis software, such as Matlab and ImageJ, mapped to any given colormap. Representative NIR-II images of the entire mouse body in prone position, mouse hind limb vasculature in medial view, and mouse brain vasculature in coronal view through intact scalp and skull are shown in Fig. 3a–c [2, 26, 29] (*see* **Note 10** for more information).

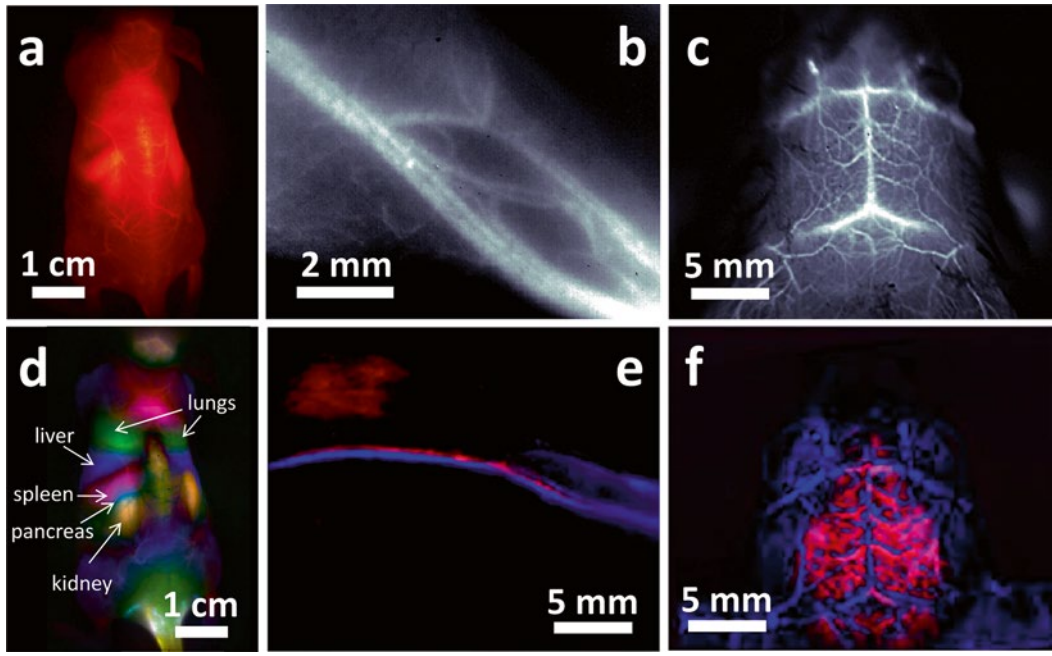

Fig. 3 Typical static and dynamic in vivo NIR-II fluorescence images. (**a**) An NIR-II fluorescence image of a nude mouse in its prone position at 69 s after intravenous injection of SWCNTs. (**b**) An NIR-II fluorescence image of the hindlimb of a nude mouse in the medial view at 10 min after intravenous injection of SWCNTs. (**c**) An NIR-IIa fluorescence image of a C57Bl/6 mouse with hair shaved off the head, showing the brain vasculature in the coronal view through intact scalp and skull. (**d**) A dynamic contrast enhanced NIR-II image showing the anatomical registration of mouse internal organs based on the difference of blood flow dynamics in these organs. (**e**) A dynamic contrast enhanced NIR-II image showing the differentiation of femoral artery (red) from the femoral vein (*blue*) based on the hemodynamic difference between arterial and venous vessels. (**f**) A dynamic contrast enhanced NIR-IIa image showing the differentiation of cerebral arteries (*red*) from the cerebral veins (*blue*) based on the hemodynamic difference between arterial and venous vessels

3. Dynamic NIR-II fluorescence images can also be processed with the above software to generate real-time videos that play the images in a continuous way.
4. Dynamically enhanced spatial contrast can be obtained by performing principal component analysis (PCA) to the time stack of 2D NIR-II fluorescence images, where each pixel of the 2D images with the same size is an independent observation, while the time of acquisition for each 2D image is an independent variable. PCA groups observations (pixels) with similar variable dependence (similar time variance) into common principal components, which can be color-coded to enhance the spatial contrast, reveal internal organs [2] and differentiate arterial and venous vessels [26, 29]. PCA can be performed using the built-in *princomp* function in Matlab and PCA overlaid images can be plotted with false color coding. Representative PCA-processed NIR-II images of the entire mouse body showing the anatomical registration of internal

organs, the mouse hindlimb showing differentiation between femoral arteries and veins, and the mouse brain showing differentiation between cerebral arteries and vein are shown in Fig. 3d–f [2, 26, 29].

4 Notes

1. Different mouse strains are usually selected for in vivo mouse imaging with different purposes. In general, athymic nude mice are typically used for NIR-II mouse whole-body imaging and hindlimb vascular imaging without the need to shave the hair before imaging [2, 23, 26, 30]. Balb/c mice are usually used for NIR-II in vivo tumor imaging owing to the ease of tumor inoculation; as a tradeoff, they need to be shaved over the imaged area before imaging [25]. C57Bl/6 mice are usually used for brain vascular imaging with surgery-induced brain vascular alterations, and their relatively larger sizes than the other two mouse strains facilitate the brain vascular surgeries [29]; similar to Balb/c mice, the hair over the imaged area (in this case, the scalp) needs to be removed before imaging.
2. To obtain the highest physical yield and fluorescence quantum efficiency of nanotube suspension during sonication, it is recommended to use a total volume between 4 and 12 mL in a 20 mL glass vial. Water bath in the sonicator should be filled to a certain level that affords the strongest sonication power. The glass vial containing the mixture of DIUF water, SWCNT and sodium deoxycholate should be fixed by a clamp, and the angle and position of the glass vial with respect to the water bath should be adjusted such that there is enough agitation of the water's surface in the glass vial.
3. The temperature of the SWCNT solution needs to be well controlled and below 50 °C, since high temperature leads to instability and precipitation of the SWCNT solution.
4. The dialysis bath needs to have stringent pH control at 7.4, since the small micellar surfactant used to suspend SWCNTs in the first place, sodium deoxycholate, is the salt of a weak acid with a pK_a of 6.58. Therefore, if the dialysis bath has a pH of <6.58 (such as in pure DIUF water or DI water with saturated CO_2), the majority of sodium deoxycholate would form an insoluble form of deoxycholic acid, leading to precipitation and less effective dialysis of SWCNTs.
5. During the centrifugal filtration step, ideally any centrifugal filter with a cutoff size of >5 kDa, which is the molecular weight of DSPE-mPEG, should be able to remove the excess surfactant in the SWCNT suspension. However, we have found in our experiments many times that, if the cutoff size is just above

5 kDa (such as 10 kDa), the removal efficiency is very low and it takes much longer time to achieve the same percentage of removal of excessive, free DSPE-mPEG surfactants; on the other hand, if the cutoff size is too large (such as 100 kDa), the SWCNTs tend to block the filter membrane, leading to very slow filtration of the solution as well. Therefore, the best cutoff size should be 30 kDa for the centrifugal filter.

6. Extreme caution should be paid when using Nair to remove the hair over the area of interest, since excessive Nair over the skin can cause inflammation and bruise to the tissue, while intravenously administered SWCNTs tend to accumulate in the inflammation sites during circulation and lead to undesired image artifacts showing higher NIR-II signals in these sites.
7. There is usually a few millimeter offset between the focal plane of the NIR-II fluorescence image and the white-light optical image for the same animal, owing to the deeper penetration depth of NIR-II fluorescence photons. Prior to dynamic NIR-II fluorescence image acquisition, focus the imaging system onto the skin of the mouse with the ambient white light, and then move the focal plane ~2 mm under the surface of the skin using the translation stage of the InGaAs camera. This new focal plane should achieve a sharp image in the NIR-II window for dynamic imaging later, during which any further adjustment of the imaging system should be avoided.
8. Synchronized intravenous injection of SWCNT solution with image acquisition turns out to be the most critical and the most difficult step throughout the entire procedure. This step is extremely tricky since the insertion of the needle needs to be performed with ambient light to guide the insertion process, while image acquisition has to be performed in complete darkness to minimize the ambient light interference. Since the bolus injection and the acquisition of dynamic NIR-II images need to be synchronized, the motion of injection needs to be performed in dark as well, following the motion of needle insertion that requires ambient light. It is thus recommended for the readers to reproduce this step as follows with at least two people cooperating on this process:
   (a) One person ("the injector") inserts the needle into the mouse tail vein in the presence of the ambient light and hold the syringe steadily without moving in any direction to avoid missing the tail vein. There are a few ways to make sure the needle is indeed inside the tail vein: the injector can push the plunge a little bit (without injecting an appreciable amount of solution) to test the resistance the plunger feels, and if the needle is inside the tail vein the resistance should be minimal; alternatively the injector can connect the insulin syringe with a catheter tubing, and

when the needle of the catheter tubing is inserted into the tail vein, venous blood can be observed to start filling back into the catheter tubing on its own blood pressure. It is important to keep the needle steadily inside the mouse tail vein, otherwise the needle may puncture through the vessel wall and miss the tail vein for bolus injection later.

(b) The other person ("the operator") should open all related programs for image acquisition on the computer and make sure image acquisition can be started by a single click. Make sure the injection site and the syringe for injection are both outside of the field of view to avoid saturation of the dynamic range of the camera. The operator turns off any ambient light when the injector has successfully inserted the needle into the tail vein and is ready to perform bolus injection. Then the operator should signal the injector to start injection when starting dynamic NIR-II image acquisition simultaneously. This ensures the first image, which is usually used for background subtraction of the camera, is taken without any ambient light interference and before any SWCNT fluorophore is injected and contributes any signal in the field of view. This practice also minimizes the amount time the injector has to hold the needle inside the tail vein without any movement.

(c) Once the bolus of SWCNT solution is all injected into the tail vein, the injector should carefully withdraw the needle without causing any appreciable motion of any part of the mouse body inside the imaging field of view.

(d) When the imaging program has finished acquiring the needed number of frames, the operator stops the program and turns on the ambient light.

9. Flat-field correction file should be taken using a perfectly flat sample with uniform autofluorescence in the NIR-II window throughout the entire field of view when illuminated by the 808-nm laser. A single-crystalline Si wafer with its area larger than the field of view should thus fit this purpose. To acquire the NIR-II image as the flat-field correction file, it is recommended to use the longest possible exposure time that does not cause any pixel saturation in the image. Number of iterations can also be increased to make a smooth enough correction file that helps reduce the noise level after flat-field correction.

10. In vivo static NIR-II vascular imaging should be performed within certain time window, which is determined by the blood circulation half-life of the SWCNT solution. For DSPE-mPEG (5 kDa) coated SWCNTs with a circulation half-life of approximately 5 h [2], in vivo static vascular imaging should be taken within 5 h post injection to minimize the tissue uptake and afford the maximum signal-to-background ratio [29].

Acknowledgments

We thank members from the Dai lab, in particular Shuo Diao, Alexander L. Antaris, and Dr. Xiaodong Zhang for helpful discussion and support. This study is supported by grants from the National Cancer Institute of US National Institute of Health to H.D. (5R01CA135109-02).

References

1. Hillman EMC, Moore A (2007) All-optical anatomical co-registration for molecular imaging of small animals using dynamic contrast. Nat Photonics 1(9):526–530
2. Welsher K, Sherlock SP, Dai HJ (2011) Deep-tissue anatomical imaging of mice using carbon nanotube fluorophores in the second near-infrared window. Proc Natl Acad Sci U S A 108(22):8943–8948
3. Ye DJ, Shuhendler AJ, Cui LN, Tong L, Tee SS, Tikhomirov G, Felsher DW, Rao JH (2014) Bioorthogonal cyclization-mediated in situ self-assembly of small-molecule probes for imaging caspase activity in vivo. Nat Chem 6(6):519–526
4. Hilderbrand SA, Weissleder R (2010) Near-infrared fluorescence: application to in vivo molecular imaging. Curr Opin Chem Biol 14(1):71–79
5. Blow N (2009) In vivo molecular imaging: the inside job. Nat Methods 6(6):465–469
6. Grewe BF, Langer D, Kasper H, Kampa BM, Helmchen F (2010) High-speed in vivo calcium imaging reveals neuronal network activity with near-millisecond precision. Nat Methods 7(5):399–405
7. Nguyen QT, Schroeder LF, Mank M, Muller A, Taylor P, Griesbeck O, Kleinfeld D (2010) An in vivo biosensor for neurotransmitter release and in situ receptor activity. Nat Neurosci 13(1):127–132
8. Marvin JS, Borghuis BG, Tian L, Cichon J, Harnett MT, Akerboom J, Gordus A, Renninger SL, Chen TW, Bargmann CI, Orger MB, Schreiter ER, Demb JB, Gan WB, Hires SA, Looger LL (2013) An optimized fluorescent probe for visualizing glutamate neurotransmission. Nat Methods 10(2):162–170
9. Chen Q, Cichon J, Wang WT, Qiu L, Lee SJR, Campbell NR, DeStefino N, Goard MJ, Fu ZY, Yasuda R, Looger LL, Arenkiel BR, Gan WB, Feng GP (2012) Imaging neural activity using Thy1-GCaMP transgenic mice. Neuron 76(2):297–308
10. Trachtenberg JT, Chen BE, Knott GW, Feng GP, Sanes JR, Welker E, Svoboda K (2002) Long-term in vivo imaging of experience-dependent synaptic plasticity in adult cortex. Nature 420(6917):788–794
11. Gao JH, Chen K, Luong R, Bouley DM, Mao H, Qiao TC, Gambhir SS, Cheng Z (2012) A novel clinically translatable fluorescent nanoparticle for targeted molecular imaging of tumors in living subjects. Nano Lett 12(1): 281–286
12. Shuhendler AJ, Pu KY, Cui L, Uetrecht JP, Rao JH (2014) Real-time imaging of oxidative and nitrosative stress in the liver of live animals for drug-toxicity testing. Nat Biotechnol 32(4):373–380
13. Weissleder R, Tung CH, Mahmood U, Bogdanov A (1999) In vivo imaging of tumors with protease-activated near-infrared fluorescent probes. Nat Biotechnol 17(4):375–378
14. Zhang XL, Tian YL, Li Z, Tian XY, Sun HB, Liu H, Moore A, Ran CZ (2013) Design and synthesis of curcumin analogues for in vivo fluorescence imaging and inhibiting copper-induced cross-linking of amyloid beta species in Alzheimer's disease. J Am Chem Soc 135(44):16397–16409
15. Sosnovik DE, Nahrendorf M, Deliolanis N, Novikov M, Aikawa E, Josephson L, Rosenzweig A, Weissleder R, Ntziachristos V (2007) Fluorescence tomography and magnetic resonance imaging of myocardial macrophage infiltration in infarcted myocardium in vivo. Circulation 115(11):1384–1391
16. Rao JH, Dragulescu-Andrasi A, Yao HQ, Yao HQ (2007) Fluorescence imaging in vivo: recent advances. Curr Opin Biotechnol 18(1):17–25
17. Lim YT, Kim S, Nakayama A, Stott NE, Bawendi MG, Frangioni JV (2003) Selection of quantum dot wavelengths for biomedical assays and imaging. Mol Imaging 2(1):50–64
18. Bashkatov AN, Genina EA, Kochubey VI, Tuchin VV (2005) Optical properties of

human skin, subcutaneous and mucous tissues in the wavelength range from 400 to 2000 nm. J Phys D Appl Phys 38(15):2543–2555

19. Bashkatov AN, Genina EA, Kochubey VI, Tuchin VV (2006) Optical properties of human cranial bone in the spectral range from 800 to 2000 nm - art. no. 616310. Saratov Fall Meeting 2005: Optical technologies in biophysics and medicine VII.6163: 16310
20. Horton NG, Wang K, Kobat D, Clark CG, Wise FW, Schaffer CB, Xu C (2013) In vivo three-photon microscopy of subcortical structures within an intact mouse brain. Nat Photonics 7(3):205–209
21. Bashkatov AN, Genina EA, Tuchin VV (2011) Optical properties of skin, subcutaneous, and muscle tissues: a review. J Innov Opt Health Sci 4(1):9–38
22. Villa I, Vedda A, Cantarelli IX, Pedroni M, Piccinelli F, Bettinelli M, Speghini A, Quintanilla M, Vetrone F, Rocha U, Jacinto C, Carrasco E, Rodríguez FS, Juarranz Á, del Rosal B, Ortgies DH, Gonzalez PH, Solé JG, Jaque GD (2015) 1.3 μm emitting SrF2: Nd3+ nanoparticles for high contrast in vivo imaging in the second biological window. Nano Res 8(2):649–665
23. Welsher K, Liu Z, Sherlock SP, Robinson JT, Chen Z, Daranciang D, Dai HJ (2009) A route to brightly fluorescent carbon nanotubes for near-infrared imaging in mice. Nat Nanotechnol 4(11):773–780
24. Robinson JT, Welsher K, Tabakman SM, Sherlock SP, Wang HL, Luong R, Dai HJ (2010) High performance in vivo near-IR (>1 μm) imaging and photothermal cancer therapy with carbon nanotubes. Nano Res 3(11):779–793
25. Robinson JT, Hong GS, Liang YY, Zhang B, Yaghi OK, Dai HJ (2012) In vivo fluorescence imaging in the second near-infrared window with long circulating carbon nanotubes capable of ultrahigh tumor uptake. J Am Chem Soc 134(25):10664–10669
26. Hong GS, Lee JC, Robinson JT, Raaz U, Xie LM, Huang NF, Cooke JP, Dai HJ (2012) Multifunctional in vivo vascular imaging using near-infrared II fluorescence. Nat Med 18(12):1841
27. Diao S, Hong GS, Robinson JT, Jiao LY, Antaris AL, Wu JZ, Choi CL, Dai HJ (2012) Chirality enriched (12,1) and (11,3) single-walled carbon nanotubes for biological imaging. J Am Chem Soc 134(41):16971–16974
28. Antaris AL, Robinson JT, Yaghi OK, Hong GS, Diao S, Luong R, Dai HJ (2013) Ultralow doses of chirality sorted (6,5) carbon nanotubes for simultaneous tumor imaging and photothermal therapy. ACS Nano 7(4):3644–3652
29. Hong GS, Diao S, Chang J, Antaris AL, Chen C, Zhang B, Zhao S, Atochin DN, Huang PL, Andreasson KI, Kuo CJ, Dai HJ (2014) Through-skull fluorescence imaging of the brain in a new near-infrared window. Nat Photonics 8:723–730
30. Hong GS, Lee JC, Jha A, Diao S, Nakayama KH, Hou LQ, Doyle TC, Robinson JT, Antaris AL, Dai HJ, Cooke JP, Huang NF (2014) Near-infrared II fluorescence for imaging hindlimb vessel regeneration with dynamic tissue perfusion measurement. Circ Cardiovasc Imaging 7(3):517–525
31. Yi HJ, Ghosh D, Ham MH, Qi JF, Barone PW, Strano MS, Belcher AM (2012) M13 phage-functionalized single-walled carbon nanotubes as nanoprobes for second near-infrared window fluorescence imaging of targeted tumors. Nano Lett 12(3):1176–1183
32. Bardhan NM, Ghosh D, Belcher AM (2014) Carbon nanotubes as in vivo bacterial probes. Nat Commun 5:4918
33. Ghosh D, Bagley AF, Na YJ, Birrer MJ, Bhatia SN, Belcher AM (2014) Deep, noninvasive imaging and surgical guidance of submillimeter tumors using targeted M13-stabilized single-walled carbon nanotubes. Proc Natl Acad Sci U S A 111(38):13948–13953
34. Zhang Y, Hong GS, Zhang YJ, Chen GC, Li F, Dai HJ, Wang QB (2012) Ag2S quantum dot: a bright and biocompatible fluorescent nanoprobe in the second near-infrared window. ACS Nano 6(5):3695–3702
35. Hong GS, Robinson JT, Zhang YJ, Diao S, Antaris AL, Wang QB, Dai HJ (2012) In vivo fluorescence imaging with Ag2S quantum dots in the second near-infrared region. Angew Chem Int Ed Engl 51(39):9818–9821
36. Zhang Y, Zhang YJ, Hong GS, He W, Zhou K, Yang K, Li F, Chen GC, Liu Z, Dai HJ, Wang QB (2013) Biodistribution, pharmacokinetics and toxicology of Ag2S near-infrared quantum dots in mice. Biomaterials 34(14): 3639–3646
37. Dong BH, Li CY, Chen GC, Zhang YJ, Zhang Y, Deng MJ, Wang QB (2013) Facile synthesis of highly photoluminescent Ag2Se quantum dots as a new fluorescent probe in the second near-infrared window for in vivo imaging. Chem Mater 25(12):2503–2509
38. Chen GC, Tian F, Zhang Y, Zhang YJ, Li CY, Wang QB (2014) Tracking of transplanted human mesenchymal stem cells in living mice using near-infrared Ag-2 S quantum dots. Adv Funct Mater 24(17):2481–2488

39. Li CY, Zhang YJ, Wang M, Zhang Y, Chen GC, Li L, Wu DM, Wang QB (2014) In vivo real-time visualization of tissue blood flow and angiogenesis using Ag2S quantum dots in the NIR-II window. Biomaterials 35(1):393–400
40. Hu F, Li C, Zhang Y, Wang M, Wu D, Wang Q (2015) Real-time in vivo visualization of tumor therapy by a near-infrared-II Ag2S quantum dot-based theranostic nanoplatform. Nano Res 8(5):1637–1647
41. Tsukasaki Y, Morimatsu M, Nishimura G, Sakata T, Yasuda H, Komatsuzaki A, Watanabe TM, Jin T (2014) Synthesis and optical properties of emission-tunable PbS/CdS core-shell quantum dots for in vivo fluorescence imaging in the second near-infrared window. Rsc Adv 4(77):41164–41171
42. Tsukasaki Y, Komatsuzaki A, Mori Y, Ma Q, Yoshioka Y, Jin T (2014) A short-wavelength infrared emitting multimodal probe for non-invasive visualization of phagocyte cell migration in living mice. Chem Commun 50(92): 14356–14359
43. Nakane Y, Tsukasaki Y, Sakata T, Yasuda H, Jin T (2013) Aqueous synthesis of glutathione-coated PbS quantum dots with tunable emission for non-invasive fluorescence imaging in the second near-infrared biological window (1000-1400 nm). Chem Commun 49(69): 7584–7586
44. Naczynski DJ, Tan MC, Zevon M, Wall B, Kohl J, Kulesa A, Chen S, Roth CM, Riman RE, Moghe PV (2013) Rare-earth-doped biological composites as in vivo shortwave infrared reporters. Nat Commun 4:2199
45. Naczynski DJ, Sun C, Türkcan S, Jenkins C, Koh AL, Ikeda D, Pratx G, Xing L (2015) X-ray induced shortwave infrared biomedical imaging using rare-earth nanoprobes. Nano Lett 15(1):96–102
46. Rocha U, Kumar KU, Jacinto C, Villa I, Sanz-Rodriguez F, de la Cruz MDI, Juarranz A, Carrasco E, van Veggel FCJM, Bovero E, Sole JG, Jaque D (2014) Neodymium-doped LaF (3) nanoparticles for fluorescence bioimaging in the second biological window. Small 10(6):1141–1154
47. Hong GS, Zou YP, Antaris AL, Diao S, Wu D, Cheng K, Zhang XD, Chen CX, Liu B, He YH, Wu JZ, Yuan J, Zhang B, Tao ZM, Fukunaga C, Dai HJ (2014) Ultrafast fluorescence imaging in vivo with conjugated polymer fluorophores in the second near-infrared window. Nat Commun 5:4206
48. Tao ZM, Hong GS, Shinji C, Chen CX, Diao S, Antaris AL, Zhang B, Zou YP, Dai HJ (2013) Biological imaging using nanoparticles of small organic molecules with fluorescence emission at wavelengths longer than 1000 nm. Angew Chem Int Ed Engl 52(49):13002–13006
49. Kam NWS, O'Connell M, Wisdom JA, Dai HJ (2005) Carbon nanotubes as multifunctional biological transporters and near-infrared agents for selective cancer cell destruction. Proc Natl Acad Sci U S A 102(33): 11600–11605
50. Matthes R, Cain CP, Courant D, Freund DA, Grossman BA, Kennedy PA, Lund DJ, Mainster MA, Manenkov AA, Marshall WJ, McCally R, Rockwell BA, Sliney DH, Smith PA, Stuck BE, Tell SA, Wolbarsht ML, Zheltov GI, Cheney F, McLin L, Ness J, Schulmeister K, Steinman RM, Sutter E, Zwick H, Protect I.C.N.-I.R (2000) Revision of guidelines on limits of exposure to laser radiation of wavelengths between 400 nm and 1.4 μm. Health Phys 79(4):431–440

Chapter 16

Ex Vivo Imaging, Biodistribution, and Histological Study in Addition to In Vivo Imaging

Shaojuan Zhang

Abstract

In addition to in vivo fluorescence imaging, ex vivo evaluations including ex vivo imaging, biodistribution, and histological study are often conducted to further investigate the biological behavior of fluorescent probes. These studies can further confirm the localization of fluorescent probes at the target sites and demonstrate the probe distribution in various organs and tissues. Such studies can also be extended to cellular level for biochemical analysis. Therefore, ex vivo evaluations are valuable to fully characterizing fluorescent probes in a living system. This chapter provides an overview of techniques for evaluating pharmacological profiles of fluorescent probes ex vivo.

Key words Ex vivo imaging, Biodistribution, Histological study, Pharmacokinetic, Fluorescence imaging

1 Introduction

Ex vivo imaging is a practical way to visualize the accumulation of fluorescent probes in tumors, tissues and organs that are otherwise inaccessible by in vivo imaging due to the limited tissue penetration. It can also be used to validate the result obtained during the in vivo imaging. The result can be further quantified to characterize the biodistribution profile of the fluorescent probes, which is an important component of the preclinical evaluation. The characterization of the probe presence, persistence, and clearance profile can inform the selection of the fluorescent probe dosing schedule, the monitoring schedule for various activity/safety parameters, and the animal sacrifice time points in the definitive preclinical studies [1, 2]. Such information is also valuable in optimizing the fluorescent probes to achieve more desirable pharmacokinetic profiles. For example, to reach a high level of accumulation at the target site, significant amount of targeted fluorescent probes should transition from circulation blood to the tissue of interest. However, many systemically injected fluorescent probes are

Mingfeng Bai (ed.), *In Vivo Fluorescence Imaging: Methods and Protocols*, Methods in Molecular Biology, vol. 1444,
DOI 10.1007/978-1-4939-3721-9_16,

rapidly cleared by the reticuloendothelial system (RES), resulting in poor imaging contrast and undesired toxicity. The biodistribution profiles are therefore essential in accessing fluorescent probes, and can be used to facilitate probe optimization, which can be achieved by changing the size, hydrophilicity, linker, and charge of fluorescent probes.

Following the ex vivo imaging and biodistribution study, targets of interest are often processed by frozen section technique for histological interpretation of fluorescent probes' capability to label certain cells or tissues. In some cases, the high sensitivity of histological study helps to overcome difficulties in visualizing probes with weak signals or otherwise obscured by autofluorescence. Histological studies are often assisted with multiple immunofluorescent staining to reveal fluorescent probe localization. After visualizing multiple markers in individual cell or tissue constituent, staining patterns can be overlapped to provide mixed-color images at the same subcellular level (e.g., membrane, cytoplasm, and nucleus) that identify the fluorescent probe localization [3].

2 Materials

2.1 Ex Vivo Imaging and Biodistribution Study

1. In vivo optical imaging system (IVIS Lumina XR).
2. Small animal surgical instruments (Harvard Apparatus).
3. 1/2 mL BD Lo-Dose™ U-100 insulin syringe with 29 G×1/2 in. (BD: #309306).
4. 24-well cell culture plates (Greiner Bio-One CELLSTAR: #662160).
5. Alfalfa-free imaging diet (Harlan Laboratories).
6. Disposable surgical pads.

2.2 Histological Study

1. 1× phosphate buffered saline (PBS).
2. 4% paraformaldehyde in PBS (Affymetrix: 19943).
3. 30% sucrose in 1× PBS.
4. Tissue-Tek® O.C.T. Compound (Sakura Finetek: #4583).
5. Tissue-Tek® Cryomold (Sakura Finetek: #4557).
6. Microm HM 500 DM Cryostat (MICROM International GmbH, Walldorf, Germany).
7. Fisherbrand™ Superfrost™ Plus Microscope Slides (Fisher Scientific: #12-550-15).
8. MX35 Premier Disposable Low-Profile Microtome Blades (Thermo Scientific: #3051835).
9. Aqua-Hold Pap Pen 2 (Fisher Scientific: #23-769-533).

10. Triton X-100 (Sigma-Aldrich: #T9284) in 1× PBS. Dilute to 0.1 % in PBS prior to use.
11. Bovine serum albumin (BSA).
12. Tween 20 (Sigma-Aldrich: #P9416).
13. DAPI (4′,6-diamidino-2-phenylindole) solution (Thermo Scientific: #62248).
14. Hoechst 33342 solution (Thermo Scientific: #H3570).
15. ProLong Gold antifade mounting medium (Life Technologies: #P36930).
16. Nail polish.

3 Methods

3.1 Ex Vivo Imaging

1. Upon completion of in vivo imaging study, animals are euthanized, and tumors, tissues and organs (e.g., blood, liver, kidneys, spleen, heart, lung, urinary bladder, intestine, stomach, pancreas, muscle, bone, and brain) are collected.
2. Place the tissues and organs of interest on a clean black paper (*see* **Note 1**) or a 24-well plate (*see* **Note 2**).
3. Acquire fluorescence image with an optical imaging system (*see* **Note 3**).
4. Freeze the samples of interest in liquid nitrogen for further histology study (*see* Subheading 3.3).

See Fig. 1 for example [4]. After in vivo fluorescence imaging study involving three treatment groups, including targeted probe (NIR760-mbc94), free dye (non-targeted NIR760), and blocking (blocking agent SR144528 + NIR760-mbc94), tumor and select organs were harvested from the mice and imaged on a black paper.

3.2 Biodistribution Study

1. The fluorescent intensity of the fluorescent probes in the corresponding animal groups is evaluated by drawing ROI along the excised tumor and organs.
2. Optional: The contrast profiles (T/N ratio) are obtained by dividing the fluorescent intensity for the targets by that from normal tissue (e.g., muscle).
3. Create the biodistribution profile graph using GraphPad Prism.
4. Perform statistical analysis using software (e.g., SAS statistical software, etc.).

See Fig. 2 for example [4]. The fluorescent intensity from tumor and selected organs shown in Fig. 1 was quantified and analyzed.

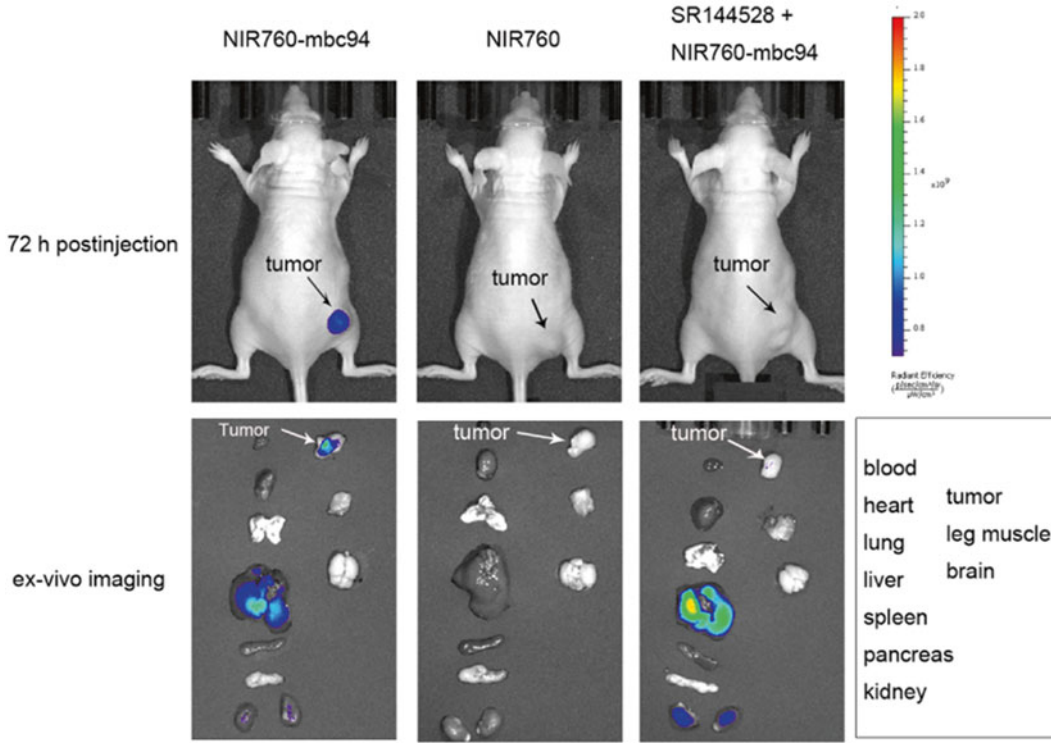

Fig. 1 In vivo and ex vivo optical imaging using near infrared fluorescent probes in tumor bearing nude mice. At 72 h post-injection of NIR760-mbc94, free NIR760, or SR144528 + NIR760-mbc94, tumor (*arrow*) and selected organs (blood, heart, lung, liver, spleen, pancreas, kidney, leg muscle, and brain) were harvested and imaged using IVIS Lumina XR optical imaging system. Reprinted with permission from Ref. 4

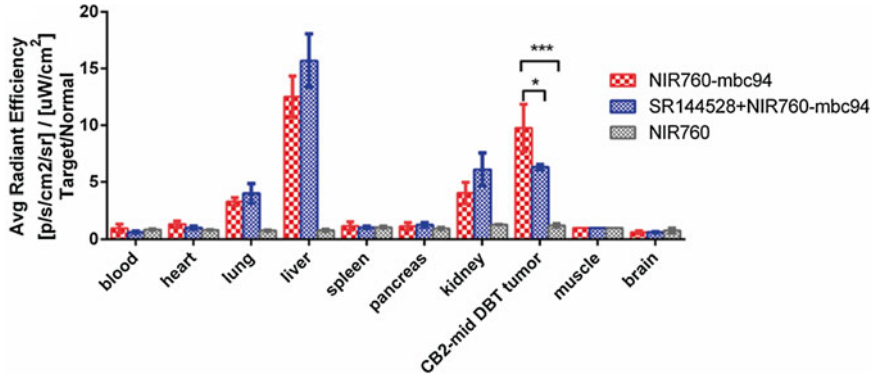

Fig. 2 Biodistribution study using near infrared fluorescent probes in tumor bearing nude mice. Graphical representation of target/normal contrast ratio for the ex vivo study among the NIR760-mbc94, free NIR760, and SR144528 + NIR760-mbc94 groups. Reprinted with permission from Ref. 4

3.3 Histological Study

3.3.1 Embed Tissue into Frozen Blocks

1. Thaw the sample to room temperature.
2. Rinse the sample in cold 1× PBS.
3. Place the sample in freshly thawed 4% paraformaldehyde in PBS for 3 h at 4 °C.
4. Submerge the sample in 30% sucrose in PBS solution at 4 °C for 24 h. Maintain the sucrose level in the solution by routinely replacing with fresh solution.
5. Embed the sample in O.C.T. compound (*see* **Note 4**) in a labeled cassette (*see* **Note 5**).
6. Immerse the cassette completely in liquid nitrogen for 20 s. It will turn white as it freezes.
7. Optional: The sample may be stored in −80 °C freezer for future use.

3.3.2 Preparation of Frozen Sections

8. Add a small quantity of O.C.T. compound on top of the specimen holder inside the cryostat.
9. While the O.C.T. compound starts to freeze, place the frozen block of the tissue sample in O.C.T. compound flatly on the specimen holder (*see* **Note 6**). Make sure the sample is "glued" onto the specimen holder.
10. Secure the specimen holder in the cryostat.
11. Adjust the orientation of the blade to parallel to the desired sample surface.
12. Start sectioning the sample in 20 μm sections until the actual tissue is exposed.
13. Adjust the section thickness to 5–10 μm (*see* **Note 7**).
14. Continue sectioning the sample (*see* **Note 8**). Collect the sliced samples (*see* **Note 9**) using labeled microscope slides (*see* **Note 10**). Routinely clean the knife surface with brushes to remove any O.C.T. traces.
15. Store the sections in −80 °C freezer.

3.3.3 Staining and Fluorescence Imaging of Frozen Sections

16. Thaw the sample to room temperature.
17. Draw a liquid repellent area around the tissue sample using an appropriate pen.
18. Rinse the tissue sections for 2–3 times with 1× PBS.

Optional: Multiple immunofluorescent staining (**steps 19–24**).

To obtain fluorescent probe localization result, fluorescence microscopy is often assisted using immunofluorescent staining techniques. Depending on the antibody, there are two common strategies: (1) direct immunofluorescent staining in which the primary antibody is labeled with fluorescence dye, and (2) indirect immunofluorescent staining in which a secondary antibody labeled with fluorochrome is used to recognize a primary antibody.

19. Cover the sample with 1 % BSA in PBS for 45–60 min to block nonspecific binding sites.
20. Wash the section with PBS for 3–5 times.
21. Cover the sample with 0.1 % Triton X-100 in PBS for 10 min to permeabilize the sample (*see* **Note 11**).
22. Wash the section with PBS for 3–5 times.
23. Primary antibody staining:
    - Cover the sample with 100–150 μL primary antibody solution (*see* **Note 12**).
    - Incubate the sample for 1 h at room temperature or overnight at 4 °C (*see* **Note 13**).
    - Wash the section with PBS for 3–5 times.
24. Optional for indirect staining only: secondary antibody staining:
    - Cover the sample with 100–150 μL secondary antibody solution (*see* **Note 12**).
    - Incubate the sample for 1 h at room temperature (*see* **Note 14**).
    - Wash the section with PBS for 3–5 times.
25. Cover the sample with 1 μg/mL DAPI solution for 15 min at room temperature.
26. Wash the section with PBS for 3–5 times.
27. Put 25 μL of ProLong® mounting medium onto the center of the section slide.
28. Cover the sample with coverslip.
29. Allow the ProLong® mounting medium to dry overnight at room temperature (*see* **Note 15**).
30. Visualize the sample using a fluorescence microscope equipped with the appropriate filters (*see* **Note 16**) and capture fluorescence images (*see* **Note 17**).
31. Analyze the fluorescent images using image-processing and analysis software such as Image J.

See Fig. 3 for example [3]. Macrophages in an inflamed paw and an ischemic hind-limb frozen sections were identified using a fluorescent probe (MF800) and verified by two macrophage-associated surface markers, CD169 and CD68.

4 Notes

1. Use of high quality black paper is highly recommended to prevent illumination reflections. Strathmore, Artagian, coal black paper (part no. 445-109) is known to outperform many other similar products in this regard.

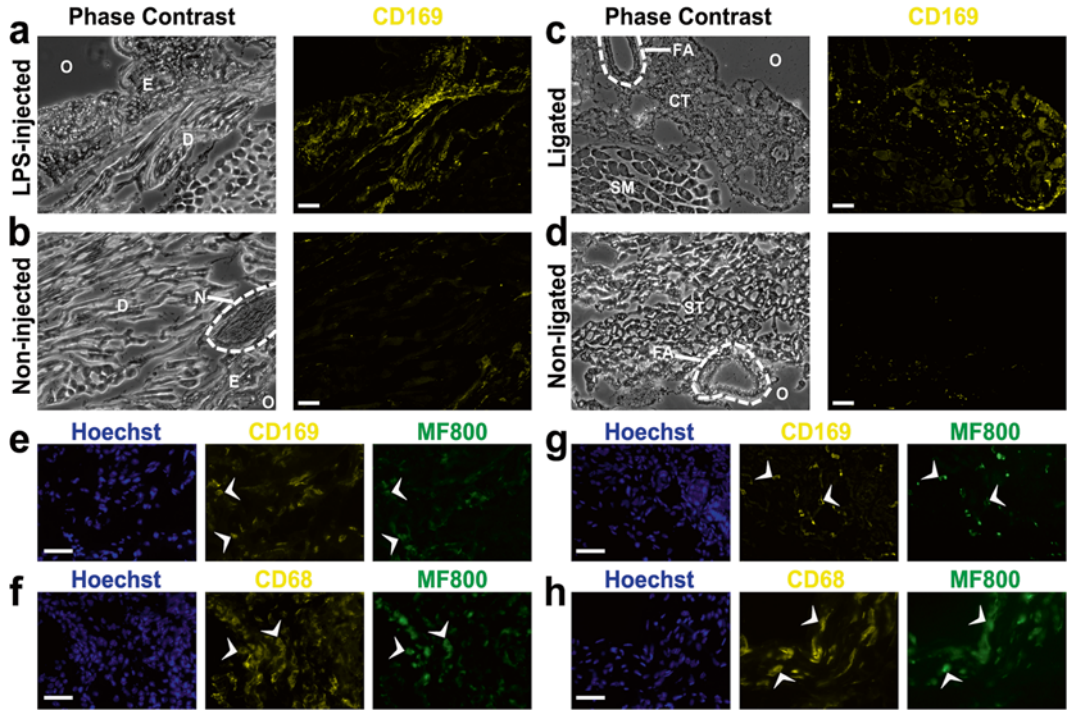

Fig. 3 Immunofluorescence identification for in vivo labeling of macrophages with MF800 in an inflamed paw and an ischemic hind-limb. (**a**–**d**) CD169 macrophage-specific marker expression from regions that emitted (**a**, **c**) strong and (**b**, **d**) minimal MF800 signals in vivo from the paw inflammation (**a**, **b**) and the hind-limb ischemia (**c**, **d**) models. The strong in vivo NIRF regions were characterized by massive macrophage infiltration compared with the dark regions. Scale bars are 100 μm. *O* outside of tissue, *E* epidermis, *D* dermis, *N* nerve, *FA* femoral artery, *CT* connective tissue, *SM* semimembranosus, *ST* semitendinosus. (**e**–**h**) Characterization of cells labeled in vivo with MF800 using two macrophage-associated surface markers, CD169 and CD68 (*yellow*) from the LPS-injected paw (**e**, **f**) and the ligated paw (**g**, **h**). Co-expression of the selected markers on MF800+ cells (pseudo-colored *green*) was confirmed. *Arrowheads* indicate representative co-labeled cells. Scale bars are 40 μm. Reprinted from Ref. 3 under Creative Commons Attribution (CC BY) license

2. High accumulation of fluorescent probes in organs like liver and kidneys is often observed. Target of interest (e.g., tumor) should be imaged separately to avoid false negative results due to the high fluorescence signal from organs in close proximity.
3. Autofluorescence is always a potential problem in fluorescence imaging experiments. Autofluorescence can be minimized by (a) using dyes in the near-infrared region, which does not overlap with general autofluorescence in tissues; (b) feeding animals with appropriate fluorescent imaging diet (e.g., alfalfa-free imaging diet) starting 3 days before in vivo imaging.
4. Avoid air bubbles in O.C.T. compound, which may lead to unsatisfactory sectioning.

5. Make sure the cassette is labeled with appropriate marker pen prior to freezing. It could be challenging to label the cassette afterwards.
6. Sample block edge trimming is optional.
7. The ideal thickness of samples needs to be optimized. It is challenging to cut consistent thin sections. However, thick sections may result in stacking cells that may interfere with the result interpretation due to difficulty of focusing cells of interest.
8. A complete sectioning for fluorescent microscopy should be flat and free of cracks. Carefully examine each sectioning and adjust the next cut for better result. The following aspects may affect the cutting: (a) angle of sectioning, (b) speed of the blade movement, (c) sharpness of blade edge, (d) cutting interval, or (e) the position of the anti-roll plate.
9. Always collect as many sections as possible to ensure sufficient supplies for successful staining.
10. Use adhesion slides to collect the sectioning. Tissue sectioning may fall off from general slides during the staining process due to the lack of binding agent. The slides should be labeled with marker pens certified for histological use. General marker pens might be washed off in the subsequent steps.
11. This is generally achieved with a mild surfactant, which dissolves cell membranes in order to allow large molecules to enter inside the cell. The choice of surfactant should be optimized.
12. Primary and secondary antibody solutions are normally diluted in PBS. The ratio should be optimized. Addition of BSA and Tween 20 is optional.
13. The incubation time needs be determined empirically in your experiment. When overnight incubation at 4 °C is necessary, the sample should be kept in a humid environment (i.e., place wet paper towel in the slide box). For indirect staining, multiple primary antibodies can be added together, but the host must be from different species.
14. The secondary antibody step should be kept to within an hour. Secondary antibodies can be added together if using more than one, but they must be against separate species and corresponding to their primary antibody.
15. Alternatively, the coverslips may be sealed to the slide by applying nail polish or glue along the edges.
16. Select appropriate filter cube for the fluorochrome you want to observe. Common filters include DAPI dye filter, fluorescein isothiocyanate dye (FITC) filter, Texas Red dye filter, and ICG filter.

17. When comparing fluorescent molecules (e.g., targeted probe versus non-targeted probe in tissue samples), fluorescence microscope parameters (i.e., filter set, exposure time, gain, and other parameters) should first be optimized. The same condition should be used throughout the subsequent experiments. It is critical that fluorescence images captured are not saturated.

References

1. Oliveira S, Cohen R, Walsum MS, van Dongen GA, Elias SG, van Diest PJ, Mali W, van Bergen En Henegouwen PM (2012) A novel method to quantify IRDye800CW fluorescent antibody probes ex vivo in tissue distribution studies. EJNMMI Res 2(1):50
2. Kunjachan S, Gremse F, Theek B, Koczera P, Pola R, Pechar M, Etrych T, Ulbrich K, Storm G, Kiessling F, Lammers T (2012) Noninvasive optical imaging of nanomedicine biodistribution. ACS Nano 7(1):252–262
3. Yoo JS, Das RK, Jow ZY, Chang Y-T (2014) In vivo detection of macrophage recruitment in hind-limb ischemia using a targeted near-infrared fluorophore. PLoS One 9(7):e103721
4. Zhang S, Shao P, Bai M (2013) In vivo type 2 cannabinoid receptor-targeted tumor optical imaging using a near infrared fluorescent probe. Bioconjug Chem 24(11):1907–1916

Chapter 17

Experimental Design and Data Analysis of In Vivo Fluorescence Imaging Studies

Ying Ding and Hui-Min Lin

Abstract

The objective of this chapter is to provide researchers who conduct in vivo fluorescence imaging studies with guidance in statistical aspects in the experimental design and data analysis of such studies. In the first half of this chapter, we introduce the key statistical components for designing a sound in vivo experiment. Particular emphasis is placed on the issues and designs that pertain to fluorescence imaging studies. Examples representing several popular types of fluorescence imaging experiments are provided as case studies to demonstrate how to appropriately design such studies. In the second half of this chapter, we explain the fundamental statistical concepts and methods used in the data analysis of typical in vivo experiments. We also provide specific examples in in vivo imaging studies to illustrate the key steps of analysis procedure.

Key words Confidence interval, Hypothesis testing, Power, Randomization, Repeated measures, Sample size, Variation

1 Introduction

The purpose of conducting an in vivo experiment is to test a scientific hypothesis or a series of scientific hypotheses using laboratory animals. Appropriate statistical support is critical in planning and conducting such experiment, as well as in analyzing and interpreting the resulting data. Investigators are always urged to work with statisticians at the beginning of the design stage and are reminded that no experiment should be started without a clear plan of how the resulting data will be collected and analyzed [1, 2].

In this chapter, we address the key statistical aspects in experimental design and data analysis that pertain to in vivo experiments with specific examples tailored to fluorescence imaging studies. The content in this chapter is not intended to be a comprehensive guidance to all the statistical issues in such studies. Rather it focuses on the key components of statistical thinking in designing and analyzing an in vivo fluorescence imaging experiment, so that the researchers will be acquainted to these terms which will help the

Mingfeng Bai (ed.), *In Vivo Fluorescence Imaging: Methods and Protocols*, Methods in Molecular Biology, vol. 1444,
DOI 10.1007/978-1-4939-3721-9_17,

communication between researchers and statisticians. On the other hand, most statistical elements presented here are applicable to all in vivo studies rather than only specific to the fluorescence imaging experiments.

2 Experimental Design

Before conducting an in vivo experiment, most scientists are willing to spend great efforts to ensure that the experiment will address an important research question in a biologically valid and meaningful way [3]. However, oftentimes there are insufficient communications with statisticians regarding how the experiment will be designed and whether the data will be collected in an appropriate way so that they can answer the research question. Without a careful thought on experimental design, the experiment may produce a biased or inconclusive answer to the research question. In principle, the experimental design depends on the objectives of the study and a well-designed experiment is sufficiently powerful to provide unbiased estimates of the effects that are of biological importance. In this section, the key elements that are required to be considered in designing an in vivo experiment are discussed.

2.1 Three Rs

Any researcher who plans an in vivo study should first consider the ethical use of animals. A guideline for this consideration is to use the Three Rs tenet by Russell and Burch [4]: Replacement, Reduction, and Refinement.

Replacement refers to any alternative method that can avoid or replace the use of animals. Reduction refers to any strategy that can reduce the number of animals to the minimum required to achieve the objectives of the experiment. Refinement refers to the modification of husbandry or experimental procedures to minimize pain and distress of the animals. One of these Rs, Reduction, can be particularly achieved by good experimental design and statistical methods, as we illustrate in the following paragraphs.

2.2 Hypothesis Formulation

Once the scientists have identified their research question(s), the immediate next step in the experimental design process is to formally formulate the hypothesis. A research hypothesis is a statement of expectation or prediction to be tested through experiment. In statistics, hypothesis formulation involves the construction of two statements: the null hypothesis and the alternative hypothesis. The null hypothesis reflects that there will be no observed effect or no difference between the comparisons. It is typically formulated through an equality sign and denoted by *H0*. The alternative hypothesis reflects the expected or predicted effect of the experiment. It is typically formulated through an inequality or a "not equal to" sign and is denoted by H_a or *H1*.

The hypothesis has to be clearly stated and appropriately translated into mathematical formulation. For example, a study aims to compare an active treatment to a control treatment in terms of its effect on inhibiting the tumor growth in mice. The tumor size in each mouse will be measured through an imaging technique. Denote by μRx the mean tumor size of the active treatment group and μC the mean tumor size of the control treatment group, then the null hypothesis can be formulated as $H_0 : \mu_{Rx} = \mu_C$. The alternative hypothesis can be formulated either as $H_a : \mu_{Rx} \neq \mu_C$ if the direction of the comparison can be either side or $H_a : \mu_{Rx} < \mu_C$ if the active treatment is expected to reduce the tumor size as compared to the control. The way of how the hypothesis is formulated usually determines the corresponding hypothesis testing procedure, which will be covered in Section 3: Data Analysis.

2.3 Sources of Variation

Variation occurs in every experiment. A well-designed experiment will help identify and control the variation. For a typical in vivo experiment, there are two main sources of variation. One is the biological variation and the other is the technical variation. Two mice from the same genetic strain respond differently from the same treatment. This is due to a biological variation. The two replicate measurements on tumor size from the same mouse through the same measuring method have small differences. This is due to a technical variation, which is oftentimes referred to as a measurement error.

The biological variation can result from differences in species, strain, age, sex and experimental conditions. These usually can be controlled in the experimental design. For example, in a mouse study with the objective to compare different treatment effects, all the factors that may cause different responses (except the treatment) should be well controlled (e.g., choose the mice from the same strain with the same age, balance the sex ratio in all treatment arms, perform the experiment in similar conditions). Only in this way, the observed differences between treatment groups can be attributed to the treatment effect.

The technical variation typically is unavoidable but can be minimized through the choice of design and conduct of the experiment. For example, use the same technique to perform the measurement and/or repeat the reading from an imaging result for a few times.

2.4 Basic Principles

The three basic principles of experimental design are replication, randomization, and blocking [5]. Replication is the repetition of an experiment on a large group of experimental units. Replication allows a researcher to obtain an estimate of the experimental error to determine whether the observed differences in the data are really statistically different. In addition, replication reduces variability in experimental results, increasing the significance and the confidence level. Randomization means the allocation of the

experimental units and the order of performing the runs or trials of the experiment is randomly determined. Statistical methods require that the observations (or errors) to be independently distributed. Randomization usually makes this assumption valid. Blocking is grouping the experimental units with relatively similar background conditions into a block. It is a design technique used to improve the precision of comparing the treatment effects. Blocking is often used to reduce or eliminate the variability from nuisance factors which may influence the experimental response but are not directly interested.

2.5 Design Types

2.5.1 Completely Randomized Design

Completely randomized design is widely used for animal experiments. Animals or experimental units are assigned to different treatments at random. The advantages are simplicity and tolerance of unequal numbers in each group. However, simple randomization cannot take account of heterogeneity of experimental material or variation [2].

2.5.2 Randomized Complete Block Design

Randomized complete block design is used when the nuisance factor (e.g., litters, batches) is known and controllable. Animals or experimental units with similar background conditions are grouped into blocks and then each treatment is randomly assigned to one experimental unit in each block. This design improves the accuracy of comparing the treatments by eliminating the variability among the blocks [5].

For example, an experiment uses 20 female and 20 male mice to study the treatment effects. The technician can only work with four mice per day. Both gender and experiment day may affect the treatment response. Figure 1a is a treatment allocation table from a completely randomized design. Notice that on Tuesday and Wednesday of week 1, all the mice are from the same gender and the treatment assignment within each day is not balanced (e.g., all the mice on Monday of week 2 received control). Figure 1b is a treatment allocation table from a randomized complete block design in which case the treatment assignment and gender are balanced within each day. Clearly the block design is preferred in this example as it effectively controls the nuisance factors that may influence the treatment effect.

2.5.3 Factorial Design

Factorial design is used when studying the effects of two or more factors that are crossed with each other. All possible combinations of the levels of each factor are investigated. Factorial design is also called crossed design. Factorial designs allow a researcher to measure the main effect of each factor as well as the interaction between factors [6]. For example, a phototherapy experiment aims to study the combination effect of a photosensitizer (with or without) and a light irradiation (with or without). In this case, there are two factors of interest and each has two levels. A factorial design will allow animals to be assigned to all the treatment combinations (no treat-

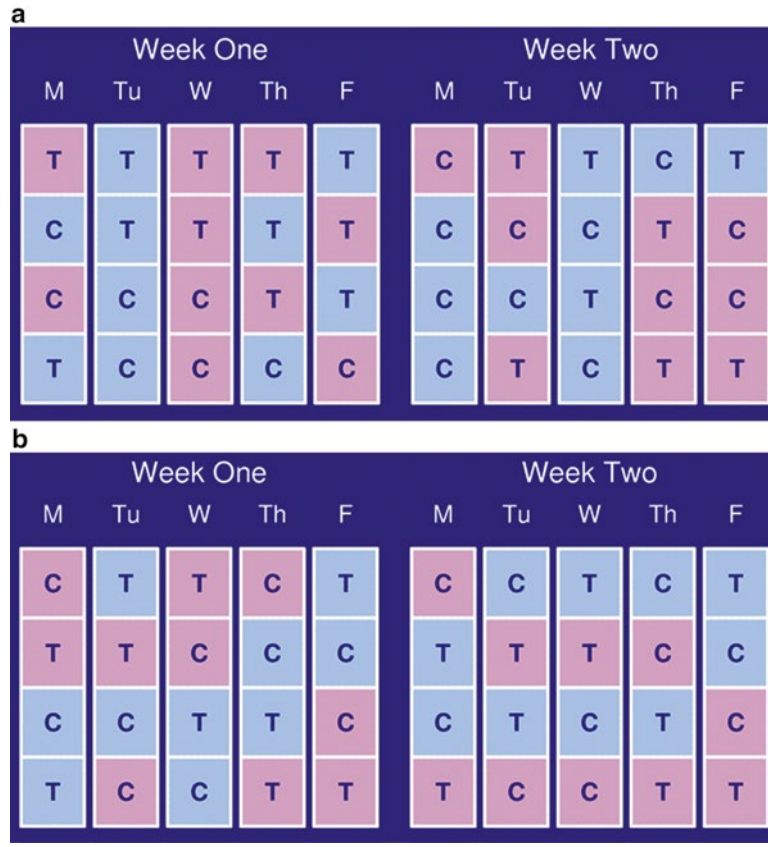

Fig. 1 (**a**) Treatment allocation from a completely randomized design; (**b**) treatment allocation from a randomized complete block design. *T* = treated, *C* = control, *pink* = female, *blue* = male

ment, photosensitizer only, light irradiation only, photosensitizer and light irradiation) and any comparisons among these combinations can be made.

2.5.4 Repeated Measures Design

Repeated measures design is the design in which repeated measurements are made on each experimental unit. The repeated assessments might be measured under different experimental conditions. Measurements on the same experimental unit are correlated. Unlike the block design, which treats the block effects as fixed; the effects of experimental units are typically considered as random in the repeated measures design. Figure 2 provides an example of a repeated measures experiment where the tumor volume from each mouse was measured daily for 6 consecutive days (Day 0–5). The objective of this experiment is to study the tumor growth after receiving the phototherapy (administered on Day 0), where the experimental mice are randomized to two types of phototherapies. When analyzing the data from this kind of experiment, the correlation among the measurements from the same experimental unit has to be appropriately modeled.

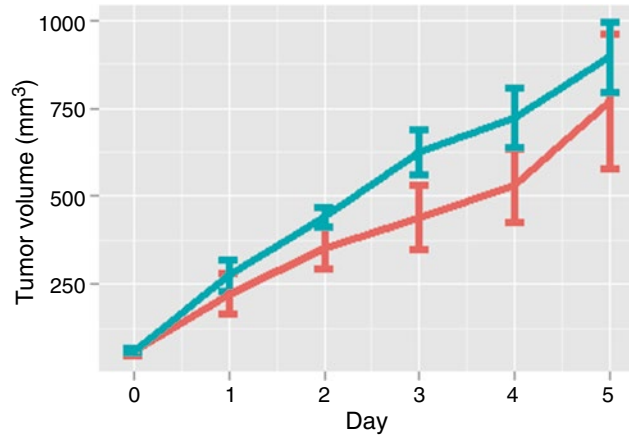

Fig. 2 An example of a repeated measures experiment where each mouse has multiple measures. The mean and SEM (standard error of the mean) for each Day are plotted for each phototherapy treatment

2.6 Sample Size and Power

An experiment that has too few samples and thus is lack of the power to test the hypothesis is unable to reach needed statistical significance. An experiment that uses too many samples is also wasteful and deviates from the Three Rs guideline. Therefore, before starting the experiment, it is very important to perform the sample size estimation. Before calculating the sample size for an experiment, we have to know/estimate the following quantities: (1) effect size (defined below) that we hypothesize to observe, (2) variance or standard deviation of the response variable, (3) significance level, (4) desired power. In addition to these quantities, we also need to know the test/analysis method, which we will defer to Section 3.

2.6.1 Effect Size

The effect size is usually the difference in means (for a continuous outcome variable) or proportions (for a binary outcome variable) that the investigators want the experiment to be able to detect. Such a quantity often has to be a biologically meaningful difference in order to be interested to detect. For example, for an experiment to compare a targeted phototherapy approach versus a non-targeted phototherapy approach in inhibiting the tumor growth in mice, the absolute mean difference in tumor volume (e.g., 50 mm^3) between the two treatment groups after certain days of the therapy can be the effect size of interest. A smaller effect size requires a larger sample size.

2.6.2 Standard Deviation

Often times, the investigators are clear about the effect size of their experiment but uncertain or unaware that variability of the response variable (i.e., the outcome measure) is also very crucial. Unlike the effect size, such variability has to be estimated through previous experiments or literature data. For the same example as we described in the Effect Size paragraph, the investigators need to have an

appropriate estimate of the standard deviation of the tumor volume among the mice in each treatment group. A bigger standard deviation (of the response variable) requires a larger sample size.

2.6.3 Significance Level

Significance level is also called the α level, which is the probability of rejecting the null hypothesis when the null hypothesis is true. It is also known as the type I error or false positive rate. It is typically set at 5% and that is why a p-value is often compared to 0.05 to claim significance or not. A smaller significance level requires a larger sample size.

2.6.4 Power

Statistically, the power is the probability of rejecting the null hypothesis when the alternative hypothesis is true. It is the chance that an experiment will detect the specified effect size and to be considered significant under the given significance level. Choice of power depends on whether the experiment is exploratory or confirmatory, with the latter requires a bigger power in general. A higher power requires a larger sample size.

After presenting the key aspects in experimental design, we provide several examples that are commonly seen in in vivo fluorescence imaging experiments to further illustrate how to take these key aspects into consideration in practice.

Example 1: Independent Sample Experiment

The independent sample experiment is the most common type of study to evaluate the effects of different treatments on a response variable. The experiment unit is typically an independent animal and a single measurement for the response variable is observed from each animal. In this case, all the observations are independent. The hypothesis is often formulated as $H_0 : \mu_1 = \mu_2$ vs. $H_a : \mu_1 \neq \mu_2$ if there are two groups. In designing this type of experiment, it is important to make sure that the animals across the groups are the same or balanced with respect to all the factors (except the treatment assignment) that may affect the response. A blocked randomized design is usually more preferable than the completely randomized design. In this case, the effect size of interest is the between group difference and the variation to estimate is the between animal variation in the response variable. Frequently, equal sample size across groups is used as this allocation ratio maximizes the power.

Example 2: Paired Sample Experiment

In a paired sample experiment, the experimental unit can be a pair of animals (usually matched) or can be a single animal with the measurements being in pairs. For example, an experiment aims to study the inflammation response to a given compound. An active treatment to stimulate inflammation is injected into the footpad of left paw of each mouse, and the untreated right paw is used as the negative control. After 12 h post-injection, a pair of measures is taken from each mouse (one from each paw). The comparison

within the same mouse (left–right) is the quantity of interest. In this case, the hypothesis is often formulated as $H_0 : \mu_D = 0$ vs. $H_a : \mu_D \neq 0$, where D denotes the difference within the same mouse in the response variable. Since each mouse is served as its own control, the only thing differs between the pair of observations is the treatment. In such an experiment, a completely randomized design is usually sufficient. The variation to estimate is the between animal variation in the *difference* of the response (not the response itself), which is typically smaller than the variance in the response itself. Thus, the sample size required in such a paired sample experiment is generally smaller than an independent two-sample experiment.

Example 3: Repeated Measures Experiment

In most fluorescence imaging studies, multiple images will be captured from the same animal at different time points. In this case, the experiment unit is still a single animal but the collected observations are multiple measures on each animal. This allows researchers to track the time course of the treatment effects as such effects usually change over time. The observations within the same animal are correlated and such a correlation needs to be taken into account in both experimental design and data analysis, even if the primary interested outcome may be at a specific (single) time point. For example, in estimating the sample size, if the researchers have a good idea about the correlation in treatment response among these different time points, it could help reduce the required sample size [7]. A positive within animal correlation typically results in a smaller sample size required. The optimal analysis should model all the data together instead of analyzing each time point separately. The primary hypothesis can be specific to a time point if the experiment is mostly interested in comparing the treatment effects at a specific time point, e.g., 48 h after the injection of the treatment.

3 Data Analysis

After collecting the data from a well-designed and conducted experiment, an appropriate statistical analysis is required to assess the experiment result. In principle, the statistical analysis should reflect the objective of the study and should correctly reveal the experimental design. It should extract all the useful information in the resulting data in a way that the result is interpretable, after taking account of the biological variability and the measurement error [2].

Hypothesis testing is the formal procedure to determine whether to accept or reject statistical hypotheses. In hypothesis testing, we are collecting the evidence based on sample data to reject the null hypothesis. Failure to reject the null hypothesis implies that the data are not sufficiently persuasive for us to prefer the alternative hypothesis over the null hypothesis.

There are two types of errors can result from a hypothesis test, type I error and type II error. Type I error occurs when the researcher rejects a null hypothesis when it is true. The probability of making a Type I error is called the significance level and denoted by α. Type II error occurs when the researcher fails to reject a null hypothesis when it is false. The probability of making a Type II error is denoted by β. The probability of *not* making a Type II error is called the power of the test. Table 1 demonstrates the relationship between the hypothesis testing decisions and the two types of errors.

3.1 One-Tailed and Two-Tailed Tests

Two-tailed test is used when a researcher is interested in testing whether there is no effect or no difference between two means (e.g., $H_0 : \mu_1 = \mu_2$) and *Ha* can be in either direction (e.g., $H_a : \mu_1 \neq \mu_2$). The *H0* is rejected if the test statistic is located at either end of the sampling distribution. One-tailed test is used when a researcher want to focus on one specific direction of the *H0* than just no difference (e.g., $H_0 : \mu_1 \leq \mu_2$ and $H_a : \mu_1 > \mu_2$). The *H0* is only rejected if the test statistic is located at the corresponding end of the sampling distribution. Figure 3 gives an example of

Table 1
Relationship between the testing decision and the two types of errors

	Truth	
Decision	H_0	H_a
Do not reject H_0		*Type II error* (β)
Reject H_0	*Type I error* (α)	*Power* (*1-β*)

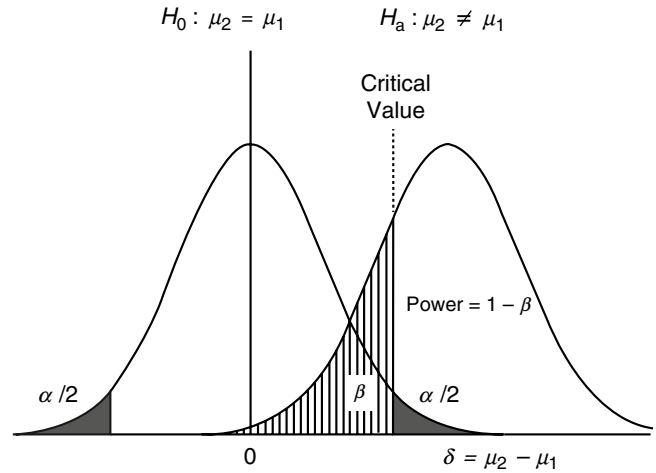

Fig. 3 An example of a two-tailed test

a two-tailed test. The left normal curve is centered at zero, which reflects the situation under the null. The right normal curve is centered at a positive value $\delta > 0$, which reflects the situation under the alternative. The critical value is determined by the significance level α. In this two-tailed test example, the area to the right side of the critical value (under the left normal curve) equals to $\alpha/2$. When the computed test statistic value is greater than the critical value, we reject the null hypothesis. Therefore, in this case, the power is the area under the alternative (right) normal curve to the right side of the critical value.

3.2 *T* Tests

T-test is used when a study aims to compare the means of two groups. The most commonly used t-tests include one-sample *t*-test, two-sample *t*-test, and paired *t*-test.

One-sample *t*-test is used to determine whether the mean of a population significantly differs from a specific value. For example, a researcher is interested in whether the mean tumor size of the active treatment group is reduced to a targeted size, say, 20 mm^3 (e.g., $H_0 : \mu = 20$ and $H_a : \mu < 20$). Suppose the mean tumor size of a sample with n mice is $\bar{x}$ and the standard deviation is s. The t-statistic is calculated as $t = \dfrac{\bar{x} - 20}{s / \sqrt{n}}$. The numerator in the formula measures the strength of the signal (or effect size) in the sample data and the denominator in the formula measures the noise (or variation) in sample data. The *t*-statistic compares the strength of the signal to the amount of noise in the data. If the signal is weak relative to the noise, the *t*-statistic will be smaller. So the difference is not likely to be statistically significant. Then the *t*-statistic is compared to a *t* distribution with $n-1$ degrees of freedom to determine whether it reaches the threshold of statistical significance.

Two-sample *t*-test is used to determine whether the mean of a population significantly differs from the mean of another population. For example, a researcher is interested in whether the mean tumor size of the active treatment group is different from the mean tumor size of the control treatment group (e.g., $H_0 : \mu_{Rx} = \mu_C$ and $H_a : \mu_{Rx} \neq \mu_C$). Suppose the mean and standard deviation of a sample with *na* mice from the active treatment group is $\bar{x}_a$ and *sa*, respectively; and the mean and standard deviation of a sample with *nb* mice from the control treatment group is $\bar{x}_b$ and *sb*, respectively. The *t*-statistic is calculated as $t = \dfrac{\bar{x}_a - \bar{x}_b}{s_p / \sqrt{1/n_a + 1/n_b}}$, where $s_p^2 = \dfrac{(n_a - 1)s_a^2 + (n_b - 1)s_b^2}{n_a + n_b - 2}$ is an estimate of the common (pooled) variance. Similarly, the *t*-statistic is compared to a *t* distribution

with $n_a + n_b - 2$ degrees of freedom to determine whether it reaches the threshold of statistical significance.

Paired *t*-test is used to determine whether the mean of a population significantly differs from the mean of another population where observations in one sample can be paired with the observations in the other sample. Take the Example 2 in the previous section to illustrate. The difference within the same mouse $D = x_{left} - x_{right}$ is the quantity of interest. We first calculate the mean and standard deviation of the differences, $\bar{D}$ and *sd*, then the standard error of the mean difference $SE(\bar{D}) = s_d / \sqrt{n}$. The *t*-statistic is then calculated as $t = \dfrac{\bar{D}}{SE(\bar{D})}$ and compared to a t distribution with $n-1$ degrees of freedom to determine the significance.

However, all the above *t*-tests require the data to be normally distributed. With non-normal data, there are two basic choices. Transform the data (such as logarithm or square root) so that the transformed data appear more normally distributed, or use the nonparametric methods of analysis. Wilcoxon Rank-Sum Test (also called Wilcoxon–Mann–Whitney test) is a nonparametric alternative to the two-sample *t*-test, which is based solely on the rank of the experimental units from the two samples [8]. Wilcoxon Sign-Rank Test is a nonparametric alternative to the paired *t*-test which is based on the sign of the difference from each experimental unit [9].

3.3 ANOVA

Analysis of variance (ANOVA) is a statistical technique for partitioning and analyzing the variation in a continuous response variable, which is developed by Fisher in the 1920s [10]. The purpose of ANOVA is to test whether the means of two or more groups are significantly different. If only two groups are compared, ANOVA will produce the same results as the two-sample *t*-test. One-way and two-way ANOVA are the most commonly used forms of ANOVA.

One-way ANOVA deals with one single factor situation. For example, a researcher is interested in whether the mean tumor sizes of k treatment groups are significantly different (e.g., $H_0 : \mu_1 = \mu_2 = \ldots = \mu_k$ and *Ha*: at least one μi is different from the rest). Suppose a sample of tumor sizes from k treatment groups is collected. The total variation (*SST*) is described as the sum of the squared differences between each observation and the overall mean. The corresponding degrees of freedom (*df*) for the total variation are the total number of observations across all groups minus one ($n-1$). ANOVA partitions the total variation in the response variable into "*within-group*" variation and "*between-group*" variation. The within-group variation (*SSW*) is described as the sum of the squared differences between each observation and the group mean, with the corresponding *df* $n-k$; and the between-group variation (*SSB*) is described as the sum of the squared differences between

Table 2
One-way ANOVA result

Source of variation	*SS*	*df*	*MS*	*F*-statistic
Between	SSB	$k-1$	$SSB\ /\ (k-1)$	$\frac{SSB\ /\ (k-1)}{SSW\ /\ (n-k)}$
Within	SSW	$n-k$	$SSW\ /\ (n-k)$	
Total	SST	$n-1$		

each group mean and overall mean, with the corresponding df $k-1$. Since the sum of squares (SS) depends on the number of observations that contribute to it, the SS is converted into mean squares (MS) by dividing them by their df. The F-statistic is then calculated as the ratio of the between-group MS to the within-group MS. A standard one-way ANOVA result table is shown in Table 2. The F-statistic is compared to an F distribution with $k-1$ and $n-k$ degrees of freedom to determine the significance.

Two-way ANOVA deals with two-factor situation. Take the phototherapy experiment described in the factorial design paragraph as an example. Suppose there are a groups of photosensitizer (denoted as factor A) and b groups of light irradiation (denoted as factor B), and a sample of tumor sizes in all the combination groups is collected. Similar to the one-way ANOVA, the total variation (SST) is also described as the sum of the squared differences between each observation and the overall mean, with the corresponding df $n-1$. The two-way ANOVA partitions the total variation into within-group variation, between factor A group variation, between factor B group variation, and the interaction variation. The within-group variation (SSW) is described as the sum of the squared differences between each observation and the group mean, with the corresponding df $n-ab$; the between factor A group variation (SSA) is described as the sum of the squared differences between each group mean in factor A and overall mean, with the corresponding df $a-1$; the between factor B group variation (SSB) is described as the sum of the squared differences between each group mean in factor B and overall mean, with the corresponding df $b-1$; the interaction variation is denoted as SSAB with the corresponding df $(a-1)(b-1)$. Dividing SS by their df provide MS for each variation. The F-statistic for testing the interaction effect is calculated as the ratio of the interaction MS to the within-group MS. The F-statistic for main effects of factor A and factor B can be calculated as the ratio of the between factor A group MS to the within-group MS, and the ratio of the between factor B group MS to the within-group MS, respectively. A standard two-way ANOVA result table is shown in Table 3.

Similar to the t-test, ANOVA requires the data to be normally distributed as well. Kruskal–Wallis Test is a nonparametric alterna-

Table 3
Two-way ANOVA result

Source of variation	*SS*	*df*	*MS*	*F*-statistic
Factor A	SSA	$a-1$	$\frac{SSA}{a-1}$	$\frac{SSA\ /\ (a-1)}{SSW\ /\ (n-ab)}$
Factor B	SSB	$b-1$	$\frac{SSB}{b-1}$	$\frac{SSB\ /\ (b-1)}{SSW\ /\ (n-ab)}$
Interaction AB	$SSAB$	$(a-1)(b-1)$	$\frac{SSAB}{(a-1)(b-1)}$	$\frac{SSAB\ /\ \{(a-1)(b-1)\}}{SSW\ /\ (n-ab)}$
Within	SSW	$n-ab$	$\frac{SSW}{n-ab}$	
Total	SST	$n-1$	$\frac{SST}{n-1}$	

tive to one-way ANOVA [11]. Kruskal–Wallis test generalizes the Wilcoxon rank-sum test to compare more than two samples. It is also based on the rank of the experimental units from all samples.

3.4 ANCOVA

As discussed in the basic principles, *blocking* is often used to reduce or eliminate the effect of controllable nuisance factors. If a nuisance factor is uncontrollable in the experiment, but it can be measured (usually with a continuous value), then the analysis of covariance (ANCOVA) can be used to improve the precision of an experiment. For example, a researcher is interested in whether the mean tumor sizes of k treatment groups are significantly different after accounting for the weight of mice. In this case, the tumor size is linearly related to weight, but weight is not of interest. The variable weight is called a covariate. ANCOVA adjusts the effect of the weight and reduce the variability from it, so that make the true differences in the tumor size due to treatment groups easier to detect. ANCOVA is an analysis procedure which combines ANOVA and linear regression.

3.5 Repeated Measures ANOVA or ANCOVA

A repeated measures ANOVA is also referred to as an ANOVA for correlated samples. It is the analysis method for the data generated from a repeated measures design. In in vivo studies, typically two types of experiments generate correlated data: a study with measurements taken (on the same experiment unit) repeatedly over time; a study with the experimental unit being a group of animals, for example, the mice from the same litter where litter is the experimental unit. These two types of studies are also referred to as the longitudinal study and the clustered study, respectively. Different from the traditional ANOVA, the outcomes are no longer independent, and the within-unit correlation is modeled in the repeated measures ANOVA. In this analysis model, there are two types of

"effects", namely, the fixed effects and the random effects. For example, the treatment and time variables are typically treated as the fixed effects, as they are nonrandom and predetermined. The animal (in a longitudinal experiment) and the litter (in a clustered experiment) are usually treated as the random effects, as they are considered as random samples from their underlying population.

When there are continuous covariate(s) that need to be adjusted in the repeated measures experiment, the corresponding statistical method is called repeated measures ANCOVA. The model is an extension of the linear regression to handle the correlated data. The key to the repeated measures ANOVA or ANCOVA is the specification of the fixed and random effects.

3.6 Chi-Square Test

All the above methods are for analyzing continuous outcome variables. In frequent cases, the responses are binary and they can take one of two possible values (e.g., respond or not respond). Pearson's chi-square test or Fisher's exact test are the popular methods to evaluate the homogeneity of proportions across different groups. A $2\times k$ contingency table is commonly produced to summarize the data when there are k groups. The formula for calculating the chi-square test statistics is $X^2 = \sum_{2k}^{i=1} \frac{(O_i - E_i)^2}{E_i}$, where Oi is the observed count for the ith cell and Ei is the expected count under independence (between the treatment and response) for the ith cell [12]. The expected count is calculated assuming the marginal row totals are fixed. The degrees of freedom for the test statistics is k-1.

When the sample size is small, Fisher's exact test is usually a preferred alternative to the chi-square test for testing independence. The p-value from the Fisher's exact test is exact while the p-value from the chi-square test is an approximation. The general rule of thumb is that if the expected cell count in any cell is less than or equal to 5, use a Fisher's exact test. If there is more than one factor or there are continuous covariate(s) that the experiment is interested to evaluate or adjust for, the logistic regression is the common approach to handle the binary outcome. We refer to Agresti 2007 for the details of this approach [13].

3.7 Summary Statistics and Inference Statistics

Summary statistics are often used to provide descriptive information about the raw data, such as mean for continuous variables and proportion for binary variables. Standard deviation and standard error are often confused by researchers when they are used to describe the variability. We provide clarification to these two summary statistics in the next paragraph. Inference statistics are often used to make judgments of whether the observed differences between groups are statistically significant or just happen by chance. Inference statistics help researcher to reach conclusions and make inferences from the sample data to general population. Most commonly used inference statistics are p-value and confidence interval.

3.7.1 Standard Deviation vs. Standard Error

Standard deviation (SD) describes the variability or the spread of values in the sample. The sample standard deviation varies from sample to sample, but it stays the same on average when the sample size increases. Standard error (SE) is the standard deviation of an estimator (e.g., standard error of the mean is the standard deviation of the sample mean). It describes the accuracy of an estimator. When the sample size increases, the estimator is based on more information and becomes more accurate, so its standard error decreases.

3.7.2 P-Value

P-value is the probability of obtaining a test statistic as extreme as the one that was actually observed, assuming that the null hypothesis is true. P-value can be viewed as the strength of evidence in support of a null hypothesis. If the *P*-value is less than the significance level, we reject the null hypothesis.

3.7.3 Confidence Interval

Confidence interval is an interval estimate of a population parameter. Suppose we use the same sampling method to select different samples and compute an interval estimate for each sample. Some interval estimates would include the true population parameter and some would not. A 95 % confidence level means that we would expect 95 % of the interval estimates to include the population parameter.

3.8 Multiplicity Adjustment

In many experiments, multiple endpoints are collected and analyzed. Even in an experiment with just one endpoint, multiple comparisons (e.g., among multiple treatment groups) are oftentimes performed. It has been well recognized by statisticians and researchers that multiplicity inflates the type I error of the experiment. The multiplicity adjustment is typically more rigorously discussed and applied in clinical studies than in the in vivo experiments (except for the high-throughput experiment such as a microarray study or a proteomics study). Many multiplicity adjustment procedures have been developed in the statistical literature. The adjustment approach could be very conservative such as the Bonferroni adjustment [14] and some could be less conservative such as the Benjamini–Hochberg FDR (false discovery rate) adjustment [15].

In practice, besides which procedure should be used, the most important question is whether any multiplicity adjustment is needed. For an experiment with multiple endpoints, it is strongly recommended to prespecify a primary endpoint and leave the rest as secondary or exploratory endpoints. For example, if the experiment measures the tumor volume daily for 5 consecutive days, instead of comparing the tumor volume between treatment groups for all days with even important weights, the researcher should determine the primary time point that is of the most scientific/biological interest. If the primary objective of the experiment focuses on one endpoint with one comparison, there is no multiplicity adjustment needed. For the secondary and exploratory endpoints, analysis results without multiplicity adjustment are usually

presented. But both the researchers and readers should be aware that multiple comparisons have been made and a p-value of 0.04 does not really suggest a significant finding under an experiment-wise type I error of 0.05.

Before closing the Data Analysis part, we provide three examples to demonstrate the application of some statistical methods described above.

Example 1: Continuous Data Without Repeated Measures

We continue to use the phototherapy example presented in the factorial design paragraph to illustrate the two-way ANOVA model. This experiment aims to study the combination effect of a photosensitizer (with or without) and a light irradiation (with or without) in inhibiting the tumor growth. The primary outcome of interest is the tumor volume after 7 days of the therapy. There are 5 mice in each photosensitizer-by-irradiation combination group. A two-way ANOVA model with interaction suitably applies to this experiment. Table 4 presents the two-way ANOVA sum of squares result.

In this example, the photosensitizer main effect is significant ($p = 0.0039$), while light irradiation main effect and the interaction effect are not significant ($p = 0.16$ or 0.40). However, the ANOVA table does not directly provide the pairwise comparisons between the treatments. Contrasts need to be specified to evaluate particular pairwise comparisons. In this particular example, photosensitizer alone and the combo therapy show significant inhibition in tumor growth as compared to no treatment, but not the irradiation alone therapy.

Example 2: Continuous Data with Repeated Measures

We use a similar phototherapy example to illustrate the one-way repeated ANOVA model. Instead of 4 ($= 2 \times 2$) different therapies as in Example 2, there are only two therapies being evaluated. The tumor volume is measured at Day 0 right before the treatment administration, and then daily for 5 consecutive days. A popular practice is to use a one-way ANOVA model (equivalent to two sample *t*-test in this case) to analyze each time point separately. Clearly this is suboptimal as it treats each time point as a separate experi-

Table 4
A two-way ANOVA sum of squares result table where each factor has two levels

Source of variation	*SS*	*df*	*MS*	*F*	*p*-value
Photosensitizer	329,445.1	1 (=2 – 1)	329,445.1	16.02	0.0039
Irradiation	48,467.1	1 (=2 – 1)	48,467.1	2.37	0.16
Interaction	16,309.7	1 (=(2 – 1) x (2 – 1))	16,309.7	0.79	0.40
Within	329,102.4	16	20,568.9		
Total	**72,3324.3**	**19**			

Table 5
An example of 2 × 2 contingency table to illustrate the chi-square test

	Treatment	Control	Row total
Respond	15 [11.5]	8 [11.5]	**23**
Not-respond	5 [8.5]	12 [8.5]	**17**
Column total	**20**	**20**	**40 (grand total)**

ment. The correct way is to use a one-way repeated ANOVA to analyze all the data together. Here treatment and time are both treated as the fixed effects, and mouse is treated as a random effect. Moreover, the "treatment" is a between subject effect and the 'time' is a within subject effect. This model separates the total variance into two parts: the between-mouse variance and the within-mouse variance (also called the residual variance). If the primary endpoint is a specific time point, e.g., Day 5, a contrast between two therapies at this time point can be constructed to test the difference.

Example 3: Binary Data (Without Repeated Measures)

The following 2×2 contingency table presents the summary result from an animal experiment which aims to evaluate whether the treatment yields the same response rate or not as compared to the control. A total of 40 mice were randomized to receive either the treatment ($n = 20$) or the control ($n = 20$). After the experiment was done, each mouse was evaluated and then classified as either a responder or a nonresponder. In Table 5, the integer number in each cell is the count of mice. For example, 15 mice in the treatment group responded to the treatment and the rest 5 did not respond to the treatment. In this example, we have the value for the chi-square test statistics as

$$X_2 = \frac{(15-11.5)^2}{11.5} + \frac{(5-8.5)^2}{8.5} + \frac{(8-11.5)^2}{11.5} + \frac{(12-8.5)^2}{8.5} = 5.01 .$$

The expected counts are calculated from the row totals assuming the response rate is independent of the treatment (i.e., $= 0.5$). The numbers in the bracket are the expected counts under independence (e.g., $11.5 = 23 \times 0.5$). The degrees of freedom in this case is $2 - 1 = 1$. The associated p-value is 0.025, which is considered as significant at the 0.05 level.

4 Conclusion

There are many textbooks and articles on experimental design and statistical data analysis. A lot of them are written in the direction for specific disciplines or research types (e.g., agriculture, clinical trials), but the terminologies and methods are mostly general and applicable to in vivo experiments. At the end of [2], the authors

provide a good list of the textbooks for the purpose of consulting and referring.

Many good statistical software tools are available to perform the statistical analysis. Such tools are generally able to perform a wide range of different statistical methods. The most commonly used one by statisticians is SAS. R is another software popularly used by statisticians and it is an open source tool. Both of them require professional trainings in statistics to be able to use them. There are also software packages developed in a way that the researchers with less statistical training are also able to use, for example, SPSS. Recently, a statistical tool specific for analyzing the in vivo studies (InVivoStat) becomes available [16]. No matter which statistical tool is chosen for the data analysis, the person who performs the analysis should always have sufficient knowledge about the underlying statistical methods and should be capable to interpret the results appropriately.

References

1. Festing MF (2002) The design and statistical analysis of animal experiments. ILAR J 43(4): 191–193
2. Festing MF, Altman DG (2002) Guidelines for the design and statistical analysis of experiments using laboratory animals. ILAR J 43(4): 244–258
3. Hanfelt JJ (1997) Statistical approaches to experimental design and data analysis of in vivo studies. Breast Cancer Res Treat 46(2-3): 279–302
4. Russell W, Burch R (1959) The principles of humane experimental technique. Methuen, London
5. Douglas CM (2001) Design and analysis of experiments. Wiley, Hoboken, NJ
6. Quinn GP, Keough MJ (2002) Experimental design and data analysis for biologists. Cambridge University Press, Cambridge, UK
7. Brown H, Prescott R (2006) Applied mixed models in medicine. Wiley, Hoboken, NJ, 2nd Edition Chapter 6.7
8. Mann HB, Whitney DR (1947) On a test of whether one of two random variables is stochastically larger than the other. Ann Math Stat 15:50–60
9. Wilcoxon F (1945) Individual comparisons by ranking methods. Biometrics 1(6):80–83
10. Fisher RA (1919) The causes of human variability. Eugenics Rev 10(4):213
11. Kruskal WH, Wallis WA (1952) Use of ranks in one-criterion variance analysis. J Am Stat Assoc 47(260):583–621
12. Pearson K (1900) X. On the criterion that a given system of deviations from the probable in the case of a correlated system of variables is such that it can be reasonably supposed to have arisen from random sampling. The London, Edinburgh, and Dublin Philosophical Magazine and Journal of Science 50(302):157–175
13. Agresti A (2007) An introduction to categorical data analysis. Wiley, Hoboken, NJ
14. Bonferroni CE (1936) Teoria statistica delle classi e calcolo delle probabilita. Libreria internazionale Seeber
15. Benjamini Y, Hochberg Y (1995) Controlling the false discovery rate: a practical and powerful approach to multiple testing. J Roy Statist Soc B 57(1995):289–300
16. Bate ST, Clark RA (2014) The design and statistical analysis of animal experiments. Cambridge University Press, Cambridge, UK

INDEX

A

Absorption 3, 41, 47, 48, 52, 53, 56, 57, 73, 76, 78, 88, 116, 124, 125, 128, 149, 171
Activatable probes 46
Adipose tissue 110, 113, 114, 117, 119, 120
Analysis of covariance (ANCOVA) 205–206
Analysis of variance (ANOVA) 203–206, 208, 209
Anatomical priors 127
Anesthetic 68, 69, 88, 145, 147, 157
Animal model 49, 58, 67, 128
Antibody 187, 188, 190
Athymic nude mice 30, 39, 41, 75, 78, 169, 176
Autofluorescence 11, 42, 46, 63, 71, 82, 112, 116, 127, 130, 131, 134, 145, 168, 173, 178, 184, 189

B

Binding
  affinity 1, 9, 12, 82
  specificity 1, 6–7, 11, 12, 76–78
Bioconjugation 15–24, 28–29, 38
Biodistribution 27, 34, 82, 99, 105, 106, 183–190
Bioluminescence imaging 67–69
Bioorthogonal 16, 74
Blocking 6–8, 12, 32, 77–82, 158, 164, 185, 195, 205
Blood analysis 143, 148–149, 151
Blood collection 142–143, 147–148

C

Cancer 27, 30, 33, 38, 45, 55–62, 64, 74, 75, 82, 85, 86, 90, 94, 153
Carbon nanotubes 167, 169–171, 173–178
CD13 receptor 74, 76–78, 80
Cell culture 3, 4, 10, 78, 100, 102, 103, 157, 158, 184
Cell tracking 71
Charge-coupled device (CCD) 154
Chi-square test 206, 209
Clonogenic assays 2
Colocalization 2
Computed tomography (CT) 46, 86, 153, 154
Confidence interval 207
Confocal microscopy 68, 79
Conjugation 15, 23, 46–48, 52, 98
Contrast agent 27, 28, 46–47, 58, 89, 98, 124
Control study 50–52
Copper 140, 142, 144, 149
Co-registration 155, 158, 161–163
Coupling reaction
  amide coupling 15–19, 24
  catalyst free inverse electron demand Diels–Alder [4+2] cycloaddition 17, 21–22
  click chemistry (Huisgen cycloaddition) 17, 20
  Michael addition 15, 17, 20
  palladium-catalyzed coupling 17, 20–21, 24
  Suzuki coupling 24
  Thiourea coupling 16, 19–20
CT-FMT 155, 158, 161–163
Cyanine dye 46
Cytotoxicity 1–12

D

Diffraction 168
Diffuse fluorescence tomography (DFT) 123–125, 127, 128, 130, 132–135
Diffuse optical 126
Diffuse spectroscopy 55
3D imaging 87, 110, 154, 161
Drug delivery 97, 98, 160–162
Drug delivery tracking 153, 154, 156–165
Dye exclusion assays 2

E

Effect size 198, 199, 202
Emission 7, 8, 10, 41, 46–49, 55–58, 60, 61, 63–65, 68, 71, 76, 78, 79, 87, 88, 91, 104, 107, 112, 113, 116, 117, 123, 125, 128, 132–135, 140, 141, 150, 153, 154, 157, 158, 161, 162, 170–173
Enhanced green fluorescent protein (EGFP) 110, 112–114, 117, 118

Mingfeng Bai (ed.), *In Vivo Fluorescence Imaging: Methods and Protocols*, Methods in Molecular Biology, vol. 1444,
DOI 10.1007/978-1-4939-3721-9, © Springer Science+Business Media New York 2016

Enhanced permeability and retention (EPR) effect....28
Enzyme....2, 37, 46, 57, 58, 139
Ex vivo imaging....34, 183–185, 187–190

F

Fibroblast activation protein alpha (FAPα)....37–39, 41
Fixed-cell imaging....5
Flow cytometry....68, 98
Fluorescence imaging....5–6, 11, 27, 29, 30, 32, 34, 46–49, 68, 69, 71, 91–93, 139, 157, 158, 161, 162, 167, 168, 171–173, 185, 189, 193, 194, 199, 200
Fluorescence lifetime (FLT) imaging....55–62, 64
Fluorescence microscopy....1–12, 187
Fluorescence molecular tomography (FMT)....67–72, 154
Fluorescence reflectance imaging....27–30, 32, 33, 154, 155
Fluorescence resonance energy transfer (FRET)....37–42, 55
Fluorescence tracer....88, 133
Fluorescent probe....1–12, 15, 18, 37, 38, 57, 74, 82, 154, 183–189
Fluorescent protein....56, 57, 60, 63, 64, 69, 71, 99, 109, 110, 113, 116–117
Fluorescent reporter....57, 59, 60, 67–72
Fluorophore....28, 37, 38, 52, 53, 55–57, 69–71, 74, 124, 128, 130, 135, 154, 169, 178
Frozen sections....164, 184, 187–188
Fur removal....72, 142, 144

G

Goggle system....85–93

H

HDL....153
Histology analysis....50–52
Hydrogels....98, 99, 101–103
Hypothesis testing....195, 200, 201

I

Image-guided surgery....87–90
Image reconstruction....124, 128–130, 132, 135
Imaging....55–62, 64
  analysis....52
  contrast....46–47, 98, 184
  procedure....58, 145–148
Immunofluorescent staining....184, 187
In vitro imaging....22, 38, 57, 60, 99, 140
In vivo imaging....1–12, 27–30, 32, 33, 38, 46, 49, 60, 140, 141, 148, 173, 183–185, 187–190
Independent sample....199
Indocyanine green (ICG)....5–6, 10–12, 28–32, 88–90, 94, 190
Inference statistics....206–207
Inflammation....98–100, 104–106, 177, 189, 199
Integrin $\alpha_v\beta_3$....28, 98
Internal charge transfer (ICT)....139, 151
Intraoperative fluorescence imaging....85–94
Intraperitoneal injection....145
Ischemia....45, 46, 49, 50, 189
Isoflurane....30, 49, 50, 58, 59, 68, 78, 100, 104, 126, 127, 142, 144–147, 157, 160–162, 169, 174
IVIS spectrum....142, 145, 150

L

Lentiviral vector....110
Live-cell imaging....4–5, 139, 140
Luciferase....67, 71, 157
Lymph node....89, 110, 112, 117, 118

M

Magnetic resonance imaging (MRI)....46, 86, 88, 91–94, 98, 124–131, 133, 153–155, 157, 161
Matrix metalloproteinases (MMPs)....37
Metal ion....139–144, 146, 147, 149–151
Microenvironment....55
Molecular imaging....27, 57, 123, 124, 133
Mouse....30, 32–34, 41, 49, 50, 58, 60, 62, 64, 68–70, 72, 78, 98, 100, 104, 105, 107, 110, 113, 116, 117, 119, 141, 145, 147, 148, 150, 157, 163, 171–178, 195, 197–200, 203, 209
MRI-DFT....124–134
MTT assay....3, 12
Multimodal imaging....86, 91, 92, 99, 117
Multiphoton microscopy....111
Multiplate reader....1–12
Multiplicity adjustment....207–209

N

Nanoemulsions....97–106
Nanoparticle....28, 58, 154–157, 159–160, 165, 169
Near-infrared (NIR)....38, 46, 73–76, 78, 80, 82, 88, 97–102, 104–107, 189
NIRFAST....126, 129, 130, 132, 133
NIR-II fluorescence imaging....169, 171–173
Noninvasive....27, 67–72, 153–155

O

Oncology....55
One-tailed test....201
One-way ANOVA....204, 208

Optical imaging 4, 29, 56–60, 67, 78–81, 99, 126, 127, 184–186
Organ harvesting 141–143, 147–148
Organ imaging 146
Organic fluorophore 28, 57
Orthotopic tumor 63, 155

P

Paired sample 199–200
Peptide
  peptide-based probes 37
  synthesis, 38–40
Perfluorocarbon (PFC) 98, 100, 104
Perfusion 142–143, 147–148, 151
Pharmacokinetic 82, 98, 183
Photobleaching 57, 150, 151
Photo-induced electron transfer (PET) 139, 140, 151
Photon scattering 154, 167
Polymerase chain reaction (PCR) 141, 158, 164
Positron emission tomography (PET) 46, 73, 123, 153, 154
Power analysis 198
Preclinical 56, 58, 59, 88–90, 92, 98, 183
Prostate cancer 141, 155, 157, 160–161, 165
P-value 34, 199, 206–209

Q

Quantum dots 28, 71, 169
Quantum yield 55–57, 93, 128
Quencher 37, 38, 46

R

Randomization 195–197, 199, 200, 209
Reactive oxygen species (ROS) 2, 45–48, 50, 53
Repeated measures 197–198, 200, 205–206, 208–209
Reporter gene 69
Reticuloendothelial system (RES) 184
RNA interference (RNAi) 153, 155

S

Sample size 149, 198–200, 206, 207
Saturation binding assay 7–9, 12
Second harmonic generation (SHG) 109, 112, 113, 115–119
Second near-infrared (NIR-II) window 167–171, 173–178
Sentinel lymph node (SLN) mapping 86–89
Signal-to-noise ratio (SNR) 121, 123, 167, 174
Significance level 199, 201, 202
Single-photon emission tomography (SPECT) 123
Single-walled carbon nanotubes (SWCNTs) 169–171, 174–178
Small interfering RNA (siRNA) 154–156, 160–163, 165
Smart probe 37–42
Standard deviation (SD) 8, 34, 80, 81, 106, 198, 199, 202, 203, 206, 207
Standard error (SE) 203, 206, 207
Statistical analysis 33, 34, 52, 82, 133, 147, 185, 200
Stereoscopic imaging 87, 88, 90, 93
Subcutaneous mouse tumor model 27–30, 32, 33
Summary statistics 206–207
Surgical navigation 85–93
Synthesis 18–24, 38, 39, 74

T

Targeting specificity 1, 2
Temporal point spread function (TPSF) 56, 62–65
Terminal deoxynucleotidyl transferase dUTP nick end labeling (TUNEL) assay 158–159, 164–165
Theranostic 98, 155
Therapeutic efficacy 141, 155, 158–159, 164–165
Third-harmonic generation (THG) 109, 112, 117–121
Time-domain 56–58, 60
Tissue penetration 71, 97, 140, 154, 183
Transgenic mouse models 110
Transgenics 69, 72, 110
t-test 34, 82, 202–204
Tumor angiogenesis 28, 73–76, 78, 80, 82
Tumor targeting probe 31, 34
Tumor volume 78, 157, 161, 197–199, 207, 208
Two-photon excited fluorescence (TPEF) 109, 114, 115
Two-photon microscopy 113–117
Two-tailed test 201–202
Two-way ANOVA 204, 205, 208

U

Ultrasound imaging 86, 87, 90, 91, 98

V

Variation 12, 86, 106, 195, 196, 199, 200, 202–205, 208

W

Wilson's disease 141

X

Xenograft 31, 64, 74, 78